# Adventures Through Time and Phase Space: Characterizing the Dynamic Radio Sky, From MHz to GHz, From Seconds to Years

Thesis by
Marin M. Anderson

In Partial Fulfillment of the Requirements for the
Degree of
Doctor of Philosophy

**Caltech**

CALIFORNIA INSTITUTE OF TECHNOLOGY
Pasadena, California

2019
Defended 2019 May 07

© 2019

Marin M. Anderson
ORCID: 0000-0003-2238-2698

# ABSTRACT

Time domain radio astronomy is on the cusp of a revolution. This is particularly true at low radio frequencies, where wide-field arrays are conducting deeper surveys than ever before, in pursuit of elusive transient phenomena. This thesis has opened an unprecedented window on the dynamic radio sky, spanning a wide range in frequency – from MHz to GHz – and a wide range of phenomena – from searches for coherent radio bursts indicative of coronal mass ejections from nearby stars, to the detection of incoherent synchrotron emission from an outflow associated with the tidal disruption of a star by a supermassive black hole at the center of a galaxy.

A significant part of this work has involved the building of the Owens Valley Radio Observatory Long Wavelength Array (OVRO-LWA), a uniquely powerful radio telescope, with the ability to image the entire viewable sky at a 10 second cadence and across nearly 60 MHz of bandwidth. With the OVRO-LWA, I have developed the methods and techniques necessary for pushing further into unexplored regions of radio transient phase space, in the pursuit of sources of radio emission that provide unique insight into various astrophysical phenomena. This includes the follow-up of gravitational wave events in order to search for the signatures of prompt, coherent radio emission associated with compact object mergers, as well as targeted searches for stellar and exoplanetary radio emission as a means of better understanding planetary habitability.

# PUBLISHED CONTENT AND CONTRIBUTIONS

Anderson, M. M., G. Hallinan, M. W. Eastwood, R. M. Monroe, T. A. Callister, J. Dowell, B. Hicks, Y. Huang, N. E. Kassim, J. Kocz, T. J. W. Lazio, D. C. Price, F. K. Schinzel, and G. B. Taylor. 2019. "New Limits on the Low Frequency Radio Transient Sky Using 31 Hours of All-Sky Data with the OVRO-LWA". *ApJ, submitted*.

M.M.A. participated in the building of the instrument, took the observations, participated in the construction of the data reduction pipeline, wrote and conducted the data analysis pipeline, and wrote the manuscript.

Anderson, M. M., G. Hallinan, M. W. Eastwood, R. M. Monroe, H. K. Vedantham, S. Bourke, L. J. Greenhill, J. Kocz, T. J. W. Lazio, D. C. Price, F. K. Schinzel, Y. Wang, and D. P. Woody. 2018. "A Simultaneous Search for Prompt Radio Emission Associated with the Short GRB 170112A Using the All-sky Imaging Capability of the OVRO-LWA". *ApJ* 864 (22): 1–11.

M.M.A. participated in the building of the instrument, took the observations, participated in the construction of the data reduction pipeline, wrote and conducted the data analysis pipeline, and wrote the manuscript. Reprinted with permission from AAS. doi:`10.3847/1538-4357/aad2d7`. arXiv: `1711.06665` `[astro-ph.HE]`.

# TABLE OF CONTENTS

# LIST OF ILLUSTRATIONS

# LIST OF TABLES

*C h a p t e r   1*

# INTRODUCTION

The field of time domain astronomy has undergone a revolution in recent years, spurred by technological advances that have enabled the monitoring of wide swathes of sky with high cadence over extended periods of time. This time domain revolution applies particularly to optical, X-ray, and gamma-ray wavelengths, where optical ground-based facilities (e.g., ZTF, Pan-STARRS, ASAS-SN, and soon LSST), as well as high-energy space-based observatories (e.g., *Swift* and *Fermi*) have already refined the methods of transient detection, rapid follow-up, and classification. The rich discovery phase space in optical and higher energies revealed by these facilities attests to their success in opening up their respective dynamic skies. The next revolution in time domain astronomy has already begun in the new era of gravitational wave detections.

In contrast, systematic searches of the dynamic *radio* sky lag notably far behind their shorter wavelength counterparts, despite the vast number of source classes that are either known or expected to fill radio transient phase space (see Cordes 2007). These include exoplanet emission, brown dwarfs, flare stars, supernovae (SNe), gamma ray bursts (GRBs), tidal disruption events (TDEs), and Galactic Center Radio Transients (GCRTs). High time resolution surveys, generally conducted with single dish instruments, have revealed a rich phase space of sources, e.g., pulsars and fast radio bursts (FRBs). However, at slower (seconds to years) timescales, which are better probed through interferometric imaging surveys, progress has been slower. Radio transients can play a valuable role in providing complementary information to higher-energy observations (e.g., reliable calorimetry for jetted events at higher energies and unobscured population event rates) and in probing the properties (e.g., density, turbulence, magnetic field strength) of the intervening interstellar or intergalactic medium. Critically, sources of transient radio emission can offer insight into unique emission mechanisms with larger scientific implications, as in the case of stellar and exoplanetary transient radio emission informing conditions for habitability.

Direct evidence of the richness of the radio transient sky has been demonstrated with observations triggered by events detected at other wavelengths. These triggered ob-

servations at GHz frequencies (centimeter[1] wavelengths) have had considerable success relative to blind surveys in detecting slow (timescales of days to years) transients. These include radio SNe (e.g., engine-driven SNe; Kulkarni et al. 1998; Berger et al. 2003; Soderberg et al. 2010), GRBs (see Chandra and Frail 2012), TDEs (e.g., Zauderer et al. 2011), and recently binary neutron star (BNS) mergers (Hallinan et al. 2017; Mooley et al. 2018). See Figure 1.1 for the upper limits placed by previous GHz surveys in radio transient phase space, as well as the expected surface density as a function of flux density for a sample of extragalactic radio transient populations.

Low frequency (somewhat arbitrarily defined here as $\lesssim 350\,\mathrm{MHz}$) transient searches have the potential for similarly high yield, given the inherently wide field-of-view of low frequency dipole arrays. This has motivated the slew of new low frequency telescopes and projects conducting transient surveys at low frequencies. These include the Long Wavelength Array (LWA; Ellingson et al. 2009), the Murchison Widefield Array (MWA; Tingay et al. 2013), the Low Frequency Array (LOFAR; van Haarlem et al. 2013), the VLA Low Band Ionospheric and Transient Experiment (VLITE; Polisensky et al. 2016), and the Giant Metrewave Radio Telescope (GMRT; Intema et al. 2017). These surveys are attempting to place more sensitive and constraining limits on the radio transient sky across a wide range of timescales, targeting sources of coherent radio emission, which are bright enough and which evolve on timescales fast enough[2] to be accessible to current low frequency surveys. Given the complexities of low frequency arrays, including challenges associated with calibration, wide-field imaging, and extremely high data rates, technical challenges have been a significant barrier.

At extragalactic distances, potential transient sources at low frequencies include bright, coherent pulses predicted to accompany GRBs and BNS mergers, as well as fast radio bursts (FRBs). The Canadian Hydrogen Intensity Mapping Experiment (CHIME; Bandura et al. 2014), originally designed to measure the power spectrum of neutral hydrogen for mapping baryon acoustic oscillations, is now also outfitted with a back end for detecting FRBs (CHIME/FRB Collaboration et al. 2018) that regularly detects FRBs, including at frequencies as low as $400\,\mathrm{MHz}$ (Amiri et

---

[1]One should also include millimeter wavelengths, which have recently joined the fray (see Ho et al. 2019).

[2]As Metzger, Williams, and Berger 2015 comment, low frequency surveys from facilities like LOFAR are not suited for detecting extragalactic synchrotron transients, due to both flux density and temporal arguments. In the latter case, the slow timescale of evolution at low frequencies leads to the misidentification of these sources as persistent.
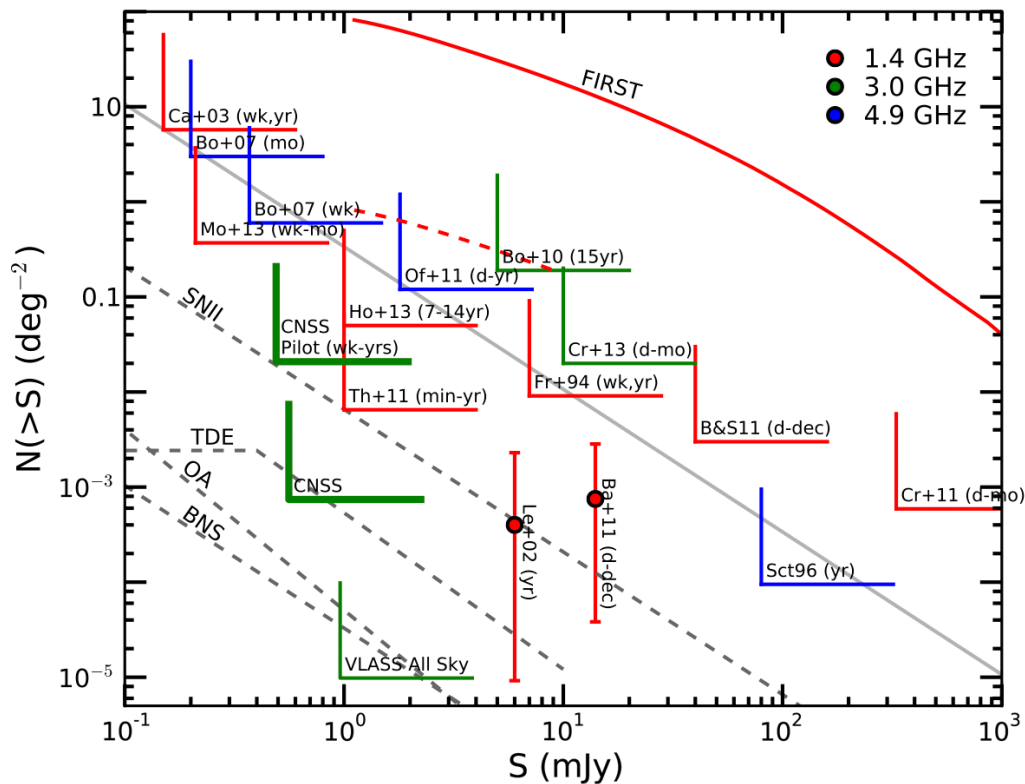
Figure 1.1: Radio transient phase space plot, showing the transient surface density as a function of flux density, for surveys conducted at GHz frequencies for extragalactic transients. All of the surveys placed upper limits, with the exception of the detection of a radio Type II SN (denoted Le+02; Levinson et al. 2002; Gal-Yam et al. 2006) and a nuclear transient (denoted Ba+11; Bannister et al. 2011). Figure 22 of Mooley et al. 2016 reprinted with permission from AAS.

al. 2019). The degree of scatter broadening from the current sample of FRBs indicates the potential for detecting this population at sub-100 MHz frequencies (Ravi 2019).

At galactic distances, potential transient sources at low frequencies include stellar flares and coherent radio bursts (Spangler and Moffett 1976; Bastian 1990; Lynch et al. 2017; Villadsen and Hallinan 2019) as well as radio aurorae on brown dwarfs (Hallinan et al. 2015; Kao et al. 2018), a phenomenon that likely also extends down in mass to exoplanets (Lazio et al. 2004; Kao et al. 2018). Within Earth's atmosphere, potential transient sources include radio emission from meteor after-

glows recently discovered at low frequencies (Obenberger et al. 2014), as well as radio emission from cosmic ray showers and neutrinos (Falcke and Gorham 2003).

Table 4.1 and Figure 1.2 summarize the details and results from previous non-targeted, "blind" radio transient surveys conducted at frequencies below 350 MHz. From these surveys there have been seven distinct transient discoveries, all of which remain mysterious in origin, with no identified progenitors, and no corresponding larger population yet uncovered. These include the following:
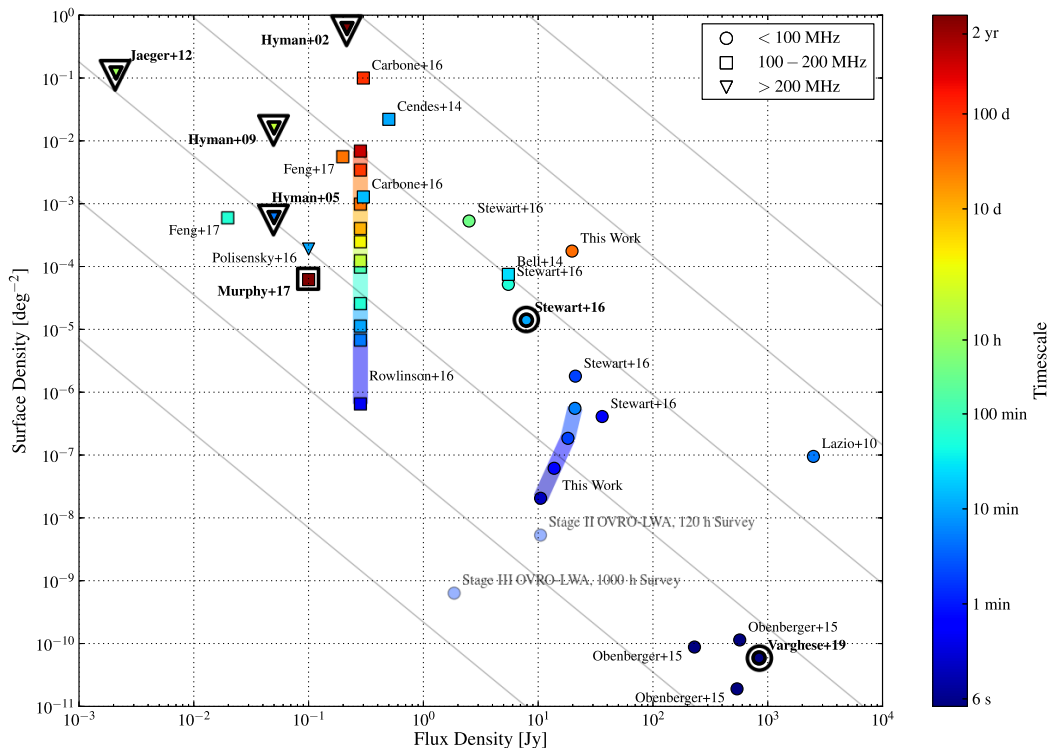


Figure 1.2: Radio transient phase space plot, showing the transient surface density as a function of flux density, for surveys conducted at MHz frequencies. All of the surveys placed upper limits with the exception of 7 transients, marked in bold, described below. The transient work conducted in this thesis (the upper limits denoted as "This Work") are described in Chapter 4.

- There are 3 sources denoted as Galactic Center Radio Transients (GCRTs), due to their discovery during separate monitoring campaigns of the Galactic center. The first of these, GCRT J1746-2757, was found in 330 MHz VLA observations. The source evolved on the timescale of a few months and reached approximately 200 mJy flux densities (Hyman et al. 2002). GCRT J1745-3009 was also discovered at 330 MHz with the VLA, and subsequently

detected with the GMRT. Its inferred brightness temperature and spectral behavior indicates a coherent, steep-spectrum source, exhibiting Jy-level bursts of approximately 10 minutes in duration. These pulses were repeatedly detected with a 77 min period (Hyman et al. 2005; Hyman et al. 2007). GCRT J1742-3001 was discovered at 235 MHz with the GMRT, and reached 100 mJy flux densities and evolved on a month timescale (Hyman et al. 2009).

- Jaeger et al. 2012 detected the source J103916.2+585124 in 325 MHz VLA archival observations that were selected based on their coverage of the Spitzer-Space-Telescope Wide-area Infrared Extragalactic Survey (SWIRE) Deep Field. The source reached 2 mJy flux densities with duration of approximately 12 hours, and has no identified progenitor, despite extensive multi-wavelength coverage of the field in which it was detected.

- TGSSADR J183304.4-384046 was found in comparison of the 150 MHz GaLactic and Extragalactic All-sky MWA (GLEAM) and TIFR GMRT Sky Survey (TGSS) catalogs. Given the 180 mJy flux density and long (1–3 yr) timescale of evolution of this source, this candidate transient may be an example of an extragalactic synchrotron transient detected at low frequencies, the first of many such transients which may be uncovered by the Square Kilometre Array (SKA; see Metzger, Williams, and Berger 2015) – follow-up observations are ongoing (Murphy et al. 2017).

- From 10,240 hours of simultaneous monitoring with LWA1 and LWA Sevilleta (LWA-SV; Cranmer et al. 2017), a possible transient was discovered at 34 MHz with an approximately 830 Jy flux density, with a duration of 15–20 seconds (Varghese et al., *ApJ* submitted). The simultaneous detection of the source by both LWA stations, and consistent sky position as measured by the 2 stations (which are $\sim$ 75 km apart) is used to rule out an atmospheric origin.

- Stewart et al. 2016 detected the source ILT J225347+862146 at 60 MHz in the LOFAR Multifrequency Snapshot Sky Survey (MSSS). It reached peak flux densities of 15–25 Jy over the timescale of a few minutes, and lasted for 11 minutes in total. Although the origin of this transient emission remains a mystery, with no identified higher-energy counterpart, the flux density and implied rate of this event suggests that this may be a dominant population in the low frequency transient sky.

Existing radio transient searches have still only scratched the surface of the vast available parameter space, and the handful of detections yielded thus far at MHz frequencies remain poorly understood or characterized. At GHz frequencies, transient discovery is still dominated (on timescales > 1 s) by follow-up of events detected at other wavelengths.

This thesis aims to open a new window on the dynamic radio sky, placing more sensitive constraints on as-yet unexplored regions of the transient phase space. It also aims to emphasize the critical importance of surveys at radio frequencies for characterizing sources through emission mechanisms that can provide new insight on the relevant physics, as well as for targeting populations that are otherwise inaccessible at other wavelengths. This is done through surveys that are designed to target, or are otherwise optimized to find, specific transient populations. In the following, I detail the sources of transient radio emission, in both the MHz and GHz regimes, explored in this thesis and the motivation behind the detection of these source classes. I end by outlining the contents of this thesis.

## 1.1 The MHz Transient Sky

**Compact Object Mergers**

Searches for prompt, coherent radio counterparts to GRBs date back as far as 1975, when GRBs were still mysterious phenomena of unknown origin but suspected to be extragalactic in nature (Baird et al. 1975). The possibility of detection of a pulse with measurable dispersion was sought after as a means of definitively proving the extragalactic distances to GRBs. Even after host galaxy identification demonstrated the extragalactic origins of GRBs, targeted searches for prompt radio emission continued (e.g., Inzani et al. 1982; Koranyi et al. 1995; Dessenne et al. 1996; Benz and Paesold 1998; Balsano 1999; Bannister et al. 2012; Granot and van der Horst 2014). Systematic detection would provide a radio source population with the ability to probe the density and turbulence of the intergalactic medium (Inoue 2004), and with utility as a diagnostic of accretion-powered jet physics (Macquart 2007). Searches for prompt radio emission have continued to the present day (Obenberger et al. 2014; Kaplan et al. 2015), motivated by the value of such emission as an electromagnetic counterpart to gravitational wave events associated with compact object mergers (Kaplan et al. 2016). See Table 3.2 for details on all previous searches targeting GRBs for prompt, coherent radio emission.

There are numerous models predicting this speculative but potentially very valuable

counterpart to GRBs and BNS (as well as neutron star–black hole) mergers in the form of a short, bright, coherent pulse of low frequency radio emission. The models predicting this coherent radio emission span all stages of the compact object merger process, from (phase 1) the final in-spiral of the binary neutron stars; to (phase 2) a short-lived, post-merger supramassive neutron star; to (phase 3) the post-collapse stage during which the gamma-ray emission is produced.

In the pre-merger stage (phase 1), Hansen and Lyutikov 2001 consider the magneto-spheric interaction of a magnetar–NS binary system and the generation of a coherent radio burst in the surrounding plasma environment (see also Lyutikov 2013). This has parallels in the Jupiter–Io system, whereby the latter supplies the plasma current and is electrodynamically coupled to the magnetosphere of the former. From Equation 13 of Lyutikov 2013, the observed flux is given by

$$F = \epsilon_R \, \frac{(G \, M_{\mathrm{NS}})^3 \, B_{\mathrm{NS}}^2}{4\pi c^5 d^2 \nu \, (-t/t_t)^{1/4}}. \tag{1.1}$$

The critical component of this formulation for the flux is $\epsilon_R$, the efficiency with which wind power is converted into coherent radio emission. Lyutikov 2013 estimate $\epsilon_R = 10^{-5}$, however the uncertainty on this efficiency factor is likely orders of magnitude. The value estimated for $\epsilon_R$ by Lyutikov 2013 is such that Equation 1.1 is approximately equal to the flux density of the Lorimer burst (Lorimer et al. 2007). The other key feature of this model is that the coherent radio emission is predicted to increase as $t^{-1/4}$ until it peaks at the time of merger $t_t$ (where $t_t$ is on the order of a few ms).

Pshirkov and Postnov 2010 consider a low-frequency radio burst generated in the relativistic plasma outflow from the highly magnetized, rapidly rotating magnetar which is predicted to form in the brief stage (phase 2) between the merger and final collapse. Rotational energy in the rotationally-supported supramassive NS is converted to radio luminosity. From Equation 7 of Pshirkov and Postnov 2010,

$$F = 8 \times 10^{3+15\gamma} \dot{E}_{50}^{1+\gamma} \left(\frac{1 \, \mathrm{Gpc}}{d}\right)^2 \, \mathrm{Jy}, \tag{1.2}$$

where the efficiency with which rotational energy $\dot{E}$ is converted into radio luminosity is parameterized as $\eta$, which scales with $\dot{E}$ as

$$\eta = 10^{-5} \left(\frac{\dot{E}}{10^{35} \, \mathrm{erg \, s^{-1}}}\right)^{\gamma}, \tag{1.3}$$

for a $\gamma$ in the range of $-1/2$ to $0$.

Finally, Usov and Katz 2000 predict a low-frequency radio burst that may be produced in the post-merger (phase 3) stage (as well as in long GRBs) through the interaction of a strongly magnetized wind with the circumburst medium. In this model, the coherent low-frequency emission is produced by the time-variable surface current that exists at the wind/ambient plasma-boundary. From Equation 14 of Usov and Katz 2000,

$$F = \frac{\delta(\beta - 1)}{\Delta t \, \nu_{max}} \left(\frac{\nu}{\nu_{max}}\right)^{-\beta} S_\gamma, \tag{1.4}$$

where $S_\gamma$ is the fluence in gamma-rays for the corresponding GRB, $\nu_{max}$ is the frequency at the lower cut-off (maximal flux) of the power spectrum (power law index $\beta$) describing the radio emission, and $\delta$ is the efficiency factor describing the relative radio and gamma-ray fluences. As with the efficiency factors given in the previous models, the value of $\delta$ is highly uncertain.

Other models predicting post-merger coherent radio emission include synchrotron maser emission generated during the GRB fireball phase (Sagiv and Waxman 2002) and inverse Compton radiation generated in the surrounding magnetized plasma by magnetohydrodynamic modes excited by the gravitational waves produced in the merger (Moortgat and Kuijpers 2005).

This diverse array of models are generally consistent in their prediction of a coherent and intrinsically short-duration burst of radio emission that occurs within a window of several seconds to the production of the gamma-ray emission, with a steep negative spectral index that favors observations at lower frequencies.

**Extrasolar Space Weather**

Transient sources in the radio sky were first uncovered at MHz frequencies, with the discovery of the Sun as a source of bright, non-thermal, and bursty radio emission at 50 MHz, when it was found to be the cause of intermittent interference in British radar during WWII (Hey 1946). The detection of varying, non-thermal radio emission from Jupiter followed at 20 MHz (Burke and Franklin 1955). It is fitting that both Jupiter and the Sun were the first transient radio sources at meter-wavelengths – similar transient radio emissions, but from stars and planets outside the solar system, are now one of the primary targets in low frequency transient surveys as a means of understanding conditions for planetary habitability.

All of the planets in our solar system with internal dynamos capable of generating large-scale magnetic fields are also capable of generating radio emission (Zarka

1998). This radio emission is powered by the electron cyclotron maser instability (ECMI; see Treumann 2006) that produces coherent emission at the cyclotron frequency, which scales linearly with the local magnetic field strength, as

$$\nu_{\mathrm{cyc}} \, \mathrm{MHz} = 2.8B \, \mathrm{G}. \tag{1.5}$$

In most cases, the keV electrons producing this emission are provided by the coupling between the incident solar wind and the planetary magnetosphere. An important exception to this is Jupiter, whose emission is dominated by its electrodynamic interaction with Io, which is an important source of plasma in the Jovian magnetosphere. In either case, the interaction results in magnetic field-aligned currents which deposit energy into the upper atmosphere, generating auroral emission (at visible, UV, and other wavelengths) as well as electron cyclotron maser emission (ECME).

Figure 1.3 shows the "radiometric Bode's law" relating the output planetary radio power for magnetized bodies in the solar system to the power in the solar wind at the distance to those bodies. It was originally formulated by Desch and Kaiser 1984 to correctly predict the radio flux from Uranus and Neptune (as measured by Voyager 2), and later used by Farrell, Desch, and Zarka 1999 and Zarka et al. 2001 to extrapolate this relation in application to exoplanets. The scaling relation demonstrates that the median, isotropic radio power is strongly correlated with the amount of energy deposited into the magnetosphere by the steady-state solar wind, and which is therefore a proxy for distance (for Jupiter, this is applicable only to the non-Io auroral emission). The scaling up of Bode's law for exoplanetary systems relies on this relationship by bringing the planetary magnetosphere closer to the host star where it will experience a denser and faster stellar wind and therefore larger stellar wind pressure.

Critically, this scaling relation does not take into account variability in the stellar wind nor transient mass loss events impacting the planetary magnetosphere. For example, the Earth's radio power increases by 2 to 3 orders of magnitude for a factor of 2 increase over the steady-state solar wind velocity (see Figure 1.4; Gallagher and Dangelo 1981).

This planetary radio emission, and the possibility of its detectability from exoplanets, has motivated monitoring programs of individual (known, or expected) exoplanetary systems, typically at low frequencies[3] where this emission is most likely (e.g., Jovian

---

[3]Although, the possibility of kG magnetic fields in young and hot, massive planets with strong magnetic dynamos motivates searches at GHz frequencies (Reiners and Christensen 2010).
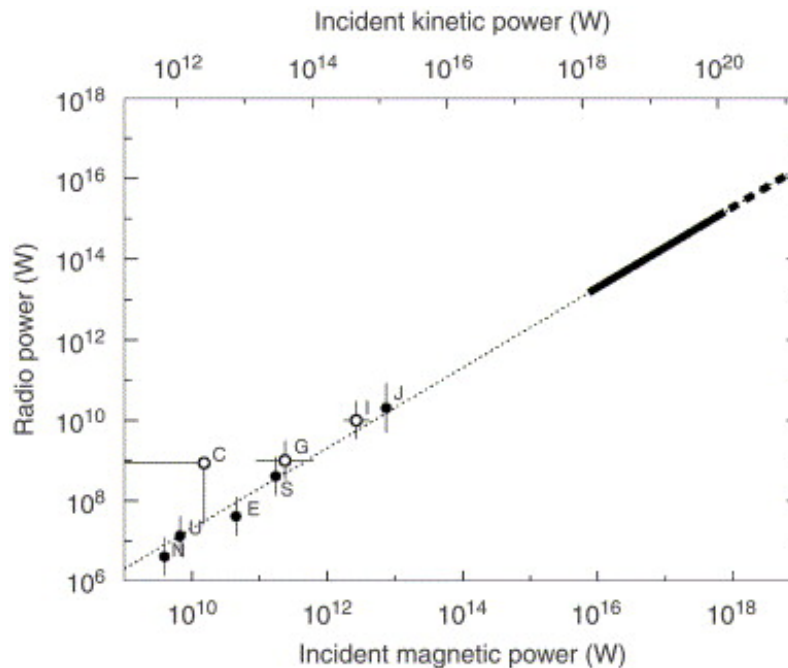
Figure 1.3: Radiometric Bode's law, relating the output planetary radio power with the power input into the magnetosphere from either the magnetic energy flux of the Solar wind (bottom axis), or its kinetic energy (top axis). This empirical relation is shown for all the magnetized bodies in the solar system, and extrapolated up to hot Jupiters for the case of power provided by the stellar wind–planet magnetospheric interaction (thick solid line) and the case of dipolar and unipolar star–planet interaction (thick dashed line). Figure 6 of Zarka 2007 reprinted with permission from Elsevier.

decametric emission cuts off above approximately 40 MHz). Table 5.1 details all radio surveys targeting exoplanets to-date. In addition, the transient brightening of planetary radio emission associated with variability in the activity of the host star motivates long-term monitoring of as many planetary systems as possible, in order to increase the likelihood of observing this transient emission.

Detecting exoplanetary radio emission, and therefore probing exoplanet magnetic fields and dynamos, provides insight into conditions for habitability – specifically, how susceptible a planetary atmosphere is to erosion from quiescent and transient mass loss events from its host star (Khodachenko et al. 2007; Lammer et al. 2012; Ribas et al. 2016). In addition to understanding the prevalence of strong, planetary magnetic dynamos, characterizing the magnetic activity, and particularly the transient mass loss, of host stars is necessary to form a complete picture of extrasolar space weather environments, and the associated impact on habitability, around other
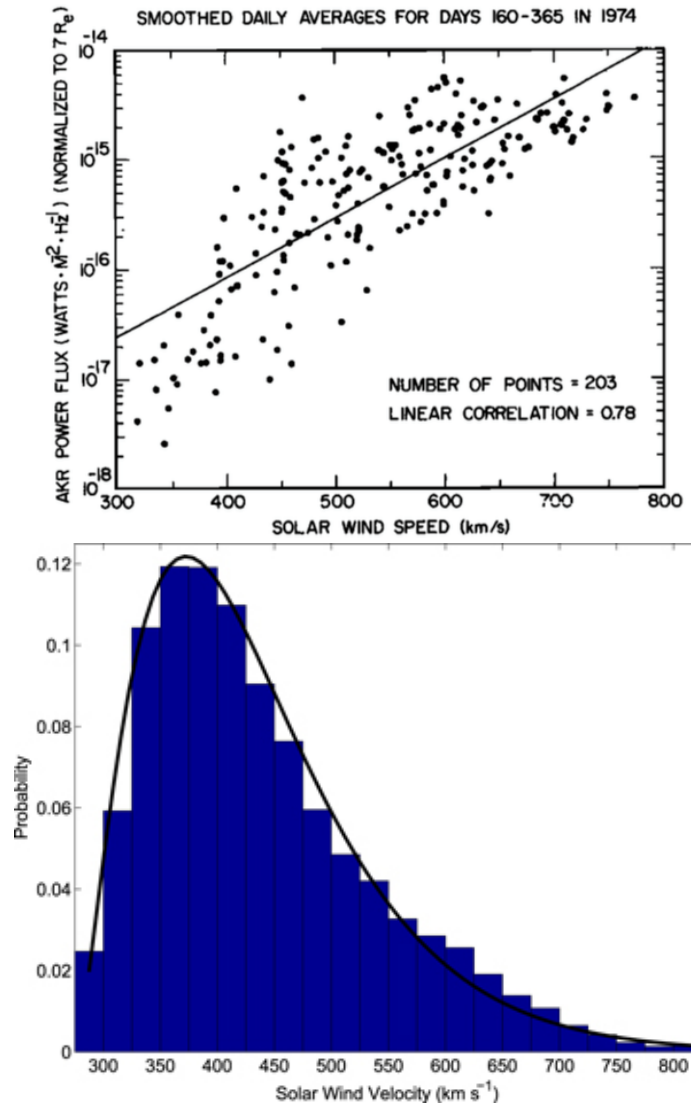
Figure 1.4: The power in Earth's auroral kilometric radiation (AKR) as a function of incident stellar wind speed (top), from Gallagher and Dangelo 1981, and a histogram of the probability distribution of solar wind speeds from Li, Zhanng, and Feng 2016. The implication is that radio emission from an exoplanet may brighten significantly relative to the steady state power, motivating the monitoring of a large number of exoplanets for extended periods to catch transient increases in planetary radio flux from temporary increases in stellar wind speed. Figure 5 of Gallagher and Dangelo 1981 reprinted with permission from the American Geophysical Union. Figure 2 of Li, Zhanng, and Feng 2016 reprinted with permission from AAS.

stars.

Coronal mass ejection (CME) events can be traced on the Sun through Type II radio bursts – coherent plasma emission generated by electrons accelerated at the shock

front of the CME as it propagates through the outer atmosphere of the Sun (Gopal-swamy et al. 2001). This emission is generated at the local plasma frequency and its higher harmonics, as

$$\nu_p \, \text{kHz} \approx 9 \, \sqrt{n_e \, \text{cm}^{-3}}. \tag{1.6}$$

Therefore, drifts in the frequency of the emission can be traced to propagation of the shock into the outer (inner) regions of the corona where the density drops (increases). The rate of drift indicates the speed of the shock.

Type II radio bursts, and CMEs, have never been observed in stars other than the Sun. However, understanding how transient mass loss behavior scales with magnetic activity in other stars is critical in the context of habitability, where the majority of habitable zone planets orbit around low mass M dwarfs, which are both more magnetically active and have longer activity lifetimes than the Sun. Figure 1.5 shows an empirical scaling relation from the Sun between ejected CME mass and observed flare flux (Aarnio et al. 2011). It is an open question whether this relation can be extrapolated into the regime of more magnetically active stars, or whether the different magnetic topologies present on active stars can play a role in confining CMEs and preventing their release into the surrounding space weather environment (see, e.g., Alvarado-Gómez et al. 2018). This motivates the need for low frequency radio surveys that are sensitive to Type II stellar bursts that can monitor a large sample of systems for extended periods of time, in order to begin characterizing transient mass loss for a wide range of spectral types and levels of magnetic activity.

## 1.2 The GHz Transient Sky

The radio emission from extragalactic explosions is powered by synchrotron emission generated from the interaction between the associated shock and the surrounding medium, which accelerates the electrons that generate synchrotron emission from the magnetic fields amplified in the shock (Chevalier 1982). Radio emission can therefore provide information on the density of the surrounding medium and a constraint on the pre-explosion environment, as well as constraints on the outflow geometry, size, energy, and ejecta mass (Chevalier 1998).

Radio-detected synchrotron explosions also present an alternate means of detecting known transient populations (e.g., TDEs, SNe, GRBs, binary neutron star mergers, as well as the orphan off-axis afterglows of all populations) from the more traditional
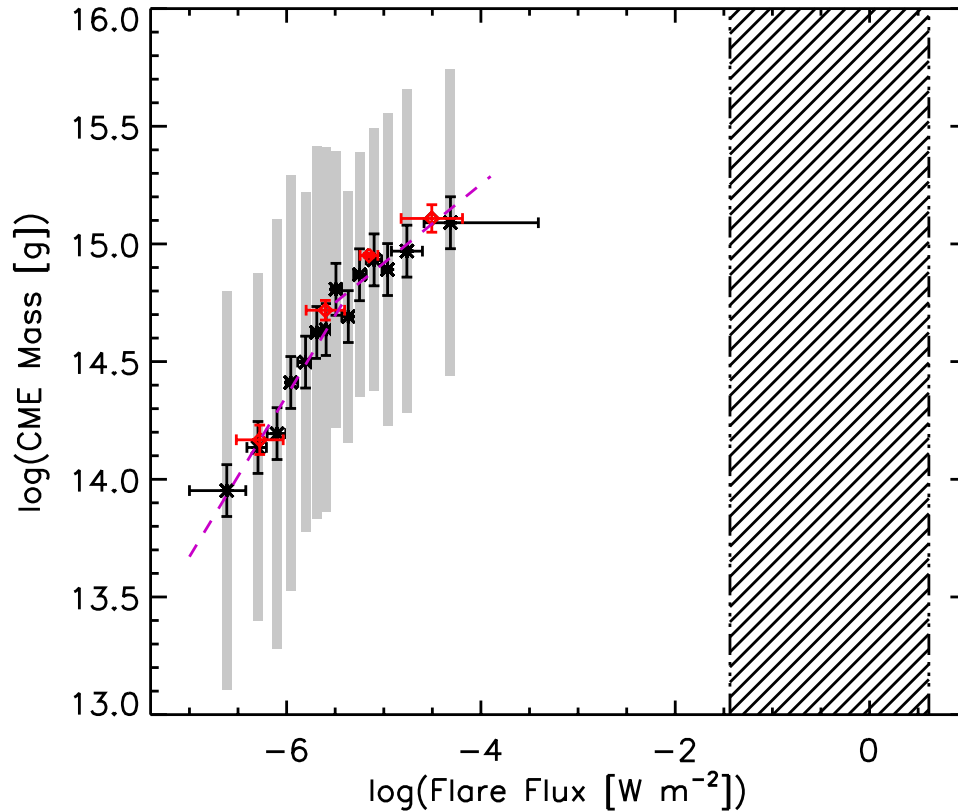
Figure 1.5: The relationship seen for the Sun between measured CME mass and associated X-ray flare flux. The two quantities show a power-law scaling relation on either side of the "knee". The hatched region denotes the flare fluxes observed from young, active stars. A major open question is whether this Solar CME-flare flux relation can be reliably extrapolated into the region of highest flare flux from active stars. Figure 15 of Aarnio et al. 2011 reproduced with permission from Springer.

methods of time domain optical and higher energy surveys, which can be biased[4] against highly dust obscured events in the case of the former (Mattila et al. 2012) and biased against highly jetted (and beamed away from Earth) events in the case of the latter (Granot et al. 2002).

However, despite these intrinsic benefits for the radio detection of extragalactic explosions in further characterizing events and their true rates, systematic discovery of these sources in radio surveys is distinctly lacking, with the vast majority of detections made through follow-up observations. This is beginning to change with the advent of radio surveys uniquely and optimally designed to detect and classify

---

[4]Although, radio searches may present their own bias against significantly underdense environments (e.g., with type Ia SNe; Chomiuk et al. 2012).

these extragalactic synchrotron events. This was demonstrated by the Karl G. Jansky VLA Caltech NRAO Stripe 82 Survey (CNSS), which combined (1) a survey cadence well-matched to the expected timescale of evolution of the radio emission with (2) a fast survey speed, designed be wide and shallow in order to target a large and local (< 200 Mpc) population of transients, which minimizes the number of false positive transients (in the form of AGN variability) and increases the likelihood of host galaxy identification. It was this survey technique that led to the discovery of the radio TDE described in Chapter 6, and which is now being applied to the VLA Sky Survey (VLASS) and is expected to find many 100s of such extragalactic explosion events.

## 1.3 Outline of This Thesis

This thesis is outlined as follows. Chapter 2 details the construction, commissioning, and development work that went into making the Owens Valley Radio Observatory Long Wavelength Array (OVRO-LWA) a science-ready instrument. Each of the remaining chapters of this thesis explores a different class of transient phenomena: Chapter 3 describes the deepest search for prompt, low-frequency radio emission associated with compact object mergers to-date; Chapter 4 describes the most sensitive non-targeted search for low-frequency, coherent transients on timescales ranging from seconds to days; Chapter 5 describes the largest survey designed to search for extrasolar space weather (stellar radio bursts and exoplanetary radio emission); and finally, Chapter 6 shifts to the GHz-radio transient sky to describe the first radio-discovered tidal disruption event (TDE). In Chapter 7, I summarize and look to the future.

**References**

Aarnio, A. N., et al. 2011. "Solar Flares and Coronal Mass Ejections: A Statistically Determined Flare Flux - CME Mass Correlation". *SoPh* 268 (): 195–212. doi:`10.1007/s11207-010-9672-7`. arXiv: `1011.0424 [astro-ph.SR]`.

Alvarado-Gómez, J. D., et al. 2018. "Suppression of Coronal Mass Ejections in Active Stars by an Overlying Large-scale Magnetic Field: A Numerical Study". *ApJ* 862, 93 (): 93. doi:`10.3847/1538-4357/aacb7f`. arXiv: `1806.02828 [astro-ph.SR]`.

Amiri, M., et al. 2019. "Observations of fast radio bursts at frequencies down to 400 megahertz". *Nature* in press. doi:`10.1038/s41586-018-0867-7`.

Baird, G. A., et al. 1975. "A search for VHF radio pulses in coincidence with celestial gamma-ray bursts". *ApJL* 196 (): L11–L13. doi:`10.1086/181732`.

Balsano, R. J. 1999. "A search for radio emission coincident with gamma-ray bursts". PhD thesis, PRINCETON UNIVERSITY.

Bandura, K., et al. 2014. "Canadian Hydrogen Intensity Mapping Experiment (CHIME) pathfinder". In *Ground-based and Airborne Telescopes V*, 9145:914522. Proc. SPIE. doi:`10.1117/12.2054950`. arXiv: `1406.2288 [astro-ph.IM]`.

Bannister, K. W., et al. 2011. "A 22-yr southern sky survey for transient and variable radio sources using the Molonglo Observatory Synthesis Telescope". *MNRAS* 412 (): 634–664. doi:`10.1111/j.1365-2966.2010.17938.x`. arXiv: `1011.0003`.

Bannister, K. W., et al. 2012. "Limits on Prompt, Dispersed Radio Pulses from Gamma-Ray Bursts". *ApJ* 757, 38 (): 38. doi:`10.1088/0004-637X/757/1/38`. arXiv: `1207.6399 [astro-ph.HE]`.

Bastian, T. S. 1990. "Radio emission from flare stars". *SoPh* 130 (): 265–294. doi:`10.1007/BF00156794`.

Benz, A. O., and G. Paesold. 1998. "A search for prompt radio emission of gamma-ray bursts". *A&A* 329 (): 61–67.

Berger, E., et al. 2003. "A Radio Survey of Type Ib and Ic Supernovae: Searching for Engine-driven Supernovae". *ApJ* 599 (): 408–418. doi:`10.1086/379214`. eprint: `astro-ph/0307228`.

Burke, B. F., and K. L. Franklin. 1955. "Observations of a Variable Radio Source Associated with the Planet Jupiter". *J. Geophys. Res.* 60 (): 213–217. doi:`10.1029/JZ060i002p00213`.

Chandra, P., and D. A. Frail. 2012. "A Radio-selected Sample of Gamma-Ray Burst Afterglows". *ApJ* 746, 156 (): 156. doi:`10.1088/0004-637X/746/2/156`. arXiv: `1110.4124`.

Chevalier, R. A. 1998. "Synchrotron Self-Absorption in Radio Supernovae". *ApJ* 499 (): 810–819. doi:`10.1086/305676`.

– . 1982. "The radio and X-ray emission from type II supernovae". *ApJ* 259 (): 302–310. doi:`10.1086/160167`.

CHIME/FRB Collaboration et al. 2018. "The CHIME Fast Radio Burst Project: System Overview". *ApJ* 863, 48 (): 48. doi:`10.3847/1538-4357/aad188`. arXiv: `1803.11235 [astro-ph.IM]`.

Chomiuk, L., et al. 2012. "EVLA Observations Constrain the Environment and Progenitor System of Type Ia Supernova 2011fe". *ApJ* 750, 164 (): 164. doi:`10.1088/0004-637X/750/2/164`. arXiv: `1201.0994 [astro-ph.HE]`.

Cordes, J. 2007. "Axes of discovery: The time variable Universe". In *From Planets to Dark Energy: the Modern Radio Universe*, 35.

Cranmer, M. D., et al. 2017. "Bifrost: A Python/C++ Framework for High-Throughput Stream Processing in Astronomy". *Journal of Astronomical Instrumentation* 6, 1750007 (): 1750007. doi:`10.1142/S2251171717500076`. arXiv: `1708.00720 [astro-ph.IM]`.

Desch, M. D., and M. L. Kaiser. 1984. "Predictions for Uranus from a radiometric Bode's law". *Nature* 310 (): 755–757. doi:`10.1038/310755a0`.

Dessenne, C. A.-C., et al. 1996. "Searches for prompt radio emission at 151 MHz from the gamma-ray bursts GRB 950430 and GRB 950706." *MNRAS* 281 (): 977–984. doi:`10.1093/mnras/281.3.977`.

Ellingson, S. W., et al. 2009. "The Long Wavelength Array". *IEEE Proceedings* 97 (): 1421–1430. doi:`10.1109/JPROC.2009.2015683`.

Falcke, H., and P. Gorham. 2003. "Detecting radio emission from cosmic ray air showers and neutrinos with a digital radio telescope". *Astroparticle Physics* 19 (): 477–494. doi:`10.1016/S0927-6505(02)00245-1`. eprint: `astro-ph/0207226`.

Farrell, W. M., M. D. Desch, and P. Zarka. 1999. "On the possibility of coherent cyclotron emission from extrasolar planets". *J. Geophys. Res.* 104 (): 14025–14032. doi:`10.1029/1998JE900050`.

Gallagher, D. L., and N. Dangelo. 1981. "Correlations between solar wind parameters and auroral kilometric radiation intensity". *Geophys. Res. Lett.* 8 (): 1087–1089. doi:`10.1029/GL008i010p01087`.

Gal-Yam, A., et al. 2006. "Radio and Optical Follow-up Observations of a Uniform Radio Transient Search: Implications for Gamma-Ray Bursts and Supernovae". *ApJ* 639 (): 331–339. doi:`10.1086/499157`. eprint: `astro-ph/0508629`.

Gopalswamy, N., et al. 2001. "Characteristics of coronal mass ejections associated with long-wavelength type II radio bursts". *J. Geophys. Res.* 106 (): 29219–29230. doi:`10.1029/2001JA000234`.

Granot, J., and A. J. van der Horst. 2014. "Gamma-Ray Burst Jets and their Radio Observations". *PASA* 31, e008 (): e008. doi:`10.1017/pasa.2013.44`.

Granot, J., et al. 2002. "Off-Axis Afterglow Emission from Jetted Gamma-Ray Bursts". *ApJL* 570 (): L61–L64. doi:`10.1086/340991`. eprint: `astro-ph/0201322`.

Hallinan, G., et al. 2017. "A radio counterpart to a neutron star merger". *Science* 358 (): 1579–1583. doi:`10.1126/science.aap9855`. arXiv: `1710.05435 [astro-ph.HE]`.

Hallinan, G., et al. 2015. "Magnetospherically driven optical and radio aurorae at the end of the stellar main sequence". *Nature* 523 (): 568–571. doi:`10.1038/nature14619`. arXiv: `1507.08739 [astro-ph.SR]`.

Hansen, B. M. S., and M. Lyutikov. 2001. "Radio and X-ray signatures of merging neutron stars". *MNRAS* 322 (): 695–701. doi:`10.1046/j.1365-8711.2001.04103.x`. eprint: `astro-ph/0003218`.

Hey, J. S. 1946. "Solar Radiations in the 4-6 Metre Radio Wave-Length Band". *Nature* 157 (): 47–48. doi:`10.1038/157047b0`.

Ho, A. Y. Q., et al. 2019. "AT2018cow: A Luminous Millimeter Transient". *ApJ* 871, 73 (): 73. doi:`10.3847/1538-4357/aaf473`. arXiv: `1810.10880 [astro-ph.HE]`.

Hyman, S. D., et al. 2007. "A Faint, Steep-Spectrum Burst from the Radio Transient GCRT J1745-3009". *ApJl* 660 (): L121–L124. doi:`10.1086/518245`. eprint: `astro-ph/0701098`.

Hyman, S. D., et al. 2005. "A powerful bursting radio source towards the Galactic Centre". *Nature* 434 (): 50–52. doi:`10.1038/nature03400`. eprint: `astro-ph/0503052`.

Hyman, S. D., et al. 2009. "GCRT J1742-3001: A New Radio Transient Toward the Galactic Center". *ApJ* 696 (): 280–286. doi:`10.1088/0004-637X/696/1/280`. arXiv: `0811.1972`.

Hyman, S. D., et al. 2002. "Low-Frequency Radio Transients in the Galactic Center". *AJ* 123 (): 1497–1501. doi:`10.1086/338905`. eprint: `astro-ph/0110151`.

Inoue, S. 2004. "Probing the cosmic reionization history and local environment of gamma-ray bursts through radio dispersion". *MNRAS* 348 (): 999–1008. doi:`10.1111/j.1365-2966.2004.07359.x`. eprint: `astro-ph/0309364`.

Intema, H. T., et al. 2017. "The GMRT 150 MHz all-sky radio survey. First alternative data release TGSS ADR1". *A&A* 598, A78 (): A78. doi:`10.1051/0004-6361/201628536`. arXiv: `1603.04368`.

Inzani, P., et al. 1982. "Search for associations of radio pulses and gamma ray bursts". In *Gamma Ray Transients and Related Astrophysical Phenomena*, ed. by R. E. Lingenfelter, H. S. Hudson, and D. M. Worrall, 77:79–84. American Institute of Physics Conference Series. doi:`10.1063/1.33213`.

Jaeger, T. R., et al. 2012. "Discovery of a Meter-wavelength Radio Transient in the SWIRE Deep Field: 1046+59". *AJ* 143, 96 (): 96. doi:`10.1088/0004-6256/143/4/96`. arXiv: `1201.6290 [astro-ph.HE]`.

Kao, M. M., et al. 2018. "The Strongest Magnetic Fields on the Coolest Brown Dwarfs". *ApJs* 237, 25 (): 25. doi:`10.3847/1538-4365/aac2d5`. arXiv: `1808.02485 [astro-ph.SR]`.

Kaplan, D. L., et al. 2015. "A Deep Search for Prompt Radio Emission from the Short GRB 150424A with the Murchison Widefield Array". *ApJL* 814, L25 (): L25. doi:`10.1088/2041-8205/814/2/L25`. arXiv: `1511.03656 [astro-ph.HE]`.

Kaplan, D. L., et al. 2016. "Strategies for Finding Prompt Radio Counterparts to Gravitational Wave Transients with the Murchison Widefield Array". *PASA* 33, e050 (): e050. doi:`10.1017/pasa.2016.43`. arXiv: `1609.00634 [astro-ph.IM]`.

Khodachenko, M. L., et al. 2007. "Coronal Mass Ejection (CME) Activity of Low Mass M Stars as An Important Factor for The Habitability of Terrestrial Exoplanets. I. CME Impact on Expected Magnetospheres of Earth-Like Exoplanets in Close-In Habitable Zones". *Astrobiology* 7 (): 167–184. doi:`10.1089/ast.2006.0127`.

Koranyi, D. M., et al. 1995. "Search for a radio counterpart to the gamma-ray burst GRB 940301". *MNRAS* 276 (): L13–L17. doi:`10.1093/mnras/276.1.L13`.

Kulkarni, S. R., et al. 1998. "Radio emission from the unusual supernova 1998bw and its association with the $\gamma$-ray burst of 25 April 1998". *Nature* 395 (): 663–669. doi:`10.1038/27139`.

Lammer, H., et al. 2012. "Variability of solar/stellar activity and magnetic field and its influence on planetary atmosphere evolution". *Earth, Planets, and Space* 64 (): 179–199. doi:`10.5047/eps.2011.04.002`.

Lazio, T. J., W., et al. 2004. "The Radiometric Bode's Law and Extrasolar Planets". *ApJ* 612 (): 511–518. doi:`10.1086/422449`.

Levinson, A., et al. 2002. "Orphan Gamma-Ray Burst Radio Afterglows: Candidates and Constraints on Beaming". *ApJ* 576 (): 923–931. doi:`10.1086/341866`. eprint: `astro-ph/0203262`.

Li, K. J., J. Zhanng, and W. Feng. 2016. "A Statistical Analysis of 50 Years of Daily Solar Wind Velocity Data". *AJ* 151, 128 (): 128. doi:`10.3847/0004-6256/151/5/128`.

Lorimer, D. R., et al. 2007. "A Bright Millisecond Radio Burst of Extragalactic Origin". *Science* 318 (): 777. doi:`10.1126/science.1147532`. arXiv: `0709.4301`.

Lynch, C. R., et al. 2017. "154 MHz Detection of Faint, Polarized Flares from UV Ceti". *ApJl* 836, L30 (): L30. doi:`10.3847/2041-8213/aa5ffd`. arXiv: `1702.03030 [astro-ph.SR]`.

Lyutikov, M. 2013. "The Electromagnetic Model of Short GRBs, the Nature of Prompt Tails, Supernova-less Long GRBs, and Highly Efficient Episodic Accretion". *ApJ* 768, 63 (): 63. doi:`10.1088/0004-637X/768/1/63`. arXiv: `1202.6026 [astro-ph.HE]`.

Macquart, J.-P. 2007. "On the Detectability of Prompt Coherent Gamma-Ray Burst Radio Emission". *ApJL* 658 (): L1–L4. doi:`10.1086/513424`. eprint: `astro-ph/0702098`.

Mattila, S., et al. 2012. "Core-collapse Supernovae Missed by Optical Surveys". *ApJ* 756, 111 (): 111. doi:`10.1088/0004-637X/756/2/111`. arXiv: `1206.1314 [astro-ph.CO]`.

Metzger, B. D., P. K. G. Williams, and E. Berger. 2015. "Extragalactic Synchrotron Transients in the Era of Wide-field Radio Surveys. I. Detection Rates and Light Curve Characteristics". *ApJ* 806, 224 (): 224. doi:`10.1088/0004-637X/806/2/224`. arXiv: `1502.01350 [astro-ph.HE]`.

Mooley, K. P., et al. 2018. "Superluminal motion of a relativistic jet in the neutron-star merger GW170817". *Nature* 561 (): 355–359. doi:`10.1038/s41586-018-0486-3`. arXiv: `1806.09693 [astro-ph.HE]`.

Mooley, K. P., et al. 2016. "The Caltech-NRAO Stripe 82 Survey (CNSS). I. The Pilot Radio Transient Survey In 50 deg$^2$". *ApJ* 818, 105 (): 105. doi:`10.3847/0004-637X/818/2/105`. arXiv: `1601.01693 [astro-ph.HE]`.

Moortgat, J., and J. Kuijpers. 2005. "Indirect Visibility of Gravitational Waves in Magnetohydrodynamic Plasmas". In *22nd Texas Symposium on Relativistic Astrophysics*, ed. by P. Chen et al., 326–331. eprint: `gr-qc/0503074`.

Murphy, T., et al. 2017. "A search for long-time-scale, low-frequency radio transients". *MNRAS* 466 (): 1944–1953. doi:`10.1093/mnras/stw3087`. arXiv: `1611.08354`.

Obenberger, K. S., et al. 2014. "Limits on Gamma-Ray Burst Prompt Radio Emission Using the LWA1". *ApJ* 785, 27 (): 27. doi:`10.1088/0004-637X/785/1/27`. arXiv: `1403.3674 [astro-ph.HE]`.

Polisensky, E., et al. 2016. "Exploring the Transient Radio Sky with VLITE: Early Results". *ApJ* 832, 60 (): 60. doi:`10.3847/0004-637X/832/1/60`. arXiv: `1604.00667 [astro-ph.HE]`.

Pshirkov, M. S., and K. A. Postnov. 2010. "Radio precursors to neutron star binary mergings". *Ap&SS* 330 (): 13–18. doi:`10.1007/s10509-010-0395-x`. arXiv: `1004.5115 [astro-ph.HE]`.

Ravi, V. 2019. "The observed properties of fast radio bursts". *MNRAS* 482 (): 1966–1978. doi:`10.1093/mnras/sty1551`. arXiv: `1710.08026 [astro-ph.HE]`.

Reiners, A., and U. R. Christensen. 2010. "A magnetic field evolution scenario for brown dwarfs and giant planets". *A&A* 522, A13 (): A13. doi:`10.1051/0004-6361/201014251`. arXiv: `1007.1514 [astro-ph.EP]`.

Ribas, I., et al. 2016. "The habitability of Proxima Centauri b. I. Irradiation, rotation and volatile inventory from formation to the present". *A&A* 596, A111 (): A111. doi:`10.1051/0004-6361/201629576`. arXiv: `1608.06813 [astro-ph.EP]`.

Sagiv, A., and E. Waxman. 2002. "Collective Processes in Relativistic Plasma and Their Implications for Gamma-Ray Burst Afterglows". *ApJ* 574 (): 861–872. doi:`10.1086/340948`. eprint: `astro-ph/0202337`.

Soderberg, A. M., et al. 2010. "Radio and X-ray Observations of the Type Ic SN 2007gr Reveal an Ordinary, Non-relativistic Explosion". *ApJ* 725 (): 922–930. doi:`10.1088/0004-637X/725/1/922`. arXiv: `1005.1932`.

Spangler, S. R., and T. J. Moffett. 1976. "Simultaneous radio and optical observations of UV Ceti-type flare stars". *ApJ* 203 (): 497–508. doi:10.1086/154105.

Stewart, A. J., et al. 2016. "LOFAR MSSS: detection of a low-frequency radio transient in 400 h of monitoring of the North Celestial Pole". *MNRAS* 456 (): 2321–2342. doi:10.1093/mnras/stv2797. arXiv: 1512.00014 [astro-ph.HE].

Tingay, S. J., et al. 2013. "The Murchison Widefield Array: The Square Kilometre Array Precursor at Low Radio Frequencies". *PASA* 30, e007 (): e007. doi:10.1017/pasa.2012.007. arXiv: 1206.6945 [astro-ph.IM].

Treumann, R. A. 2006. "The electron-cyclotron maser for astrophysical application". *Astronomy & Astrophysics Reviews* 13 (): 229–315. doi:10.1007/s00159-006-0001-y.

Usov, V. V., and J. I. Katz. 2000. "Low frequency radio pulses from gamma-ray bursts?" *A&A* 364 (): 655–659. eprint: astro-ph/0002278.

van Haarlem, M. P., et al. 2013. "LOFAR: The LOw-Frequency ARray". *A&A* 556, A2 (): A2. doi:10.1051/0004-6361/201220873. arXiv: 1305.3550 [astro-ph.IM].

Villadsen, J., and G. Hallinan. 2019. "Ultra-wideband Detection of 22 Coherent Radio Bursts on M Dwarfs". *ApJ* 871, 214 (): 214. doi:10.3847/1538-4357/aaf88e. arXiv: 1810.00855 [astro-ph.SR].

Zarka, P. 1998. "Auroral radio emissions at the outer planets: Observations and theories". *J. Geophys. Res.* 103 (): 20159–20194. doi:10.1029/98JE01323.

– . 2007. "Plasma interactions of exoplanets with their parent star and associated radio emissions". *Planet. Space Sci.* 55 (): 598–617. doi:10.1016/j.pss.2006.05.045.

Zarka, P., et al. 2001. "Magnetically-Driven Planetary Radio Emissions and Application to Extrasolar Planets". *Ap&SS* 277 (): 293–300. doi:10.1023/A:1012221527425.

Zauderer, B. A., et al. 2011. "Birth of a relativistic outflow in the unusual $\gamma$-ray transient Swift J164449.3+573451". *Nature* 476 (): 425–428. doi:10.1038/nature10366. arXiv: 1106.3568 [astro-ph.HE].

*Chapter 2*

# THE OWENS VALLEY RADIO OBSERVATORY LONG WAVELENGTH ARRAY (OVRO-LWA)

## 2.1 Instrument Overview

The Owens Valley Radio Observatory Long Wavelength Array (OVRO-LWA) is a low-frequency ($< 100\,\mathrm{MHz}$) dipole array located at the Caltech Owens Valley Radio Observatory (37:14:02N, 118:16:56W). The OVRO-LWA is a zenith-pointing telescope with stationary crossed-dipole elements (see Figure 2.1). Full cross-correlation of all elements in the array provides a primary beam field-of-view that is equivalent to that of a single element, which for a dipole is the entire viewable hemisphere. This makes the OVRO-LWA a uniquely powerful instrument amongst low-frequency dipole arrays – its full-sky imaging capability across a wide (28–84 MHz) bandwidth provides an unparalleled combination of sensitivity and wide field-of-view. The majority of low-frequency dipole arrays (e.g., LOFAR, MWA) regularly operate in a mode whereby "stations" of dipoles are used to form beams (and which are then correlated with all other station beams). This allows the exchange of fewer correlated inputs for higher time and/or frequency resolution, but severely limits the field-of-view. Some of these arrays have alternate back ends that enable full cross-correlation of large numbers of single dipole inputs – e.g. PASI (Obenberger et al. 2015) on LWA1 and AARTFAAC (Prasad et al. 2016) on LOFAR – and therefore all-sky fields-of-view comparable to that of the OVRO-LWA. However, they are frequently limited to narrow bandwidths (a few channels wide, corresponding to ~few MHz at most) which significantly degrades sensitivity. The OVRO-LWA is therefore uniquely positioned among low-frequency dipole arrays for achieving its science goals, which includes characterizing the early universe during the Cosmic Dawn era, radio-only detections of cosmic rays, Solar and Jovian monitoring, and what I broadly categorize as low-frequency transient science. This includes searches for prompt radio emission from compact object mergers (Chapter 3), non-targeted transient searches (Chapter 4), and extrasolar space weather encompassing stellar and planetary radio emission (Chapter 5).

My time at Caltech has mirrored that of the OVRO-LWA – approximately consistent arrival dates, similar growth and development timelines, and culminating recently

in scientific output. A significant component of my thesis has been the participation in every major stage of the OVRO-LWA, from construction and commissioning, to pipeline development. During this time, the OVRO-LWA has undergone upgrades, debugging, and has recently emerged as a science-ready instrument. In the following, I describe the different stages of the array, as well as the calibration, imaging, and reduction pipelines I built to enable the transient science goals outlined above and discussed in detail in the chapters that follow.



Figure 2.1: A photograph of the OVRO-LWA, taken from within the 251-element core, facing east towards the White Mountains. On the west side of the array is the Sierra Nevadas. The radio observatory's placement within the Owens Valley, shielded on either side by two large mountain ranges, creates a comparatively clean RFI environment. The predominant sources of RFI are the FM band above 88 MHz, short wave reflecting off the ionosphere below 25 MHz, and RFI associated with power-lines running along the valley that is broad-band in nature.

**Stage I OVRO-LWA: The Core**

Construction on the Stage I OVRO-LWA began in 2013 and was completed in 2014. The Stage I array consists of 251 crossed dipole antennas spread across a 200 m-diameter "core", with a minimum separation of 5 m between antennas to minimize the effects of cross-talk between adjacent antennas. Each antenna is equipped with two front ends (FEs; one for each of the crossed dipoles) that amplifies the signal and is connected via coaxial cable to the electronics shelter (located at the southern end of the core). Each antenna contains 2 signals – one from the X dipole (oriented N–S) and one from the Y dipole (oriented E–W).[1]

---

[1] I note that each of the dipoles is intrinsically elliptically polarized, so that each crossed-dipole pair is not simply measuring linear polarization along the N–S and E–W axes.

In addition to the 251-element core, there are an additional 5 "outrigger" antennas located at a distance of approximately 30 m from the edge of the core, which are used for total power measurements. As such, they are equipped with special noise switching FEs and utilized for the Large Aperture Experiment to Detect the Dark Ages (LEDA; Price et al. 2018), and are therefore excluded from the data reduction pipeline discussed here.

Both the antenna and analog electronics utilized for the Stage I construction of the OVRO-LWA are taken directly from the LWA1 design. However, beyond this, and particularly with regards to the design of the 512-input LEDA correlator, the OVRO-LWA departs significantly from the LWA1.

The 200-m diameter core, operating at frequencies between 28–84 MHz, provides approximately 1 degree resolution on the sky and an approximately 20,000 deg$^2$ field-of-view. At 1° resolution, the array is severely classically confusion limited, whereby unresolved sources contribute to the flux within the synthesized beam, to the level of approximately a few Jy. See Figure 2.2 for a map of the Stage I array, the corresponding snapshot uv-coverage, synthesized beam, and all-sky image from the array.

**Stage II OVRO-LWA: The Long Baseline Demonstrator Array**

The Stage II OVRO-LWA was built between 2015–2016, and added an additional 32 "expansion" antennas as part of the Long Baseline Demonstrator Array (LBDA) out to maximum baselines of 1.5 km, and increasing the resolution of the array from 1° to 10′ at the top of the band. The 64 (2 polarizations per antenna) signal paths corresponding to the LBDA replaced 64 core antenna inputs into the correlator, and are transported to the electronics shelter through fiber optic cable, which is significantly cheaper and avoids issues related to signal reflections within coaxial cable that manifest as bandpass ripples. Junction boxes buried in the ground and located at each expansion antenna contain power and a laser diode board[2] to convert the signal from the coaxial cable connected to the FE to optical fiber for transport back to the electronics shelter.

The Stage II OVRO-LWA is the current operational stage of the array as of this thesis, and delivered the first set of science from the OVRO-LWA (Eastwood et al. 2017; Anderson et al. 2018; Price et al. 2018; Monroe et al. 2019, *NIM-A* submitted; Eastwood et al. 2019, *AJ* submitted; Anderson et al. 2019, *ApJ* submitted). Substan-

---

[2]Junction boxes also occasionally contain either water or scorpions.
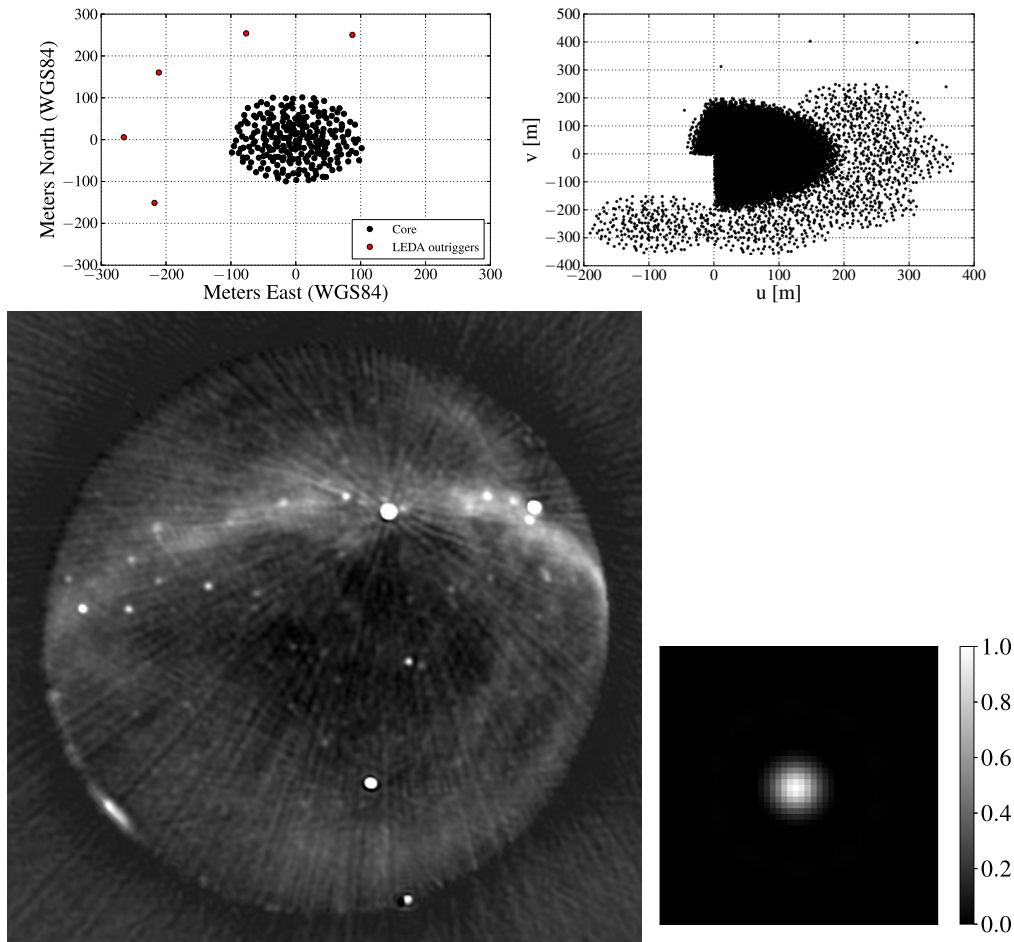
Figure 2.2: The Stage I OVRO-LWA. Map of antenna locations in the core (top left), the corresponding uv coverage (top right), the point spread function (PSF) using a Briggs robust weighting of 0 (bottom right), and an all-sky image from the Stage I array (bottom left).

tial effort was required in going between completion of the Stage II construction and obtaining science-quality data. Significant issues had to be identified and solved, including installation of attenuators on all 32 coax to fiber laser diode boards, which were being driven non-linear, as well as other issues which are described in more detail below. See Figure 2.3 for a map of the Stage II antenna locations, the corresponding snapshot uv-coverage, synthesized beam, and all-sky image from the array. At 10′ resolution, the OVRO-LWA remains confusion-limited, with single snapshot (13 s) sensitivity of approximately 800 mJy. In addition to the LBDA antennas, a major improvement of the Stage II OVRO-LWA was the upgrade of the All-Sky Transient Monitor (ASTM), the calibration and imaging cluster for the array, located in the electronics shelter. The current data rate of the array is 2.5 GB per snapshot

(corresponding to 32640 baselines × 4 polarizations × 2398 frequency channels × 32 + 32 bits output data rate). For the 13 s integration times used during the Stage II array operations, this corresponds to $16\,\mathrm{TB}\,\mathrm{d}^{-1}$ of output science data. This massive data rate, and the time requirements for processing the data, limit the initial science data with the Stage II array to a set of survey data that were used for both cosmology and transient science products (a continuous 28 h observation), and a circular buffer of tunable duration that is typically set to 24 h. A set of 120 h observations taken in 2018 March will also be used for transient science, and reduction is ongoing.
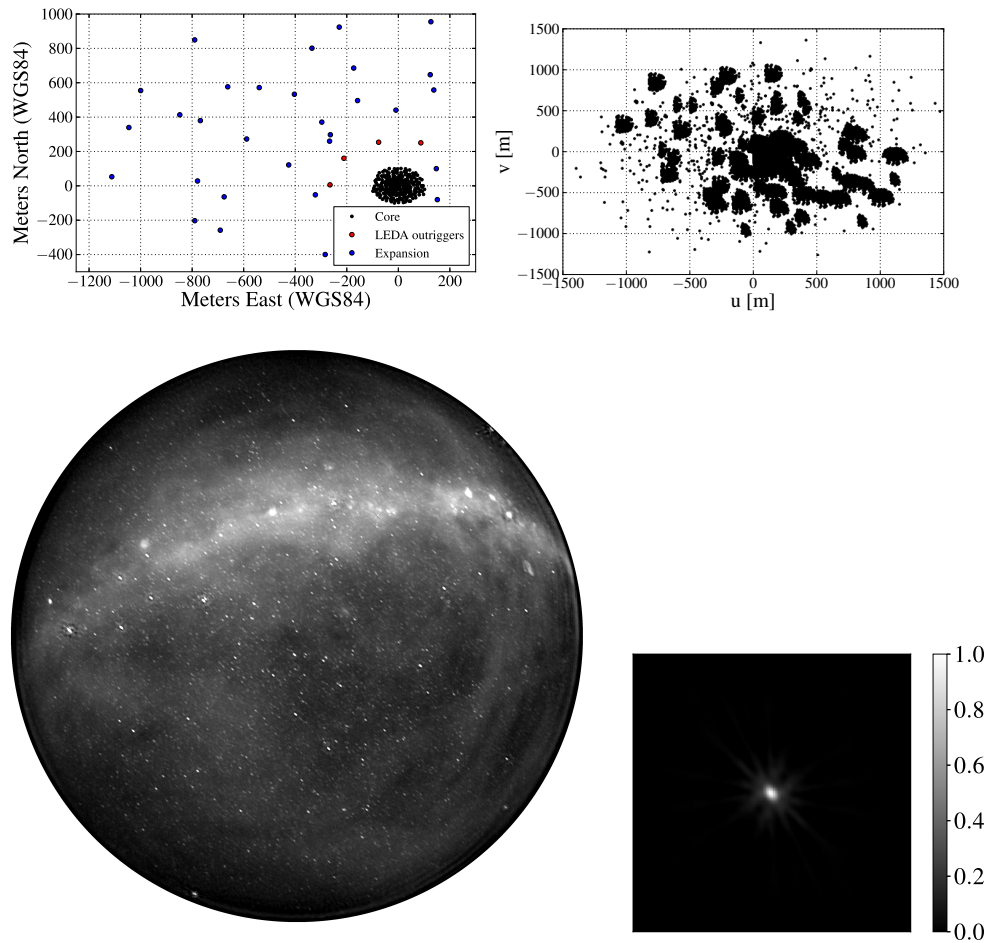


Figure 2.3: The Stage II OVRO-LWA. Map of antenna locations in the core and LBDA (top left), the corresponding uv coverage (top right), the PSF using a Briggs robust weighting of 0 (bottom right), and an all-sky image from the Stage II array (bottom left).

**Stage III OVRO-LWA-352**

The final Stage III OVRO-LWA will incorporate an additional 64 antennas out to maximum baselines of 2.6 km, and will feature a complete redesign of the analog and digital systems, including a new correlator that will incorporate all 704 signals and a larger 70 MHz-wide bandwidth. Construction is set to begin for a 2 year period starting in the summer of 2019. With the larger bandwidth and increased number of inputs to the correlator, the output data rate will increase to 5 GB per snapshot, for a daily data rate (for 10 s integrations) of 40 TB d$^{-1}$; this is a larger data rate than the LSST. The stated goal of the final OVRO-LWA-352 is the delivery of a 1000 h-long continuous survey (or 1.7 PB of data) and a circular buffer that is 100 TB in size. In addition to the standard cross-correlation operation of the correlator, the upgrade will incorporate additional observational modes, including a beamformer mode of operation to form 12 simultaneous beams and the ability to dump raw voltage data following a cosmic-ray or GW trigger.

**Ionosphere and RFI Environment**

The ionosphere is particularly problematic in the OVRO-LWA observing band, given its proximity to the ionospheric plasma cutoff frequency (between $\sim 10 - 20$ MHz). The ionosphere is a significant source of scintillation and refraction, with positions of point sources wandering by as much as 30′ from snapshot-to-snapshot during ionospheric substorms. While this presents a significant challenge for transient searches (see Chapter 4), the OVRO-LWA is in the regime of wide-field but compact arrays (see Figure 1(3) of Intema et al. 2009). While the total electron content (TEC) of the ionosphere is not constant over the wide field-of-view of the array, the ionosphere is coherent between antennas – that is, each antenna is seeing through the same patch of ionosphere for a given direction in the field-of-view. This means that the significant challenges that are faced by, for example, LOFAR stations with baselines in excess of 100 km due to ionospheric phase errors are avoided by the OVRO-LWA.

In addition, OVRO is situated in a relatively radio quiet site, with most of the RFI occurring outside the observing band ($> 88$ MHz and $< 25$ MHz, associated with FM and HF interference, respectively). See Figure 2.4 for a dynamic spectrum taken with a spectrum analyzer and an LWA antenna stationed at the OVRO-LWA site over a 48-hour period from an RFI survey conducted in 2013 (Anderson & Eastwood, internal memo). The primary source of RFI for the OVRO-LWA is due to power line insulators arcing on timescales as short as nanoseconds, which consequently

creates band-limited, broadband RFI. See Figure 2.5 for a dynamic spectrum I have generated for one such power line RFI source showing its temporal and frequency behavior. However, individual problematic insulators can be localized with the array (and further identified through the use of a Yagi antenna mounted on a truck, and substantial graduate student and observatory staff effort) and repaired with the cooperation of the relevant power company. This has already been done for the brightest RFI source affecting the array.
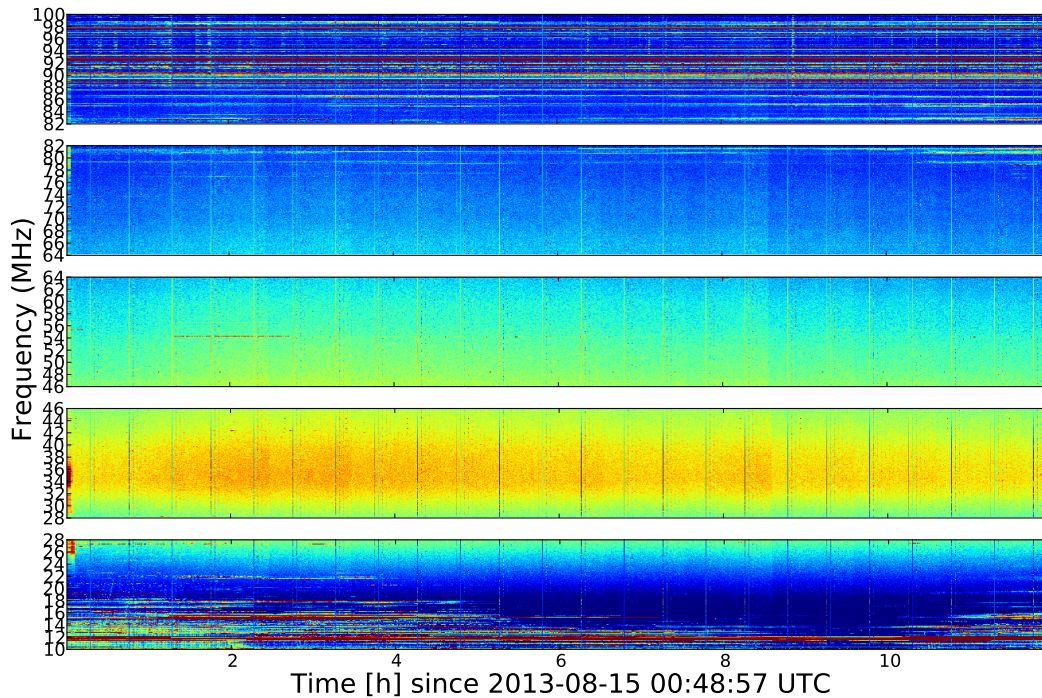


Figure 2.4: Dynamic spectrum from the OVRO-LWA site taken with a spectrum analyzer hooked up to an LWA antenna, across 12 h, as part of an RFI survey that was conducted in 2013. The diurnal variation in the HF interference is visible at the bottom of the band. The observing band is relatively clean of RFI (middle 3 panels).
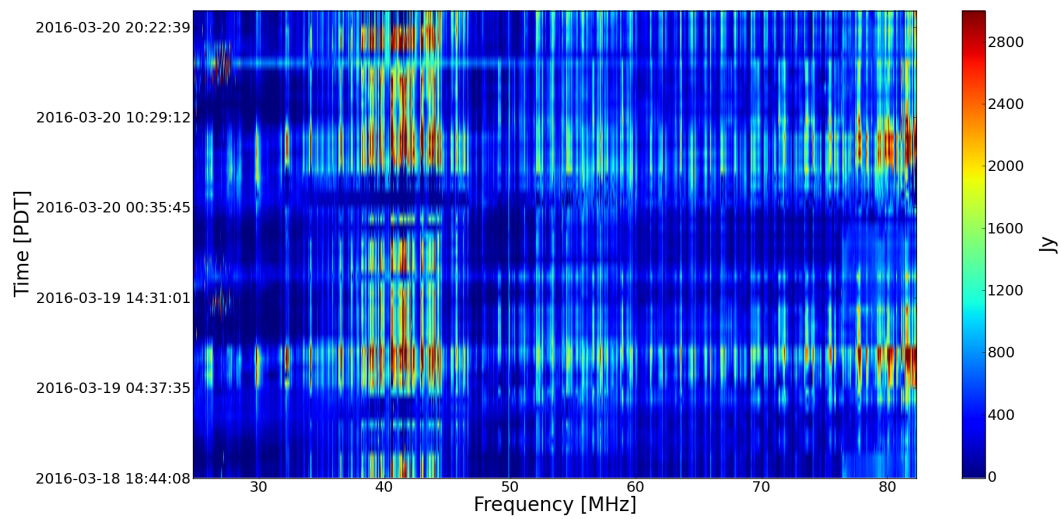
Figure 2.5: Dynamic spectrum taken at approximately 1 h intervals for a power line RFI source across approximately 100 hours.
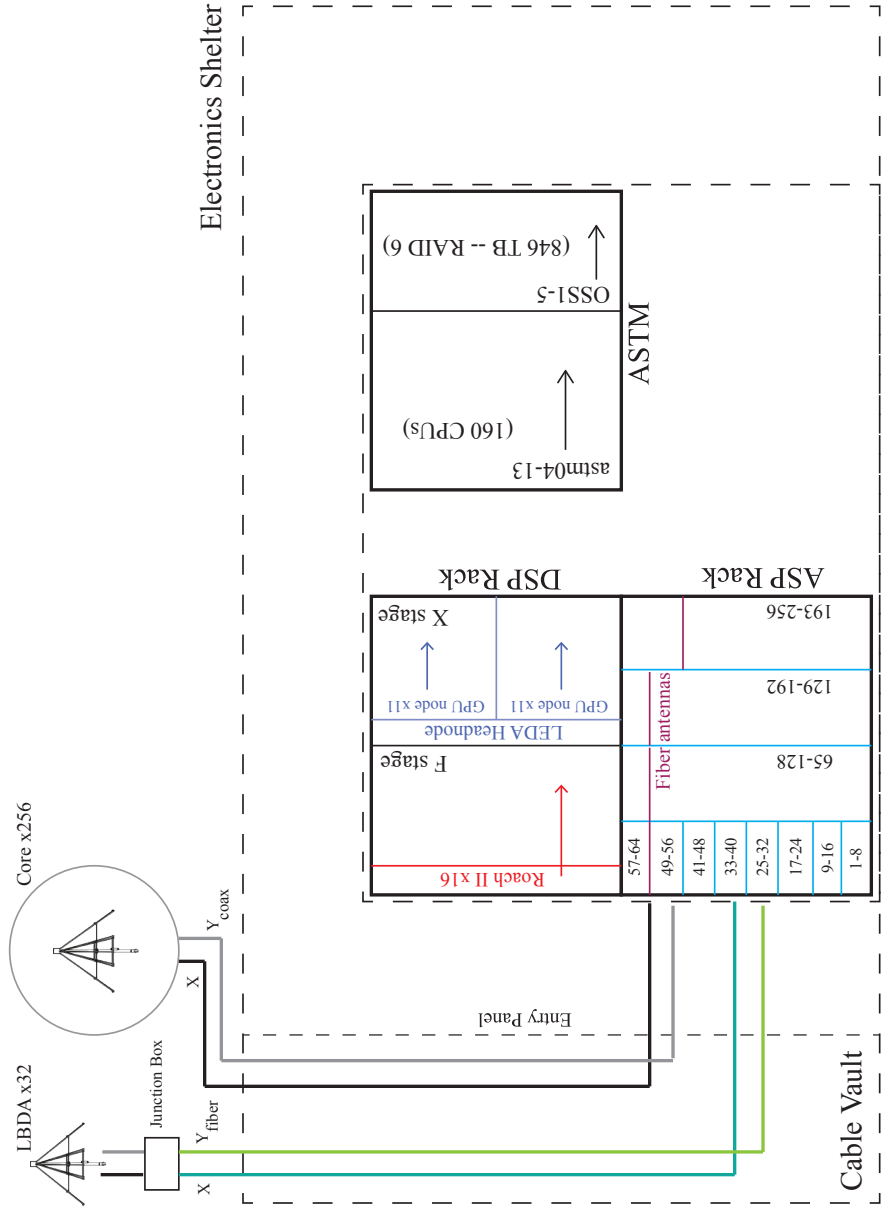
Figure 2.6: OVRO-LWA system diagram, showing the signal path from the antennas into the electronics shelter; and through the analog signal path (ASP) and digital signal path (DSP) racks. Core antenna signals (2 signal paths per antenna, for the X and Y polarizations) are transported via coaxial cable to the electronics shelter. LBDA antenna signals first pass through a junction box to convert the signal from radio to optical fiber for transport to the electronics shelter. There are 4 analog receiver (ARX) boards (16 signal paths per board) in the ASP rack that are specially equipped with daughter boards designed to handle the fiber connections from the long baseline antennas. All data storage and processing is done on site in the All Sky Transient Monitor (ASTM).

## 2.2 System Overview

### Antenna

The LWA antenna consists of a pair of linear orthogonal crossed-dipoles, angled at 45° with respect to the ground in order to increase forward gain over the whole sky (rather than towards zenith). Each antenna is located above a 3 m × 3 m ground screen consisting of a wire grid that helps to isolate the antenna from the ground and any variability in conductivity as a function of soil moisture. Each antenna is equipped with 2 front end electronics (FEE) boards, one for each crossed dipole, that are equipped with an amplifier that provides 36 dB of gain (Hicks et al. 2012). Because the Galactic synchrotron emission is so bright at sub-100 MHz frequencies, the OVRO-LWA is sky-noise dominated – the antenna temperature from the Galactic emission is significantly higher (on the order of 6 dB) than the receiver temperature and electronics associated with the FEs.

### Analog Stage

Signals from all antennas enter the electronics shelter through the cable vault, pass through an exterior entry panel, and connect to the analog receiver (ARX) boards, where signals are attenuated and filtered, prior to analog-to-digital conversion. There are 32 ARX boards located in the analog signal path (ASP) rack, with each board processing 16 signals (8 antennas). There are 3 variable filtering options – a wide-band mode (10–88 MHz), a split-filter mode that allows for attenuation at the bottom ~third of the band, and a narrow-band mode (28–54 MHz). All science observations with the array have used the split-filter mode.

A known, but unsolved, issue with the ARX boards is related to common-mode pick-up and cross-talk between adjacent signal paths on a given board. This manifests as time-variable, correlated noise, with the most problematic signal paths generally confined to one or two boards at a time. For the final stage of the array, a complete redesign of the ARX boards will isolate individual lines within each board, and prevent the current issues which are limiting the array sensitivity, including preventing the integrating up of data to improve the noise beyond approximately one integration.

### Digital Stage

The 512-input Large Aperture Experiment to Detect Dark Ages (LEDA; Kocz et al. 2015) correlator is an FX correlator that consists of a combination of Field Programmable Gate Arrays (FPGAs) and Graphics Processing Units (GPUS) and

which correlates all inputs across 58 MHz of instantaneous bandwidth. The Analog to Digital Converters (ADCs) digitize the signal, which passes to the FPGAs mounted on ROACH II boards (16 boards handling 32 signals each). A polyphase filterbank (PFB) in the FPGA Fast Fourier Transforms (FFTs) the data from the time domain into frequency domain, with a resolution of 24 kHz. An additional set of digital gains are applied (averaged across the whole band prior to 2017, and then per sub-band post-2017), and the signal is then requantized from $18 + 18$ bit to $4 + 4$ bit. Finally, 2398 channels corresponding to 58 MHz of bandwidth, tunable to anywhere in the 0–98 MHz baseband but nominally set from 28–86 MHz, are sent to the X-engine, where the data are cross multiplied and integrated on a set of GPUs (11 GPU nodes containing 2 GPUs each, corresponding to one GPU per sub-band).

**All Sky Transient Monitor (ASTM)**

Data from the LEDA correlator are transported to the ASTM for long-term storage and processing of visibility data. The ASTM contains 10 compute nodes (16 CPUs and 64 MB of RAM per node) and 5 storage nodes with 846 TB of storage configured in RAID 6. The data processing pipelines (data editing, calibration, imaging, science pipelines) are hosted on the ASTM, and were developed for delivery of calibrated data products, as well as pipelines specific to each science case – including dedispersion of dynamic spectra to search for a pulse of coherent radio emission accompanying short gamma-ray bursts (GRBs) and gravitational wave (GW) events; a difference imaging and transient identification and classification pipeline; time series analysis targeting catalogued sources that is used for extrasolar spaceweather monitoring; m-mode analysis and 21 cm pipelines; and cosmic ray detection pipeline. I developed all except the latter 2 of these pipelines.

See Figure 2.6 for a graphical depiction of the OVRO-LWA system overview.

## 2.3 Data Processing and Pipelines

In the following I describe the data processing pipeline that I have developed for the OVRO-LWA. These include flagging and other data editing, bandpass and polarization calibration, imaging, and science target-specific reduction pipelines. Figure 2.7 shows a graphical depiction of the data processing pipeline.

**Flagging and Data Editing**

Antenna and baseline flags are relatively static over time, and need only be determined once per observation and applied across the whole dataset. Antenna flags
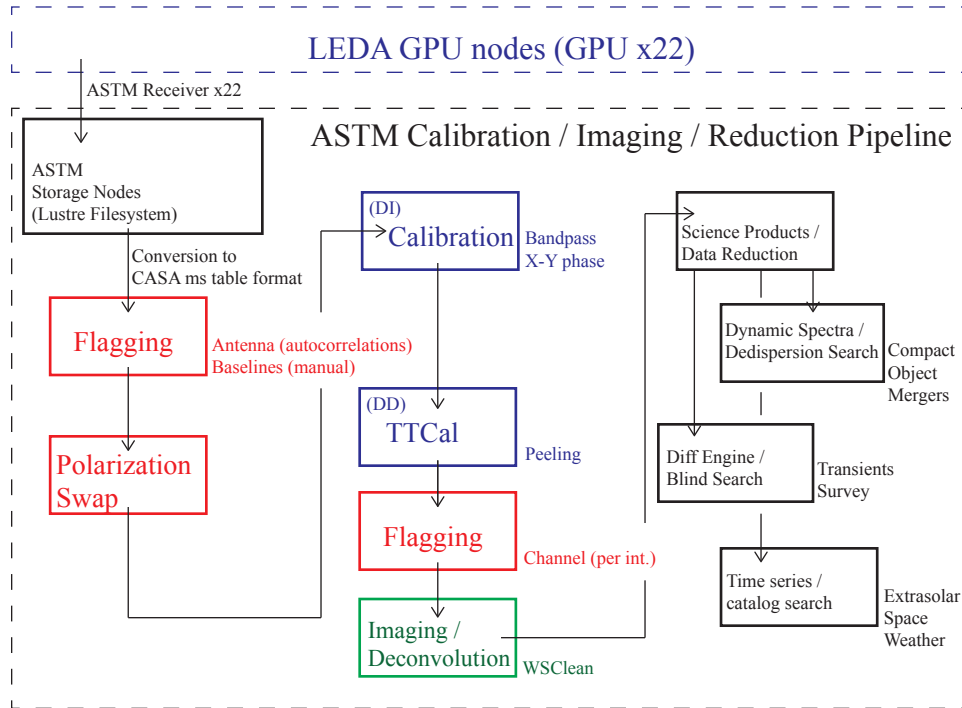
Figure 2.7: Schematic of the standard imaging pipelines: calibration, imaging, and science pipelines. Data are streamed from the LEDA correlator to the ASTM for processing and long-term storage on the Lustre filesystem. Each of the 22 LEDA GPUs processes a single sub-band (2.6 MHz), which are sent to the ASTM and stored in the `dada` file format. The first processing step is to convert from `dada` to CASA measurement set (MS) table format. The pipeline steps in red denote data editing including flagging of visibilities and any necessary swapping of correlation products due to switching of antenna polarizations somewhere along the signal path. Blue denotes calibration, green denotes imaging, and black denotes each science-specific data reduction pipeline.

are identified through deviations ($> 2\sigma$) of an individual antenna autocorrelation spectrum from the median spectral power across all antennas (see Figure 2.8). This is sufficient for identifying all antennas with issues along the signal path resulting in a loss, or significant distortion, of sky signal. This includes antennas without power (typically core antennas although occasionally LBDA antennas with shorted power or other maintenance related issues) as well as antennas whose signal paths are located on ARX boards that are affected by excessive levels of cross-talk and other noise. The total number of antennas flagged is generally on the order of as many as 50 out of 256 (flagging is always done on both antenna polarizations, even if only one signal path is problematic, in order to avoid issues associated with a varying PSF

shape between the X- and Y-arrays). Temporal variability in antenna flags can occur with regards to noise-affected ARX boards (generally on the timescale of ~hours), however all problematic ARX boards for a given dataset are identified and flagged throughout. Baselines between all adjacent signals, as well as all adjacent+1 signals, are flagged due to cross-talk between lines in the analog signal path. Additional problematic baselines are inspected and flagged manually. In total, the number of baselines flagged is typically less than 2% of all baselines.

Frequency-based flags are generated automatically on a per-integration basis, due to the fact that frequency channels affected by RFI are time-variable across an observation, and even on timescales as short as an integration time (13 s). Necessary channel flags are identified as frequencies that are outliers in their mean and max visibility amplitudes relative to the median values as a function of frequency calculated for all visibilities across a given sub-band. This typically results in fewer than 240 out of the total 2398 channels flagged. Channel flagging is performed in the pipeline following the calibration and peeling steps, due to the fact that the peeling process (which calibrates and subtracts source visibilities on a per-channel basis) may fail to find a solution for a number of channels that were otherwise missed in the channel flagging step, and which leaves behind visibilities with anomalously large amplitudes that can affect the noise when averaged across the entire frequency band.

For the majority of OVRO-LWA datasets, the number of flagged visibilities per integration is approximately 40%, with the majority of these due to malfunctioning antennas. However, because the bulk of flagged antennas are located in the core, where the uv-plane is already well sampled, and because the array is still dominated by confusion noise and other systematics even at single-integration timescales, the removal of such a large fraction of visibilities does not significantly impact the sensitivity of the array.

In 2016, I identified an additional and necessary data editing step from visibilities predominantly associated with baselines with large uv distances having anomalously high amplitudes. Inspection of average relative power between the co- (XX, YY) and cross-correlations (XY, YX) for a subset of LBDA antennas revealed that their polarizations had been swapped somewhere along the signal path, such that the input received by the correlator and labeled as Y-polarization is actually X-polarization (and vice versa). Attempting to calibrate using the visibilities of affected LBDA baselines as XX and YY correlations when they are actually XY, YX correlations

(and should therefore see significantly lower flux than expected) results in vastly incorrect complex antenna gain solutions for those antennas. Figure 2.9 shows how incorrectly labeled X–Y LBDA antenna polarizations are identified through their relative co- and cross-correlation amplitudes. Corrections for polarization swaps are done in data-processing through re-ordering of XX, XY, YX, and YY visibility columns in the measurement set. Figure 2.10 shows the improvement in image quality following this correction.
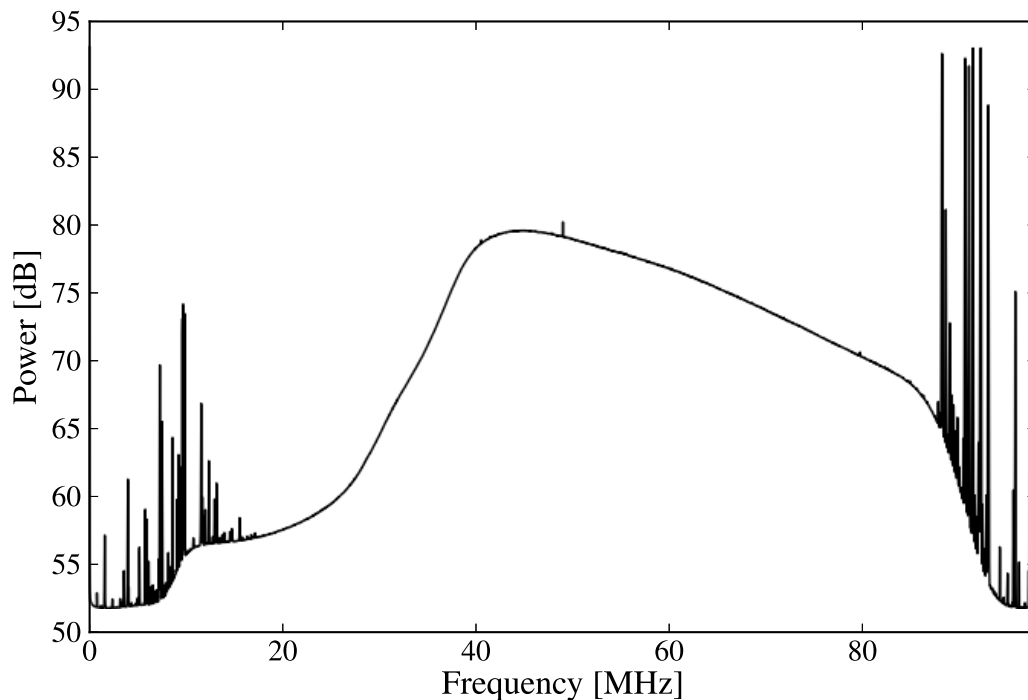


Figure 2.8: Median antenna power spectrum (across all 512 signals) from 2019 March 05. The science band is between approximately 28–86 MHz. The out-of-band RFI due to the HF and FM bands is apparent immediately above and below the science band. The FFT sampling frequency spike is at 196.608/4 MHz. The shape of the spectrum reflects a combination of the antenna frequency response, Galactic sky emission ($T \propto \nu^{-2.5}$), and ARX filtering at the bottom third of the band.

**Bandpass and Polarization Calibration**

The data are calibrated using a simplified sky model consisting of the two brightest sources in the sub-100 MHz sky: the radio galaxy Cygnus (Cyg) A and the supernova remnant Cassiopeia (Cas) A. Model flux values and spectral indices for these sources are taken from Baars et al. 1977 and Perley and Butler 2017, and attenuated based on their location in the primary beam at the time when the calibration solutions are
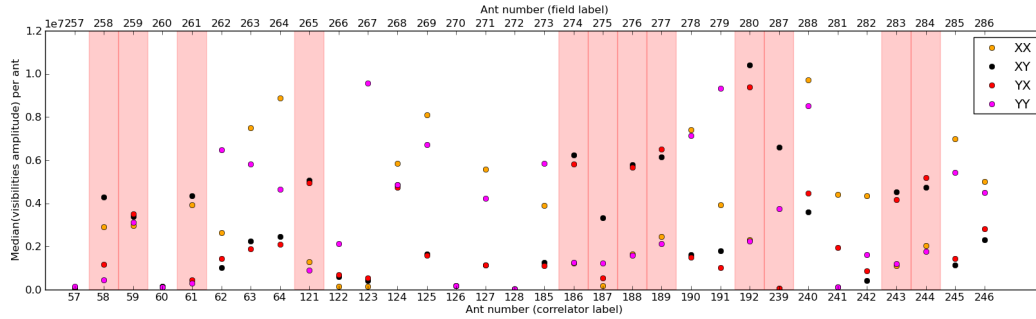
Figure 2.9: The identification of LBDA antennas with X–Y polarizations that have been switched (marked in pink). Antennas with this issue are automatically identified through the relative median visibility amplitudes (taken for all baselines that include a given antenna) between the 2 co- (XX, YY) and cross-polarizations (XY, YX). Because the sky is dominated by unpolarized emission, the XX and YY correlations should always contain more power. Antennas with higher XY and YX correlations indicates these actually correspond to XX and YY, and that somewhere along the signal path between antenna and input to the correlator, the X and Y signals were switched.
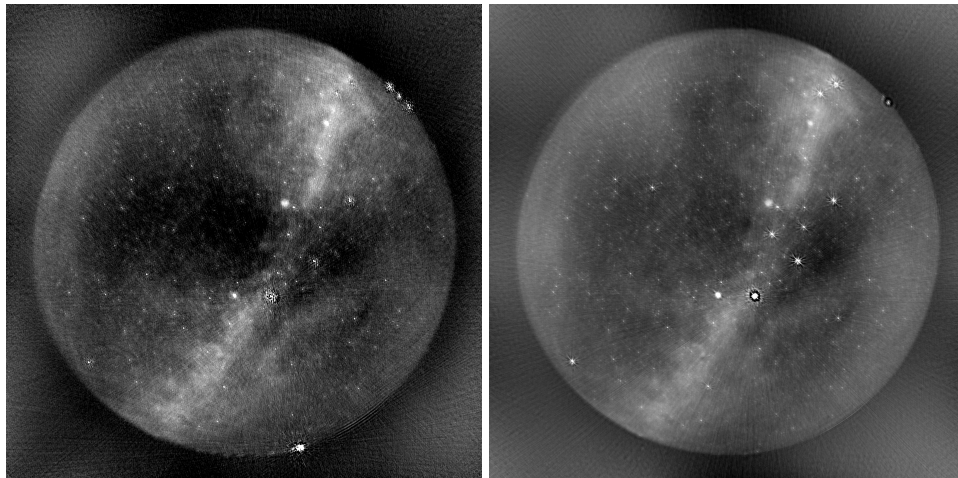


Figure 2.10: Snapshot, full bandwidth images taken in 2016 (left) and 2017 (right), highlighting the significant improvements made with the array in the intervening year. These improvements were largely due to the localization and subsequent removal of the source of RFI to the south-west of the array (associated with sparking power lines and visible in the image on the left as an extended source on the south-west horizon), the identification of cross-talk between adjacent signal paths, and the identification of LBDA antennas with swapped polarizations. The result of these fixes is significantly improved noise and lower sidelobe artifacts.

determined. For the data reduction pipelines described here, calibration solutions are derived from a single integration – typically when Cyg A is at its highest elevation

in the beam ($\sim 87°$), corresponding to when Cas A is at an elevation of $51°$. For an approximate dipole forward gain pattern given by $\sin\theta^{1.6}_{elev}$, the flux of Cas A is attenuated by nearly 30%, and therefore taking into account the primary beam pattern of the array when generating the calibration model is important. Because the antenna gain is sufficiently stable over 24 h periods, complex antenna gains are solved for only once per day and are generally only needed once per observation. The complex (amplitude and phase) solutions are determined on a per-frequency-channel basis using the CASA `bandpass` task.

While this method of calibration has been sufficient to-date, it introduces errors in two significant ways. (1) The 2-point source sky model is grossly over-simplified, and while the effect of the diffuse Galactic synchrotron emission is mitigated when solving for calibration solutions by using only baselines greater than 15 wavelengths, the Galactic emission is not fully resolved out, nor are the thousands of discrete point sources accounted for. (2) While a single integration provides sufficient signal-to-noise on Cyg A and Cas A to solve for a set of complex antenna gains, variations in both flux and position due to scintillation and refraction in the ionosphere affect the solutions. Future improvements in calibrating the array will involve the use of a more complete sky model (generated from the full-sky maps of Eastwood et al. 2018) using data spaced over multiple integrations to average out the effects of the ionosphere.

While the above steps are used to derive direction-independent (DI) calibration solutions (one set of amplitude and phase values per antenna per channel per day), an additional direction-dependent calibration and source subtraction (peeling) towards Cyg A and Cas A are performed on single-integration timescales, using visibilities with baselines greater than 10 wavelengths. This is necessitated by variations in the antenna gain pattern between individual dipole beams, caused by mutual coupling between adjacent antennas, and to a lesser degree, deviations in antenna orientation and ionospheric fluctuations. Peeling is performed using the `TTCal` calibration software package developed by Eastwood 2016.

Polarization calibration is a critical step in the pipeline for specific OVRO-LWA science cases — for transients, polarization calibration is necessary for producing accurate Stokes V maps, which allow the search for circularly polarized stellar and planetary radio emission, in images that are not confusion noise-limited. Because all 4 correlation products are produced by the correlator, the OVRO-LWA is capable

of generating maps of all 4 Stokes parameters:

$$
\begin{bmatrix} I \\ Q \\ U \\ V \end{bmatrix} = \frac{1}{2} \begin{bmatrix} 1 & 0 & 0 & 1 \\ 1 & 0 & 0 & -1 \\ 0 & 1 & 1 & 0 \\ 0 & j & -j & 0 \end{bmatrix} \begin{bmatrix} \langle XX^* \rangle \\ \langle XY^* \rangle \\ \langle YX^* \rangle \\ \langle YY^* \rangle \end{bmatrix},
\tag{2.1}
$$

where $X(t) = E_{o,x} e^{j\phi}$ and $Y(t) = E_{o,y} e^{j\phi}$, $j$ is the imaginary number, $^*$ represents the complex conjugate, and $\phi$ is the phase difference between the X and Y polarizations (Hamaker, Bregman, and Sault 1996). From Equation 2.1, the Stokes I total intensity (as well as Stokes Q linear polarization) is a linear combination of the XX and YY correlations, and therefore the X and Y dipole arrays can be calibrated separately from one another. Stokes V (and Stokes U), however, are constructed from the XY and YX correlations, and the relative phase between the X and Y dipole arrays must be determined.

However, correctly calibrating the X and Y phase of the array is a non-trivial challenge for a wide-field, low frequency array like the OVRO-LWA, for the following reasons. (1) Polarization calibration requires the measurement of a source of known polarization and flux with sufficient signal-to-noise. There is no equivalent polarized calibrator source for the OVRO-LWA that can sufficiently dominate over the substantial amount of Stokes I leakage from both the galaxy and Cas A and Cyg A into the cross-polarization signals. The possible exception to this is the Sun during a bright, Type II bursting event, however such events are too rare to be relied upon as regular calibration sources, and would require knowing a priori the flux and degree of polarization of such an event. (2) For traditional polarization calibration procedures, a source of known polarized flux is typically observed at the center of the beam, where the instrumental polarization of the array is well-behaved, and in a narrow field-of-view to provide isolation from the rest of the sky. The nearly $20,000\,\mathrm{deg}^2$ field-of-view of the OVRO-LWA fails to provide the latter, and the complicated dependence of the complex (amplitude and phase) antenna beam with azimuth and elevation introduces another unknown when attempting to calibrate with a source of known polarization.

In order to solve for the relative X–Y phase of the array and make a first-order correction to the leakage across the beam in full Stokes maps, I have developed a technique that utilizes the polarization introduced by the antenna to non-polarized sources, in combination with our knowledge of a theoretical LWA dipole complex beam. This is used to determine a model for (extrinsically) polarized sources in

the OVRO-LWA field-of-view as well as the intrinsic antenna Stokes maps in order to perform a polarization calibration and a direction-dependent correction for the leakage in the beam. This avoids the polarization calibration issues detailed above.

A single LWA dipole with a $3\,\mathrm{m} \times 3\,\mathrm{m}$ ground screen is simulated in GRASP using the Method of Moments to evaluate the complex beam pattern of the dipole at a series of azimuth and elevation grid points (over the entire field-of-view), and as a function of frequency (Dave Woody, internal memo). The output is a set of complex (amplitude and phase) values at each grid point in 2 orthogonal directions. Interpolating across the azimuth, elevation, and frequency gives the complex beam pattern for a single dipole, along two orthogonal axes as defined by a given coordinate system. Antenna beam measurements are typically done in one of Ludwig's 3 coordinate systems (Ludwig 1973); in the following we describe the antenna beam pattern in both Ludwig's 2nd and 3rd coordinate systems, using the former because it is akin to polar coordinates and is intuitively easier to understand when describing dipole radiation patterns, and the latter because when forming a Jones matrix from the radiation pattern it does not suffer a discontinuity at zenith in the way that $\theta$ in Ludwig's 2nd does.

Beam values for the far-field complex voltage pattern for a single dipole in Ludwig's 2nd ($E_\theta$, $E_\phi$) and 3rd ($E_{\mathrm{co}}$, $E_{\mathrm{cx}}$) coordinate systems can be used to construct a Jones matrix to describe the beam for two crossed dipoles. From the coordinate systems depicted in Figure 2.11, we can write the Jones matrix $J_{\mathrm{beam}}$ describing the direction-dependent effects of the polarized beam for two crossed-dipoles as

$$J_{\mathrm{beam,2nd}} = \begin{bmatrix} E_\theta & E_\phi \\ E_{\theta,90} & E_{\phi,90} \end{bmatrix}, \tag{2.2}$$

$$J_{\mathrm{beam,3rd}} = \begin{bmatrix} E_{\mathrm{co}} & E_{\mathrm{cx}} \\ -E_{\mathrm{cx},90} & E_{\mathrm{co},90} \end{bmatrix}, \tag{2.3}$$

where I have assumed that the far-field complex voltage pattern for one dipole is equivalent to that of the other, but rotated by $90°$ (denoted by the $_{90}$ subscript, which represents a counterclockwise rotation around zenith).

Using

$$\mathbf{B} = \begin{bmatrix} B_{XX} & B_{XY} \\ B_{YX} & B_{YY} \end{bmatrix} = \frac{1}{2} \begin{bmatrix} I + Q & U + jV \\ U - jV & I - Q \end{bmatrix}, \tag{2.4}$$

where **B** is the brightness matrix that describes the polarized sky as a function of ($l$,$m$) direction (Smirnov 2011), we can write

$$\mathbf{B}_{\text{apparent}} = J_{\text{beam}} \, \mathbf{B}_{\text{sky}} \, J_{\text{beam}}^{H}, \tag{2.5}$$

where $^{H}$ denotes the Hermitian transpose of the Jones matrix. In this analysis, I have assumed that the direction-dependent effects represented by the polarized beam are the same for all baselines (e.g., our beam model is consistent across antennas). In practice, this assumption is wrong, for reasons described above regarding additional complexities in individual antenna beams, however we assume it here for simplicity, and because this is currently our best model for the beam of the array. Equation 2.5 is the matrix equivalent of the Radio Interferometer Measurement Equation (see also Smirnov 2011), and it allows us to turn the far-field complex voltage pattern for a single dipole into a crossed-dipole full Stokes beam map.
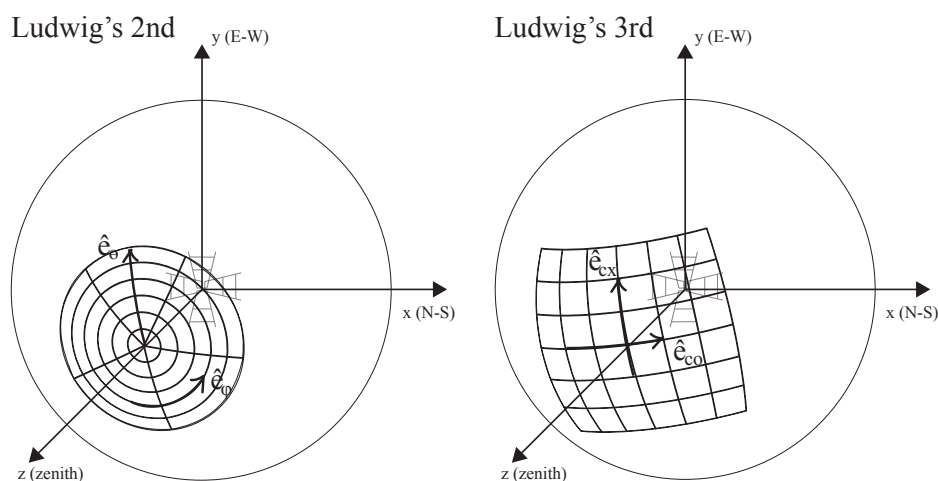


Figure 2.11: Ludwig's 2nd (left) and 3rd (right) coordinate systems. See also Figure 1 of Ludwig 1973.

## References

Anderson, M. M., G. Hallinan, M. W. Eastwood, R. M. Monroe, H. K. Vedantham, S. Bourke, L. J. Greenhill, J. Kocz, T. J. W. Lazio, D. C. Price, F. K. Schinzel, Y. Wang, and D. P. Woody. 2018. "A Simultaneous Search for Prompt Radio Emission Associated with the Short GRB 170112A Using the All-sky Imaging
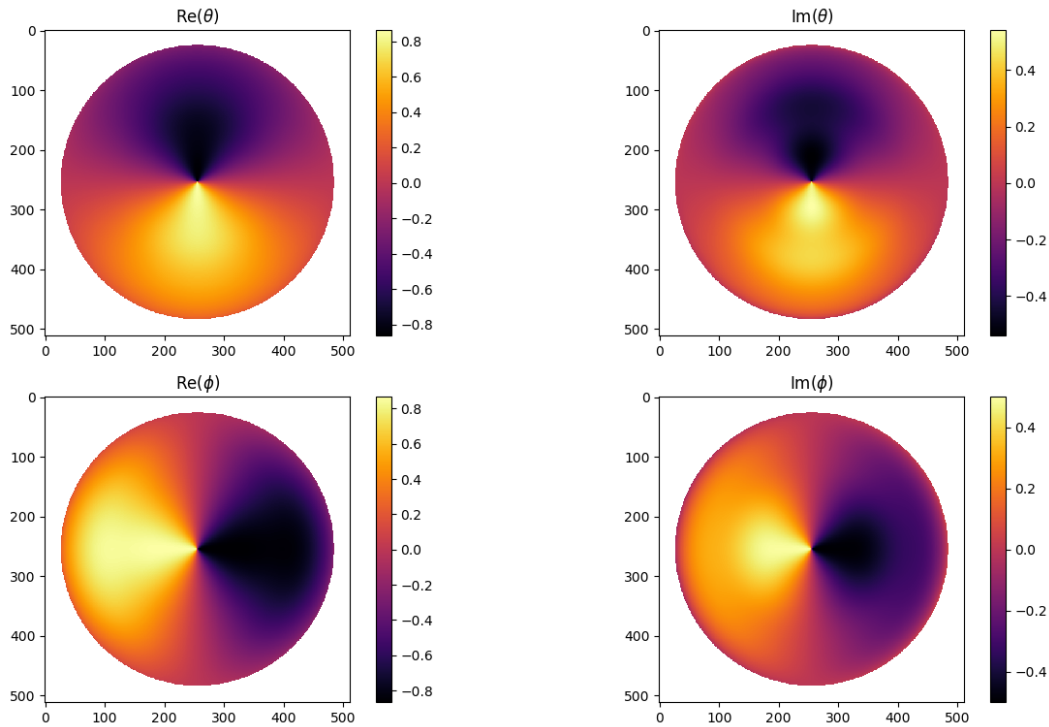
Figure 2.12: Simulated maps for the real and imaginary components of the far-field voltage pattern of a single LWA dipole in Ludwig's 2nd $(E_\theta, E_\phi)$ coordinate system.

Capability of the OVRO-LWA". *ApJ* 864 (22): 1–11. doi:`10.3847/1538-4357/aad2d7`. arXiv: `1711.06665 [astro-ph.HE]`.

Baars, J. W. M., et al. 1977. "The absolute spectrum of CAS A - an accurate flux density scale and a set of secondary calibrators". *A&A* 61 (): 99–106.

Eastwood, M. W., et al. 2018. "The Radio Sky at Meter Wavelengths: m-mode Analysis Imaging with the OVRO-LWA". *AJ* 156, 32 (): 32. doi:`10.3847/1538-3881/aac721`. arXiv: `1711.00466 [astro-ph.IM]`.

– . 2017. "The Radio Sky at Meter Wavelengths: m-Mode Analysis Imaging with the Owens Valley Long Wavelength Array". *ArXiv e-prints* (). arXiv: `1711.00466 [astro-ph.IM]`.

Eastwood, Michael W. 2016. *TTCal*. Version 0.3.0. doi:`10.5281/zenodo.1049160`. `https://doi.org/10.5281/zenodo.1049160`.

Hamaker, J. P., J. D. Bregman, and R. J. Sault. 1996. "Understanding radio polarimetry. I. Mathematical foundations." *A&A* 117 (): 137–147.

Hicks, B. C., et al. 2012. "A Wide-Band, Active Antenna System for Long Wavelength Radio Astronomy". *PASP* 124 (): 1090. doi:`10.1086/668121`. arXiv: `1210.0506 [astro-ph.IM]`.
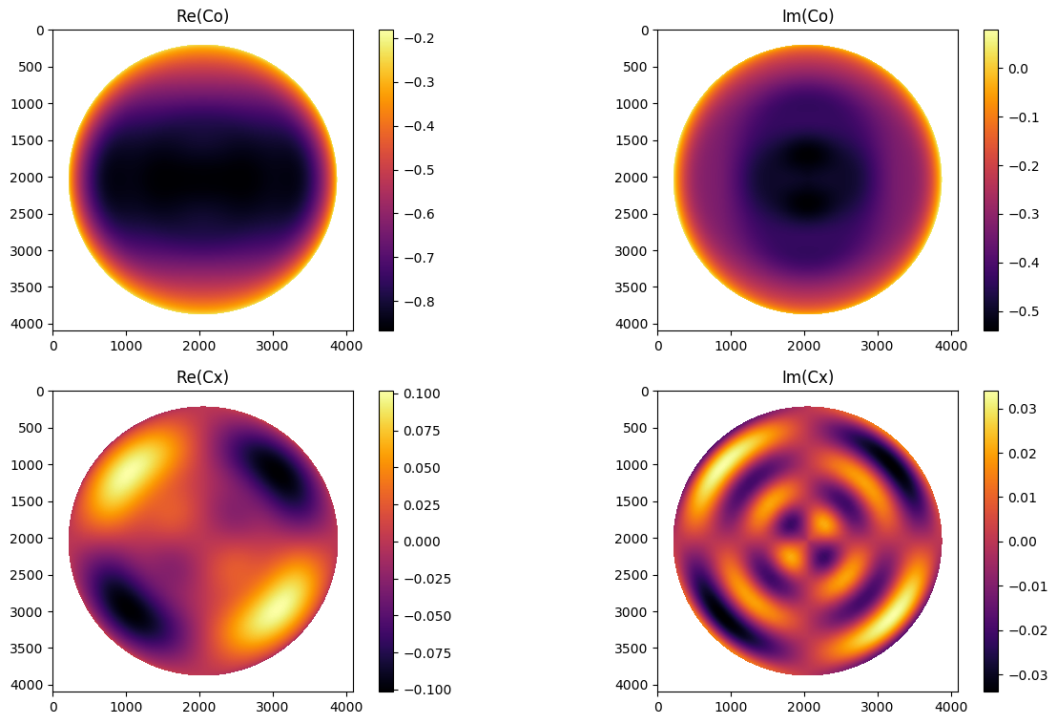
Figure 2.13: Simulated maps for the real and imaginary components of the far-field voltage pattern of a single LWA dipole in Ludwig's 3rd ($E_{\text{co}}$, $E_{\text{cx}}$) coordinate system.

Intema, H. T., et al. 2009. "Ionospheric calibration of low frequency radio interferometric observations using the peeling scheme. I. Method description and first results". *A&A* 501 (): 1185–1205. doi:`10.1051/0004-6361/200811094`. arXiv: `0904.3975 [astro-ph.IM]`.

Kocz, J., et al. 2015. "Digital Signal Processing Using Stream High Performance Computing: A 512-Input Broadband Correlator for Radio Astronomy". *Journal of Astronomical Instrumentation* 4, 1550003 (): 1550003. doi:`10.1142/S2251171715500038`. arXiv: `1411.3751 [astro-ph.IM]`.

Ludwig, A. C. 1973. "The definition of cross polarization." *IEEE Transactions on Antennas and Propagation* 21:116–119. doi:`10.1109/TAP.1973.1140406`.

Obenberger, K. S., et al. 2015. "Monitoring the Sky with the Prototype All-Sky Imager on the LWA1". *Journal of Astronomical Instrumentation* 4, 1550004-1104 (): 1550004–1104. doi:`10.1142/S225117171550004X`. arXiv: `1503.05150 [astro-ph.IM]`.

Perley, R. A., and B. J. Butler. 2017. "An Accurate Flux Density Scale from 50 MHz to 50 GHz". *ApJs* 230, 7 (): 7. doi:`10.3847/1538-4365/aa6df9`. arXiv: `1609.05940 [astro-ph.IM]`.
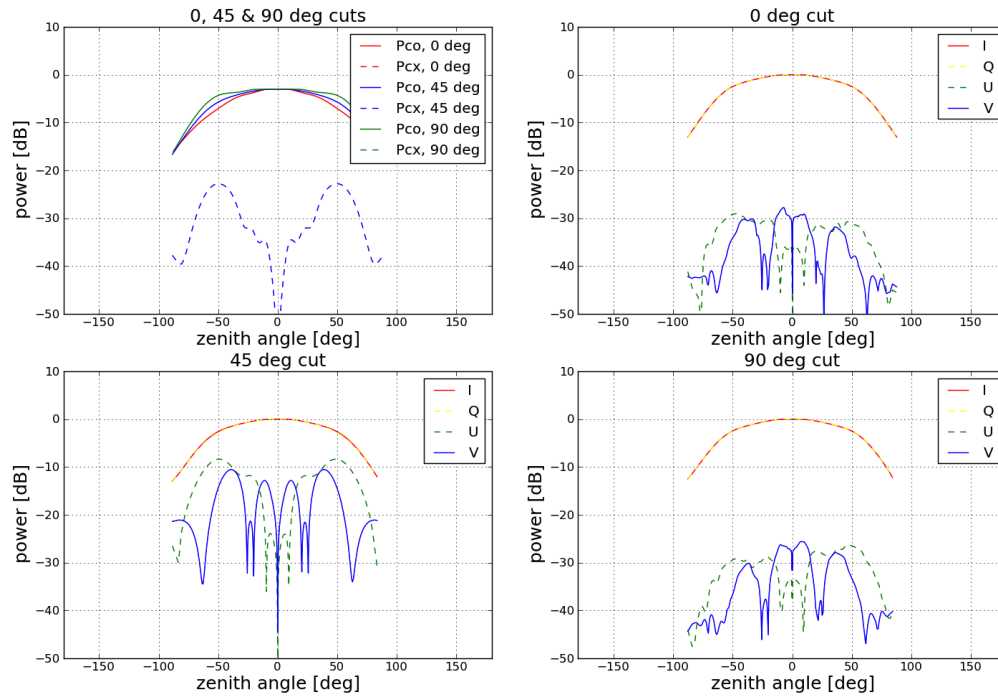
Figure 2.14: Simulated LWA dipole beam at 47 MHz, in Ludwig's 3rd coordinate system. The top left panel shows the power in the two linear polarizations, $P_{co}$ and $P_{cx}$, for cuts through the beam at angles of 0°, 45°, and 90° azimuth. The corresponding antenna Stokes beams are shown at different azimuth slices in the remaining 3 panels.

Prasad, P., et al. 2016. "The AARTFAAC All-Sky Monitor: System Design and Implementation". *Journal of Astronomical Instrumentation* 5, 1641008 (): 1641008. doi:`10.1142/S2251171716410087`. arXiv: `1609.04205 [astro-ph.IM]`.

Price, D. C., et al. 2018. "Design and characterization of the Large-aperture Experiment to Detect the Dark Age (LEDA) radiometer systems". *MNRAS* 478 (): 4193–4213. doi:`10.1093/mnras/sty1244`. arXiv: `1709.09313 [astro-ph.IM]`.

Smirnov, O. M. 2011. "Revisiting the radio interferometer measurement equation. I. A full-sky Jones formalism". *A&A* 527, A106 (): A106. doi:`10.1051/0004-6361/201016082`. arXiv: `1101.1764 [astro-ph.IM]`.
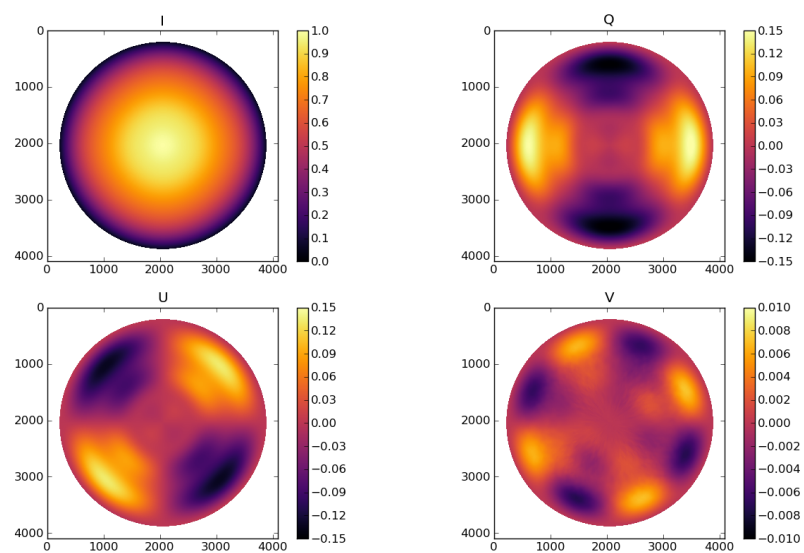
Figure 2.15: LWA full Stokes beam maps. The color scale shows normalized gain values, set to 1 at zenith in Stokes I. The maps are derived using Equation 2.5, and assuming a uniformly illuminated unpolarized sky.

*Chapter 3*

# A SIMULTANEOUS SEARCH FOR PROMPT RADIO EMISSION ASSOCIATED WITH THE SHORT GRB 170112A USING THE ALL-SKY IMAGING CAPABILITY OF THE OVRO-LWA

Marin M. Anderson[1], Gregg Hallinan[1], Michael W. Eastwood[1], Ryan M. Monroe[1], Harish K. Vedantham[1], Stephen Bourke[1,2], Lincoln J. Greenhill[3], Jonathon Kocz[1], T. Joseph W. Lazio[4], Danny C. Price[3,5], Frank K. Schinzel[6,7], Yuankun Wang[1], David P. Woody[8]

**Abstract**

We have conducted the most sensitive low-frequency (below 100 MHz) search to date for prompt, low-frequency radio emission associated with short-duration gamma-ray bursts (GRBs), using the Owens Valley Radio Observatory Long Wavelength Array (OVRO-LWA). The OVRO-LWA's nearly full-hemisphere field of view (~ 20,000 square degrees) allows us to search for low-frequency (sub-100 MHz) counterparts for a large sample of the subset of GRB events for which prompt radio emission has been predicted. Following the detection of short GRB 170112A by *Swift*, we

[1]California Institute of Technology, 1200 E California Boulevard MC 249-17, Pasadena, CA 91125, USA

[2]Department of Space, Earth and Environment, Chalmers University of Technology, Onsala Space Observatory, SE-439 92 Onsala, Sweden

[3]Harvard-Smithsonian Center for Astrophysics, 60 Garden Street, Cambridge MA 02138, USA

[4]Jet Propulsion Laboratory, California Institute of Technology, 4800 Oak Grove Drive, Pasadena, CA 91109, USA

[5]Centre for Astrophysics & Supercomputing, Swinburne University of Technology, P.O. Box 218, Hawthorn, VIC 3122, Australia

[6]National Radio Astronomy Observatory, P.O. Box O, Socorro, NM 87801, USA

[7]Department of Physics and Astronomy, University of New Mexico, Albuquerque, NM 87131, USA

[8]California Institute of Technology, Owens Valley Radio Observatory, Big Pine, CA 93513, USA

used all-sky OVRO-LWA images spanning one hour prior to and two hours following the GRB event to search for a transient source coincident with the position of GRB 170112A. We detect no transient source to within a $3\sigma$ flux density limit of 4.5 Jy at 13 s timescales for frequencies spanning 27–84 MHz. We place constraints on a number of models predicting prompt, low-frequency radio emission accompanying short GRBs and their potential binary neutron star merger progenitors, and place an upper limit of $L_{\mathrm{radio}}/L_\gamma \lesssim 3.5 \times 10^{-6}$ on the fraction of energy released in the prompt radio emission, under the assumptions of negligible scattering of the radio pulse and beaming of emission along the line of sight. These observations serve as a pilot effort for a program targeting a wider sample of both short and long GRBs with the OVRO-LWA, including bursts with confirmed redshift measurements that are critical to placing constraining limits on prompt radio emission models, as well as a program for the follow-up of gravitational wave compact binary coalescence events detected by advanced LIGO and Virgo.

*Key words:* gamma-ray burst: general, gamma-ray burst: individual (170112A), gravitational waves, radiation mechanisms: non-thermal, radio continuum: general

## 3.1 Introduction

The detection of the first gamma-ray bursts (GRBs) in 1967 heralded a race to better characterize, classify, and identify the nature of the progenitors of these seconds-long bursts of MeV gamma-rays, which appeared to be isotropically distributed across the sky and thus likely of cosmic origin (Klebesadel, Strong, and Olson 1973). Systematic detections of GRBs over the following decades revealed two distinct classes of events: the spectrally hard, short (typical duration < 2 s) GRBs and the spectrally soft, long (typical duration > 2 s) GRBs (Kouveliotou et al. 1993). The rapid follow-up capabilities of the BATSE instrument and BeppoSAX led to the detection of X-ray, optical, and, later, radio afterglows that provided critical information regarding distance, host galaxy association, isotropic energy estimates, source size evolution, and insight into GRB progenitors (Costa et al. 1997; Frail et al. 1997; van Paradijs et al. 1997). Routine follow-up and afterglow detection revealed that the distinct phenomenology of short and long GRBs also reflects distinct progenitor systems. Long GRB hosts are exclusively star forming galaxies (Savaglio, Glazebrook, and Le Borgne 2009), and the location of long GRBs within their host galaxies correlates strongly with ultraviolet light, implying that long GRBs trace regions of active massive star formation (Fruchter et al. 2006). This, combined with the association of long GRBs with Type Ic core-collapse supernovae (SNe), points

to massive stars as the progenitors of long GRBs (Woosley and Bloom 2006).

The progenitors of short GRBs, however, have remained more elusive. While significant evidence exists for the association of short GRBs with compact object mergers consisting of neutron star binaries (NS–NS) or neutron star black hole binaries (NS–BH; Narayan, Paczynski, and Piran 1992), the association is not as definitive as that of long GRBs with core-collapse supernovae (see, e.g., Lyutikov 2009). However, the compact object merger scenario is the favorable progenitor model for short GRBs for the following reasons: (1) short GRBs are found in both early- and late-type galaxies, consistent with the formation of progenitor binary systems following a delay-time distribution and therefore being found in both young and old stellar populations; (2) localization within the host galaxy provided by detections of short GRB afterglows indicates a population distribution with significantly larger host galaxy offset relative to the long GRB / core-collapse SN population, as expected for a compact object binary progenitor born with a natal kick (Bloom, Sigurdsson, and Pols 1999; Belczynski et al. 2006); and (3) unlike long GRBs, short GRBs have no established association with supernovae (Berger et al. 2005; Bloom et al. 2006; Soderberg et al. 2006; Berger 2009), although they are associated with kilonovae / macronovae believed to be powered by r-process nucleosynthesis in the expanding post-merger ejecta (Li and Paczyński 1998; Tanvir et al. 2013; Yang et al. 2015).

A number of models predict a highly speculative but potentially very valuable counterpart to GRBs and NS–NS(BH) mergers in the form of a short, bright, coherent pulse of low-frequency radio emission (Table 3.1). The models predicting this coherent radio emission span all stages of the compact object merger process, from (1) the final in-spiral of the binary neutron stars, to (2) a short-lived, post-merger supramassive neutron star, to (3) the post-collapse stage during which the gamma-ray emission is produced. Hansen and Lyutikov 2001 consider the magnetospheric interaction of an NS-magnetar binary system and the generation of a coherent radio burst in the surrounding plasma environment during the pre-merger (1) phase (see also Lyutikov 2013). Pshirkov and Postnov 2010 consider a low-frequency radio burst generated in the relativistic plasma outflow from the highly magnetized, rapidly rotating magnetar, which is predicted to form in the brief stage (2) between the merger and final collapse. Usov and Katz 2000 predict a low-frequency radio burst that may be produced in the post-merger (3) phase (as well as in long GRBs) through the interaction of a strongly magnetized wind with the circumburst medium. In this model, the coherent low-frequency emission is produced by the time-variable surface

current that exists at the wind/ambient plasma boundary. Other models predicting coherent radio emission post-merger include synchrotron maser emission generated during the GRB fireball phase (Sagiv and Waxman 2002), and inverse Compton radiation generated in the surrounding magnetized plasma by magnetohydrodynamic modes excited by the gravitational waves (GWs) produced in the merger (Moortgat and Kuijpers 2005).

Despite the diversity of models, common to all is the prediction that a GRB is accompanied by a coherent and intrinsically short-duration burst of radio emission that occurs within a window of several seconds to the production of the gamma-ray emission, with a steep negative spectral index that favors observations at lower frequencies. In the case of Usov and Katz 2000, the emission is predicted to peak at ~MHz frequencies and fall off rapidly above roughly 30 MHz. Many of the models also require the presence of extreme, magnetar-strength magnetic fields (e.g. as high as $10^{15}$ G) – atypical given the expected age of these systems at the time of merger (Goldreich and Reisenegger 1992), but justified in the models through magnetic field amplification during the coalescence of the system (and through numerical simulations, e.g., Duez et al. 2006). Magnetic field amplification has also been predicted for post-merger hypermassive neutron star remnants and invoked to explain short GRB extended emission (Metzger, Quataert, and Thompson 2008) and the kilonova emission of GW1701817 (Metzger, Thompson, and Quataert 2018).

Searches for prompt, coherent radio counterparts to GRBs are made difficult by the need for observations that satisfy the requirements for high sensitivity at sufficiently low frequency, and are coincident with (or, dependent on the amount of dispersive delay, shortly after) the detection of the corresponding GRB. There have been many searches for prompt, coherent radio counterparts to GRBs to date, but none have yielded detections thus far (e.g., Baird et al. 1975; Inzani et al. 1982; Koranyi et al. 1995; Dessenne et al. 1996; Benz and Paesold 1998; Balsano 1999; Bannister et al. 2012; see Granot and van der Horst 2014 for brief summary). Most recently, Obenberger et al. 2014 searched for prompt emission from 32 GRBs using the LWA1 Prototype All Sky Imager (PASI; Ellingson et al. 2013; Obenberger et al. 2015), and Kaplan et al. 2015 conducted follow-up observations of the short GRB 150424A, starting within 23 s of the detected gamma-rays, with the Murchison Widefield Array (MWA; Tingay et al. 2013) at frequencies above 80 MHz. See Table 3.2 for a summary of previous radio surveys specifically targeting prompt emission associated with GRBs.

Table 3.1: Models for prompt radio counterparts to GRBs

| (1)<br>Reference(s) | (2)<br>Delay Relative to GRB | (3)<br>$t_{intrinsic,R}$ | (4)<br>Flux Density<br>(Jy) | (5)<br>Spectral Index | (6)<br>B-field<br>(G) | (7)<br>$L_R/L_\gamma$ |
|---|---|---|---|---|---|---|
| Hansen and Lyutikov 2001 / Lyutikov 2013[a] | 10-100 ms before | $\sim 4$ ms | 0.09 | -1 | $10^{12}$ | $10^{-10} \propto \epsilon_R$ |
| Pshirkov and Postnov 2010[b] | $\sim 10$s of ms before | 10-100 ms | $9 \times 10^4$ | -2 | $10^{14} - 10^{16}$ | $10^{-5} \equiv \eta$ |
| Usov and Katz 2000[c] | simultaneous | $t_{\gamma,prompt}$ | 350 | -0.6 | $10^{15} - 10^{16}$ | $10^{-4} \equiv \delta$ |

[a]Coherent radio emission is generated in the pre-merger phase through the magnetospheric interactions between the two components of the binary system; the resulting magnetized wind produces coherent radio emission with luminosity that scales as $t^{-1/4}$ until it peaks at the time of merger, which is estimated to occur between 10 and 100 ms prior to the production of the GRB. Flux density prediction in column (4) is calculated at 30 MHz for the $\sim 4$ ms period during which the emission peaks as the neutron stars make contact and finally merge. The flux density prediction also assumes that the efficiency with which wind power is converted into coherent radio emission is $\epsilon_R = 10^{-5}$. See Equation 13 in Lyutikov 2013.

[b]Coherent radio emission is generated by the rapid conversion of rotational energy into magnetic energy in the rotationally supported massive NS, which forms following the merger of the BNS system, but prior to its final collapse and the generation of the GRB. The flux density prediction in column (4) is calculated at 30 MHz, and assumes a conversion coefficient $\eta$, defined by the authors as the efficiency with which spin-down energy is converted into radio luminosity, as $\eta = 10^{-5}$. See Equation 7 in Pshirkov and Postnov 2010.

[c]Coherent radio emission occurs simultaneously to gamma-ray emission, and is powered by Langmuir waves generated at the boundary between the highly magnetized outflow and the surrounding ambient medium of the GRB. The flux density prediction in column (4) is calculated at 30 MHz, for a burst like GRB 170112A with duration 0.06 s and fluence $0.13 \times 10^{-7}$ erg cm$^{-2}$, and assumes $\delta$, defined by the authors as the fluence in radio emission relative to the fluence measured in gamma-rays, as $\delta = 10^{-4}$. See Equation 14 in Usov and Katz 2000.

NOTE – The estimates and parameters used to calculate the predicted flux density $S$ use the approximate values reported in the respective model papers as astrophysically plausible and/or most-likely values. We emphasize that many of the parameters estimated in these models are unknown and not constrained astrophysically; therefore, the appropriate ranges for these values can vary by orders of magnitude.
(1) Reference for model predicting coherent radio emission associated with GRB.
(2) Onset of radio emission relative to onset of gamma-ray emission.
(3) Duration of coherent radio emission, before dispersion.
(4) Model-predicted flux density for a burst located at $D = 1$ Gpc, the approximate distance upper limit to GRB 170112A.
(5) Spectral index.
(6) Magnetic field strengths required by the model in the GRB progenitor in order to satisfy conditions necessary for producing coherent radio emission.
(7) Luminosity ratio between energy released in radio frequencies to energy released in gamma-rays, during the prompt emission stage. See Palmer 1993.

Table 3.2: Searches targeting prompt, coherent radio emission associated with GRBs

| (1) Reference(s) | (2) Instrument | (3) Frequency (MHz) | (4) Bandwidth (MHz) | (5) Sensitivity (Jy) | (6) Time Res. (s) | (7) Frequency Res. (MHz) | (8) $t_{\rm on\,sky}$ | (9) $N_{\rm GRBs}$ |
|---|---|---|---|---|---|---|---|---|
| Baird et al. 1975 | spaced receivers[a] | 151 | 1 | $10^5$ | 0.3 | 0.2 | ~1 hr | 19 |
| Cortiglioni et al. 1981 | VHF/UHF station at Medicina | 151, 408 | 1, 2 | $10^4$ | 0.3 | ... | ~1 hr | 32 |
| Inzani et al. 1982 | VHF/UHF station at Medicina | 151, 408 | 1 | $10^4$ | 1 | ... | ~1 hr | 65 |
| Koranyi et al. 1995 | CLFST | 151 | ... | 200 | 1.5 | ... | 1 hr | 1 |
| Dessenne et al. 1996 | CLFST | 151 | 0.7 | 73, 35, 15 | 1.5 | ... | −280, 6, 16 min | 2 |
| Benz and Paesold 1998 | solar radio spectrometers[b] | 40 – 1000 | ... | $10^5$ | 0.25 | 1 | simultaneous | 7 |
| Balsano 1999 | FLIRT | 74 | 1.9 | $10^3$ | 0.05 | ... | 10 s | 32 |
| Bannister et al. 2012 | 12-m dish at Parkes Observatory | 1400 | 220 | 7 | $64 \times 10^{-6}$ | 0.390 | 200 s | 9 |
| Obenberger et al. 2014 | LWA1 | 37.9, 52, 74 | 0.075 | 68, 65, 70 | 5 | 0.0167 | simultaneous | 34 |
| Kaplan et al. 2015 | MWA | 80, 88.9, 97.9, 108.1, 119.7, 132.5 | 2.56 | 8.7, 7.7, 5.7, 4.9, 4.2, 3.0 | 4 | ... | 23 s | 1 |
| This Work | OVRO-LWA | 56 | 57 | 4.5 | 13 | 0.024 | ~1 hr | 1 |

[a]The receivers were located in stations at Cambridge, UK; Dublin, Ireland; Glasgow, UK; Harwell, UK; Jodrell Bank, UK; and Malta.

[b]Located in Bleien Radio Observatory, Switzerland; Tremsdorf, Germany; and Weissenau Observatory, Germany.

NOTE –
(8) Start of observations, relative to the time of GRB.
(9) Number of GRBs targeted in the radio observations.

Despite these difficult observational requirements, and the speculative nature of the models, low-frequency radio searches for counterparts to short GRBs remain valuable. Systematic detection would provide a radio source population with the ability to probe the density and turbulence of the intergalactic medium (IGM; Inoue 2004), with utility as a diagnostic of accretion-powered jet physics (Macquart 2007), and as a valuable electromagnetic (EM) counterpart for radio follow-up of GW events (e.g., Kaplan et al. 2016). Most critically, the detection of a radio pulse associated with a short GRB would provide independent confirmation of the association of short GRBs with neutron star mergers. This is especially relevant in the current era of multimessenger astronomy ushered in by the detection of GW170817 (Abbott et al. 2017d), which provided the long sought-after first direct association between GRBs and binary neutron star mergers. However, the GRB detected in association with GW170817 remains distinct from the "classical" short GRBs that are systematically detected at larger distance (Abbott et al. 2017a). A coherent, low-frequency radio counterpart to binary neutron star mergers would provide a direct link between short GRBs and their more local GW-detected counterparts.

We have conducted the most sensitive search to date at frequencies below $100\,\text{MHz}$ for a prompt, coherent radio counterpart associated with GRBs, using the Owens Valley Radio Observatory Long Wavelength Array (OVRO-LWA) to observe the field of the short GRB 170112A. The low-frequency ($27-85\,\text{MHz}$) and simultaneous nature of our observations provides constraining limits on a number of the prompt radio emission counterpart models. In § 3.2, we describe the OVRO-LWA and our observations of GRB 170112A. In § 3.3, we describe the analysis, including our dedispersion search. In § 3.4, we place limits on any prompt radio emission associated with 170112A and the resulting constraints on the models, as well the relevance of the OVRO-LWA observations in the context of GW follow-up. We conclude in § 3.5.

## 3.2 Observations

**OVRO-LWA**

The OVRO-LWA is a 352-element, dual-polarization dipole array currently under development at the Owens Valley Radio Observatory (OVRO) in Owens Valley, California, operating at frequencies below $100\,\text{MHz}$. The final array will be spread over a $2.5\,\text{km}$ diameter area, providing a roughly $5\,\text{arcmin}$ spatial resolution. Full cross-correlation of all 352 elements will enable imaging of the entire viewable sky, with a cadence of a few seconds and $100\,\text{mJy}$ snapshot sensitivity. Early science

observations have commenced on OVRO-LWA, with key science including low-frequency radio transients, exo-space weather monitoring of nearby stellar systems, cosmic dawn 21 cm science (see Eastwood et al. 2017; Price et al. 2018), ionospheric studies, solar dynamic imaging spectroscopy, and monitoring of the Jovian system. A unique design feature of the array is the nonconflicting nature of these disparate science goals, which all share a common mode of observing and initial data products, meaning that all science objectives can be served simultaneously.

The current, stage II OVRO-LWA, which incorporates 256 elements from the 200 m diameter core and the 32-element Long Baseline Demonstrator Array (LBDA), has been observing continuously since 2016 December, operating from 27 to 84 MHz (2400 channels) with a 13 s cadence. Full cross-correlation of 512 inputs (256 antennas $\times$ 2 polarizations) by the Large-Aperture Experiment to Detect the Dark Age (LEDA) correlator (Kocz et al. 2015) provides a full-sky field of view with an approximately 10 arcmin resolution at the top of the observing band. Data are continuously written to a multiday buffer. Data corresponding to triggers of interest are copied to the on-site All-Sky Transient Monitor (ASTM) for storage and processing. Example triggers of interest include *Swift* and *Fermi* alerts for both short and long GRBs as well as GW LIGO-Virgo Collaboration (LVC) events, as distributed by the Gamma-ray Coordinates Network[1]. The short GRB 170112A represents the first short GRB with sufficient position localization to search for a coherent radio emission counterpart with the OVRO-LWA, following the onset of our stage II continuous mode of observing. The results of follow-up observations of a larger sample of both long and short GRBs with known redshift will be released once the stage II OVRO-LWA continuous operations have completed.

**Short GRB 170112A**

The short GRB 170112A was detected on 2017 January 12 02:02:00 UTC by the *Swift* Burst Alert Telescope (BAT; Gehrels et al. 2004; Krimm et al. 2013) at the position (R.A., decl.) = ($01^{\rm h}00^{\rm m}55^{\rm s}.7$, $-17°13'57''.9$), to within a 90% error region of radius 2.5 arcmin (Lien et al. 2017; Mingo et al. 2017). The burst was identified as a hard, short burst (power-law index $\alpha_{\rm PL} = -1.2$ and burst fluence $S = 0.13 \times 10^{-7}\,{\rm erg\,cm^{-2}}$ in the *Swift*-BAT 15-150 keV band), with an atypically short duration of $T_{90} = 0.06$ s (Lien et al. 2017, see the discussion in Section 3.3). No extended emission was found, as is typical of the majority of short GRBs (Bostancı, Kaneko, and Göğüş 2013). Due to the lack of detected X-ray flare or afterglow emission,

---

[1]GCN: `https://gcn.gsfc.nasa.gov/`

by either the *Swift* X-Ray Telescope (D'Ai et al. 2017) or *Swift* Ultraviolet/Optical Telescope (Siegel and Mingo 2017), following the initial BAT trigger, the position of 170112A is known only to within the 2.5 arcmin position as measured by BAT. No afterglow counterpart or associated host galaxy was found in the observations conducted by follow-up ground-based optical and NIR facilities. D'Avanzo et al. 2017 observed the location of GRB 170112A with the REM 60 cm robotic telescope at La Silla Observatory in Chile and placed an 18.0 mag H band upper limit on an afterglow counterpart. Mazaeva et al. 2017 report the detection by the 0.7 m AS-32 telescope at Abastumani Observatory of a source, inside the BAT error region, which is not present in the USNO-B1.0 catalog but is detected in the DSS2 (red) survey. We therefore disregard the association of this source with GRB 170112A, and in the remaining analysis consider GRB 170112A as a short burst with neither detected afterglow emission nor associated host galaxy.

The OVRO-LWA was observing simultaneously to the detection of 170112A by *Swift*-BAT. Following the GCN detection notice, and after receiving the verification by the GCN circular (Mingo et al. 2017) that *Swift* had detected a short GRB, we saved three hours of data from the OVRO-LWA transient buffer, corresponding to one hour prior to and two hours after the *Swift* detection (UT range 01:02:02-04:02:18). The data consist of 832 contiguous integrations of 13 s duration, with 2398 frequency channels spanning 27.38-84.92 MHz (24 kHz frequency resolution). The OVRO-LWA is a zenith-pointing telescope, and 170112A was located at an elevation of approximately $35°$ in the primary beam.

The visibility data delivered from the LEDA correlator are converted from their raw format into the standard Common Astronomy Software Applications (CASA; McMullin et al. 2007) visibility table measurement sets. The data are then flagged in frequency, antenna, and baseline space, using a combination of manual inspection and an automated in-house algorithm that fits for smoothness in the visibilities across frequency, time, and *uvw*-space (Monroe et al. 2018, in preparation). Roughly 60 antennas are flagged for the duration of the observation, the majority of these due to issues along the signal path resulting in a loss of sky signal from a subset of antennas. Less than 10% of the frequency band is flagged for radio frequency interference (RFI). The result is that approximately 45% of visibilities are flagged per integration. The data are calibrated using a simplified sky model consisting of the two brightest sources in the sub-100 MHz sky: the radio galaxy Cygnus (Cyg) A and the supernova remnant Cassiopeia (Cas) A. The complex (amplitude

and phase) antenna gains are determined on a per-channel basis from the Cyg A–Cas A sky model using the CASA `bandpass` task. The calibration solutions are derived from an integration taken at 2017 January 11 20:26 UT, 4 hr prior to the start of the GRB follow-up observations, when Cyg A is at its highest elevation in the beam ($\sim 87°$). The flux scale and bandpass are corrected by modifying the antenna gain amplitudes to fix the spectrum of Cyg A to that of Baars et al. 1977. Direction-dependent calibration in the directions of Cyg A and Cas A is performed using the `TTCal` calibration software package developed for the OVRO-LWA (Eastwood 2016). This is necessary in order to accurately peel the sources from the visibilities and avoid sidelobe contamination in the images, caused by antenna gain pattern variations between individual dipoles. Imaging and deconvolution are performed with `WSClean` (Offringa et al. 2014a, 2014b). The full field of view is imaged over $4096 \times 4096$ pixels, with a pixel scale of $1'.875$ and using a robust visibility weighting of 0 (Briggs 1995). At the time of these observations, a set of northeast LBDA antennas were not operational, resulting in an abnormally elongated synthesized beam with a major axis of $29'$, a minor axis of $13'.5$, and a position angle of $50°$.

Figure 3.1 shows the 13 s, full-band snapshot OVRO-LWA image corresponding to the time of the GRB detection by *Swift*. The images are confusion-noise limited to $\sim 800$ mJy at zenith. The image cutout in Figure 3.1 shows the $10° \times 10°$ region surrounding the position of 170112A, including two nearby VLA Low Frequency Sky Survey (VLSS; Lane et al. 2014) sources, VLSS J0108.2-1604 (3C 032), and VLSS J0102.6-2152. These were used to verify the flux scale at this part of the primary beam and track the position offset of sources over the course of the observation caused by ionospheric refraction. An ionospheric substorm can be seen moving through this region of the sky, particularly during the first hour of observations; however, the maximum source position offsets are within the size of the synthesized beam, and on average are of the order of a few arcminutes.

## 3.3  Analysis

To search for the presence of a low-frequency counterpart to 170112A in our data, we searched the flux density time series at the position of 170112A, known to within one synthesized beam, for statistically significant peaks indicative of a radio burst on our shortest, 13 s integration timescales. In each integration, the median flux of an annulus around the GRB position of width $6 \pm 1$ synthesized beams was subtracted from the flux measured at the pixel corresponding to the position
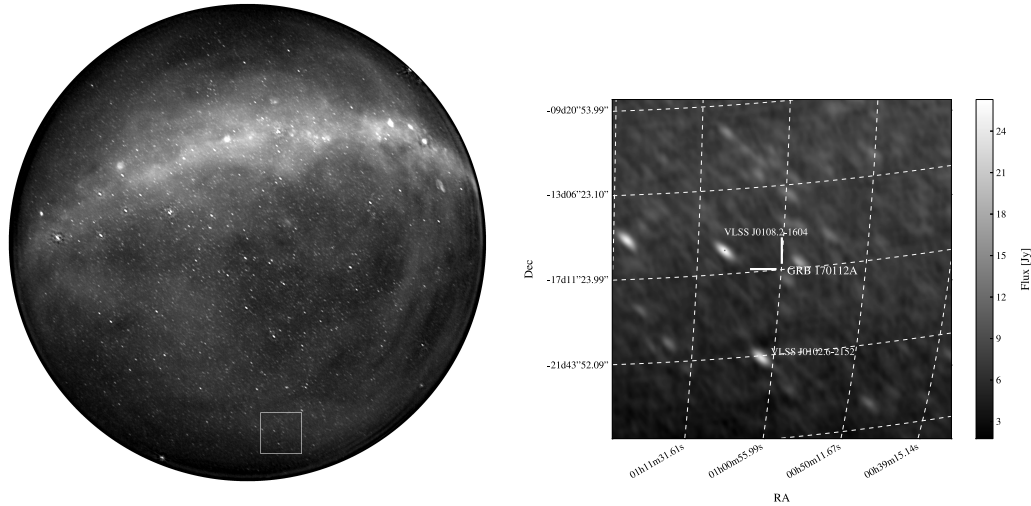
Figure 3.1: Left panel is a 13 s, full-band snapshot OVRO-LWA image corresponding to the time of the GRB detection by *Swift*, at 02:02:05 UT. The center of the image is zenith and the border of the image is the horizon line. The extended emission cutting across the top half of the image is predominantly synchrotron emission from our own galaxy. Cas A and Cyg A have been peeled from this integration. There are roughly 10,000 point sources in this 13 s image. The noise at zenith is approximately 800 mJy. The square box at 35° elevation in the southwest of the image corresponds to the right panel, which shows a $10° \times 10°$ box, centered on the location of 170112A at (R.A., decl.) = $(01^h00^m55^s.7, -17°13'57''.9)$. VLSS J0108.2-1604 and VLSS J0102.6-2152 are also labeled.

of GRB 170112A in order to remove additional flux from any large-scale, diffuse structure. This was done for the full 57 MHz bandwidth, as well as the bottom (centered at 37 MHz), middle (56 MHz), and top (75 MHz) thirds of the band. Figure 3.2 shows the dedispersed time series for these four bands for the duration of the three-hour observation, for a dispersion measure (DM) of $260 \, \text{pc} \, \text{cm}^{-3}$ (see §3.3). We find no statistically significant peaks at 13 s timescales in any of the four bands, with typical noise in the full band, bottom band, middle band, and top band light curves of 1.5 Jy, 3.6 Jy, 2.2 Jy, and 1.9 Jy, respectively.

**Pulse Propagation: Dispersion and Scattering**

The propagation of a coherent radio pulse associated with 170112A would be affected by the cold plasma in the intervening medium between the birth site of the pulse and the Earth. The signal will be dispersed, with lower frequencies arriving at later times relative to higher frequencies, following $t_{\text{arrival}} = 4.2 \, \text{DM} \, \nu_{\text{GHz}}^{-2} \, \text{ms}$ (Cordes and McLaughlin 2003). The amount of dispersion, quantified by the DM, is deter-
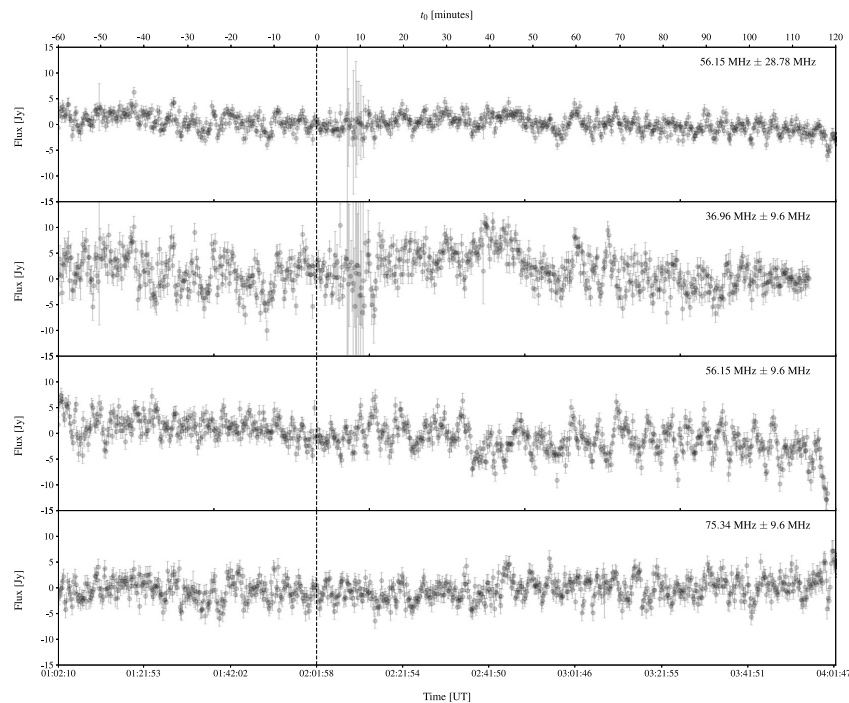
Figure 3.2: Flux density at the position of short GRB 170112A in each 13 s integration for the dedispersed time series using a DM of 260 pc cm$^{-3}$, at 56 MHz with the full 57 MHz bandwidth (top), the bottom third of the band centered at 37 MHz (second from top), the middle third of the band at 56 MHz (third from top), and the top third of the band at 75 MHz (bottom). The time series shows the full three-hour observation, starting one hour prior to the *Swift* detection of 170112A at $t_0 = 0$ (dashed line) and ending two hours later. The noise in each band is 1.5 Jy, 3.6 Jy, 2.2 Jy, and 1.9 Jy, respectively. We detect no statistically significant emission on 13 s timescales indicative of prompt radio emission associated with the short GRB, and place a full band $3\sigma$ upper flux limit of < 4.5 Jy.

mined by the column density of electrons along the pulse path (density of electrons integrated along the line of sight), and is equal to DM = $\int_0^D n_e(l)dl$, where $D$ is the distance to the source and $n_e$ is the density of electrons. The DM can be approximated as the sum of DM contributions from the Milky Way (DM$_{MW}$), the intergalactic medium (DM$_{IGM}$), and the host galaxy of the burst (DM$_{host}$). The DM contribution from the Milky Way is minimal due to the location of 170112A at high Galactic latitude ($l = 135°.9$, $b = -79°.9$); DM$_{MW} \sim 30$ pc cm$^{-3}$ based on the NE2001 model of Cordes and Lazio 2002[2]. We assume that the contributions from the host galaxy and circumburst environment of 170112A are similarly small, given the likely binary NS–NS(BH) progenitors of short GRBs and the typically

---

[2]https://www.nrl.navy.mil/rsd/RORF/ne2001/

large (4.5 kpc projected median) offsets from the center of their hosts galaxies (Fong and Berger 2013). We assume a $DM_{host} \approx DM_{MW}$. The DM contribution from the IGM can be estimated as $DM_{IGM} \sim 1000\,z\,pc\,cm^{-3}$ (Zheng et al. 2014). Because 170112A has no optical afterglow detection and no identified host galaxy, and thus is of unknown redshift, $DM_{IGM}$ is highly uncertain. However, we exploit the relationship between redshift and minimum burst duration of the prompt gamma-ray emission ($T_{90}$) determined using the sample of *Swift*-detected GRBs with redshift identifications from the third *Swift*-BAT GRB catalog (Lien et al. 2016) to place an upper limit on the redshift of 170112A of $z \lesssim 0.2$. The correlation between minimum detectable $T_{90}$ and redshift found by Lien et al. 2016 reflects that longer exposure times, and therefore longer burst durations, are needed to detect lower flux bursts. The three-burst sample with $T_{90} < 0.1$ s all having redshifts $z \lesssim 0.2$ indicates that extremely short bursts must be brighter (and thus very nearby) to be detected. However, this correlation is necessarily restricted to bursts of known redshift, and we state the caveat that bright, short bursts at high redshift may indeed be detected but are simply lacking in redshift measurements. Based on the assumptions and estimates given above, we assume an upper limit of DM $\lesssim 260\,pc\,cm^{-3}$. This corresponds to a maximum dispersive delay of $\sim 1330$ s across the full OVRO-LWA 57 MHz bandwidth, and a maximum arrival time at the top of the band of 155 s after the GRB, indicating our observation covering 2 hr post-GRB-detection is more than sufficient for capturing a coincident radio burst. The corresponding dispersion smearing across the 24 kHz channel at the bottom of the frequency band is $\tau_{DM} = 8.3 \times 10^3$ s $(\Delta\nu/\mathrm{MHz})(\nu_c/\mathrm{MHz})^{-3}(\mathrm{DM}/pc\,cm^{-3}) \approx 2.5$ s, shorter than the integration time $t_{int} = 13$ s of these observations.

Figure 3.3 shows the undispersed dynamic spectrum at the location of GRB 170112A, formed by measuring the flux at the location of GRB 170112A in the 24 kHz wide channel images across the full bandwidth, for every 13 s integration across the duration of the observation (832 integrations in total). Similar to the process by which the time series of Figure 3.2 was formed, we subtracted the median flux of an annulus around the GRB position of width $6 \pm 1$ synthesized beams from the flux measured at the pixel corresponding to the position of GRB 170112A in order to remove additional flux from any large-scale, diffuse structure. We performed a series of dedispersion trials on the dynamic spectrum, with the spacing between DM trials set by the amount of dispersion smearing acceptable across the full bandwidth in the final, dedispersed time series. We set this equal to the integration time $t_{int} = 13$ s.
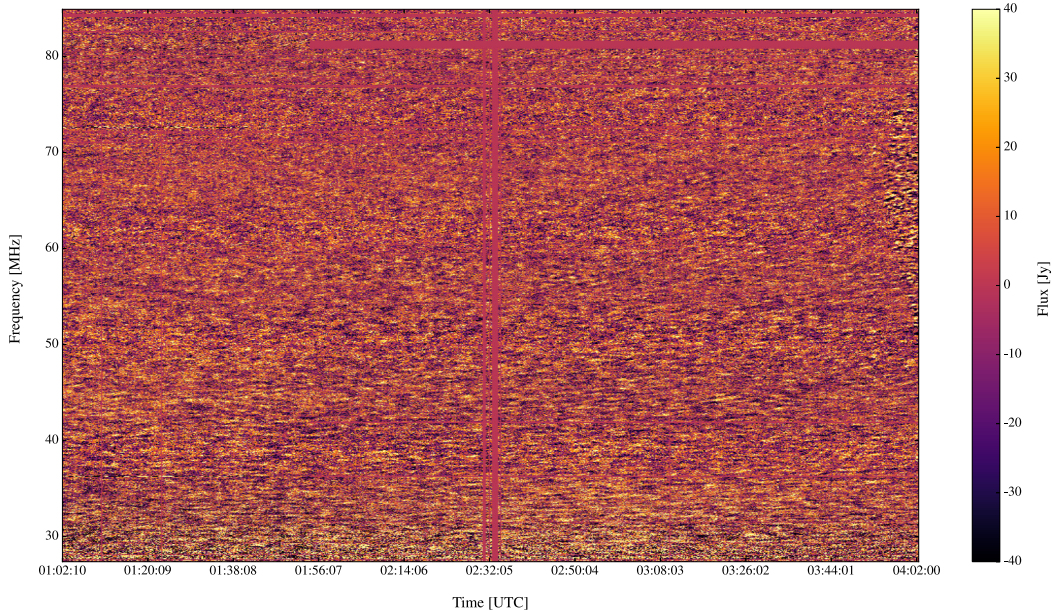
Figure 3.3: Dynamic spectrum measured at the position of GRB 170112A. The data span 1 hr prior to and 2 hr following the gamma-ray emission, at a time resolution of 13 s. The frequency channel width is 24 kHz, with 2398 channels spanning 27.4 through 84.9 MHz. Some frequency and time bins have been flagged due to RFI (e.g., integrations surrounding 02:32:05 UTC).

Following from

$$\Delta t_{\text{smearing}} = t_{\text{int}} = 4.15 \text{ ms DM}_{\text{step}} \left[ \frac{1}{\nu^2_{1,\text{GHz}}} - \frac{1}{\nu^2_{2,\text{GHz}}} \right], \tag{3.1}$$

this gives a DM step size of $\text{DM}_{\text{step}} = 2.5 \text{ pc cm}^{-3}$. We search DMs spanning 0 through 1000 pc cm$^{-3}$, despite our assumption of low DM, so as not to preclude the possibility of larger distances to the source or a significant contribution from the host galaxy or circumburst medium.

In order to search for the presence of a pulse in each of the trial DM dedispersed time series, we searched for statistically significant emission in every time series trial. Figure 3.4 shows the full-band dedispersed time series for every DM trial. We assume that our coarse 13 s integration time resolution is greater than the intrinsic pulse width (see Table 3.1), as well as any additional broadening due to scattering or remaining dispersion smearing due to the finite spacing of our DM trials, thus no additional smoothing is performed on the time series. Our nondetection of a radio pulse is consistent with the flat behavior of S/N we see as a function of DM channel.
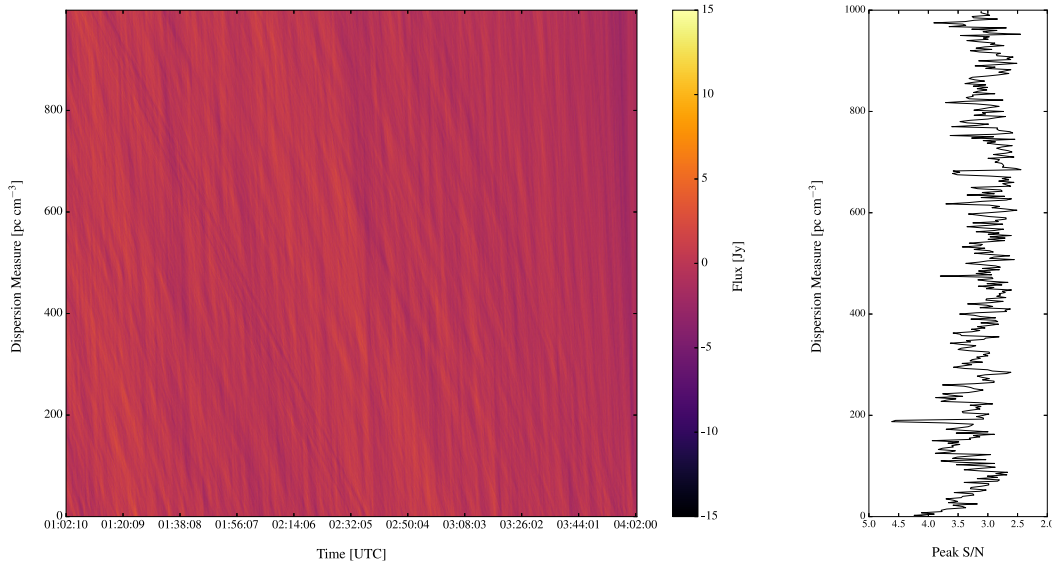
Figure 3.4: Dedispersed time series for every DM trial ranging from 0 to 1000 pc cm$^{-3}$, at 2.5 pc cm$^{-3}$ intervals. The right panel shows the peak S/N in each dedispersed time series as a function of DM trial. No time series contains a peak S/N greater than our significance threshold. The 4.5$\sigma$ spike just below a DM of 200 pc cm$^{-3}$ is 2 DM channels wide, and is due to spurious unflagged frequency channels.

In addition to the removable effect of dispersive delay caused by the intervening plasma along the path of pulse propagation, the signal is also subject to nonre-movable scatter broadening by turbulence and plasma density variations along the line of sight. The contribution to scattering from the Milky Way is negligible (a pulse broadening timescale of $\tau = 0.06\,\mu$s at 1 GHz will be $\tau < t_{\text{int}} = 13$ s at 10 MHz, assuming a Kolmogorov $\nu^{-4}$ power-law; Cordes and Lazio 2002). Additional contributions to scattering are possible from the host galaxy, however, for the same reasons mentioned above with regards to host galaxy contribution to DM, we assume a negligible contribution from the host, given the likely significant offset of the short GRB from its host galaxy. The remaining source of scattering to be considered is the IGM. Given both the lack of correlation between DM and $\tau$ for the extragalactic fast radio bursts (FRBs) and their systematically under-scattered, relative to the Galactic DM–$\tau$ relation for pulsars, nature (Cordes et al. 2016), we assume a minimal contribution to scattering from the IGM (which we have taken as the largest contribution to the DM), and assume $\tau < t_{\text{int}}$.

## 3.4 Discussion

**Constraints on Models for Prompt Radio Emission**

Using our deepest limit for the prompt radio emission associated with the short GRB 170112A (57 MHz bandwidth flux density limit at a center frequency of 56 MHz), we can place limits on the efficiency factors (listed in column 7 of Table 3.1) used in the models for prompt radio emission to predict the strength of emission, as well as place an upper limit on the fractional energy released in low-frequency radio emission relative to gamma-rays in the prompt emission stage of a short GRB. Figure 3.5 shows the predictions for the prompt radio emission models of Hansen and Lyutikov 2001, Pshirkov and Postnov 2010, and Usov and Katz 2000, associated with a 170112A-like burst, compared with our $3\sigma$ flux density limit $S(56\,\mathrm{MHz}) = 4.5\,\mathrm{Jy}$ (assuming a burst at a distance of $D = 1\,\mathrm{Gpc}$, and the model-predicted spectral indices $\alpha$ given in column 5 of Table 3.1). For the magnetized wind resulting from the magnetospheric interaction of the binary neutron stars prior to coalescence model of Hansen and Lyutikov 2001, we place an upper limit on the efficiency of wind power conversion to radio emission of $\epsilon_R \lesssim 7.2 \times 10^{-3}$ (using Equation (13) of Hansen and Lyutikov 2001 for the integrated flux density for a 13 s integration time that ends when the emission peaks as the neutron stars merge, and assuming a magnetic field strength of $B = 10^{12}\,\mathrm{G}$ for the non-magnetar component of the BNS system considered in the model). For the pulsar-like coherent radio emission powered by the rapid spin-down of the post-merger supramassive magnetar model of Pshirkov and Postnov 2010, we place an upper limit on the efficiency with which spin-down energy is converted into coherent radio emission of $\eta \lesssim 3.8 \times 10^{-8}$, corresponding to a total energy loss rate of roughly $\dot{E} = 6.1 \times 10^{51}\,\mathrm{ergs\,s^{-1}}$ and a power law for the spin-down power ($\eta \propto \dot{E}^{\gamma}$) of $\gamma = -0.1$ (using Equations (6) and (7) of Pshirkov and Postnov 2010 with a spectral index of $\alpha = -2$, and assuming the intrinsic pulse duration is 10 ms). For the magnetized outflow generating coherent radio emission simultaneous to the gamma-ray emission powering the GRB model of Usov and Katz 2000, we place an upper limit on the ratio of emitted radio to gamma-ray fluence of $\delta \lesssim 4.8 \times 10^{-4}$ (using Equation (14) of Usov and Katz 2000 with a spectral index of $\alpha = 1.6$, an intrinsic radio pulse duration that equals the gamma-ray $T_{90}$ of 0.06 s, and using the measured fluence of GRB 170112A in the $15 - 150\,\mathrm{keV}$ band of $0.13 \times 10^{-7}\,\mathrm{erg\,cm^{-2}}$).

Finally, we can place an upper limit on the fraction of energy released in the prompt radio emission (across our 27–85 MHz band) relative to gamma-rays. Assuming the same timescale of emission for both the prompt radio and gamma-ray emission

(0.06 s for GRB 170112A); assuming a spectral index of $\alpha = -2$; using the gamma-ray fluence of $0.13 \times 10^{-7}\,\mathrm{erg\,cm^{-2}}$; and integrating over 27–85 MHz, the upper limit on the luminosity ratio is $L_{\mathrm{radio}}/L_\gamma \lesssim 3.5 \times 10^{-6}$.

**Gravitational Wave Follow-up**

Verifying the existence of a prompt low-frequency radio counterpart to NS–NS(BH) merger events has taken on new significance with the detection of the binary neutron star merger GW170817 in GWs and the detection of its counterparts across the electromagnetic spectrum (Abbott et al. 2017d, 2017c; Coulter et al. 2017; Evans et al. 2017; Hallinan et al. 2017; Kasliwal et al. 2017; Troja et al. 2017). Strategies for follow-up of GW events with EM facilities are now being regularly deployed as GW alerts are released to partner observers and facilities, spanning the entire EM spectrum from radio to gamma-rays, and including neutrino facilities (Singer et al. 2014). Though the current models predicting prompt radio counterparts to both short and long GRBs remain very speculative, the utility of such a population for constraining important jet physics (Macquart 2007), probing the IGM (Inoue 2004), and serving as an identifiable counterpart to GW events makes the search for such events extremely valuable (e.g., Kaplan et al. 2016). The particular value of a low-frequency prompt counterpart to NS–NS(BH) mergers over counterparts at higher energies is the (1) inherently wide field of view of low-frequency facilities for rapidly and efficiently covering the entire (often $> 10^3$ sq. deg) localization regions of GW events detected by aLIGO; (2) the time delay of as much as minutes, caused by the dispersion of a radio pulse by the media along the path of propagation, that allows for the pointing of telescopes; and (3) the relative dearth of variable and unrelated transient sources that could serve as false positives (unlike at optical frequencies; see, e.g. Bhalerao et al. 2017, , and references therein).

The OVRO-LWA, in particular, is a uniquely powerful follow-up facility for GW transients. The nearly full-hemisphere (~20,000 sq. deg.) field of view can instantaneously cover the entire 90% confidence localization region released by the two aLIGO and Virgo detectors roughly 50% of the time. The dispersive delay of a prompt radio counterpart enables timely follow-up by a number of low-frequency facilities. However, the benefits of dispersive delay become less relevant as latency between GW detection and notification of detection to partner EM facilities increases. During the first aLIGO observing run (O1), the median latency between detection and notification was approximately 60 s; however the largest latencies extended beyond 180 s (Abbott et al. 2016). For GW170104, detected during the
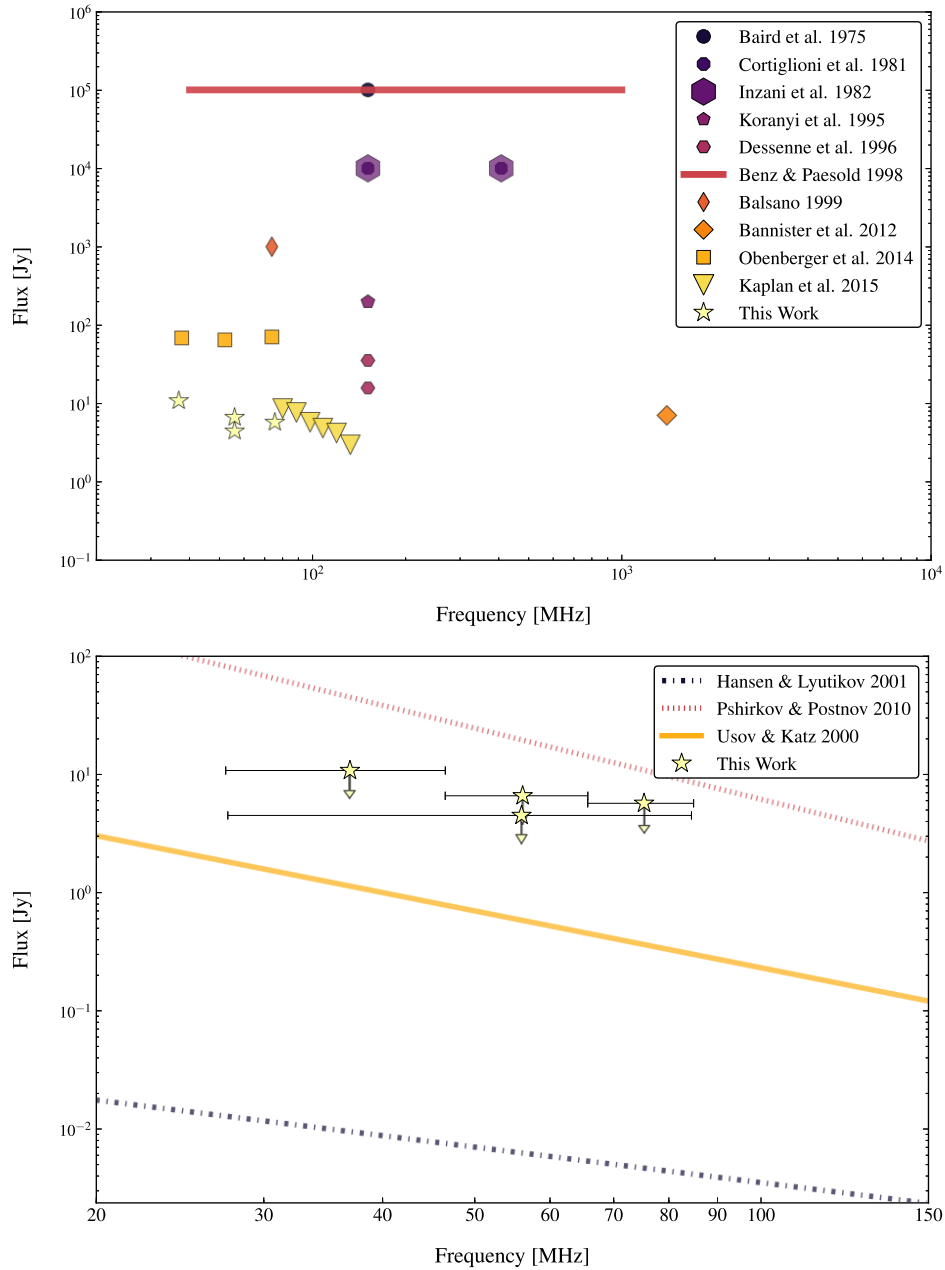
Figure 3.5: Top: flux density limits from all previous searches targeting prompt coherent radio emission associated with GRBs. See also Table 3.2. Surveys reporting limits at multiple frequencies show the corresponding number of limits in the plot. Bottom: the $3\sigma$ flux density limits from the full 57 MHz band and the three 19 MHz subbands for GRB 170112A, and the model-predicted flux densities from Table 3.1, scaled to the 13 *texts* integration time of these observations.

O2 run, the latency was approximately 5 hr (Abbott et al. 2017b; LIGO Scientific Collaboration and Virgo Collaboration 2017). However, large latency is not a limit-

ing factor in the follow-up strategy of the OVRO-LWA, where the continuous mode of operation allows for the recovery of data from within the ring buffer, enabling contemporaneous coverage of a GW event and making possible the detection of any precursor radio emission, provided only that the GW alert latency is less than the duration of the OVRO-LWA buffer (which is typically > 24 hr).

The OVRO-LWA was observing continuously during the aLIGO O2 observing run, but was unable to search for prompt coherent emission associated with GW170817 due to the unlucky placement of the binary neutron star merger below the horizon of the OVRO-LWA at the time of the event. GW170817 was located at a distance of only 40 Mpc (Abbott et al. 2017c), and coincident observations of a burst at this distance would have placed the model flux density predictions in Figure 3.5 well above the current OVRO-LWA flux density limits and allowing significant constraints on the validity of the models. The detection horizon for the Advanced LIGO and Virgo detectors during the O3 run to NS–NS(BH) mergers will be 220(400) Mpc (averaged over direction and inclination angle of system, Abadie et al. 2010), still well within the 1 Gpc distance upper limit to GRB 170112A, and still closer than any short GRB of known redshift detected through prompt gamma- or X-ray emission. Any burst occurring within that horizon and detected by *Swift* or *Fermi* with unknown redshift would have had to have been extremely under-luminous compared to any burst of known redshift; indeed, this was the case with GRB 170817A, which was identified in association with GW170817 but was extremely under-luminous and below the standard detection threshold of *Fermi* (Abbott et al. 2017a). The implication of a population of nearby merging BNS systems that do not follow the same brightness distribution or emission characteristics in their prompt high energy emission compared to their higher redshift counterparts underscores the value of an EM signature and emission mechanism that is detectable at low frequencies, for characterizing and providing an additional EM counterpart for a GW NS–NS(BH) coalescence event. The OVRO-LWA will continue the program for monitoring and triggering on GW events during the O3 run, which is expected to detect between ~6 and 120 binary neutron star merger events per year at design sensitivity.

## 3.5 Conclusion

We have placed the most constraining upper limits to-date on prompt radio emission associated with GRBs using the OVRO-LWA to observe the field of short GRB 170112A. We searched for a pulse at the location of GRB 170112A starting 1 hr prior to the detection of gamma-ray emission by *Swift* through the subsequent 2 hr,

to accommodate even extremely conservative estimates for pre-merger coherent radio emission models as well as the expected dispersive delayed onset of radio emission. We see no evidence for emission in the full-band ($\Delta \nu = 57$ MHz) time series or following a search through the dedispersed time series for DMs ranging from 0 to $1000 \, \mathrm{pc \, cm^{-3}}$. We place a $1\sigma$ flux density limit of 4.5 Jy at 56 MHz for 13 s timescales, which, assuming a nominal distance of $D = 1$ Gpc to 170112A, allows us to place upper limits on the efficiency factors used by the models in their predictions for the luminosity of coherent radio emission associated with GRBs. We place an upper limit on the fraction of energy released in the prompt radio emission (across our $27 - 85$ MHz band) relative to gamma-rays of $L_{\mathrm{radio}}/L_\gamma \lesssim 3.5 \times 10^{-6}$.

The contemporaneous follow-up of and sensitivity limits placed for the short GRB 170112A demonstrate the capabilities of the OVRO-LWA for targeted follow-up, particularly with regards to GW events. The OVRO-LWA is the only facility with the ability to instantaneously cover up to the full aLIGO/Virgo localization region with zero latency, and with typical sensitivities of $\sim 800$ mJy at low frequencies. In addition, a GRB follow-up campaign with the OVRO-LWA is ongoing and will provide limits on prompt radio emission for a sample that includes both long and short GRBs, in order to encompass a wide range of potential progenitor parameters. We emphasize the caveat that the use of limits associated with GRB 170112A to constrain model parameters relies on the assumptions that any coherent radio emission will be beamed along our line of sight and that the timescale for scatter broadening of the coherent pulse is negligible compared to our integration time. These assumptions highlight the value of following up a statistical sample of GRBs, in order to place meaningful constraints on the progenitor models that do not fully rely on the aforementioned assumptions of favorable viewing.

Fund Program.

*Software:* TTCal (Eastwood 2016), WSClean (Offringa et al. 2014b).

## References

Abadie, J., et al. 2010. "TOPICAL REVIEW: Predictions for the rates of compact binary coalescences observable by ground-based gravitational-wave detectors". *Classical and Quantum Gravity* 27, no. 17, 173001 (): 173001. doi:`10.1088/0264-9381/27/17/173001`. arXiv: `1003.2480 [astro-ph.HE]`.

Abbott, B. P., et al. 2017a. "Gravitational Waves and Gamma-Rays from a Binary Neutron Star Merger: GW170817 and GRB 170817A". *ApJL* 848, L13 (): L13. doi:`10.3847/2041-8213/aa920c`. arXiv: `1710.05834 [astro-ph.HE]`.

— . 2017b. "GW170104: Observation of a 50-Solar-Mass Binary Black Hole Coalescence at Redshift 0.2". *Physical Review Letters* 118, no. 22, 221101 (): 221101. doi:`10.1103/PhysRevLett.118.221101`. arXiv: `1706.01812 [gr-qc]`.

— . 2017c. "GW170817: Observation of Gravitational Waves from a Binary Neutron Star Inspiral". *Physical Review Letters* 119, no. 16, 161101 (): 161101. doi:`10.1103/PhysRevLett.119.161101`. arXiv: `1710.05832 [gr-qc]`.

— . 2017d. "Multi-messenger Observations of a Binary Neutron Star Merger". *ApJL* 848, L12 (): L12. doi:`10.3847/2041-8213/aa91c9`. arXiv: `1710.05833 [astro-ph.HE]`.

Abbott, B. P., et al. 2016. "Upper Limits on the Rates of Binary Neutron Star and Neutron Star-Black Hole Mergers from Advanced LIGO's First Observing Run". *ApJL* 832, L21 (): L21. doi:`10.3847/2041-8205/832/2/L21`. arXiv: `1607.07456 [astro-ph.HE]`.

Baars, J. W. M., et al. 1977. "The absolute spectrum of CAS A - an accurate flux density scale and a set of secondary calibrators". *A&A* 61 (): 99–106.

Baird, G. A., et al. 1975. "A search for VHF radio pulses in coincidence with celestial gamma-ray bursts". *ApJL* 196 (): L11–L13. doi:`10.1086/181732`.

Balsano, R. J. 1999. "A search for radio emission coincident with gamma-ray bursts". PhD thesis, PRINCETON UNIVERSITY.

Bannister, K. W., et al. 2012. "Limits on Prompt, Dispersed Radio Pulses from Gamma-Ray Bursts". *ApJ* 757, 38 (): 38. doi:`10.1088/0004-637X/757/1/38`. arXiv: `1207.6399 [astro-ph.HE]`.

Belczynski, K., et al. 2006. "A Study of Compact Object Mergers as Short Gamma-Ray Burst Progenitors". *ApJ* 648 (): 1110–1116. doi:`10.1086/505169`. eprint: `astro-ph/0601458`.

Benz, A. O., and G. Paesold. 1998. "A search for prompt radio emission of gamma-ray bursts". *A&A* 329 (): 61–67.

Berger, E. 2009. "The Host Galaxies of Short-Duration Gamma-Ray Bursts: Luminosities, Metallicities, and Star-Formation Rates". *ApJ* 690 (): 231–237. doi:`10.1088/0004-637X/690/1/231`. arXiv: `0805.0306`.

Berger, E., et al. 2005. "The afterglow and elliptical host galaxy of the short $\gamma$-ray burst GRB 050724". *Nature* 438 (): 988–990. doi:`10.1038/nature04238`. eprint: `astro-ph/0508115`.

Bhalerao, V., et al. 2017. "A tale of two transients: GW170104 and GRB170105A". *ArXiv e-prints* (). arXiv: `1706.00024 [astro-ph.HE]`.

Bloom, J. S., S. Sigurdsson, and O. R. Pols. 1999. "The spatial distribution of coalescing neutron star binaries: implications for gamma-ray bursts". *MNRAS* 305 (): 763–769. doi:`10.1046/j.1365-8711.1999.02437.x`. eprint: `astro-ph/9805222`.

Bloom, J. S., et al. 2006. "Closing in on a Short-Hard Burst Progenitor: Constraints from Early-Time Optical Imaging and Spectroscopy of a Possible Host Galaxy of GRB 050509b". *ApJ* 638 (): 354–368. doi:`10.1086/498107`. eprint: `astro-ph/0505480`.

Bostancı, Z. F., Y. Kaneko, and E. Göğüş. 2013. "Gamma-ray bursts with extended emission observed with BATSE". *MNRAS* 428 (): 1623–1630. doi:`10.1093/mnras/sts157`. arXiv: `1210.2399 [astro-ph.HE]`.

Briggs, D. S. 1995. "High Fidelity Deconvolution of Moderately Resolved Sources". PhD thesis, New Mexico Institute of Mining and Technology.

Cordes, J. M., and T. J. W. Lazio. 2002. "NE2001.I. A New Model for the Galactic Distribution of Free Electrons and its Fluctuations". *ArXiv Astrophysics e-prints* (). eprint: `astro-ph/0207156`.

Cordes, J. M., and M. A. McLaughlin. 2003. "Searches for Fast Radio Transients". *ApJ* 596 (): 1142–1154. doi:`10.1086/378231`. eprint: `astro-ph/0304364`.

Cordes, J. M., et al. 2016. "Radio Wave Propagation and the Provenance of Fast Radio Bursts". *ArXiv e-prints* (). arXiv: `1605.05890 [astro-ph.HE]`.

Cortiglioni, S., et al. 1981. "A systematic search for radio pulses associated with gamma-ray bursts". *Ap&SS* 75 (): 153–161. doi:`10.1007/BF00651392`.

Costa, E., et al. 1997. "Discovery of an X-ray afterglow associated with the $\gamma$-ray burst of 28 February 1997". *Nature* 387 (): 783–785. doi:`10.1038/42885`. eprint: `astro-ph/9706065`.

Coulter, D. A., et al. 2017. "Swope Supernova Survey 2017a (SSS17a), the optical counterpart to a gravitational wave source". *Science* 358 (): 1556–1558. doi:`10.1126/science.aap9811`. arXiv: `1710.05452 [astro-ph.HE]`.

D'Ai, A., et al. 2017. "GRB 170112A: Swift-XRT observations". *GRB Coordinates Network* 20440.

D'Avanzo, P., et al. 2017. "GRB 170112A: REM optical/NIR observations." *GRB Coordinates Network* 20438.

Dessenne, C. A.-C., et al. 1996. "Searches for prompt radio emission at 151 MHz from the gamma-ray bursts GRB 950430 and GRB 950706." *MNRAS* 281 (): 977–984. doi:`10.1093/mnras/281.3.977`.

Duez, M. D., et al. 2006. "Evolution of magnetized, differentially rotating neutron stars: Simulations in full general relativity". *PhRvD* 73, no. 10, 104015 (): 104015. doi:`10.1103/PhysRevD.73.104015`. eprint: `astro-ph/0605331`.

Eastwood, M. W., et al. 2017. "The Radio Sky at Meter Wavelengths: m-Mode Analysis Imaging with the Owens Valley Long Wavelength Array". *ArXiv e-prints* (). arXiv: `1711.00466 [astro-ph.IM]`.

Eastwood, Michael W. 2016. *TTCal*. Version 0.3.0. doi:`10.5281/zenodo.1049160`. `https://doi.org/10.5281/zenodo.1049160`.

Ellingson, S. W., et al. 2013. "Design and Commissioning of the LWA1 Radio Telescope". *ArXiv e-prints* (). arXiv: `1307.0697 [astro-ph.IM]`.

Evans, P. A., et al. 2017. "Swift and NuSTAR observations of GW170817: Detection of a blue kilonova". *Science* 358 (): 1565–1570. doi:`10.1126/science.aap9580`. arXiv: `1710.05437 [astro-ph.HE]`.

Fong, W., and E. Berger. 2013. "The Locations of Short Gamma-Ray Bursts as Evidence for Compact Object Binary Progenitors". *ApJ* 776, 18 (): 18. doi:`10.1088/0004-637X/776/1/18`. arXiv: `1307.0819 [astro-ph.HE]`.

Frail, D. A., et al. 1997. "The radio afterglow from the $\gamma$-ray burst of 8 May 1997". *Nature* 389 (): 261–263. doi:`10.1038/38451`.

Fruchter, A. S., et al. 2006. "Long $\gamma$-ray bursts and core-collapse supernovae have different environments". *Nature* 441 (): 463–468. doi:`10.1038/nature04787`. eprint: `astro-ph/0603537`.

Gehrels, N., et al. 2004. "The Swift Gamma-Ray Burst Mission". *ApJ* 611 (): 1005–1020. doi:`10.1086/422091`.

Goldreich, P., and A. Reisenegger. 1992. "Magnetic field decay in isolated neutron stars". *ApJ* 395 (): 250–258. doi:`10.1086/171646`.

Granot, J., and A. J. van der Horst. 2014. "Gamma-Ray Burst Jets and their Radio Observations". *PASA* 31, e008 (): e008. doi:`10.1017/pasa.2013.44`.

Hallinan, G., et al. 2017. "A radio counterpart to a neutron star merger". *Science* 358 (): 1579–1583. doi:`10.1126/science.aap9855`. arXiv: `1710.05435 [astro-ph.HE]`.

Hansen, B. M. S., and M. Lyutikov. 2001. "Radio and X-ray signatures of merging neutron stars". *MNRAS* 322 (): 695–701. doi:`10.1046/j.1365-8711.2001.04103.x`. eprint: `astro-ph/0003218`.

Inoue, S. 2004. "Probing the cosmic reionization history and local environment of gamma-ray bursts through radio dispersion". *MNRAS* 348 (): 999–1008. doi:`10.1111/j.1365-2966.2004.07359.x`. eprint: `astro-ph/0309364`.

Inzani, P., et al. 1982. "Search for associations of radio pulses and gamma ray bursts". In *Gamma Ray Transients and Related Astrophysical Phenomena*, ed. by R. E. Lingenfelter, H. S. Hudson, and D. M. Worrall, 77:79–84. American Institute of Physics Conference Series. doi:`10.1063/1.33213`.

Kaplan, D. L., et al. 2015. "A Deep Search for Prompt Radio Emission from the Short GRB 150424A with the Murchison Widefield Array". *ApJL* 814, L25 (): L25. doi:`10.1088/2041-8205/814/2/L25`. arXiv: `1511.03656 [astro-ph.HE]`.

Kaplan, D. L., et al. 2016. "Strategies for Finding Prompt Radio Counterparts to Gravitational Wave Transients with the Murchison Widefield Array". *PASA* 33, e050 (): e050. doi:`10.1017/pasa.2016.43`. arXiv: `1609.00634 [astro-ph.IM]`.

Kasliwal, M. M., et al. 2017. "Illuminating gravitational waves: A concordant picture of photons from a neutron star merger". *Science* 358 (): 1559–1565. doi:`10.1126/science.aap9455`. arXiv: `1710.05436 [astro-ph.HE]`.

Klebesadel, R. W., I. B. Strong, and R. A. Olson. 1973. "Observations of Gamma-Ray Bursts of Cosmic Origin". *ApJL* 182 (): L85. doi:`10.1086/181225`.

Kocz, J., et al. 2015. "Digital Signal Processing Using Stream High Performance Computing: A 512-Input Broadband Correlator for Radio Astronomy". *Journal of Astronomical Instrumentation* 4, 1550003 (): 1550003. doi:`10.1142/S2251171715500038`. arXiv: `1411.3751 [astro-ph.IM]`.

Koranyi, D. M., et al. 1995. "Search for a radio counterpart to the gamma-ray burst GRB 940301". *MNRAS* 276 (): L13–L17. doi:`10.1093/mnras/276.1.L13`.

Kouveliotou, C., et al. 1993. "Identification of two classes of gamma-ray bursts". *ApJL* 413 (): L101–L104. doi:`10.1086/186969`.

Krimm, H. A., et al. 2013. "The Swift/BAT Hard X-Ray Transient Monitor". *ApJs* 209, 14 (): 14. doi:`10.1088/0067-0049/209/1/14`. arXiv: `1309.0755 [astro-ph.HE]`.

Lane, W. M., et al. 2014. "The Very Large Array Low-frequency Sky Survey Redux (VLSSr)". *MNRAS* 440 (): 327–338. doi:`10.1093/mnras/stu256`. arXiv: `1404.0694 [astro-ph.IM]`.

Li, L.-X., and B. Paczyński. 1998. "Transient Events from Neutron Star Mergers". *ApJL* 507 (): L59–L62. doi:`10.1086/311680`. eprint: `astro-ph/9807272`.

Lien, A. Y., et al. 2017. "GRB 170112A: Swift-BAT refined analysis". *GRB Coordinates Network* 20443.

Lien, A., et al. 2016. "The Third Swift Burst Alert Telescope Gamma-Ray Burst Catalog". *ApJ* 829, 7 (): 7. doi:`10.3847/0004-637X/829/1/7`. arXiv: `1606.01956 [astro-ph.HE]`.

LIGO Scientific Collaboration and Virgo Collaboration. 2017. "LIGO/Virgo G268556: Identification of a GW CBC Candidate". *Gamma-ray Coordinates Network/Transient Astronomy Network Circular* 20364.

Lyutikov, M. 2009. "Gamma Ray Bursts: back to the blackboard". *ArXiv e-prints* (). arXiv: 0911.0349 [astro-ph.HE].

– . 2013. "The Electromagnetic Model of Short GRBs, the Nature of Prompt Tails, Supernova-less Long GRBs, and Highly Efficient Episodic Accretion". *ApJ* 768, 63 (): 63. doi:10.1088/0004-637X/768/1/63. arXiv: 1202.6026 [astro-ph.HE].

Macquart, J.-P. 2007. "On the Detectability of Prompt Coherent Gamma-Ray Burst Radio Emission". *ApJL* 658 (): L1–L4. doi:10.1086/513424. eprint: astro-ph/0702098.

Mazaeva, E., et al. 2017. "GRB 170112A : AbAO optical observations." *GRB Coordinates Network* 20472.

McMullin, J. P., et al. 2007. "CASA Architecture and Applications". In *Astronomical Data Analysis Software and Systems XVI*, ed. by R. A. Shaw, F. Hill, and D. J. Bell, 376:127. Astronomical Society of the Pacific Conference Series.

Metzger, B. D., E. Quataert, and T. A. Thompson. 2008. "Short-duration gamma-ray bursts with extended emission from protomagnetar spin-down". *MNRAS* 385 (): 1455–1460. doi:10.1111/j.1365-2966.2008.12923.x. arXiv: 0712.1233.

Metzger, B. D., T. A. Thompson, and E. Quataert. 2018. "A Magnetar Origin for the Kilonova Ejecta in GW170817". *ApJ* 856, 101 (): 101. doi:10.3847/1538-4357/aab095. arXiv: 1801.04286 [astro-ph.HE].

Mingo, B., et al. 2017. "GRB 170112A: Swift detection of a short burst." *GRB Coordinates Network* 20436.

Moortgat, J., and J. Kuijpers. 2005. "Indirect Visibility of Gravitational Waves in Magnetohydrodynamic Plasmas". In *22nd Texas Symposium on Relativistic Astrophysics*, ed. by P. Chen et al., 326–331. eprint: gr-qc/0503074.

Narayan, R., B. Paczynski, and T. Piran. 1992. "Gamma-ray bursts as the death throes of massive binary stars". *ApJL* 395 (): L83–L86. doi:10.1086/186493. eprint: astro-ph/9204001.

Obenberger, K. S., et al. 2014. "Limits on Gamma-Ray Burst Prompt Radio Emission Using the LWA1". *ApJ* 785, 27 (): 27. doi:10.1088/0004-637X/785/1/27. arXiv: 1403.3674 [astro-ph.HE].

Obenberger, K. S., et al. 2015. "Monitoring the Sky with the Prototype All-Sky Imager on the LWA1". *Journal of Astronomical Instrumentation* 4, 1550004-1104 (): 1550004–1104. doi:10.1142/S225117171550004X. arXiv: 1503.05150 [astro-ph.IM].

Offringa, A. R., et al. 2014a. "WSCLEAN: an implementation of a fast, generic wide-field imager for radio astronomy". *MNRAS* 444 (): 606–619. doi:`10.1093/mnras/stu1368`. arXiv: `1407.1943 [astro-ph.IM]`.

– . 2014b. *WSClean: Widefield interferometric imager*. Astrophysics Source Code Library. ascl: `1408.023`.

Palmer, D. M. 1993. "Radio Dispersion as a Diagnostic of Gamma-Ray Burst Distances". *ApJL* 417 (): L25. doi:`10.1086/187085`.

Price, D. C., et al. 2018. "Design and characterization of the Large-aperture Experiment to Detect the Dark Age (LEDA) radiometer systems". *MNRAS* (). doi:`10.1093/mnras/sty1244`. arXiv: `1709.09313 [astro-ph.IM]`.

Pshirkov, M. S., and K. A. Postnov. 2010. "Radio precursors to neutron star binary mergings". *Ap&SS* 330 (): 13–18. doi:`10.1007/s10509-010-0395-x`. arXiv: `1004.5115 [astro-ph.HE]`.

Sagiv, A., and E. Waxman. 2002. "Collective Processes in Relativistic Plasma and Their Implications for Gamma-Ray Burst Afterglows". *ApJ* 574 (): 861–872. doi:`10.1086/340948`. eprint: `astro-ph/0202337`.

Savaglio, S., K. Glazebrook, and D. Le Borgne. 2009. "The Galaxy Population Hosting Gamma-Ray Bursts". *ApJ* 691 (): 182–211. doi:`10.1088/0004-637X/691/1/182`. arXiv: `0803.2718`.

Siegel, M. H., and B. Mingo. 2017. "GRB 170112A: Swift/UVOT Upper Limits". *GRB Coordinates Network* 20451.

Singer, L. P., et al. 2014. "The First Two Years of Electromagnetic Follow-up with Advanced LIGO and Virgo". *ApJ* 795, 105 (): 105. doi:`10.1088/0004-637X/795/2/105`. arXiv: `1404.5623 [astro-ph.HE]`.

Soderberg, A. M., et al. 2006. "The Afterglow, Energetics, and Host Galaxy of the Short-Hard Gamma-Ray Burst 051221a". *ApJ* 650 (): 261–271. doi:`10.1086/506429`. eprint: `astro-ph/0601455`.

Tanvir, N. R., et al. 2013. "A 'kilonova' associated with the short-duration $\gamma$-ray burst GRB 130603B". *Nature* 500 (): 547–549. doi:`10.1038/nature12505`. arXiv: `1306.4971 [astro-ph.HE]`.

Tingay, S. J., et al. 2013. "The Murchison Widefield Array: The Square Kilometre Array Precursor at Low Radio Frequencies". *PASA* 30, e007 (): e007. doi:`10.1017/pasa.2012.007`. arXiv: `1206.6945 [astro-ph.IM]`.

Troja, E., et al. 2017. "The X-ray counterpart to the gravitational-wave event GW170817". *Nature* 551 (): 71–74. doi:`10.1038/nature24290`. arXiv: `1710.05433 [astro-ph.HE]`.

Usov, V. V., and J. I. Katz. 2000. "Low frequency radio pulses from gamma-ray bursts?" *A&A* 364 (): 655–659. eprint: `astro-ph/0002278`.

van Paradijs, J., et al. 1997. "Transient optical emission from the error box of the $\gamma$-ray burst of 28 February 1997". *Nature* 386 (): 686–689. doi:`10.1038/386686a0`.

Woosley, S. E., and J. S. Bloom. 2006. "The Supernova Gamma-Ray Burst Connection". *ARA&A* 44 (): 507–556. doi:`10.1146/annurev.astro.43.072103.150558`. eprint: `astro-ph/0609142`.

Yang, B., et al. 2015. "A possible macronova in the late afterglow of the long-short burst GRB 060614". *Nature Communications* 6, 7323 (): 7323. doi:`10.1038/ncomms8323`. arXiv: `1503.07761 [astro-ph.HE]`.

Zheng, Z., et al. 2014. "Probing the Intergalactic Medium with Fast Radio Bursts". *ApJ* 797, 71 (): 71. doi:`10.1088/0004-637X/797/1/71`. arXiv: `1409.3244 [astro-ph.HE]`.

*Chapter 4*

# NEW LIMITS ON THE LOW-FREQUENCY RADIO TRANSIENT SKY USING 31 HOURS OF ALL-SKY DATA WITH THE OVRO-LWA

Marin M. Anderson[1], Gregg Hallinan[1], Michael W. Eastwood[1], Ryan M. Monroe[1], Thomas A. Callister[2], Jayce Dowell[3], Brian Hicks[4], Yuping Huang[1], Namir E. Kassim[4], Jonathon Kocz[1], T. Joseph W. Lazio[5], Danny C. Price[6,7], Frank K. Schinzel[3,8], Greg B. Taylor[3]

## Abstract

We present the results of the first transient survey from the Owens Valley Radio Observatory Long Wavelength Array (OVRO-LWA) using 31 hours of data, in which we place the most constraining limits on the instantaneous transient surface density at timescales of 13 s to a few minutes and at frequencies below 100 MHz. The OVRO-LWA is a dipole array that images the entire viewable hemisphere with 58 MHz of bandwidth from 27–84 MHz at 13 s cadence. No transients are detected above a $6.5\sigma$ flux density limit of 10.5 Jy, implying an upper limit to the transient surface density of $2.5 \times 10^{-8} \deg^{-2}$ at the shortest timescales probed, which is orders of magnitude deeper than has been achieved at sub-100 MHz frequencies and

[1]California Institute of Technology, 1200 E California Boulevard MC 249-17, Pasadena, CA 91125, USA

[2]LIGO Laboratory, California Institute of Technology, Pasadena, CA 91125, USA

[3]Department of Physics and Astronomy, University of New Mexico, Albuquerque, NM 87131, USA

[4]Naval Research Laboratory, Washington, DC 20375, USA

[5]Jet Propulsion Laboratory, California Institute of Technology, 4800 Oak Grove Drive, Pasadena, CA 91109, USA

[6]Department of Astronomy, University of California Berkeley, Berkeley CA 94720, USA

[7]Centre for Astrophysics & Supercomputing, Swinburne University of Technology, P.O. Box 218, Hawthorn, VIC 3122, Australia

[8]National Radio Astronomy Observatory, P.O. Box O, Socorro, NM 87801, USA

comparable flux densities to date. The non-detection of transients in the OVRO-LWA survey, particularly at minutes-long timescales, allows us to place further constraints on the rate of the potential population of transients uncovered by Stewart et al. 2016. From their transient rate, we expect a detection of $8.4^{+31.8}_{-8.0}$ events, and the probability of our null detection is $1.9^{+644}_{-1.9} \times 10^{-3}$, ruling out a transient rate $> 1.4 \times 10^{-4}\,\mathrm{d}^{-1}\,\mathrm{deg}^{-2}$ with 95% confidence at a flux density limit of 18.1 Jy, under the assumption of a flat spectrum and wide-bandwidth. We discuss the implications of our non-detection for this population and further constraints that can be made on the source spectral index, intrinsic emission bandwidth, and resulting luminosity distribution.

*Key words:* instrumentation: interferometers, radiation mechanisms: non-thermal, radio continuum: general

## 4.1 Introduction

Exploration of the time domain plays a critical role in the field of astronomy, as a window into the dynamic, often cataclysmic or explosive, processes that mark a highly non-static universe. Time domain radio astronomy, in particular, serves as a unique probe of astrophysical processes which can be otherwise inaccessible at other wavelengths, either due to extrinsic factors, such as dust obscuration, or intrinsic factors, such as emission that is beamed or unique to radio frequencies.

Recent advances in the survey speed and sensitivity of radio interferometers has facilitated the expansion of radio transient science from the realm of follow-up of transient detections at shorter wavelengths, such as extragalactic, incoherent synchrotron events such as gamma-ray bursts, supernovae, and tidal disruption events (e.g., Chandra and Frail 2012; Soderberg et al. 2010; Zauderer et al. 2011), toward wide-field, non-targeted synoptic imaging surveys exploring a wide range of phase space in the dynamic radio sky (e.g., Mooley et al. 2016). Incoherent synchrotron-powered transients, due to both the lower luminosities from self-absorption and typically slow timescale of evolution at low frequencies, are better recovered at GHz frequencies (see Metzger, Williams, and Berger 2015). However, surveys at low ($< 350\,\mathrm{MHz}$) frequencies benefit from the many sources of coherent emission that fill radio transient phase space (see Cordes, Lazio, and McLaughlin 2004; Macquart et al. 2015). Coherent emission is extremely bright, and can be variable on timescales as short as nanoseconds (Hankins et al. 2003). In addition, many of the source populations that have been identified to-date either emit exclu-

sively at low frequencies, such as cyclotron maser-powered auroral radio emission from the magnetized planets in the solar system (Zarka 1998), or exhibit emission with steep negative spectral indices (Lorimer et al. 1995; Kramer et al. 1999) that motivate surveys conducted at lower frequencies. Surveys at low frequencies also benefit from the inherently wide fields-of-view and fast survey speeds of dipole arrays. This is increasingly the case with the rise of low frequency telescopes such as the Long Wavelength Array (LWA; Ellingson et al. 2009), the Murchison Widefield Array (MWA; Tingay et al. 2013), the Low-Frequency Array (LOFAR; van Haarlem et al. 2013), and now the Owens Valley Radio Observatory Long Wavelength Array (OVRO-LWA). This also includes the upgrade of low-frequency receivers on existing dish arrays such as the Very Large Array (VLA) Low Band Ionospheric and Transient Experiment (VLITE; Polisensky et al. 2016) and the Giant Metrewave Radio Telescope (GMRT; Intema et al. 2017).

At extragalactic distances, potential transient sources at low frequencies include bright, coherent pulses predicted to accompany gamma-ray bursts (GRBs) and neutron star mergers (see Anderson et al. 2018, and references therein), as well as fast radio bursts (FRBs), highly dispersed millisecond pulses that have been detected at frequencies as low as 400 MHz (Amiri et al. 2019). The degree of scatter broadening from the current sample of FRBs indicates the potential for detecting this population even at very low frequencies (Ravi 2019). At galactic distances, potential transient sources at low frequencies include stellar flares and coherent radio bursts (Spangler and Moffett 1976; Bastian 1990; Lynch et al. 2017; Villadsen and Hallinan 2018), for which our Sun serves as a prototype (Bastian, Benz, and Gary 1998), as well as radio aurorae on brown dwarfs (Hallinan et al. 2015; Kao et al. 2016), a phenomenon that likely also extends down in mass to exoplanets (Lazio et al. 2004; Kao et al. 2018), and for which the magnetized planets in our solar system serve as a prototype (Zarka 1998). Within Earth's atmosphere, potential transient sources include radio emission from meteor afterglows recently discovered at low frequencies (Obenberger et al. 2014), as well as radio emission from cosmic ray showers and neutrinos (Falcke and Gorham 2003).

Transient surveys carried out by the aforementioned low frequency facilities continue to place more sensitive and constraining limits on the radio transient sky below 350 MHz, across a wide range of timescales. Table 4.1 summarizes the parameters and results of previous blind, non-targeted transient surveys at low frequencies (< 350 MHz). From these surveys there have been seven distinct transient discoveries,

all of which remain mysterious in origin, with no identified progenitors, and no corresponding larger population yet uncovered.

- Three transient sources were discovered during separate monitoring campaigns of the galactic center, thus the label Galactic Center Radio Transient (GCRT). The first of these, GCRT J1746-2757, found in 330 MHz VLA observations of the galactic center, evolved on the timescale of a few months and reached $\sim$ 200 mJy flux densities (Hyman et al. 2002). GCRT J1745-3009, also found at 330 MHz with the VLA and subsequently re-detected with the GMRT, was a coherent, steep-spectrum source, exhibiting $\sim$ 1 Jy bursts of approximately 10 minutes in duration, that were detected repeatedly with a 77 minute period (Hyman et al. 2005; Hyman et al. 2007). And lastly, GCRT J1742-3001 was discovered at 235 MHz with the GMRT, and reached $\sim$ 100 mJy flux densities and evolved on a ~few months-long timescale (Hyman et al. 2009).

- Jaeger et al. 2012 detected the source J103916.2+585124 in 325 MHz VLA archival observations that were selected based on their coverage of the Spitzer-Space-Telescope Wide-area Infrared Extragalactic Survey (SWIRE) Deep Field. The source reached 2 mJy flux densities with duration of $\sim$ 12 hours, and has no identified progenitor, despite extensive multi-wavelength coverage of the field in which it was detected.

- TGSSADR J183304.4–384046 was found in comparison of the 150 MHz GaLactic and Extragalactic All-sky MWA (GLEAM) and TIFR GMRT Sky Survey (TGSS) catalogs. Given the 180 mJy flux density and long (1–3 yr) timescale of evolution of this source, this candidate transient may be an example of an extragalactic synchrotron transient detected at low frequencies, the first of many such transients which may be uncovered by the Square Kilometre Array (SKA; see Metzger, Williams, and Berger 2015) – follow-up observations are ongoing (Murphy et al. 2017).

- From 10 240 hours of simultaneous monitoring with LWA1 and LWA Sevilleta (LWA-SV; Cranmer et al. 2017), a possible transient was discovered at 34 MHz with an approximately 830 Jy flux density, with a duration of 15–20 seconds (Varghese et al., *ApJ* submitted), based on its simultaneous detection by both LWA stations.

- The transient detection that is most relevant to this work was detected by Stewart et al. 2016 in LOFAR Multifrequency Snapshot Sky Survey (MSSS) data. The source, ILT J225347+862146, was detected at 60 MHz and reached peak flux densities of 15–25 Jy over an 11 min timescale. Although the origin of this transient emission remains a mystery, with no identified higher-energy counterpart, the flux density and implied rate of this event suggests that this may be a dominant population in the low frequency transient sky, and one to which the OVRO-LWA is sensitive.

In order to shed light on the nature of the potential population of sources revealed by the transient of Stewart et al. 2016, as well as to explore the low frequency radio sky for other transient phenomena, we have conducted a survey with the OVRO-LWA from 27–84 MHz, imaging the entire viewable sky ($\sim 1.6\pi$ sr) every 13 seconds with approximately $10'$ spatial resolution, to search for transient sources on timescales ranging from 13 seconds to ~days, using 31 hours of observations. The survey observations and description of the OVRO-LWA are given in Section 4.2. In Section 4.3, we describe our transient detection pipeline, with the results of the survey detailed in Section 4.4. The upper limits on the transient surface density placed by the non-detection of transients in our survey are given in Section 4.5, as well as the implications of our non-detection on the potential population of transients similar to that detected by Stewart et al. 2016. We conclude in Section 4.6 and outline the future of OVRO-LWA transient science.

Table 4.1: Radio transient surveys at low frequencies ($< 350\,\mathrm{MHz}$)

| (1) Reference | (2) Instrument | (3) Center Frequency (MHz) | (4) Bandwidth (MHz) | (5) Search Sensitivity Jy | (6) Timescale searched | (7) $\Omega_{\mathrm{FOV}}$ (deg$^2$) | (8) $N_{\mathrm{epochs}}$ | (9) $N_{\mathrm{transients}}$ |
|---|---|---|---|---|---|---|---|---|
| 0 | LWA1 & LWA-SV | 34, 38 | 0.1 | 246 | 5 s, 15 s, 60 s | 10 300 | $7.4 \times 10^6$ | 1 |
| 1 | OVRO-LWA | 56 | 58 | 10.5, 13.8, 18.1, 20.8, 19.3, 19.7 | 13 s, 39 s, 2 min, 6 min, < 1 d, < 35 d | 17 045 | 8 586, 2 862, 954, 318, 1, 1 | 0 |
| 2 | LOFAR | 60 | 0.195 | 36.1, 21.1, 7.9, 5.5, 2.5 | 30 s, 2 min, 11 min, 55 min, 297 min | 176.7 | 41 340, 9 262, 1 897 328, 32 | 1 |
| 3 | LWA1 | 38, 52 74 | 0.075 | 540, 230 570 | 5 s | 8 353.7 | $6.1 \times 10^6$, $1.4 \times 10^6$ $1.0 \times 10^6$ | 0 |
| 4 | LWDA | 73.8 | 1.6 | 2 500 | 300 s | 10 000 | 29 437 | 0 |
| 5 | LOFAR | 149 | 0.781 | 0.5 | 11 min | 11.35 | 26 | 0 |
| 6 | LOFAR | 150 | 48 | 0.3 | 15 min, 100 d | 15.48 | 151 | 0 |
| 7 | MWA-32T | 154 | 30.72 | 5.5 | 26 min, 1 yr | 1 430 | 51 | 0 |
| 8 | MWA | 150 | … | 0.1 | 1–3 yr | 16 230 | 2 | 1 |
| 9 | MWA | 182 | 7.68 | 0.285 | 28 s, 5 min, 10 min, 1 h, 2 h, 1 d, 3 d, 10 d, 30 d, 90 d, 1 yr | 452 | 10 122 | 0 |
| 10 | MWA | 182 | 30.72 | 0.02, 0.200 | 1 h, 30 d | 186 | 652, 28 | 0 |
| 11 | GMRT | 235 | 15 | 0.003 - 0.01 | 1 d–2 yr | 3.2 | 20 | 1 |
| 12 | VLA | 325 | 12.5 | 0.0021 | 12 h | 6.5 | 6 | 1 |
| 13 | VLA | 330 | 3.1 | 64.8 | ~10 yr | 4.9 | 2 | 1 |
| 14 | VLA | 330 | 6.2 | 0.05 | 5 min | 7 | 440 | 1 |
| 15 | VLITE | 340 | 64 | 0.1 | 10 min–6 h | 5.5 | 2 799 | 0 |

**References** – (0) Varghese et al., *ApJ* submitted; (1) This work; (2) Stewart et al. 2016; (3) Obenberger et al. 2015b; (4) Lazio et al. 2010; (5) Cendes et al. 2014; (6) Carbone et al. 2016; (7) Bell et al. 2014; (8) Murphy et al. 2017; (9) Rowlinson et al. 2016; (10) Feng et al. 2017; (11) Hyman et al. 2009; (12) Jaeger et al. 2012; (13) Hyman et al. 2002; (14) Hyman et al. 2005; (15) Polisensky et al. 2016.

NOTE – Summary of transient surveys at low frequencies ($< 350\,\mathrm{MHz}$) conducted to-date, ordered from lowest to highest frequency. Note that only non-targeted, "blind" surveys are included here. In column 5, the search sensitivity refers to the detection threshold that was specified by each survey for transient detection – when not specified, a $6\sigma$ threshold is assumed. When only one value is given for $N_{\mathrm{epochs}}$ for a survey probing a range of timescales, the value applies to the shortest timescale reported. For Hyman et al. 2002, we consider only the two epochs that were involved in the initial discovery of GCRT J1746–2757, and exclude any follow-up analysis that targeted the field post-discovery.

## 4.2 Observations

### OVRO-LWA

The OVRO-LWA is a low frequency, dual-polarization dipole array currently under development at the Owens Valley Radio Observatory (OVRO) in Owens Valley, California, operating between 27–84 MHz. The completed array will consist of 352 elements – 251 elements contained within a 200 m diameter compact core, and 101 elements spread across maximum baselines of 2.5 km. The OVRO-LWA operates by cross-correlating the signals from all elements, providing a snapshot imaging capability with the full-sky field-of-view (FOV) of a dipole antenna, roughly 5′ spatial resolution at a cadence of a few seconds, with 100 mJy sensitivity across an instantaneous bandwidth of approximately 60 MHz.

At the time of the observations described here, the OVRO-LWA was in "stage II" of development, incorporating the 251-element core and a 32-element Long Baseline Demonstrator Array (LBDA) spread across maximum baselines of 1.5 km. The Large-Aperture Experiment to Detect the Dark Age (LEDA) correlator (Kocz et al. 2015) takes 512 inputs (256 antennas $\times$ 2 polarizations) and correlates all signals across a 27-84 MHz band (2400 channels at 24 kHz resolution) with a 13 second cadence. The stage II OVRO-LWA began operations in December 2016, and early science includes constraints on the sky-averaged HI absorption trough at $16 < z < 34$ (Price et al. 2018); high-fidelity low frequency maps for use in foreground filtering techniques, as well as the first constraints on the angular power spectrum of redshifted HI at low frequencies (Eastwood et al. 2018; Eastwood et al., *AJ* submitted); the first detection of high-energy cosmic rays without reliance on triggers from particle detectors (Monroe et al., *NIM-A* submitted); and constraints on coherent emission mechanisms associated with short gamma ray bursts (GRBs; Anderson et al. 2018).

### The 31-Hour Dataset

The first dedicated survey observation with the stage II OVRO-LWA was conducted on 2017 February 17, for 28 hours of continuous observations from 12:00 UTC through 2017 February 18 16:00 UTC. Data were recorded at 13 second integrations, with 2398 frequency channels spanning 27.38 – 84.92 MHz (24 kHz frequency resolution). The cadence was chosen because a sidereal period is almost exactly an integer multiple of 13 s, and this makes possible the subtraction of sidereally separated integrations as a means of searching for transients with sensitivity to all timescales up to a sidereal day. The OVRO-LWA is a zenith-pointing telescope,

with each snapshot image covering the full visible hemisphere – the 28 hour run consists of 7756 contiguous full sky snapshots. In addition to this dataset, a 3 hour observation (832 contiguous full sky snapshots) from 2017 January 12 01:02 – 04:02 UTC that was conducted as part of a short GRB follow-up program (Anderson et al. 2018) was included (with near identical configuration to the 28 hour dataset), to bring the amount of data used in the transient search to 31 hours (see Table 4.2).

Table 4.2: The observations and corresponding calibration times that comprise the 31-hour dataset

| (1) | (2) | (3) | (4) |
|---|---|---|---|
| Start time [UTC] | End time [UTC] | Number of snapshots | Calibration [UTC] |
| 2017-01-12 01:02:02 | 2017-01-12 04:02:05 | 832 | 2017-01-11 20:26:39 |
| 2017-02-17 11:59:54 | 2017-02-18 16:00:09 | 7756 | 2017-02-17 18:02:10 |

**Calibration and Imaging**

The raw visibility datasets produced by the LEDA correlator are converted into the standard Common Astronomy Software Applications (CASA; McMullin et al. 2007) measurement set table format (van Diepen 2015). Prior to calibration, antenna autocorrelation spectra are inspected and antennas are flagged if the median spectral power of an antenna is not within 2 standard deviations of the median power across all antennas. This is sufficient for identifying all antennas with issues along the signal path that resulted in a loss of, or sufficient distortion of, sky signal. For this dataset, 50 out of 256 antennas were flagged. An additional set of flags are applied in baseline-space, to avoid the effects of cross-coupling in adjacent lines in the analog signal path, and to remove a subset of bad baselines that are manually selected from the visibilities, resulting in the removal of less than 2% of baselines. Channel flags are generated on a per-integration basis, by identifying channels with visibility amplitudes that are outliers in their mean and max amplitudes relative to the rest of the band. This typically results in fewer than 240 out of 2398 channels flagged. In total, approximately 40% of visibilities are flagged per integration, the majority of which is due to the large number of antenna flags, however because the array is still dominated by confusion noise and other systematics even at the shortest timescales, the removal of such a large fraction of visibilities does not impact the sensitivity of the array.

The data are calibrated using a simplified sky model consisting of the two brightest sources in the sub-100 MHz sky: the radio galaxy Cygnus (Cyg) A and the supernova

remnant Cassiopeia (Cas) A, using the model flux and spectral indices given in Baars et al. 1977 for the former and Perley and Butler 2017 for the latter, extrapolated down to 28 MHz. The complex (amplitude and phase) antenna gains are determined on a per-channel basis from the two-source Cyg A-Cas A sky model using the CASA `bandpass` task, using baselines greater than 15 wavelengths in order to mitigate the effect of diffuse galactic synchrotron emission. The calibration solutions are derived from a single integration and remain sufficiently stable for roughly 24 hours, thus only one set of calibration solutions are generated per observation (see Table 4.2), from an integration when Cyg A is at its highest elevation in the beam ($\sim 87°$). We note that the two-source model used in the calibration process constitutes a grossly incomplete sky model, however it provides sufficient signal-to-noise to solve for a set of complex gains. Future surveys will incorporate a more complete sky model (generated from the full-sky maps of Eastwood et al. 2018), with calibration solutions derived from visibilities averaged over multiple integrations.

Additional direction-dependent calibration and source subtraction (peeling) towards Cyg A and Cas A are performed on single-integration timescales (when either of the two sources is above the horizon), using visibilities with baselines greater than 10 wavelengths to derive the direction-dependent calibration. This is necessitated by variations in the antenna gain pattern between individual dipole beams, caused by mutual coupling between adjacent antennas, and to a lesser degree, deviations in antenna orientation and ionospheric fluctuations. Peeling solutions are also derived on a per integration basis for a generic source in the near-field of the array. This is done to remove the effects of a stationary noise pattern in the data, which has distinct spectral, temporal, and spatial characteristics, likely caused by a combination of common-mode pickup and cross-talk in the analog electronics. Peeling is performed using the `TTCal` calibration software package developed for the OVRO-LWA (Eastwood 2016). Imaging and deconvolution are done with `WSClean` (Offringa et al. 2014a). The full FOV is imaged over $4096 \times 4096$ pixels, with a pixel scale of $1.875'$ and using a robust visibility weighting of 0 (Briggs 1995). At the time of these observations, a set of northeast LBDA antennas were not operational, resulting in an abnormally elongated synthesized beam with a major axis of $29'$, a minor axis of $13.5'$, and a position angle of $50°$. Figure 4.1 shows an example 13-second snapshot full sky image taken from the 31-hour dataset, using the full 58 MHz of bandwidth, and an approximation of the primary beam as a function of elevation angle.
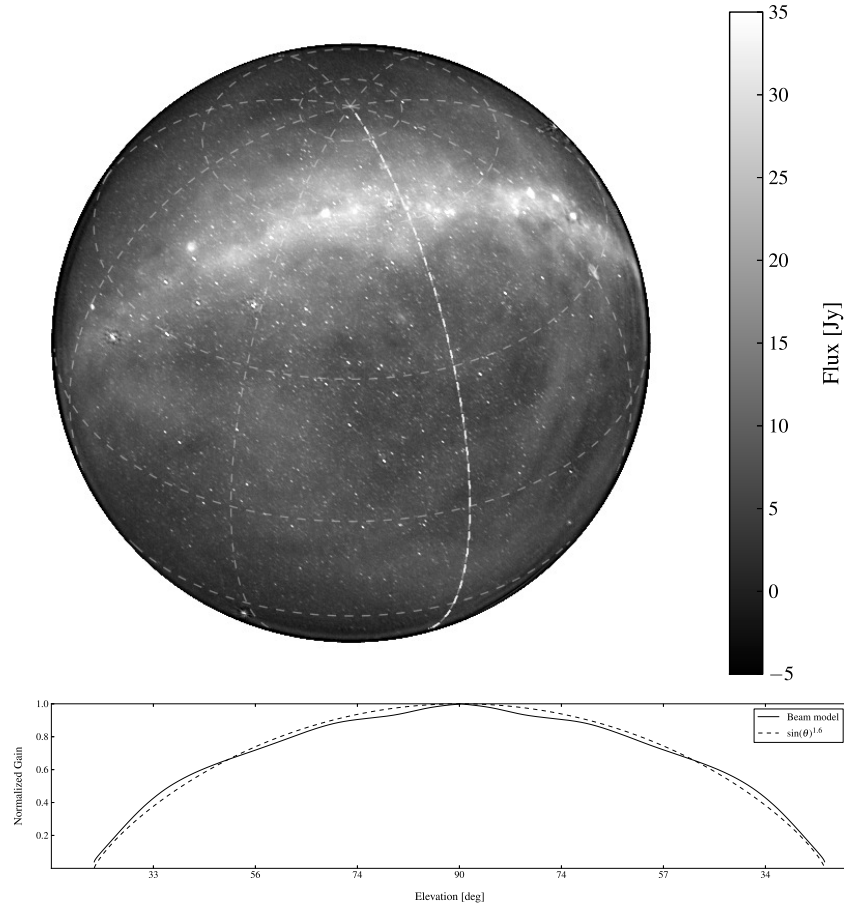
Figure 4.1: Snapshot full-sky image from the OVRO-LWA at 2017-01-12 02:02:05 UTC, with dashed contours denoting lines of constant RA and dec (top), and a cut through the primary beam at an azimuth of $0°$, comparing a simulated LWA dipole beam with ground screen to the standard dipole approximation given by $\sin^{1.6}(\theta_{el})$, as a function of elevation angle (bottom). The beam model is symmetric, so that an orthogonal cut through the beam at an azimuth of $90°$ would yield an identical normalized gain pattern. The entire field-of-view down to an elevation angle of $10°$ is searched in the transient pipeline. In the snapshot image, zenith is located in the center, with the horizon represented by the perimeter of the circle. The diffuse emission is galactic synchrotron emission. In a single snapshot image, greater than 2000 point sources are detected above the local $5\sigma$ threshold (see Section 4.3).

The transient detection by Stewart et al. 2016 in 400 hr of LOFAR Multifrequency Snapshot Sky Survey (MSSS) data with 195 kHz of bandwidth at 60 MHz, in a field centered on the north celestial pole, represents the detection of a potentially new and exciting transient source population. From this event, Stewart et al. 2016 report a transient rate of $3.9^{+14.7}_{-3.7} \times 10^{-4} \, \text{d}^{-1} \, \text{deg}^{-2}$ at a flux density level of 7.9 Jy. This corresponds to an expected detection of $8.4^{+31.8}_{-8.0}$ events in the 31-hour OVRO-LWA

transient survey, under the assumption that the transient emission is broadband in nature. Investigating and verifying this population therefore represents a primary goal of the OVRO-LWA transient survey. One of the timescales probed using the full 31 hours of the OVRO-LWA transient dataset is 6 min, which is able to capture the relevant timescale over which the Stewart et al. 2016 transient showed an appreciable increase in flux (the total duration of the event was 11 min, but showed an approximately 100% increase in flux over a 2 min period).

## 4.3 The Transient Pipeline

**Timescales**

The full 31 hr dataset comprising the OVRO-LWA transient survey was searched across a range of timescales by performing subtractions in image space of either sequential integrations or a sliding boxcar of width determined by the number of integrations in a given timescale, in order to remove the diffuse galactic emission and non-intrinsically varying sources and to generate "difference" images that are sensitive to sources which are varying on the timescale given by the integration spacing. Sequential image subtraction was used to probe timescales of 13 s (single integrations), 39 s (3 integrations), 2 min (9 integrations), and 6 min (27 integrations). In addition, sidereal subtraction using 3 hr of data with overlapping sidereal coverage between the 2017 January 12 and 2017 February 17 observations, as well as 4 hr of data with overlapping sidereal coverage within the 2017 February 17 observations, was used to search for transients on all timescales simultaneously (up to 36 d and 24 hr, respectively).

**Sensitivity**

The difference images are generated by selecting snapshots separated by $N$ integrations, matching the phase centers between the two snapshots to partially account for sky rotation, and subtracting the resulting images. Images are not deconvolved prior to subtraction due to computational limitations associated with deconvolution of many tens of thousands of all-sky images. In addition, because we are not averaging visibilities in time when performing the transient search on longer timescales, and instead selecting 2 snapshot images separated by a given timescale, there is no gain in sensitivity (by a factor $\propto \sqrt{t_{\mathrm{int}}}$) for difference images probing longer timescales. The average noise actually increases towards longer timescales, largely due to limitations associated with bright source sidelobes and incomplete sky subtraction between widely spaced integrations. The direction dependent calibration

and subtraction (peeling) which was described in Section 4.2 above is performed on the 2 brightest sources in the low frequency sky (Cas A and Cyg A). The effects which necessitate the peeling of these sources are also present for the remaining sources in the FOV, however computational limitations and signal to noise requirements for the peeling process prevent the removal of the next set of brightest sources in the low frequency sky (e.g., Taurus A and Virgo A). The result is sidelobe artifacts that cannot be successfully peeled out. These create a noise floor that is above the expected thermal noise on single integration timescales and is therefore the limiting factor when averaging visibilities on longer timescales. The direction dependent effects inherent to this issue are almost entirely dominated by beam to beam variation between dipoles, and the eventual mapping of the individual OVRO-LWA dipole beams will allow significant improvement in noise for difference image searches on longer timescales.
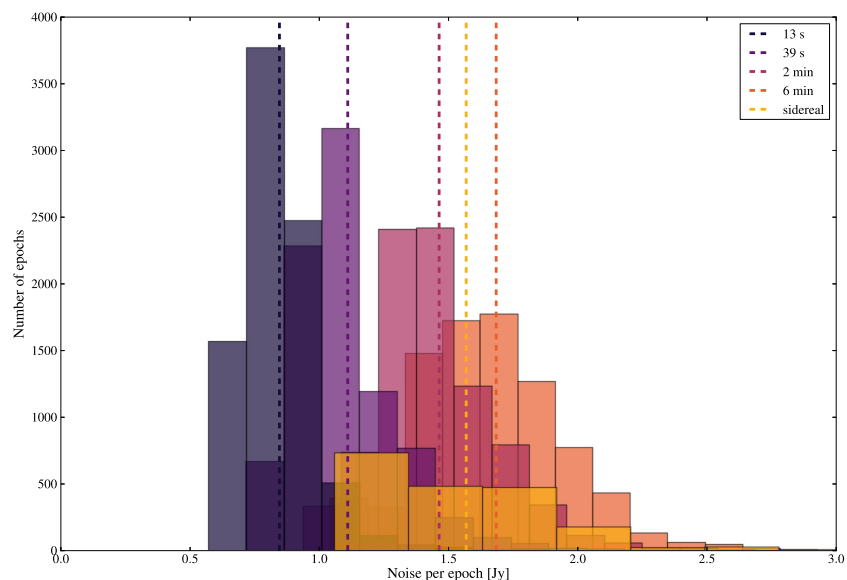


Figure 4.2: Histogram of the noise, as measured from the pixels in the $15°$ region surrounding zenith, in each difference image epoch, for all timescales probed. The dashed lines show the mean value of the noise for each timescale.

The other factor which must be taken into account when computing the sensitivity of our survey is the fact that our transient pipeline searches over nearly the entire primary beam FOV, down to an elevation angle of $10°$. The result is non-uniform sensitivity over our $\sim 17\,000\,\text{deg}^2$ FOV. To account for this, the noise is measured in the central regions of each difference image surrounding zenith. The effect of the primary beam is approximated as $1/\sin^{1.6}\theta_{\text{elevation}}$ (see Figure 4.2), and the noise

we measure across the whole field for each epoch of the survey is approximated as the noise at zenith times the mean of the primary beam pattern weighted by the fractional area of the FOV as a function of elevation angle. Taking into account the $6.5\sigma$ threshold of the transient search pipeline, this results in sensitivities at each timescale as reported in Table 4.5. Because we are using a single measurement of the noise at zenith to approximate our sensitivity across the entire FOV, we are necessarily neglecting subtle variations in the noise across the image due to things like bright source sidelobes, etc. However, given the large number of epochs over which we are computing our survey sensitivity, these variations are not likely to significantly alter our noise values.

Table 4.3 gives the average RMS noise and number of epochs for each timescale searched. We note that the noise in a difference image is equal to the quadrature sum of the noise for the two images from which it was generated (i.e., $\sigma_{\mathrm{diff}} = \sqrt{\sigma_t^2 + \sigma_{t+\Delta t}^2}$). However, this is still an improvement in noise over the confusion-limited single snapshot images (Cohen 2008).

Table 4.3: The average noise in the sequentially subtracted images for each of the transient timescales searched

| (1)<br>Timescale | (2)<br>Average RMS [Jy beam$^{-1}$] | (3)<br>Number of epochs |
|---|---|---|
| 13 s | 0.85 | 8586 |
| 39 s | 1.11 | 8582 |
| 2 min | 1.56 | 8570 |
| 6 min | 1.68 | 8534 |
| sidereal | 1.57 | 1960 |

NOTE – The noise is measured from a region centered on zenith with a radius of approximately $15°$. Single integration (13 s) images are consistent with thermal noise. There is an increase in noise on longer timescales due to the fact that the difference images are generated by subtracting non-deconvolved images generated from visibilities at different local sidereal times (LSTs), rather than averaging in time (see Section 4.3).

**Source Extraction**

Sources that are present in each subtracted image are identified through the source extraction pipeline, cross-matched with any subsequent detections of a source at the same position in later snapshots and other timescales, and added to a candidate transient list. The source extraction algorithm is custom-built for the OVRO-LWA transient pipeline, and utilizes a hierarchical clustering algorithm (using `SciPy`'s

`scipy.cluster` clustering package) that can accurately identify individual sources from the frequently non-contiguous set of pixels above the selected noise threshold which comprise a given source in the non-deconvolved subtracted images. Candidate transient sources are identified through the following:

1. Each sequential subtracted image is divided up into 16 image regions, and all pixels above a $5\sigma$ local noise threshold in each region are identified, and grouped into "islands" using a hierarchical clustering algorithm with a distance-based linkage function (see Figure 4.3). There are of order 100 candidate transients identified in each sequential subtracted image above the $5\sigma$ local noise threshold.

2. The transient candidate detections in individual subtracted images are merged together across the full dataset to create a catalog of transient candidates, which is cross-matched with the self-generated catalog of sources present within the 31-hour dataset (see Section 4.3). The vast majority of sources detected in the sequential subtracted images are persistent sources that exhibit variability on 13 second timescales due to scintillation. Any remaining sources that are not co-located with any of the known catalogued sources are classified as potential transient events. This reduces the number of sources detected in a single difference image from of order 100 to a few. At this point in the pipeline, the threshold above which a source was kept in consideration as a candidate transient event was raised to $6.5\sigma$, so as to reduce the number of false positive sources due to Gaussian noise fluctuations and maintain a manageable number of candidate events. Table 4.3 gives the approximate flux density levels this $6.5\sigma$ threshold corresponds to for all timescales.

3. Candidate sources which are detected more than 60 times across the full dataset are classified as scintillating sources that were not captured by the source catalog (either because they were below the $4.5\sigma$ detection threshold that was used to generate the catalog or they are positionally offset by more than $30'$ from the catalogued source position due to ionospheric refraction) and are therefore removed from the candidates list. In each of these cases, the presence of a source is verified against a deeper reference catalog, including a deeper OVRO-LWA map (Eastwood et al. 2018) and the VLA Sky Survey redux (VLSSr; Lane et al. 2014).

4. The remaining candidate transient sources are compiled into a list, along with corresponding metadata, including SNR in the detection images, approximate source size, coordinates, azimuth and elevation at the time of detection, number of times a source was detected at this position, the spectrum of the source at 24 kHz resolution, and an automatically generated classification label that identifies the source type based on fitted source size, spectral features, and position in the beam (see Section 4.3). Table 4.4 shows the number of candidate transients remaining at this step in the pipeline, for each of the timescales searched.

Table 4.4: Number of transient candidates remaining after major steps in the transient detection pipeline

| (1) | (2) | (3) |
|---|---|---|
| Timescale | $N_{\mathrm{candidates}}$ after first cut | $N_{\mathrm{candidates}}$ after auto-classification |
| 13 s | 4520 | 229 |
| 39 s | 3761 | 152 |
| 2 min | 3370 | 133 |
| 6 min | 4669 | 598 |
| sidereal | 1700 | 109 |

**Source Catalog**

Due to the effects of the ionosphere (refraction and scintillation) and the solar wind (interplanetary scintillation; see e.g., Kaplan et al. 2015), significant source variability is present on sub-integration, and greater, timescales for the vast majority of sources in the OVRO-LWA FOV. In order to deal with the hundreds of (extrinsically) variable sources that are present in each sequentially subtracted image, an OVRO-LWA source catalog was generated (from the 31-hour dataset) in order to provide a self-consistent catalog of sources that can be cross-matched with sources detected in the subtracted images, thereby eliminating thousands of spurious detections due to extrinsic variability of persistent sources from consideration as transient sources. We note that this method of eliminating candidates that can be matched to a source in the catalog precludes detection of not only extrinsically but intrinsically varying sources. While intrinsic variability on timescales as short as 10s of seconds from persistent sources in the catalog is not expected (e.g., incoherent synchrotron emission from active galactic nuclei in which light travel time arguments preclude the possibility of variability on such short timescales Pietka, Fender, and Keane 2015), probing intrinsic variability is of interest on the longest timescales (approx-
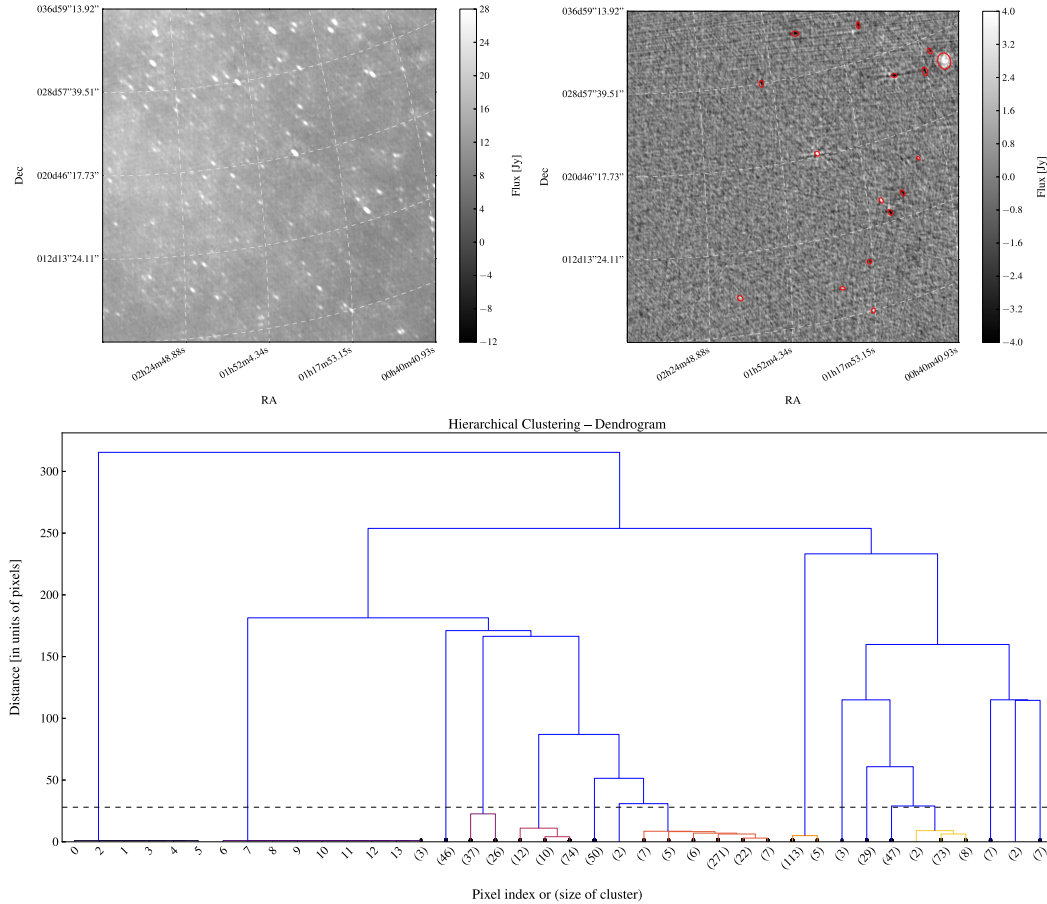
Figure 4.3: Example output from the hierarchical clustering algorithm, showing transient candidates identified in the source extraction pipeline from the difference image corresponding to the 13 s snapshot shown in (top, left). All pixels identified above a $5\sigma$ threshold in the region of the difference image shown in (top, right) are hierarchically clustered into individual sources, as shown visually in the dendrogram plot (bottom). The dashed line denotes the cutoff distance threshold used, above which all connecting nodes are disregarded and the clusters formed below this threshold represent the number of distinct sources identified in the difference image. In this example, there are 16 sources identified in the difference image, each of which is marked in (top, right) with a red ellipse.

imately a month) to which the search is sensitive. However, variability studies are beyond the scope of this current work.

The source catalog is constructed from snapshot images across the full 31-hour dataset that are separated by approximately 5 hours down to a maximum limiting elevation of 10°. These snapshot images are median filtered in image space using a kernel size of 21 pixels, and subtracted from the non-filtered image, in order to remove any large-scale diffuse galactic emission and improve the detection and

fitting accuracy of point sources (above a $4.5\sigma$ threshold) that can be recovered from the images and added to the source catalog. The source extraction algorithm used to generate the source catalog is the same algorithm used in the transient detection pipeline (see Section 4.3). The snapshot images used to construct the source catalog are filtered in image-space rather than through the tapering of visibility weights because the image space filter and subtraction removes extended emission without the "ringing" introduced by the hard tapering of short-spacing visibilities which is necessary to fully remove diffuse emission.

From the 31-hour dataset we assembled a catalog of 4500 sources that was used as a reference in the transient detection pipeline described below.

**Classification and Visual Inspection**

Human visual inspection was necessary at this point in the pipeline, both to evaluate the success with which the source extraction algorithm recovered sources above the $6.5\sigma$ threshold in the subtracted images and to ensure the accuracy of the automatically generated source classifiers. For each combination of timescale and dataset, the transient pipeline outputs an image containing relevant diagnostic information for all remaining candidate transient events, which includes image cutouts, spectra, and relevant metadata. Figure 4.4 shows an example output frame from the transient pipeline – one such frame is generated for every transient candidate, in every integration in which said transient is detected. Because the source extraction algorithm selects both for positive and negative sources, each candidate event should be detected at least twice, as it will be present in two subtraction images, first as a positive source and then as a negative source. The vast majority of all candidate events fall into one of the following categories – RFI reflection events likely associated with meteor ionization trails, airplanes passing above the array (showing either reflected or self-generated RFI), broadband RFI on or within a few degrees of the horizon associated with power lines, Cas A and Cyg A sidelobes, and scintillating sources.

2017-02-17 12:09:32.9 UTC

source00369
source00668
source00733
source02798

(10h17m11.0s 09d49m46.3s)
(-102.5 az 31.6 el)
(0.91deg x 0.74deg)
1.904 x unresolved
Source 00733

25.01 SNR
20.20 Jy peak flux
002 detections
Auto classification: Reflection

Flux [Jy]
Frequency [MHz]
Channel 1  Channel 2  Channel 3  Channel 4  Channel 5
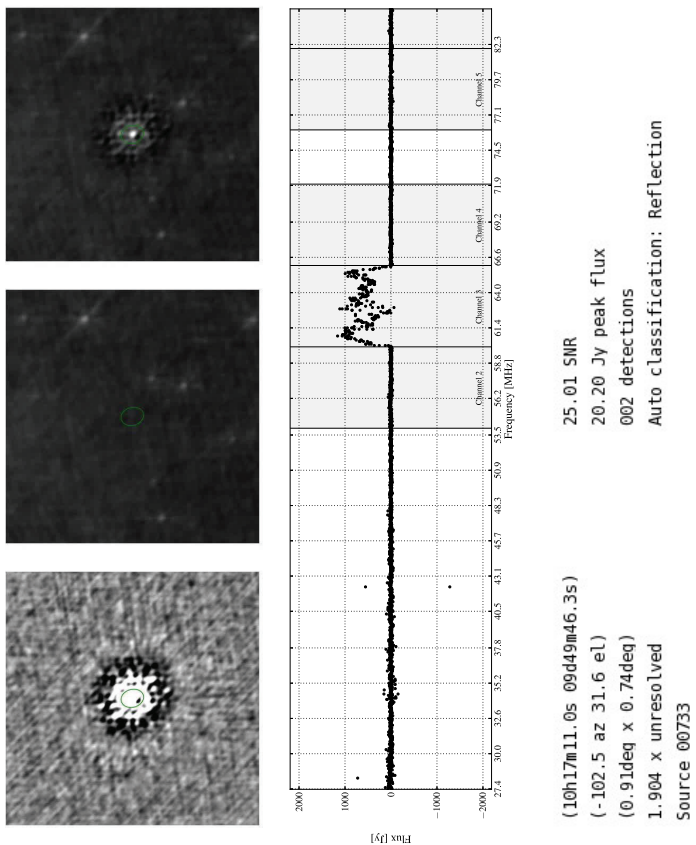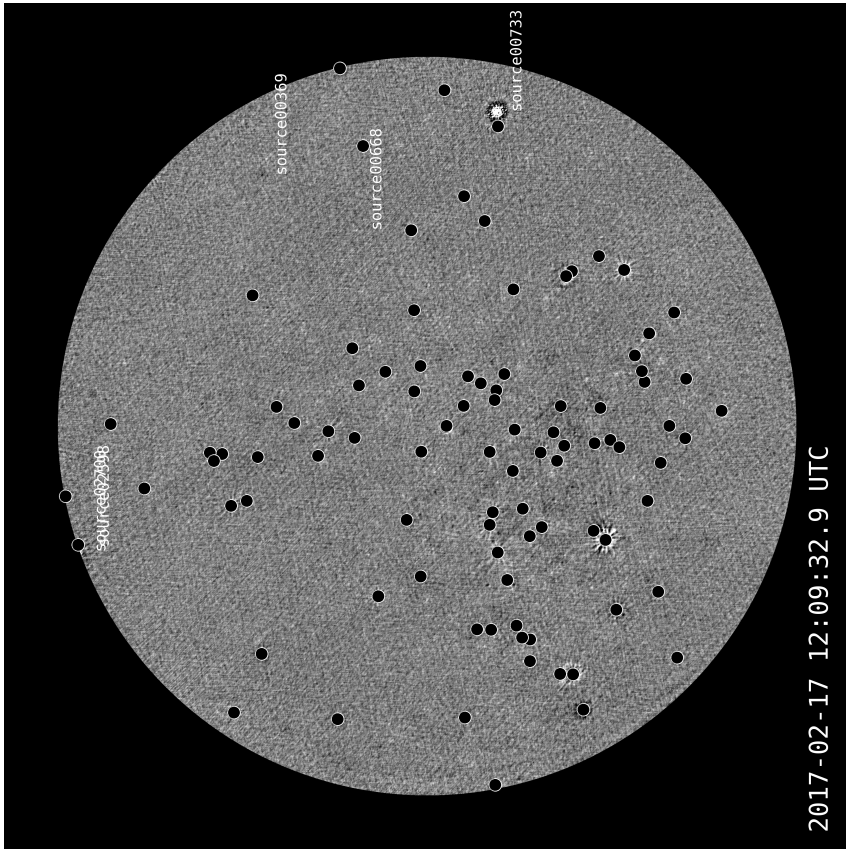
Figure 4.4: An example output image from the transient pipeline. The subtracted image in which the candidate transient source is detected (left). The color scale on the image is from -4 to 4 Jy. Black circles are covering sources that were detected in the source extraction pipeline but are present in the OVRO-LWA source catalog. Transient candidates without a catalog counterpart are labeled with their transient pipeline source ID. Image cutouts at the location of the transient candidate show the subtracted image in which it was detected, as well as the integrations which formed the subtracted image (right, top). The source difference spectrum (right, middle) provides important diagnostic information, particularly in the case of meteor reflections, which is by far the most dominant non-astrophysical transient source in the dataset, occurring at a rate of approximately 0.1 s$^{-1}$. The vertical lines in the spectrum show the digital TV channel broadcast bands which are observable from the OVRO-LWA. In this example, the source spectrum is showing reflected Channel 3 TV broadcasts, which spans 60–66 MHz. The pipeline also outputs metadata (right, bottom) on the candidate transient source, including RA and dec, azimuth and elevation, an approximate Gaussian fit to the source, the source ID, the signal to noise with which the source was detected, the peak flux (based on the approximate Gaussian fit), the number of times this source was detected, and an automatically generated classifier label.

**Follow-up of interesting events**

Each candidate transient source is automatically given an initial classification based on the difference spectrum, fitted source size, and position. It is then visually inspected to ensure that classifiers are being correctly applied and that no transient source was missed. Eventually the verification of sources by manual human inspection will be phased out of the pipeline, and replaced with a more efficient and robust method of identifying and classifying sources using a machine learning algorithm. However, for the current dataset, transient detection was automated to the point of candidate detection, which was sufficient for compiling a list of candidates and their associated metadata that could be then more robustly inspected and identified by human eyes. For those candidates that were not clearly associated with the types of events described above, and which did not have a counterpart in the VLSSr catalog at 74 MHz, the TIFR GMRT Sky Survey (TGSS; Intema et al. 2017) catalog at 150 MHz, or in the OVRO-LWA catalog generated from the (more sensitive) m-mode sky maps at 74 MHz (Eastwood et al. 2018), the following steps were taken to further characterize the candidate and verify as a transient event:

1. To better characterize the position, extent, and spectral behavior of each source, candidates are re-imaged at phase center. This is done across the full 58 MHz bandwidth, across multiple 2.6 MHz subbands, and in the frequency range over which a source shows emission in the difference spectrum.

2. Deconvolution is performed with a range of visibility weightings between natural and uniform in order to investigate the presence of flux on different spatial scales.

3. The source image is fit in order to confirm whether the source is unresolved, as expected for an astrophysical transient. If resolved, we investigate, typically confirming an atmospheric/meteoric reflection event. The source visibilities are fit in order to robustly determine whether the source is unresolved, or, if it is resolved and in the near-field of the array, to determine the source height (in which case it is most likely an atmospheric / meteor reflection event).

## 4.4 Results

Across the entire 31-hour dataset, and for all timescales probed by the survey, a total of 36 232 images were searched in the transient pipeline, with each image covering approximately 17 000 deg$^2$ and nearly $5 \times 10^4$ independent beams. After

eliminating all candidates associated with cataloged sources and repeat detections of sources at different timescales, 12 112 transient candidates were identified by the pipeline. Of these, 5 828 events were associated with meteor reflections; 2 011 events were associated with RFI reflected from and generated by airplanes; 1 430 events were associated with horizon RFI or bright source sidelobes; and 1 622 events were spurious detections of sidelobes or extended emission. None of the remaining 1 221 events, which were not automatically classified by the pipeline into one of the previous categories, were identified as astrophysical transients following human inspection – the events included scintillation of known sources, as well as detections associated with the Sun and a number of Jovian bursts.

**Meteor Reflection Events**

The most prevalent (non-astrophysical) transient source in our dataset is associated with the reflection of RFI from patches of high ionization in the atmosphere, likely caused by meteors. Meteors passing through the atmosphere are experiencing the ablation of material off their surface – this stripped material collisionally ionizes the surrounding air particles, creating a patch of ionized material with a plasma frequency > 100 MHz, and which is therefore able to reflect terrestrial RFI (Millman, McKinley, and Burland 1948; Greenhow 1952). These are easily distinguished as digital (and a likely a few remaining low power analog) TV broadcasts by their spectral signature, with all emission fully contained within one or more of the broadcast bands designated by the Federal Communications Commission: Channel 2 – 54-60 MHz; Channel 3 – 60-66 MHz; Channel 4 – 66-72 MHz; Channel 5 – 76-82 MHz; Channel 6 – 82-88 MHz (see Crane 2008). Figure 4.3 shows a typical reflection spectrum associated with a meteor. While reflection events are consistently spectrally confined within one or more of the 6 MHz-wide digital broadcast bands, within those bands they can exhibit a wide range of spectral features, as well as a wide range in characteristic flux densities. They are typically less than 13 s in duration, however particularly bright events can last as long as ~ 30 s. Multiple reflection sources that are adjacent in position and likely associated with the same meteor trail can have spectra that show emission in different broadcast bands.

The automatic classification of transient candidates associated with meteor reflections is determined by the spectrum and approximate fit to the size of the source. For every integration in which the source is detected, the spectrum is convolved with a 6 MHz-wide top-hat function, and the location of the maximum of this filtered spectrum is identified. If the maximum falls within one of the known broadcast

bands, is above a manually set detection threshold, and the fit to the source in the non-deconvolved image is resolved (in the near-field regime of the array) and circular to within a factor of 2, then the source is automatically classified as a meteor reflection (the latter specification is to distinguish it from airplane reflections – see Section 4.4 below).

We note that none of the meteor-associated emissions we observed appeared to be intrinsic in nature, i.e. akin to the fireball radio afterglows observed by Obenberger et al. 2015a. All meteor events observed by the OVRO-LWA in this dataset were clearly reflection events from ionized trails. However, this is not inconsistent with the predicted rate of fireball radio emission by Obenberger et al. 2016, which for a flux density lower limit of 540 Jy at 38 MHz corresponds to a detection rate of approximately 40 meteor afterglows year$^{-1}$.

### Airplanes

Airplanes are another prevalent terrestrial transient source. Like meteor trail reflections, they are most frequently detected through their reflection of digital TV broadcasts, although many do also exhibit spectral features outside the known digital TV broadcast bands that are likely intrinsic. Although airplanes are a major contaminant in the transient pipeline, they are easily identified and flagged by their spectral features, their elongated shape, and movement across the FOV.

### Horizon RFI and bright sources

Sources of broadband RFI, which are distinct from the reflection of television broadcast bands, are confined to the horizon in discrete directions, usually along the line-of-sight to power transmission lines. Although the RFI is restricted to the horizon, it is still frequently detected by the transient pipeline at elevation angles as high as $\sim 20°$. However, because the RFI is localized, both in position and in time, it is classified in the transient pipeline by hierarchical clustering of sources located at a specific set of azimuths and low elevations, weighted by $1/\Delta t$ where $\Delta t$ is the time between separate detections.

A similar clustering scheme is used to flag detections in the transient pipeline associated with bright source sidelobes (e.g., Taurus A, Virgo A, Perseus A and B, etc., typically sources with flux densities greater than approximately a few hundred Jy), as well as Cas A and Cyg A residuals.
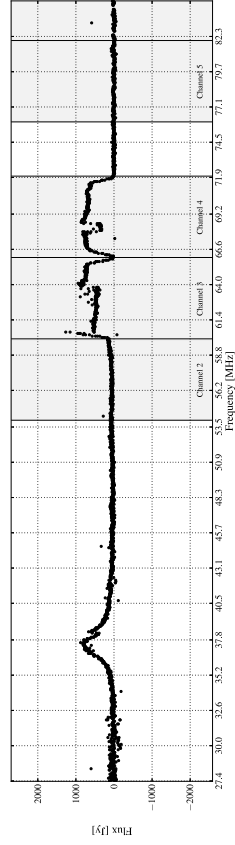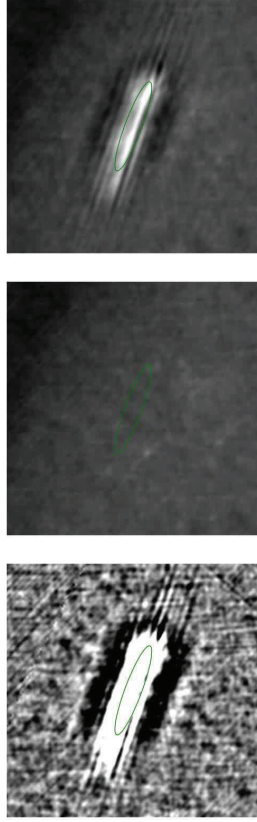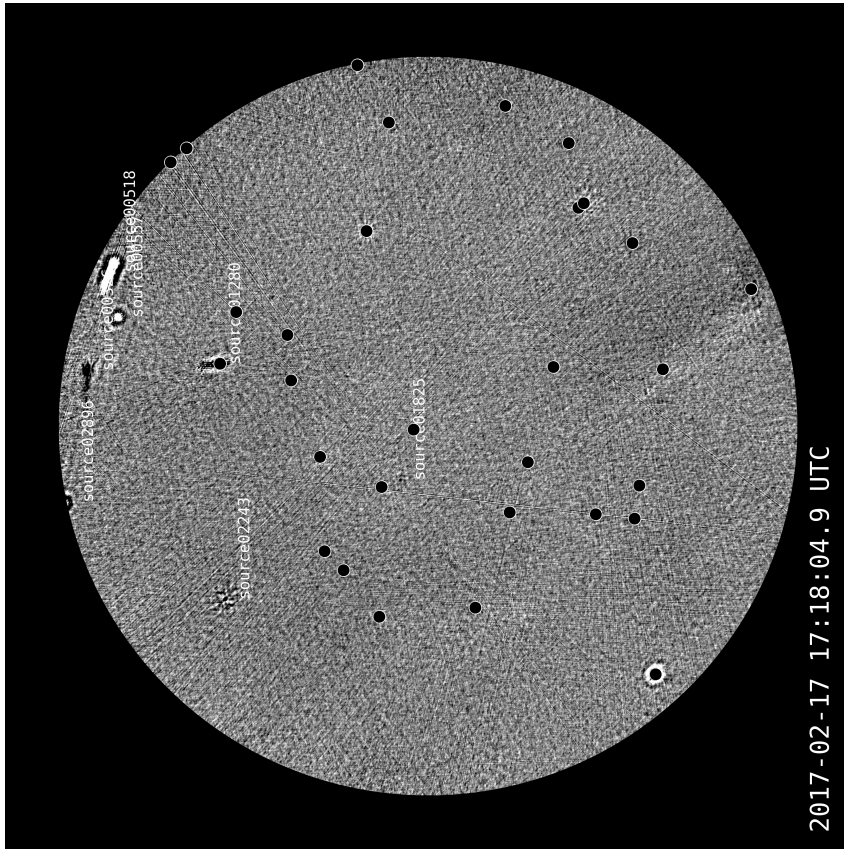
Figure 4.5: Detection of an airplane in the transient pipeline. Airplanes are a persistent contaminant in the transient pipeline, but are easily identified by their temporal, spectral, and image features. This plane was detected to the north-west of the array, in the approximate direction of Bishop Airport. In this example, the plane is detected through both reflected RFI (digital broadcast bands in Channels 3 and 4) and RFI that is generated by the plane itself (the peak at approximately 37.5 MHz).

**Scintillating sources**

Another significant source of false positive transient candidate sources detected in the pipeline is quiescent sources that are varying due to scintillation. This includes discrete sources that were previously below the detection limit of the source catalog, which scintillated above the detection threshold in one or more difference images, as well as sources which were detected and included in the source catalog but exhibited a refractive offset significant enough to not have been correctly identified by the transient pipeline as a known source (i.e. $> 20'$ positional offset). In the latter case, all sources detected more than 60 times across the dataset at a given timescale were automatically classified as such, and later manually verified as variable sources (due to scintillation effects) rather than true transient events. In the former case, the scintillating nature of the source as opposed to a transient is verified by fitting for the source position and flux across the full dataset (and accepting a lower threshold than the $4.5\sigma$ cutoff that was used for generating the source catalog), as well as cross-matching the location of the source with the m-mode analysis maps generated from the same OVRO-LWA dataset, and the VLSSr and TGSS catalogs.

A small subset of sources ($\sim 10$) detected by the pipeline exhibited large increases in flux at frequencies which roughly correspond to the critical frequency of the ionosphere, at the transition between strong and weak scattering and where the magnitude of scintillation is greatest. The sources characterized by this type of scintillation behavior showed increases in flux as large as 100s of Jy at frequencies between 30-40 MHz, and evolving on 13 s timescales and lasting for as long as a few minutes. The majority of these events occurred at low elevation ($< 20°$), however a few were detected at high elevation, usually during periods of increased scintillation due to ionospheric activity. The critical frequency occurs when the Fresnel and diffraction scales are approximately equal (see Narayan 1992). The former scales with wavelength, $\lambda$, and distance between the observer and scattering screen, $D$, as

$$r_F = \sqrt{\frac{\lambda D}{2\pi}}, \tag{4.1}$$

and the latter as

$$r_{\text{diff}} \propto \lambda^{\frac{6}{5}} D^{-\frac{3}{5}} \tag{4.2}$$

under the assumption that the ionosphere is characterized by Kolmogorov turbulence. The diffraction scale of the ionosphere is approximately 1 km for a wavelength $\lambda \approx 300$ cm and scattering screen distance of $D \approx 300$ km. The diffraction and Fresnel scales in the ionosphere are approximately equal at a frequency of $\sim 50$ MHz, which is roughly consistent with the frequencies at which we observe these events.

## 4.5    Discussion

Our transient search across 31 hours of OVRO-LWA data, at all five timescales probed, ranging from 13 s up to sidereal day subtractions, resulted in no radio transients that could be identified conclusively as astrophysical in nature. We can use these non-detections to place upper limits on the instantaneous transient surface density for each timescale searched and at the flux density limits set by each timescale's sensitivity. The instantaneous transient surface density is the number of transient sources per square degree that would appear in a snapshot of the sky at a flux density greater than or equal to the flux density at which the surface density is reported. This is distinct from a transient rate because the surface density is instantaneous and not reported per unit time. However, there is a timescale at which a transient surface density limit placed by a survey is applicable and it is set by the cadence of the survey. We report the 95 percent confidence level upper limit for the transient surface density, under the assumption that the rate of transients follows a Poisson distribution:

$$P(n) = \frac{\lambda^n}{n!} e^{-\lambda},$$ (4.3)

where $\lambda = \rho \Omega_{\text{tot}}$ is the expected number of transients on the sky at any instant in time, $\rho$ is the instantaneous transient surface density, and $\Omega_{\text{tot}} = (N_{\text{ind. epochs}} - 1) \times \Omega_{\text{FOV}}$ is the total surface area probed by the survey. For the OVRO-LWA, the FOV that is searched in each epoch is $17\,045\,\text{deg}^{-2}$. $N_{\text{ind. epochs}}$ is the number of independent epochs searched (i.e., epochs separated by at least the transient timescale probed), which for our survey is smaller than the total number of epochs searched by a factor $t_{\text{int}}/t_{\text{probed}}$. This is due to the fact that our search on longer timescales was conducted on difference images that were generated from two integrations separated by the timescale being probed, and which were shifted by single integration timescales to generate subsequent difference images. The result is over-sampling in the time domain of transients on timescales longer than the integration time. This is advantageous for maintaining sensitivity to potential transient events by providing a more matched temporal filter, however it also results in many epochs that are not independent samples of the transient sky (because they are separated in time by less than the timescale being probed).

From our survey non-detection ($n = 0$), we can place upper limits on the instantaneous transient surface density at a 95 percent confidence level ($P(0) = 0.05$), for all timescales that were searched, using Equation 4.3. Table 4.5 shows the in-

stantaneous surface density limits placed for all timescales probed by the survey. The surface density limits placed, in the context of previous transient searches, is shown in Figure 4.6. We have placed the most constraining limits on the transient surface density at low frequencies at ~few Jy-level sensitivities. In addition, our upper limits are consistent with those placed by Obenberger et al. 2015b at comparable frequencies and flux densities of a few hundred Jy and with those placed by Rowlinson et al. 2016 at 182 MHz, assuming a flat spectral index and a standard candle population of transients in a Euclidean universe.

Table 4.5: Transient surface density limits placed by the OVRO-LWA transient survey

| (1) | (2) | (3) | (4) |
|---|---|---|---|
| Timescale | $N_{\text{ind. epochs}}$ | Sensitivity ($6.5\sigma$) (Jy) | $\rho$ (deg$^{-2}$) |
| 13 s | 8586 | 10.5 | $2.50 \times 10^{-8}$ |
| 39 s | 2862 | 13.8 | $6.14 \times 10^{-8}$ |
| 2 min | 954 | 18.1 | $1.84 \times 10^{-7}$ |
| 6 min | 318 | 20.8 | $5.53 \times 10^{-7}$ |
| sidereal (1 d) | 1 | 19.3 | $1.76 \times 10^{-4}$ |
| sidereal (35 d) | 1 | 19.7 | $1.76 \times 10^{-4}$ |

NOTE – Transient surface density limits placed for all six timescales probed by the OVRO-LWA transient survey. Because the entire OVRO-LWA FOV down to an elevation angle of $10°$ is searched as part of the transient pipeline, our single snapshot FOV is approximately $1.65\pi$ sr, or $17\,045$ deg$^2$.

We can also place limits on the transient surface density as a function of flux density, $\rho(S)$, rather than reporting the surface density at a single flux density value approximated as an average of our survey sensitivity over the primary beam. Because the transient search is conducted over nearly the entire primary beam FOV, each epoch of our survey has non-uniform sensitivity, with the best and worst sensitivities achieved at zenith and $10°$ elevation angle, respectively. However, for a transient population described by a luminosity function with power law $\gamma$, varying sensitivity corresponds to probing different parts of the luminosity distribution, and therefore the number of transients we can expect to detect within the volume probed by our survey is a function of sensitivity and the corresponding fraction of the sky covered by each sensitivity. Using Equation 4.3, we can write

$$P(0) = e^{-\rho(S(\phi))\,\Omega_{\text{tot}}(\phi)},$$ (4.4)

where $\rho(S(\phi)) = \rho_o \left(\frac{S(\phi)}{S_o}\right)^{-\gamma}$ and $\Omega_{\text{tot}}(\phi) = (N_{\text{ind. epochs}} - 1) \times \Omega_{\text{FOV}}(\phi)$. The flux density to which we are sensitive is a function of zenith angle $\phi$, and determined by the primary beam gain pattern, which we approximate as $\cos^{1.6}(\phi)$. We can therefore write Equation 4.4 as

$$P(0) = e^{-\rho_o \left(\frac{S_{\text{zenith}}/\cos^{1.6}\phi}{S_o}\right)^{-\gamma} \times (N_{\text{ind. epochs}}-1) \; 2\pi \sin\phi d\phi}, \tag{4.5}$$

where $S_{\text{zenith}} = 6.5\sigma_{\text{zenith}}$ is our transient survey detection limit at zenith. Under the assumption of $\gamma = 3/2$ for a standard candle population distributed uniformly in Euclidean space, the 95% confidence level on the transient surface density as a function of flux density, $\rho_o(S_o)$, becomes

$$\rho_o(S_o) = -\frac{\ln 0.05}{(N_{\text{ind. epochs}} - 1) \; 2\pi \int_{0°}^{80°} \cos^{1.6\gamma}\phi \; \sin\phi \; d\phi} \left(\frac{6.5\sigma_{\text{zenith}}}{S_o}\right)^{\gamma}, \tag{4.6}$$

$$\rho_o(S_o) = -\frac{\ln 0.05}{(N_{\text{ind. epochs}} - 1) \; 0.6\pi} \left(\frac{6.5\sigma_{\text{zenith}}}{S_o}\right)^{3/2} \text{sr}^{-1}, \tag{4.7}$$

where $\sigma_{\text{zenith}}$ for each timescale probed is given in column 2 of Table 4.3.

With the exception of the five transient detections at $> 150\,\text{MHz}$ by Murphy et al. 2017, Jaeger et al. 2012, Hyman et al. 2002, Hyman et al. 2005, and Hyman et al. 2009, and the detections by Stewart et al. 2016 and Varghese et al. (*ApJ* submitted) of transients at $60\,\text{MHz}$ and $34\,\text{MHz}$, respectively, all of the transient surveys shown in Figure 4.6 were only able to place upper limits on the transient rate at low frequencies. We note that in the case of the three detections by Hyman et al. 2002; Hyman et al. 2005; Hyman et al. 2009, all were found in targeted observations of the galactic center and, based on their brightness temperatures and very low spatial volume covered by these surveys, are most likely located in the galactic center and therefore extrapolation of the detection of these objects to an all-sky rate is not applicable. In the case of the detection by Jaeger et al. 2012, the transient has a much longer timescale than what is probed in the bulk of our survey, and was also found at significantly higher frequencies, indicating a potential source population to which our survey would not be sensitive. The transient found by Stewart et al. 2016 was detected at the same frequency and timescale probed by the OVRO-LWA transient survey and at a comparable sensitivity, with a reported

rate of $3.9^{+14.7}_{-3.7} \times 10^{-4}\,\mathrm{d}^{-1}\,\mathrm{deg}^{-2}$, corresponding to a detection of $8.4^{+31.8}_{-8.0}$ such events in our survey. However, its detection by LOFAR at $60\,\mathrm{MHz}$ with a $200\,\mathrm{kHz}$ bandwidth cannot constrain the spectral index or intrinsic bandwidth of emission for this event. The probability of our null detection of this potential transient population is $1.9^{+644}_{-1.9} \times 10^{-3}$, which allows us to rule out a transient rate $> 1.4 \times 10^{-4}\,\mathrm{d}^{-1}\,\mathrm{deg}^{-2}$ with 95% confidence. However, this is under the assumption of a flat spectral index and that the emission is broadband in nature. Figure 4.7 shows the probability of our null detection for a range of assumed spectral indices $\alpha$ and flux density distributions $\gamma$. If, however, the emission is of a narrow bandwidth relative to our observations, our sensitivity to this event decreases by a factor $\Delta\nu_{\mathrm{intrinsic}}/\Delta\nu_{\mathrm{obs}}$, where $\Delta\nu_{\mathrm{obs}} = 58\,\mathrm{MHz}$ is our survey bandwidth. Figure 4.8 shows the transient surface density limits placed by our survey as a function of flux density, for a range of flux density distributions $\gamma$.

## 4.6 Conclusion and Future Directions

We have placed the most constraining limits on the transient surface density on timescales of $13\,\mathrm{s}$ to a few minutes and at frequencies below $100\,\mathrm{MHz}$, with 31 hours of data from the OVRO-LWA. No transients were discovered on $13\,\mathrm{s}$, $39\,\mathrm{s}$, $2\,\mathrm{min}$, or $6\,\mathrm{min}$ timescales, nor in the 7 hours of data that had a corresponding overlap in LST and that allowed us to search up to timescales as long as $1\,\mathrm{d}$ and $35\,\mathrm{d}$. From our non-detections, we place an upper limit to the transient surface density of $2.5 \times 10^{-8}\,\mathrm{deg}^{-2}$ at the shortest timescales probed at a flux density of $10.5\,\mathrm{Jy}$.

The non-detection of any sources akin to the transient event detected by Stewart et al. 2016 allows us rule out a rate $> 1.4 \times 10^{-4}\,\mathrm{d}^{-1}\,\mathrm{deg}^{-2}$ with 95% confidence, under the assumption of a flat spectrum and wide-bandwidth for this event. We further rule out a range of power-law luminosity distributions and emission spectral indices for the potential population detected by Stewart et al. 2016, indicating that the event is likely narrow-band in nature. We note, however, the danger of conducting putative population rates with a transient detection of one – the transient uncovered by Stewart et al. 2016 could indeed have been the first detection of a population, but a uniquely bright outlier from that population. The event rate drawn from that single detection could therefore be vastly overestimated.

The non-detection of the population implied by the transient detected by Stewart et al. 2016 can be used to inform the design of future planned surveys with the OVRO-LWA. The next transient survey will use additional data taken with the Stage

II OVRO-LWA in 2018 March continuous 120 hours of observations. The duration of this dataset enables the transient search pipeline to operate entirely on difference images formed from sidereally matched integrations. This allows us to probe all timescales (between the integration time of 13 s and the maximum separation of identical LSTs of 5 d) simultaneously, while avoiding the issues associated with sidelobe confusion and incomplete sky subtraction for diffuse emission away from zenith that cause an increase in noise on longer timescales. This transient survey will also feature sub-band searches in order to provide a better matched-filter in frequency space to the transient detected by Stewart et al. 2016, as well as blind transient injections to better constrain the transient surface density probed as a function of sensitivity, timescale, and frequency parameters.

Finally, the stage III OVRO-LWA, which is scheduled to begin construction in mid-2019, will provide orders of magnitude more sensitivity to transient events, with the stated goal of 1000 hours for the first transient survey with the completed array, and 150 mJy sensitivities. In addition, mapping of individual dipole beams (a stated technical goal for the final stage array) will eliminate the sidelobe confusion that necessitates peeling, and enable us to integrate down in order to achieve better sensitivity on timescales longer than the 13 s integration time.

*Software:* TTCal (Eastwood 2016), WSClean (Offringa et al. 2014b).

## References

Amiri, M., et al. 2019. "Observations of fast radio bursts at frequencies down to 400 megahertz". *Nature* in press. doi:`10.1038/s41586-018-0867-7`.

Anderson, M. M., G. Hallinan, M. W. Eastwood, R. M. Monroe, H. K. Vedantham, S. Bourke, L. J. Greenhill, J. Kocz, T. J. W. Lazio, D. C. Price, F. K. Schinzel, Y. Wang, and D. P. Woody. 2018. "A Simultaneous Search for Prompt Radio

Emission Associated with the Short GRB 170112A Using the All-sky Imaging Capability of the OVRO-LWA". *ApJ* 864 (22): 1–11. doi:`10.3847/1538-4357/aad2d7`. arXiv: `1711.06665 [astro-ph.HE]`.

Baars, J. W. M., et al. 1977. "The absolute spectrum of CAS A - an accurate flux density scale and a set of secondary calibrators". *A&A* 61 (): 99–106.

Bastian, T. S. 1990. "Radio emission from flare stars". *SoPh* 130 (): 265–294. doi:`10.1007/BF00156794`.

Bastian, T. S., A. O. Benz, and D. E. Gary. 1998. "Radio Emission from Solar Flares". *ARA&A* 36:131–188. doi:`10.1146/annurev.astro.36.1.131`.

Bell, M. E., et al. 2014. "A survey for transients and variables with the Murchison Widefield Array 32-tile prototype at 154 MHz". *MNRAS* 438 (): 352–367. doi:`10.1093/mnras/stt2200`. arXiv: `1311.2989`.

Briggs, D. S. 1995. "High Fidelity Deconvolution of Moderately Resolved Sources". PhD thesis, New Mexico Institute of Mining and Technology.

Carbone, D., et al. 2016. "New methods to constrain the radio transient rate: results from a survey of four fields with LOFAR". *MNRAS* 459 (): 3161–3174. doi:`10.1093/mnras/stw539`. arXiv: `1411.7928 [astro-ph.IM]`.

Cendes, Y., et al. 2014. "LOFAR Observations of Swift J1644+57 and Implications for Short-Duration Transients". *ArXiv e-prints* (). arXiv: `1412.3986v1 [astro-ph.HE]`.

Chandra, P., and D. A. Frail. 2012. "A Radio-selected Sample of Gamma-Ray Burst Afterglows". *ApJ* 746, 156 (): 156. doi:`10.1088/0004-637X/746/2/156`. arXiv: `1110.4124`.

Cohen, A. 2008. *Estimates of the Classical Confusion Limit for the LWA*. `https://www.faculty.ece.vt.edu/swe/lwa/memo/lwa0017.pdf`.

Cordes, J. M., T. J. W. Lazio, and M. A. McLaughlin. 2004. "The dynamic radio sky". *NewAR* 48 (): 1459–1472. doi:`10.1016/j.newar.2004.09.038`. eprint: `astro-ph/0410045`.

Crane, P. 2008. *Radio-Frequency Interference from Digital Television*. `https://www.faculty.ece.vt.edu/swe/lwa/memo/lwa0133.pdf`.

Cranmer, M. D., et al. 2017. "Bifrost: A Python/C++ Framework for High-Throughput Stream Processing in Astronomy". *Journal of Astronomical Instrumentation* 6, 1750007 (): 1750007. doi:`10.1142/S2251171717500076`. arXiv: `1708.00720 [astro-ph.IM]`.

Eastwood, M. W., et al. 2018. "The Radio Sky at Meter Wavelengths: m-mode Analysis Imaging with the OVRO-LWA". *AJ* 156, 32 (): 32. doi:`10.3847/1538-3881/aac721`. arXiv: `1711.00466 [astro-ph.IM]`.

Eastwood, Michael W. 2016. *TTCal*. Version 0.3.0. doi:`10.5281/zenodo.1049160`. `https://doi.org/10.5281/zenodo.1049160`.

Ellingson, S. W., et al. 2009. "The Long Wavelength Array". *IEEE Proceedings* 97 (): 1421–1430. doi:`10.1109/JPROC.2009.2015683`.

Falcke, H., and P. Gorham. 2003. "Detecting radio emission from cosmic ray air showers and neutrinos with a digital radio telescope". *Astroparticle Physics* 19 (): 477–494. doi:`10.1016/S0927-6505(02)00245-1`. eprint: `astro-ph/0207226`.

Feng, L., et al. 2017. "A Matched Filter Technique for Slow Radio Transient Detection and First Demonstration with the Murchison Widefield Array". *AJ* 153, 98 (): 98. doi:`10.3847/1538-3881/153/3/98`. arXiv: `1701.03557` `[astro-ph.HE]`.

Greenhow, J. S. 1952. "Characteristics of Radio Echoes from Meteor Trails: III The Behaviour of the Electron Trails after Formation". *Proceedings of the Physical Society B* 65 (): 169–181. doi:`10.1088/0370-1301/65/3/301`.

Hallinan, G., et al. 2015. "Magnetospherically driven optical and radio aurorae at the end of the stellar main sequence". *Nature* 523 (): 568–571. doi:`10.1038/nature14619`. arXiv: `1507.08739 [astro-ph.SR]`.

Hankins, T. H., et al. 2003. "Nanosecond radio bursts from strong plasma turbulence in the Crab pulsar". *Nature* 422 (): 141–143. doi:`10.1038/nature01477`.

Hyman, S. D., et al. 2007. "A Faint, Steep-Spectrum Burst from the Radio Transient GCRT J1745-3009". *ApJl* 660 (): L121–L124. doi:`10.1086/518245`. eprint: `astro-ph/0701098`.

Hyman, S. D., et al. 2005. "A powerful bursting radio source towards the Galactic Centre". *Nature* 434 (): 50–52. doi:`10.1038/nature03400`. eprint: `astro-ph/0503052`.

Hyman, S. D., et al. 2009. "GCRT J1742-3001: A New Radio Transient Toward the Galactic Center". *ApJ* 696 (): 280–286. doi:`10.1088/0004-637X/696/1/280`. arXiv: `0811.1972`.

Hyman, S. D., et al. 2002. "Low-Frequency Radio Transients in the Galactic Center". *AJ* 123 (): 1497–1501. doi:`10.1086/338905`. eprint: `astro-ph/0110151`.

Intema, H. T., et al. 2017. "The GMRT 150 MHz all-sky radio survey. First alternative data release TGSS ADR1". *A&A* 598, A78 (): A78. doi:`10.1051/0004-6361/201628536`. arXiv: `1603.04368`.

Jaeger, T. R., et al. 2012. "Discovery of a Meter-wavelength Radio Transient in the SWIRE Deep Field: 1046+59". *AJ* 143, 96 (): 96. doi:`10.1088/0004-6256/143/4/96`. arXiv: `1201.6290 [astro-ph.HE]`.

Kao, M. M., et al. 2016. "Auroral Radio Emission from Late L and T Dwarfs: A New Constraint on Dynamo Theory in the Substellar Regime". *ApJ* 818, 24 (): 24. doi:`10.3847/0004-637X/818/1/24`. arXiv: `1511.03661 [astro-ph.SR]`.

Kao, M. M., et al. 2018. "The Strongest Magnetic Fields on the Coolest Brown Dwarfs". *ApJs* 237, 25 (): 25. doi:`10.3847/1538-4365/aac2d5`. arXiv: `1808.02485 [astro-ph.SR]`.

Kaplan, D. L., et al. 2015. "A Deep Search for Prompt Radio Emission from the Short GRB 150424A with the Murchison Widefield Array". *ApJL* 814, L25 (): L25. doi:`10.1088/2041-8205/814/2/L25`. arXiv: `1511.03656 [astro-ph.HE]`.

Kocz, J., et al. 2015. "Digital Signal Processing Using Stream High Performance Computing: A 512-Input Broadband Correlator for Radio Astronomy". *Journal of Astronomical Instrumentation* 4, 1550003 (): 1550003. doi:`10.1142/S2251171715500038`. arXiv: `1411.3751 [astro-ph.IM]`.

Kramer, M., et al. 1999. "The Characteristics of Millisecond Pulsar Emission. III. From Low to High Frequencies". *ApJ* 526 (): 957–975. doi:`10.1086/308042`. eprint: `astro-ph/9906442`.

Lane, W. M., et al. 2014. "The Very Large Array Low-frequency Sky Survey Redux (VLSSr)". *MNRAS* 440 (): 327–338. doi:`10.1093/mnras/stu256`. arXiv: `1404.0694 [astro-ph.IM]`.

Lazio, T. J. W., et al. 2010. "Surveying the Dynamic Radio Sky with the Long Wavelength Demonstrator Array". *AJ* 140 (): 1995–2006. doi:`10.1088/0004-6256/140/6/1995`. arXiv: `1010.5893 [astro-ph.IM]`.

Lazio, T. J., W., et al. 2004. "The Radiometric Bode's Law and Extrasolar Planets". *ApJ* 612 (): 511–518. doi:`10.1086/422449`.

Lorimer, D. R., et al. 1995. "Multifrequency flux density measurements of 280 pulsars". *MNRAS* 273 (): 411–421. doi:`10.1093/mnras/273.2.411`.

Lynch, C. R., et al. 2017. "154 MHz Detection of Faint, Polarized Flares from UV Ceti". *ApJl* 836, L30 (): L30. doi:`10.3847/2041-8213/aa5ffd`. arXiv: `1702.03030 [astro-ph.SR]`.

Macquart, J. P., et al. 2015. "Fast Transients at Cosmological Distances with the SKA". *Advancing Astrophysics with the Square Kilometre Array (AASKA14)*, 55 (): 55. arXiv: `1501.07535 [astro-ph.HE]`.

McMullin, J. P., et al. 2007. "CASA Architecture and Applications". In *Astronomical Data Analysis Software and Systems XVI*, ed. by R. A. Shaw, F. Hill, and D. J. Bell, 376:127. Astronomical Society of the Pacific Conference Series.

Metzger, B. D., P. K. G. Williams, and E. Berger. 2015. "Extragalactic Synchrotron Transients in the Era of Wide-field Radio Surveys. I. Detection Rates and Light Curve Characteristics". *ApJ* 806, 224 (): 224. doi:`10.1088/0004-637X/806/2/224`. arXiv: `1502.01350 [astro-ph.HE]`.

Millman, P. M., D. W. R. McKinley, and M. S. Burland. 1948. "Combined Radar, Photographic and Visual Observations of the Perseid Meteor Shower of 1947". *Nature* 161 (): 278–280. doi:`10.1038/161278b0`.

Mooley, K. P., et al. 2016. "The Caltech-NRAO Stripe 82 Survey (CNSS). I. The Pilot Radio Transient Survey In 50 deg$^2$". *ApJ* 818, 105 (): 105. doi:`10.3847/0004-637X/818/2/105`. arXiv: `1601.01693 [astro-ph.HE]`.

Murphy, T., et al. 2017. "A search for long-time-scale, low-frequency radio transients". *MNRAS* 466 (): 1944–1953. doi:`10.1093/mnras/stw3087`. arXiv: `1611.08354`.

Narayan, R. 1992. "The Physics of Pulsar Scintillation". *Philosophical Transactions of the Royal Society of London Series A* 341 (): 151–165. doi:`10.1098/rsta.1992.0090`.

Obenberger, K. S., et al. 2015a. "Dynamic radio spectra from two fireballs". *Journal of Geophysical Research (Space Physics)* 120 (): 9916–9928. doi:`10.1002/2015JA021229`. arXiv: `1510.04147 [astro-ph.EP]`.

Obenberger, K. S., et al. 2014. "Limits on Gamma-Ray Burst Prompt Radio Emission Using the LWA1". *ApJ* 785, 27 (): 27. doi:`10.1088/0004-637X/785/1/27`. arXiv: `1403.3674 [astro-ph.HE]`.

Obenberger, K. S., et al. 2015b. "Monitoring the Sky with the Prototype All-Sky Imager on the LWA1". *Journal of Astronomical Instrumentation* 4, 1550004-1104 (): 1550004–1104. doi:`10.1142/S225117171550004X`. arXiv: `1503.05150 [astro-ph.IM]`.

Obenberger, K. S., et al. 2016. "Rates, flux densities, and spectral indices of meteor radio afterglows". *Journal of Geophysical Research (Space Physics)* 121 (): 6808–6817. doi:`10.1002/2016JA022606`. arXiv: `1607.03002 [astro-ph.EP]`.

Offringa, A. R., et al. 2014a. "WSCLEAN: an implementation of a fast, generic wide-field imager for radio astronomy". *MNRAS* 444 (): 606–619. doi:`10.1093/mnras/stu1368`. arXiv: `1407.1943 [astro-ph.IM]`.

– . 2014b. *WSClean: Widefield interferometric imager*. Astrophysics Source Code Library. ascl: `1408.023`.

Perley, R. A., and B. J. Butler. 2017. "An Accurate Flux Density Scale from 50 MHz to 50 GHz". *ApJs* 230, 7 (): 7. doi:`10.3847/1538-4365/aa6df9`. arXiv: `1609.05940 [astro-ph.IM]`.

Pietka, M., R. P. Fender, and E. F. Keane. 2015. "The variability time-scales and brightness temperatures of radio flares from stars to supermassive black holes". *MNRAS* 446 (): 3687–3696. doi:`10.1093/mnras/stu2335`. arXiv: `1411.1067 [astro-ph.HE]`.

Polisensky, E., et al. 2016. "Exploring the Transient Radio Sky with VLITE: Early Results". *ApJ* 832, 60 (): 60. doi:`10.3847/0004-637X/832/1/60`. arXiv: `1604.00667 [astro-ph.HE]`.

Price, D. C., et al. 2018. "Design and characterization of the Large-aperture Experiment to Detect the Dark Age (LEDA) radiometer systems". *MNRAS* 478 (): 4193–4213. doi:`10.1093/mnras/sty1244`. arXiv: `1709.09313 [astro-ph.IM]`.

Ravi, V. 2019. "The observed properties of fast radio bursts". *MNRAS* 482 (): 1966–1978. doi:`10.1093/mnras/sty1551`. arXiv: `1710.08026 [astro-ph.HE]`.

Rowlinson, A., et al. 2016. "Limits on Fast Radio Bursts and other transient sources at 182 MHz using the Murchison Widefield Array". *MNRAS* 458 (): 3506–3522. doi:`10.1093/mnras/stw451`. arXiv: `1602.07544 [astro-ph.HE]`.

Soderberg, A. M., et al. 2010. "Radio and X-ray Observations of the Type Ic SN 2007gr Reveal an Ordinary, Non-relativistic Explosion". *ApJ* 725 (): 922–930. doi:`10.1088/0004-637X/725/1/922`. arXiv: `1005.1932`.

Spangler, S. R., and T. J. Moffett. 1976. "Simultaneous radio and optical observations of UV Ceti-type flare stars". *ApJ* 203 (): 497–508. doi:`10.1086/154105`.

Stewart, A. J., et al. 2016. "LOFAR MSSS: detection of a low-frequency radio transient in 400 h of monitoring of the North Celestial Pole". *MNRAS* 456 (): 2321–2342. doi:`10.1093/mnras/stv2797`. arXiv: `1512.00014 [astro-ph.HE]`.

Tingay, S. J., et al. 2013. "The Murchison Widefield Array: The Square Kilometre Array Precursor at Low Radio Frequencies". *PASA* 30, e007 (): e007. doi:`10.1017/pasa.2012.007`. arXiv: `1206.6945 [astro-ph.IM]`.

van Diepen, G. N. J. 2015. "Casacore Table Data System and its use in the MeasurementSet". *Astronomy and Computing* 12 (): 174–180. doi:`10.1016/j.ascom.2015.06.002`.

van Haarlem, M. P., et al. 2013. "LOFAR: The LOw-Frequency ARray". *A&A* 556, A2 (): A2. doi:`10.1051/0004-6361/201220873`. arXiv: `1305.3550 [astro-ph.IM]`.

Villadsen, J., and G. Hallinan. 2018. "Ultra-Wideband Detection of 22 Coherent Radio Bursts on M Dwarfs". *ApJ* submitted (). arXiv: `1810.00855 [astro-ph.SR]`.

Zarka, P. 1998. "Auroral radio emissions at the outer planets: Observations and theories". *J. Geophys. Res.* 103 (): 20159–20194. doi:`10.1029/98JE01323`.

Zauderer, B. A., et al. 2011. "Birth of a relativistic outflow in the unusual $\gamma$-ray transient Swift J164449.3+573451". *Nature* 476 (): 425–428. doi:`10.1038/nature10366`. arXiv: `1106.3568 [astro-ph.HE]`.
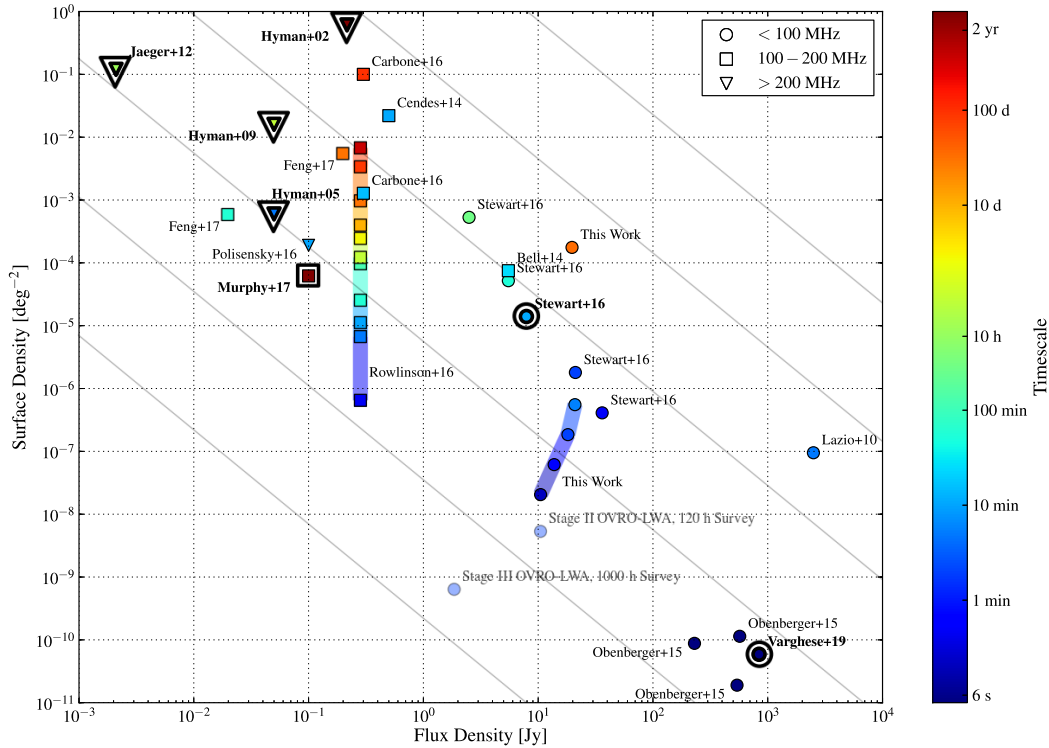
Figure 4.6: Radio transient phase space plot, showing the transient surface density as a function of flux density limits and timescales probed, for this and previous blind transient surveys (see Table 4.1 for an overview of all surveys included in this plot). The surface density limits for each survey are colored according to the timescale probed, covering timescales as short as 5 s (Obenberger et al. 2015b) to as long as 3 years (Murphy et al. 2017). This is a critical parameter, as surveys providing surface density limits at comparable sensitivities may be probing very different timescales and therefore very different regions of phase space and potential transient populations. The same is true of frequency. Surveys conducted below 100 MHz are marked with a circle, those between 100-200 MHz are marked with a square, and those between 200-350 MHz with a triangle. All points on the plot denote upper limits with the exception of the seven transient detections that are marked in bold. The solid gray lines denote hypothetical transient populations under the generic assumption that the population is a standard candle in a Euclidean universe, i.e., $N(> S) \propto S^{-\gamma}$ where N is the number density of sources, S is the flux density, and $\gamma = 3/2$. The limits (or detections) placed by transient surveys are necessarily a combination of sensitivity and total area surveyed, and it is often the case that tradeoffs must be made to improve one of these factors over the other. The optimal combination of these two parameters (and therefore how deep or wide a survey probes) depends on the goals of the survey or the source population(s) it is targeting. Also shown in this figure are the limits we expect to achieve with the OVRO-LWA in future surveys, first with the 120-hour transient survey with the stage II OVRO-LWA, and finally with the completed stage III OVRO-LWA utilizing 1000 hours of data capable of achieving 150 mJy snapshot sensitivity.
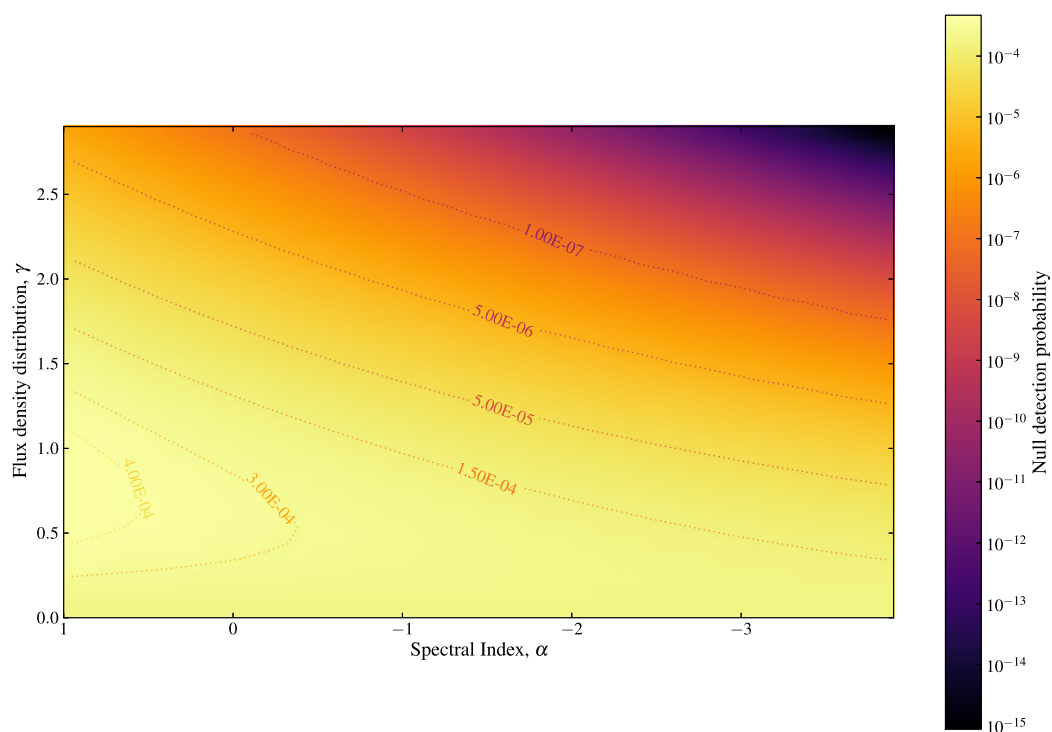
Figure 4.7: Probability of a null detection in the OVRO-LWA 31-hour survey of the potential population indicated by the event detected by Stewart et al. 2016, given their transient rate of $3.9 \times 10^{-4} \, \mathrm{d}^{-1} \, \mathrm{deg}^{-2}$, as a function of the power-law luminosity distribution $\gamma$ and source spectral index $\alpha$, using Equation 4.4.
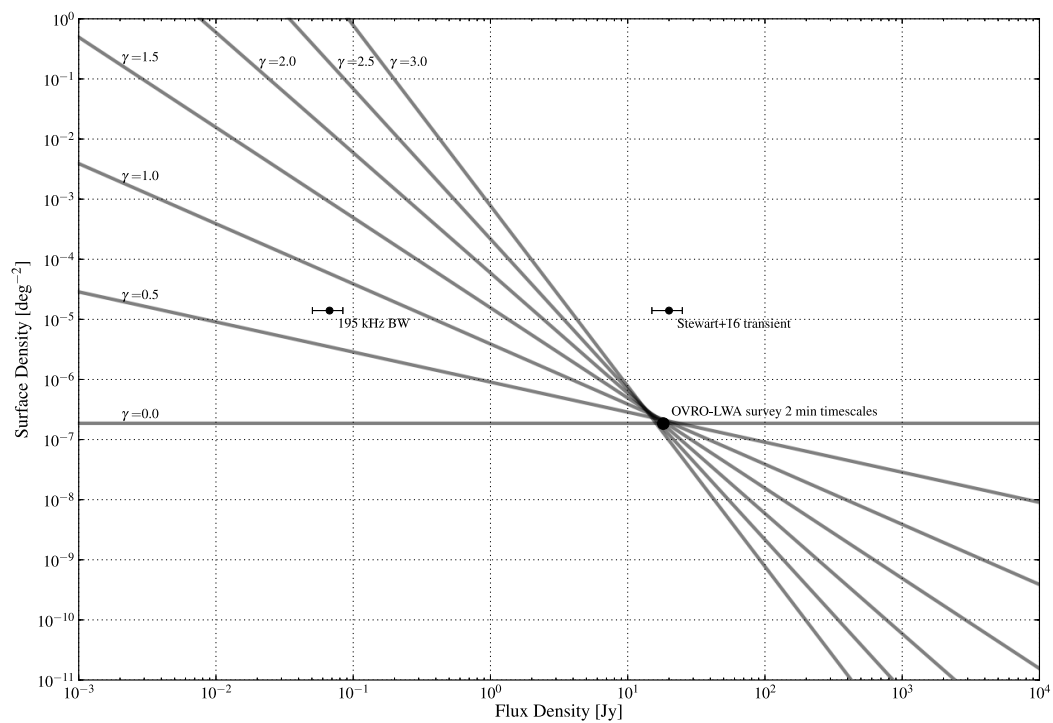
Figure 4.8: Surface density limits from the OVRO-LWA transient survey at 2 min timescales, for a range of power-law luminosity distribution $\gamma$. For reference, the surface density for the transient detected by Stewart et al. 2016, at a reported flux density of between 15–25 Jy, and at the flux density that same event would appear at in our survey for a maximum intrinsic bandwidth of 195 kHz (the bandwidth of the survey by Stewart et al. 2016).

# MONITORING 4000 STELLAR SYSTEMS SIMULTANEOUSLY TO SEARCH FOR STELLAR AND PLANETARY RADIO EMISSIONS WITH THE OVRO-LWA

## Abstract

Recent results from our own solar system demonstrate the importance of not only stellar magnetic activity, but also the critical importance of planetary magnetic field strength, in determining the conditions for planetary habitability. The detection of planetary radio emission from objects beyond the solar system will provide the first direct measurements of exoplanetary magnetic field strengths, as well as provide insight on the degree to which those magnetospheres can shield exoplanet atmospheres against the surrounding space weather environment of their host star. Despite observations spanning nearly 35 years, searches for direct detection of exoplanetary radio emission have resulted in non-detections. Stellar Type II radio bursts indicative of coronal mass ejections, and a sign of the high energy particle environment for potential planets also remain elusive. However, these previous searches were limited by a number of factors, including observations above ~100 MHz, and the targeting of single systems at a time for relatively short-duration observations that would be insensitive to rare brightening events associated with coronal mass ejections. These rare brightening events are similar to what is observed from Earth's auroral radio emission, which can increase by orders of magnitude for factors of a few increase in solar wind speed. I present here the preliminary results of a search for stellar and planetary radio emission using 31 hr of data from a sample of nearly 4000 stellar systems out to 25 pc, with the OVRO-LWA. This is by far the largest survey at radio frequencies for either stellar bursts or exoplanetary radio emission, and required the development of polarization calibration techniques for the OVRO-LWA in order to achieve sensitivities close to the thermal limit in Stokes V image data.

## 5.1 Introduction

Our growing understanding of the history of the solar system demonstrates the importance of stellar magnetic activity, as well as the critical importance of the presence and strength of planetary magnetic fields, in redefining planetary habitability. The young Sun was significantly more magnetically active than in the present

day, powered in part by its faster rotation rate (Ribas et al. 2005). This manifested in a denser and faster steady-state solar wind, as well as a higher occurrence rate of flaring and coronal mass ejection (CME) events (Grießmeier et al. 2005). The vastly different fates of Earth and Mars' atmospheres under these conditions in the early solar system are attributable to the respective strengths of their magnetic fields, and the inability, in the case of Mars' magnetosphere, to shield against atmospheric escape during CME impacts (Jakosky et al. 2015). The presence and strength of Earth's magnetic field was key in shielding our atmosphere from solar magnetic activity, and therefore in preserving its habitability. This interaction between the solar wind and planetary magnetosphere has an observable in the form of planetary auroral emission.

**Exoplanet Radio Emission**

All the magnetized planets in the solar system exhibit auroral emission in some form (Zarka 1998), which can span from low radio frequencies up to IR through UV and X-ray emission. Auroral radio emission affords the best contrast between stellar and planetary emission – Jupiter's auroral emission, for example, can outshine the quiescent Sun at decameter wavelengths and can have comparable intensity to solar radio bursts (Zarka 1998). Therefore, auroral decametric emission (DAM), if it can be detected from exoplanets, offers a unique opportunity for the direct detection of exoplanets and the characterization of their extrasolar space weather environments. DAM due to magnetic storm-driven aurorae would provide a direct measure of exoplanetary magnetic field strength, and provide insight into the ability of the magnetosphere to shield the atmosphere from its space weather environs. By measuring planetary and stellar magnetic activity for nearby stellar systems over a range of mass and age, we can begin to form a more complete picture of the relationship between planetary magnetospheres and stellar activity, and the impact of both on exoplanetary atmospheres and the implications for habitability.

Beyond the solar system, similar auroral emission has been detected in ultracool dwarfs (UCDs) across a range of spectral types from M9 to T6 (e.g., Hallinan et al. 2007; Berger et al. 2009; Route and Wolszczan 2012; Hallinan et al. 2015; Kao et al. 2016). As in the case of planets, this detected radio emission is a tracer for magnetic activity and magnetic fields on UCDs. The auroral radio emission is powered by the electron cyclotron maser instability (ECMI), which produces coherent emission at the local cyclotron frequency $\nu_c$ (MHz) $= 2.8\,B$ (G). Thus there is a strict maximum emission frequency which corresponds to the maximum

magnetic field strength. The GHz-detections of radio UCDs indicates kG magnetic field strengths. In order to detect *exoplanetary* radio emissions, we must push down into the tens of MHz regime, where field strengths are of the order 10 G (extrapolating from Jupiter).

Previous attempts at detecting planetary radio emission by targeting known hot Jupiter systems have resulted in non-detections (e.g., Lazio and Farrell 2007; Lecavelier Des Etangs et al. 2009; Lazio et al. 2010b; Hallinan et al. 2013; Murphy et al. 2015; Bower et al. 2016). There are several reasons why these surveys failed to detect exoplanetary radio emission. First, observations targeting known hot Jupiter systems were largely restricted to frequencies > 100 MHz. While estimates of planetary magnetic field strengths remain largely uncertain, models constructed using parameters (either measured or extrapolated from Jupiter) such as planetary radius, internal structure and composition, and rotation rate, combined with host star CME and stellar wind models, can be used to estimate the maximum frequency and strength of emission. Grießmeier, Zarka, and Spreeuw 2007 find that for known extrasolar planets, $\nu_c < 200$ MHz, and for those planets with $\nu_c > 70$ MHz, the radio flux is negligible.

Second, the emission is highly beamed at nearly 90 degrees from the magnetic field at the source location, which results in the emission being modulated by the planetary rotation period (for Jupiter, $\Omega \sim 1.6$ sr; Zarka 1998). This means observations must be continuous over the entire planetary rotation period to verify the presence of auroral radio emission. Indeed, a subset of systems might never be detectable due to unfavorable viewing angles. Previous observations often targeted only one or two known hot Jupiter systems at a time, and for only a fraction of their estimated rotation periods.

Third, the strength of emission is strongly dependent on incident stellar wind flux and the amount of power deposited into the planetary magnetosphere (Gallagher and Dangelo 1981; Gurnett et al. 2002). Predictions for the expected radio power for known exoplanets can be made using the empirically derived radiometric Bode's law, by extrapolating up from solar system objects into the regime of exoplanets, particularly the close-in hot Jupiter population that experiences a much larger incident solar wind power (Lazio et al. 2004). In addition, predictions for the expected radio power using more detailed models incorporating predicted properties of the planetary magnetosphere as well as varying host stellar wind conditions predict flux densities as high as 100s of mJy (Grießmeier, Zarka, and Spreeuw 2007). Addi-

tional substantial increase in flux is expected for CME-driven events – this is seen in our own solar system, where the Earth's radio flux can increase by three orders of magnitude for factors of a few increase in solar wind speed (Gallagher and Dangelo 1981). CME-driven events are rare, but could potentially be more frequent for 1) close-in planets, 2) planets orbiting young, more magnetically active stars, and 3) planets around M dwarfs, which are extremely magnetically active, producing more frequent and energetic flares than the Sun, and which remain active over a longer lifetime (Osten and Wolk 2015). In order to be sensitive to these rare brightening events, we need to monitor thousands of systems over an extended period, rather than targeting single objects for a few hours at a time. Thus, wide-field, long-duration surveys at low frequencies (< 100 MHz) with the capability of monitoring thousands of objects simultaneously are needed to detect exoplanetary auroral emission. However, understanding the degree to which CME energies and occurrence rates extrapolate with stellar flare energies and frequencies remains an open question and motivates monitoring for stellar radio bursts as well.

**Stellar Type II-like Bursts**

Wide-field, long-duration surveys at low frequencies are also critical for the detection and characterization of stellar flares and CMEs from nearby active stars. Solar radio bursts exhibit a wide range of characteristics and emission mechanisms, all of which provide information on the conditions (e.g., plasma densities and atmospheric scale heights, magnetic field strengths and configurations, particle acceleration mechanisms) in the solar corona (Bastian, Benz, and Gary 1998). Systematic detection of similar radio bursts on other stars will allow us to probe these conditions and degree of magnetic activity for objects over a range of spectral type, as well as place exoplanets and any potential auroral emission in a more complete context of habitability indicators. Stellar radio bursts have been detected and well-studied for a sample of nearby, magnetically active M dwarfs; these studies have indicated that M dwarf bursts can be orders of magnitude more luminous than the brightest solar bursts (e.g., the radio burst detected from M dwarf Wolf 424 by (Spangler and Moffett 1976), which peaked above 5 Jy at frequencies below 200 MHz). However, previous surveys of nearby active M dwarfs did not have sufficient spectral information to further classify radio bursts, and as a result there has never been a definitive detection of a stellar CME as inferred via a Type II-like burst. Type II bursts are powered by CMEs propagating through the corona, accelerating electrons at the shock front of the ejected plasma. The resulting plasma emission traces the

movement of the shock front through the corona and out through the interplanetary medium, sweeping down in frequency as it propagates out to regions of lower density ($v_p$ (kHz) $\sim 9\sqrt{n_e\,(\text{cm}^{-3})}$). Solar Type II bursts typically occur at low frequencies, in regions of the corona where the plasma frequency $v_p < 100\,\text{MHz}$, corresponding to heights in the corona where the CME velocity can exceed the local Alfvén speed, thereby creating the conditions necessary for shock formation (Liu et al. 2009). The bursts drift in frequency alongside the shock speed, and generally produces emission in two bands, at the fundamental and first harmonic of the plasma frequency (Wild, Murray, and Rowe 1954). Wide band, low frequency searches are optimal for detecting and characterizing radio bursts from nearby active stars. And, as in the case for exoplanetary auroral emission, a wide-field search that enables simultaneous monitoring of thousands of systems, rather than the targeting of individual objects, is needed to increase the chances of detecting rare but extremely bright events. See Table 5.1 for a list of previous surveys targeting exoplanetary radio emission.

**Flare–CME Scaling Relations**

Type II radio bursts have never been directly observed from other stars, but are predicted to occur based on their association with solar CMEs. Detecting these bursts from other stars would be a direct indicator of the release of a CME – solar CMEs are not always accompanied by a Type II burst, but every Type II burst coincides with a CME (Gopalswamy et al. 2001). To date, inferences about the magnetic activity and plasma environment of stars have come from observations of stellar flares (primarily in X-rays) and the application and extrapolation of solar flare–CME relations to these objects. Aarnio et al. 2011 established an empirical relation between flare flux (as measured in X-rays) and CME mass that spans 3 orders of magnitude. Osten and Wolk 2015 use energy equipartition between the bolometric radiated flare energy and the kinetic energy of the ejected mass to predict transient mass-loss associated with CMEs from solar flares. However, the connection between solar flares and CMEs remains an empirical one – while the underlying mechanism for generating the two phenomena is likely related to magnetic eruptions and reconnection events in the corona, CMEs are not generated as a result of flares, and vice versa (Gosling 1993). In addition, it's unclear how far the extrapolation from solar trends extends in flare flux and across different stellar spectral types, ages, rotation, and levels of magnetic activity. The transient mass loss rate from the sun, extrapolated up according to more energetic and frequent flares on magnetically active stars implies a transient mass loss rate that is approaching

steady state, with orders of magnitude more mass loss than what is seen in the Sun.

Understanding how transient mass loss scales with magnetic activity in the form of flares is critical in the context of habitability – the majority of stars are M dwarfs, which are also the most likely hosts of habitable zone rocky planets (Dressing and Charbonneau 2015). However M dwarfs are also more likely to create a long-lived, hostile circumstellar environment, given the age-rotation-activity relation (West et al. 2008). Increased magnetic activity, including higher energy radiation flux and increased transient mass loss events means the potential for the erosion of planetary atmospheres and conditions unlikely to foster habitability (see, e.g., Khodachenko et al. 2007; Lammer et al. 2012; Ribas et al. 2016; Vidotto et al. 2013). However, whether higher levels of magnetic activity correspond to more frequent and extreme transient mass loss events is an open question, and behavior indicating otherwise is seen even in the Sun, whereby the presence of strong magnetic fields overlying solar active regions can slow down or even suppress the release of CMEs, indicating that the presence of strong, dipolar magnetic fields in M dwarfs might similarly suppress CMEs (Sun et al. 2015; Alvarado-Gómez et al. 2018). In addition, extrapolation of the flare–CME relation for the Sun to more active stars implies an unsustainable mass loss rate that is up to four orders of magnitude higher than that of the Sun (Drake et al. 2013).

Previous attempts to search for stellar CMEs in the optical (Leitzinger et al. 2014) and radio (Crosley et al. 2016; Crosley and Osten 2018; Villadsen and Hallinan 2019) have yielded no evidence of CMEs, however there have been multiple detections of coherent radio bursts from active stars indicative of auroral processes similar to what are seen on UCDs (Lynch et al. 2017; Crosley and Osten 2018; Villadsen and Hallinan 2019). A systematic search of not only active stars, but of stellar systems spanning a range of spectral types, ages, and magnetic activity levels are needed to understand transient mass loss behavior across a wide range of host stars, as well as establish a sample size large enough to catch these potentially rare events. Radio detections of both stellar CMEs and planetary auroral emission have the potential to inform habitability searches at other wavelengths – particularly space missions like HabEx that will be searching for atmospheric signatures in exoplanets as a signpost for habitability.

Table 5.1: Radio surveys targeting exoplanetary radio emission.

| (1) Reference | (2) Instrument | (3) Frequency (MHz) | (4) Sensitivity (mJy) | (5) Number of targets | (6) Observation duration (h) |
|---|---|---|---|---|---|
| This Work | OVRO-LWA | 56 | < 1350 | 3820 | 62000 |
| Lynch et al. 2018 | MWA | 200 | < 4.5 – 45.3 | 18 | GLEAM Stokes V |
|  | GMRT | 150 |  | 1 | 24 |
| Lenc et al. 2018 | MWA | 200 | < 9 | 1506 | GLEAM Stokes V |
| O'Gorman et al. 2018 | LOFAR | 150 | < 0.57 – 0.98 | 3 | 20.5 |
| Lynch et al. 2017 | MWA | 154 | < 4 – 235 | 675[a] | 16.7 |
| Bower et al. 2016 | VLA / VLBA | 6000 | 0.919[b], < 0.066 – 0.150 | 1 | 0.2 |
| Murphy et al. 2015 | MWA | 154 | < 3.4 – 112.5 | 17 | 20.5 (MWATS) |
| Sirothia et al. 2014 | GMRT | 150 | < 8.7 – 136 | 175 | TGSS |
| Lecavelier des Etangs et al. 2013 | GMRT | 150 | 3.87[c] | 1 | 9.5 |
| Hallinan et al. 2013 | GMRT | 150 | < 1.2 | 1 | 40 |
| Stroe, Snellen, and Röttgering 2012 | WSRT | 1700 | < 0.13 | 1 | 12 |
| Lecavelier Des Etangs et al. 2011 | GMRT | 150 | < 2.1 – 3.6 | 2 | 18 |
| Lazio et al. 2010a | VLA | 325 | < 1.7 | 1 | 8 |
|  |  | 1425 | < 0.048 |  | 8 |
| Lecavelier Des Etangs et al. 2009 | GMRT | 244 | < 2 | 1 | 7.7 |
|  |  | 614 | < 0.160 |  |  |
| Smith et al. 2009 | GBT | 327 | < 81 | 1 | 5.5 |
| George and Stevens 2007 | GMRT | 150 | < 9.4 – 18.6 | 2 | 8.3 |
| Lazio et al. 2004 | VLA | 74 | < 262 – 390 | 5 | VLSS |
| Bastian, Dulk, and Leblanc 2000 | VLA | 74 / 330 | < 150 | 8 | 48.6 |
|  |  | 1465 | < 0.06 – 0.21 |  |  |
| Winglee, Dulk, and Bastian 1986 | VLA | 333 | < 30 | 6 | 21 |
|  |  | 1400 | < 0.3 |  |  |

[a] Lynch et al. 2017 are specifically targeting stars in the Upper Scorpius Association (distance of 145 pc) as a young (10–20 Myr) region with recent star star formation, and therefore a younger population of exoplanets.

[b] Bower et al. 2016 report the detection of variable 6 GHz radio emission of the T Tauri star V830 Tau, which has a known hot Jupiter companion. Given the frequency of the detection, spectral index of the emission, and lack of circular polarization, the authors associate the emission with the host star, rather than the hot Jupiter companion.

[c] Lecavelier des Etangs et al. 2013 report the tentative ($3\sigma$) detection of radio emission with light curve behavior indicative of a secondary eclipse from the planet HAT-P-11b. Repeat observations at this location yielded non-detections.

NOTE – All surveys to-date targeting (known or likely) exoplanets for radio emission. The majority of the surveys listed here observed the locations of a small (~ few objects, usually hot Jupiters) sample, as reflected in column (5). For surveys with observations of > 15 objects, sensitivity limits were derived from survey data, and were therefore restricted to single snapshots per field – see column (6). All survey upper limits are scaled to $3\sigma$, if reported at another sensitivity threshold.

(6) Number of hours of observations across all targets ($\Delta t_{obs,\ obj} \times N_{obj}$). For searches that were conducted using single snapshots from survey fields, the survey name is listed instead.

## 5.2 Observations

### 31-hour Survey

To search for stellar and planetary radio emission, we used 31 hours of OVRO-LWA observations, which in addition to being used for the first extrasolar space weather survey with the OVRO-LWA, were also utilized for placing limits on coherent low-frequency radio emission associated with compact object mergers (Anderson et al. 2018) and for conducting the most sensitive blind transient survey at low-frequencies to-date (see Chapter 4). Observations were conducted for 3 hours on 2017 January 12 between 01:02– 04:02 UTC and for 28 hours from 2017 February 17 12:00 – 2017 February 18 16:00 UTC. This near-continuous set of 31 hours of observations means that we can continuously monitor all target systems while they are above the horizon. The approximately ~20,000 deg$^2$ field-of-view of the OVRO-LWA makes possible the simultaneous targeting of thousands of systems. The 10′ resolution sufficient for localizing any transient radio emission indicative of stellar Type II bursts or exoplanetary auroral emission to known stellar systems, given the surface density of such systems out to 25 pc, the most realistic distance to which any extrasolar space weather-related emissions would be detectable.

The gain stability of the OVRO-LWA antennas means calibration can be performed on the timescale of once per 24 hours. Calibration was performed with a single snapshot observation (13 s) on 2017 January 11 20:26 UTC and another on 2017 February 17 18:02 UTC, with both calibration integrations taken when Cygnus A was at its highest elevation. Calibration was performed using a simplified 2 point source sky-model of Cygnus A and Cassiopeia A, the two brightest sources in the low-frequency sky, with short baselines ($< 15\lambda$) flagged to mitigate the effects of the diffuse galactic synchrotron emission, using the flux and spectral indices reported by Baars et al. 1977 and Perley and Butler 2017, respectively. Using this sky-model, the complex (amplitude and phase) antenna gains are determined on a per-channel basis using the Common Astronomy Software Applications (CASA; McMullin et al. 2007) `bandpass` task. The visibility data are flagged for ill-behaved antennas (due primarily to power issues with the antenna or significant amounts of cross-talk in the analog signal path), baselines (due primarily to cross-talk of adjacent lines in the analog signal path), and channels (usually due to RFI). In total, approximately 40% of visibilities are flagged per integration, the vast majority of which are due to the large number of antenna flags (50 out of 256).

Additional direction-dependent (DD) calibration and source subtraction (peeling)

is performed for every integration, with DD gain solutions derived without short baselines ($< 10\lambda$) to mitigate the the effect of diffuse galactic synchrotron emission. The DD gains are derived in the directions of Cyg A and Cas A, as well as for a generic near-field source that is used to subtract the effect of mutual coupling in the visibilities. Peeling is performed using the `TTCal` calibration software package developed for the OVRO-LWA (Eastwood 2016). Imaging and deconvolution are done with `WSClean` (Offringa et al. 2014), with the full FOV imaged across 4096 × 4096 pixels, using a pixel scale of 1.875′ and a robust visibility weighting of 0 (Briggs 1995).

A single snapshot total intensity (Stokes I) image from the OVRO-LWA contains thousands of point sources, diffuse emission from the galaxy, and is confusion-limited at 13 s. A major advantage in conducting a survey for extrasolar space weather is utilizing circular polarization (Stokes V) maps – in addition to being able to verify and more fully characterize any potential emission, which in the case of both Type II radio bursts and auroral radio emission, should be fractionally or as much as 100% circularly polarized, the radio sky is largely empty of quiescent circularly polarized emission. The effect is to remove the proverbial haystack from the needle – Stokes V images are empty of emission, and are able to achieve sensitivities much closer to the thermal noise limit because of the lack of quiescent point sources to create confusion noise. Searches for transient radio emission in Stokes V space are therefore both easier and more sensitive. However, sufficiently calibrating the cross-hand (XY) phase of the array is a significant technical challenge – we address the source of these challenges and techniques for mitigating them in the following section.

**Polarization Calibration for Stokes V Images**

Traditional polarization calibration techniques rely on the measurement of a source of known polarization, within a narrow region at the center of the antenna field-of-view, where the instrumental polarization is well-behaved. This is necessary for accurately calibrating the relative phase relationship between the gains of the orthogonally polarized receivers (e.g., between the array of X dipoles and the array of Y dipoles; Sault, Hamaker, and Bregman 1996). This is not achievable with the OVRO-LWA – a wide field-of-view encompassing the full dipole primary beam means that (1) instrumental polarization in the beam increases away from zenith (with a complicated dependence on azimuth and elevation); (2) you cannot isolate the flux of a single source of known polarization from the rest of the (much brighter)

sky; and (3) there is not a source with sufficient polarized flux with which to calibrate.

Techniques exist to mitigate these effects, including that used for the Murchison Widefield Array (MWA; Tingay et al. 2013) by Lenc et al. 2017 who use galactic diffuse emission in Stokes U and V to solve for the X-Y phase of the array, using the fact that there should be no circularly polarized diffuse emission and that the linearly polarized diffuse emission has high SNR. Further corrections for leakage in the Stokes V images are made by again utilizing the assumption that the Stokes V sky should be empty of emission, and fitting a surface across the beam using the measured Stokes V flux of point sources, and subtracting this flux from the Stokes V map (Lenc et al. 2018). This empirically derived fit for the leakage in Stokes V does not correct for phase errors in the Stokes V maps, which will affect the amount of flux present for any true sources of circularly polarized emission. And the utilization of linearly polarized diffuse emission as calibration source for the X-Y phase of the array cannot account for the varying leakage across the beam nor correct for the the effects of cross-talk between adjacent dipoles and lines in the signal path coupling emission from the X array into the Y array, and vice versa.

For the OVRO-LWA, we utilize the highly polarized dipole beam to calibrate the X-Y phase of the array using the instrumental polarization imparted to the 2 brightest sources in the sky, Cas A and Cyg A. This is a novel technique that incorporates a simulated LWA-dipole beam model that allows us to perform polarization calibration with intrinsically unpolarized sources, and then apply a beam-wide complex gain correction that takes into account the DD effects of the polarized primary beam. Using a Method of Moments model for an ideal LWA dipole with ground screen (D. Woody, internal memo), a complex voltage pattern is generated at a grid of azimuth, elevation, and frequency points for a single dipole. From this, a full crossed-dipole primary beam pattern can be generated for all four Stokes parameters as a function of frequency. We can use the simple 2-point source sky model from before, this time imparting an instrumental polarization to both sources according to the beam model. This polarized source model can be used to solve for the complex gains, as well as the correct relative phase between the X and Y arrays; an additional DD correction is made in the final images by applying the beam in image space as a DD Jones matrix. Figure 5.1 shows the corresponding Stokes I and V images following the implementation of the polarization calibration method.
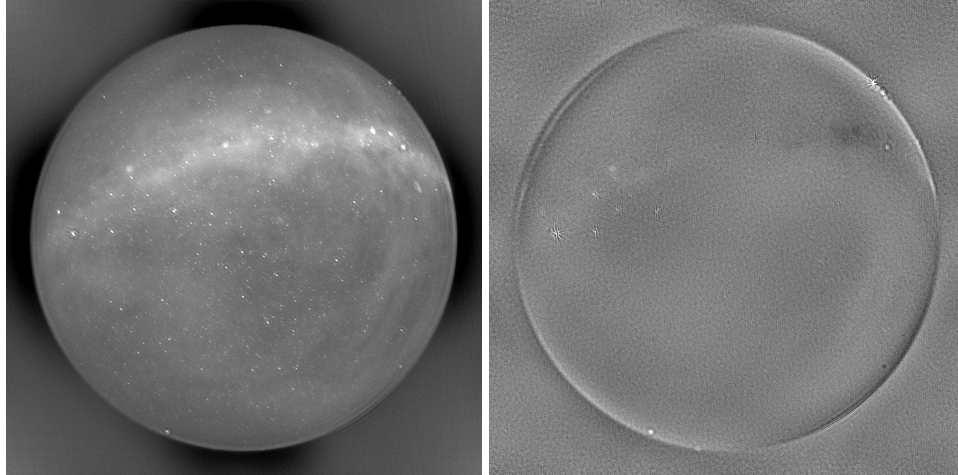
Figure 5.1: Snapshot, full bandwidth image from the OVRO-LWA in Stokes I total intensity (left) and Stokes V circular polarization (right). The flux density colorscale in the Stokes I image is set from -23 to 47 Jy. In the Stokes V image, it is set from -5 to 5 Jy. The noise towards zenith in the Stokes V image is approximately 450 mJy. The point sources that are visible in the Stokes V image are not intrinsically polarized, but are present due to instrumental leakage, however the leakage is relatively minimal, and is at maximum at low elevations in the beam at the 10% level. Cas A and Cyg A have been peeled from all 4 correlation products (XX, XY, YX, YY).

## 5.3   25 Parsec Sample

Figure 5.2 shows the number and distribution of objects contained in the assembled catalog of all systems out to approximately 25 pc. All 3820 objects are being searched, in both Stokes I and V, across the duration of the 31 hr dataset, for variability or transient emission indicative of stellar or planetary radio emission. Example light curves are shown in Figure 5.3 for the M6 flare star UV Ceti, the K2 star Epsilon Eridani, and the K5+K7 system 61 Cygni. An initial $10\sigma$ cut on each of the light curves was made to search for transient events, which yielded no candidate bursts.

Figure 5.4 shows the current sensitivity limits that have been placed with the sample thus far. Further statistical analysis is underway to verify whether any transient emission indicative of stellar radio bursts is present in any of the light curves. Particularly in the case of stellar bursts, we are likely just skimming the edge of detectability. Additional increases in sensitivity, as well as longer monitoring periods to increase the likelihood of observing rare brightening events, will be key for detecting the first stellar CMEs.
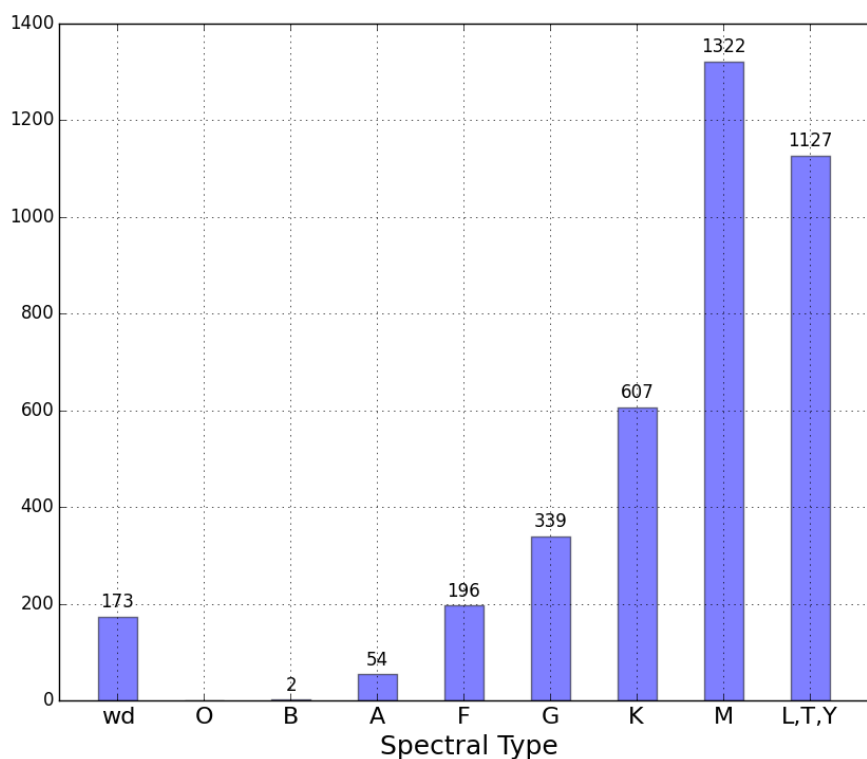
Figure 5.2: The 25-pc sample, containing 3820 objects. As expected, the sample is dominated by M dwarfs. Source are compiled from 1) the Kirkpatrick et al. 2012 8-pc volume-limited sample; 2) the Dwarf Archives database of Kirkpatrick et al. containing all known, spectroscopically determined L, T, and Y dwarfs; 3) the Gliese Catalog of Nearby Stars, 3rd Edition; 4) the Sion et al. 2014 white dwarf 25-pc sample; and 5) the M dwarf 25-pc sample c/o Evgenya Shkolnik. We have excluded sources below −33° declination.
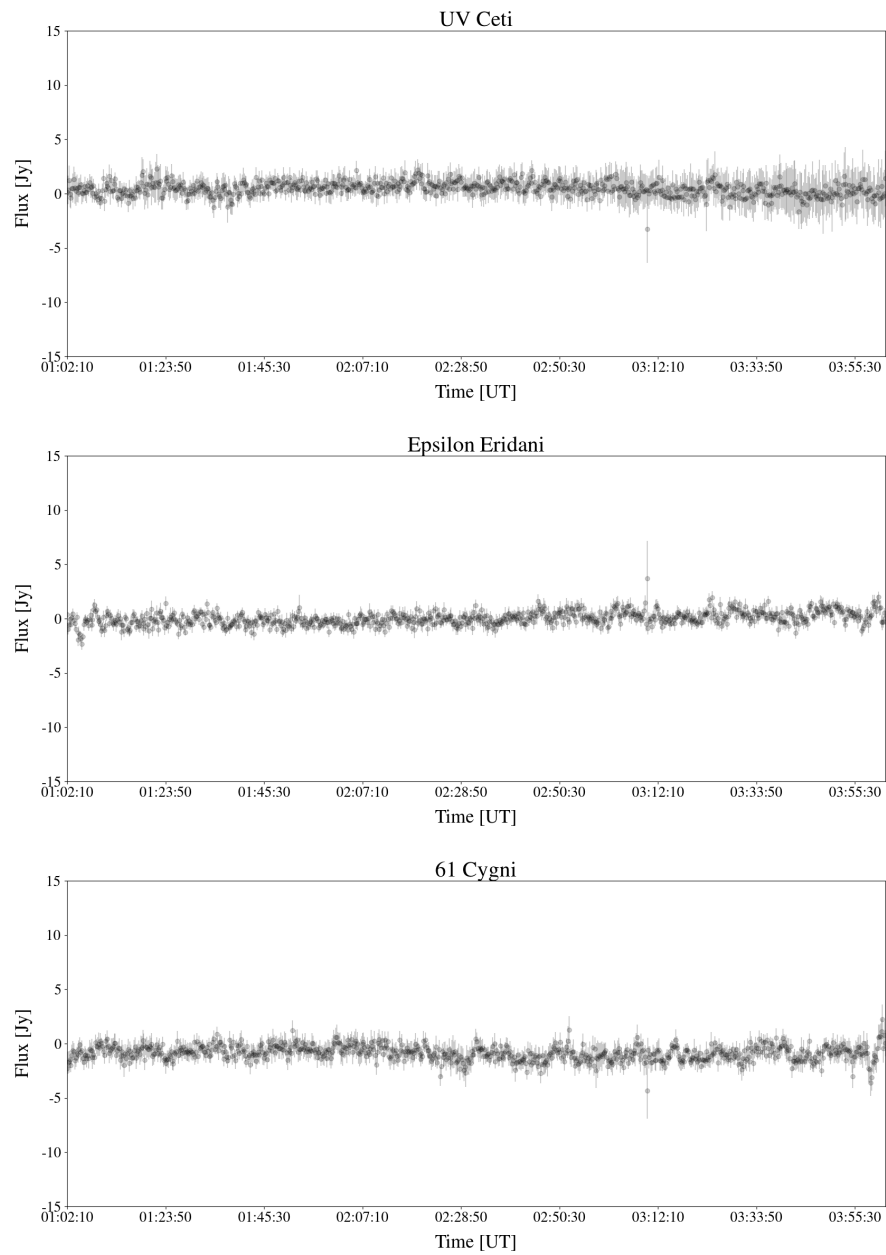
Figure 5.3: Example light curves from a subset of the data, for the M6 flare star UV Ceti, the K2 star Epsilon Eridani, and the K5+K7 system 61 Cygni. Typical noise is ~800 mJy.
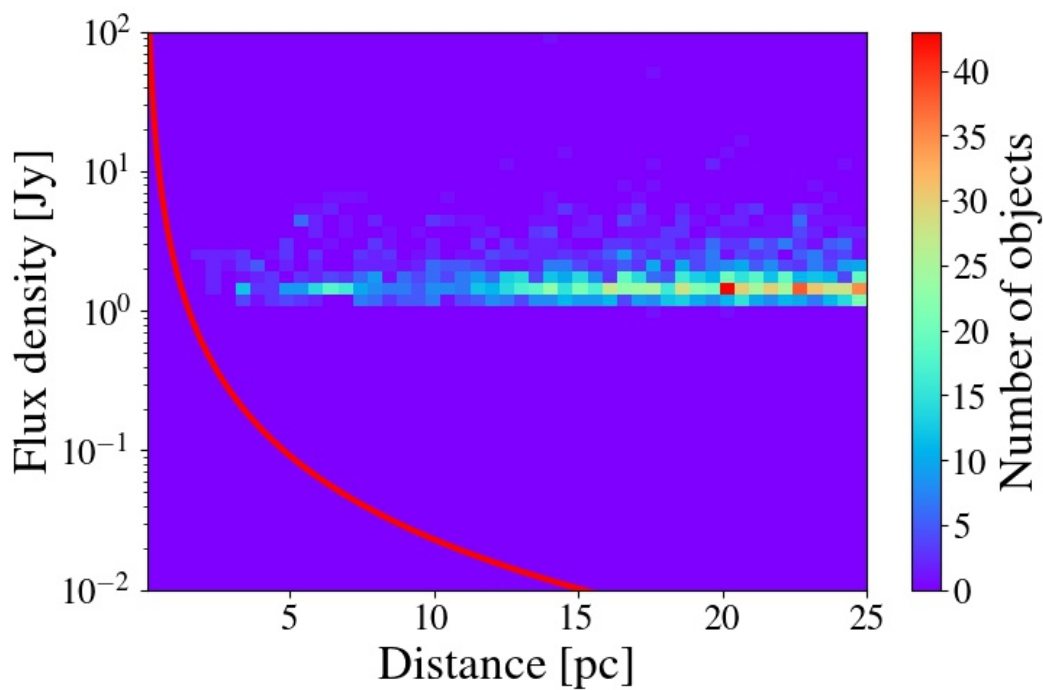
Figure 5.4: 2-D sensitivity histogram for all M dwarf and earlier spectral type systems targeted across the 31-hour dataset. The color of each pixel denotes the number of sources at a given distance and sensitivity upper limit. The red line represents the equivalent of a $10^{11}$ Jy Type II burst from the Sun, scaled as a function of distance.

**References**

Aarnio, A. N., et al. 2011. "Solar Flares and Coronal Mass Ejections: A Statistically Determined Flare Flux - CME Mass Correlation". *SoPh* 268 (): 195–212. doi:`10.1007/s11207-010-9672-7`. arXiv: `1011.0424` [`astro-ph.SR`].

Alvarado-Gómez, J. D., et al. 2018. "Suppression of Coronal Mass Ejections in Active Stars by an Overlying Large-scale Magnetic Field: A Numerical Study". *ApJ* 862, 93 (): 93. doi:`10.3847/1538-4357/aacb7f`. arXiv: `1806.02828` [`astro-ph.SR`].

Anderson, M. M., G. Hallinan, M. W. Eastwood, R. M. Monroe, H. K. Vedantham, S. Bourke, L. J. Greenhill, J. Kocz, T. J. W. Lazio, D. C. Price, F. K. Schinzel, Y. Wang, and D. P. Woody. 2018. "A Simultaneous Search for Prompt Radio Emission Associated with the Short GRB 170112A Using the All-sky Imaging Capability of the OVRO-LWA". *ApJ* 864 (22): 1–11. doi:`10.3847/1538-4357/aad2d7`. arXiv: `1711.06665` [`astro-ph.HE`].

Baars, J. W. M., et al. 1977. "The absolute spectrum of CAS A - an accurate flux density scale and a set of secondary calibrators". *A&A* 61 (): 99–106.

Bastian, T. S., A. O. Benz, and D. E. Gary. 1998. "Radio Emission from Solar Flares". *ARA&A* 36:131–188. doi:`10.1146/annurev.astro.36.1.131`.

Bastian, T. S., G. A. Dulk, and Y. Leblanc. 2000. "A Search for Radio Emission from Extrasolar Planets". *ApJ* 545 (): 1058–1063. doi:`10.1086/317864`.

Berger, E., et al. 2009. "Periodic Radio and Hα Emission from the L Dwarf Binary 2MASSW J0746425+200032: Exploring the Magnetic Field Topology and Radius Of An L Dwarf". *ApJ* 695 (): 310–316. doi:`10.1088/0004-637X/695/1/310`. arXiv: `0809.0001`.

Bower, G. C., et al. 2016. "Variable Radio Emission from the Young Stellar Host of a Hot Jupiter". *ApJ* 830, 107 (): 107. doi:`10.3847/0004-637X/830/2/107`. arXiv: `1608.00962` [`astro-ph.SR`].

Briggs, D. S. 1995. "High Fidelity Deconvolution of Moderately Resolved Sources". PhD thesis, New Mexico Institute of Mining and Technology.

Crosley, M. K., and R. A. Osten. 2018. "Constraining Stellar Coronal Mass Ejections through Multi-wavelength Analysis of the Active M Dwarf EQ Peg". *ApJ* 856, 39 (): 39. doi:`10.3847/1538-4357/aaaec2`. arXiv: `1802.03440` [`astro-ph.SR`].

Crosley, M. K., et al. 2016. "The Search for Signatures of Transient Mass Loss in Active Stars". *ApJ* 830, 24 (): 24. doi:`10.3847/0004-637X/830/1/24`. arXiv: `1606.02334` [`astro-ph.SR`].

Drake, J. J., et al. 2013. "Implications of Mass and Energy Loss due to Coronal Mass Ejections on Magnetically Active Stars". *ApJ* 764, 170 (): 170. doi:`10.1088/0004-637X/764/2/170`. arXiv: `1302.1136` [`astro-ph.SR`].

Dressing, C. D., and D. Charbonneau. 2015. "The Occurrence of Potentially Habitable Planets Orbiting M Dwarfs Estimated from the Full Kepler Dataset and an Empirical Measurement of the Detection Sensitivity". *ApJ* 807, 45 (): 45. doi:`10.1088/0004-637X/807/1/45`. arXiv: `1501.01623 [astro-ph.EP]`.

Eastwood, Michael W. 2016. *TTCal*. Version 0.3.0. doi:`10.5281/zenodo.1049160`. `https://doi.org/10.5281/zenodo.1049160`.

Gallagher, D. L., and N. Dangelo. 1981. "Correlations between solar wind parameters and auroral kilometric radiation intensity". *Geophys. Res. Lett.* 8 (): 1087–1089. doi:`10.1029/GL008i010p01087`.

George, S. J., and I. R. Stevens. 2007. "Giant Metrewave Radio Telescope low-frequency observations of extrasolar planetary systems". *MNRAS* 382 (): 455–460. doi:`10.1111/j.1365-2966.2007.12387.x`. arXiv: `0708.4079`.

Gopalswamy, N., et al. 2001. "Characteristics of coronal mass ejections associated with long-wavelength type II radio bursts". *J. Geophys. Res.* 106 (): 29219–29230. doi:`10.1029/2001JA000234`.

Gosling, J. T. 1993. "The solar flare myth". *J. Geophys. Res.* 98 (): 18937–18950. doi:`10.1029/93JA01896`.

Grießmeier, J.-M., P. Zarka, and H. Spreeuw. 2007. "Predicting low-frequency radio fluxes of known extrasolar planets". *A&A* 475 (): 359–368. doi:`10.1051/0004-6361:20077397`. arXiv: `0806.0327`.

Grießmeier, J.-M., et al. 2005. "The influence of stellar wind conditions on the detectability of planetary radio emissions". *A&A* 437 (): 717–726. doi:`10.1051/0004-6361:20041976`.

Gurnett, D. A., et al. 2002. "Control of Jupiter's radio emission and aurorae by the solar wind". *Nature* 415 (): 985–987. doi:`10.1038/415985a`.

Hallinan, G., et al. 2013. "Looking for a Pulse: A Search for Rotationally Modulated Radio Emission from the Hot Jupiter, $\tau$ Boötis b". *ApJ* 762, 34 (): 34. doi:`10.1088/0004-637X/762/1/34`. arXiv: `1210.8259 [astro-ph.EP]`.

Hallinan, G., et al. 2015. "Magnetospherically driven optical and radio aurorae at the end of the stellar main sequence". *Nature* 523 (): 568–571. doi:`10.1038/nature14619`. arXiv: `1507.08739 [astro-ph.SR]`.

Hallinan, G., et al. 2007. "Periodic Bursts of Coherent Radio Emission from an Ultracool Dwarf". *ApJL* 663 (): L25–L28. doi:`10.1086/519790`. arXiv: `0705.2054`.

Jakosky, B. M., et al. 2015. "The Mars Atmosphere and Volatile Evolution ( MAVEN) Mission". *SSRv* 195 (): 3–48. doi:`10.1007/s11214-015-0139-x`.

Kao, M. M., et al. 2016. "Auroral Radio Emission from Late L and T Dwarfs: A New Constraint on Dynamo Theory in the Substellar Regime". *ApJ* 818, 24 (): 24. doi:`10.3847/0004-637X/818/1/24`. arXiv: `1511.03661 [astro-ph.SR]`.

Khodachenko, M. L., et al. 2007. "Coronal Mass Ejection (CME) Activity of Low Mass M Stars as An Important Factor for The Habitability of Terrestrial Exoplanets. I. CME Impact on Expected Magnetospheres of Earth-Like Exoplanets in Close-In Habitable Zones". *Astrobiology* 7 (): 167–184. doi:`10.1089/ast.2006.0127`.

Kirkpatrick, J. D., et al. 2012. "Further Defining Spectral Type "Y" and Exploring the Low-mass End of the Field Brown Dwarf Mass Function". *ApJ* 753, 156 (): 156. doi:`10.1088/0004-637X/753/2/156`. arXiv: `1205.2122 [astro-ph.SR]`.

Lammer, H., et al. 2012. "Variability of solar/stellar activity and magnetic field and its influence on planetary atmosphere evolution". *Earth, Planets, and Space* 64 (): 179–199. doi:`10.5047/eps.2011.04.002`.

Lazio, T. J. W., and W. M. Farrell. 2007. "Magnetospheric Emissions from the Planet Orbiting $\tau$ Bootis: A Multiepoch Search". *ApJ* 668 (): 1182–1188. doi:`10.1086/519730`. arXiv: `0707.1827`.

Lazio, T. J. W., et al. 2010a. "Radio Observations of HD 80606 Near Planetary Periastron". *AJ* 140 (): 1929–1933. doi:`10.1088/0004-6256/140/6/1929`. arXiv: `1010.5383 [astro-ph.EP]`.

Lazio, T. J. W., et al. 2010b. "Surveying the Dynamic Radio Sky with the Long Wavelength Demonstrator Array". *AJ* 140 (): 1995–2006. doi:`10.1088/0004-6256/140/6/1995`. arXiv: `1010.5893 [astro-ph.IM]`.

Lazio, T. J., W., et al. 2004. "The Radiometric Bode's Law and Extrasolar Planets". *ApJ* 612 (): 511–518. doi:`10.1086/422449`.

Lecavelier Des Etangs, A., et al. 2009. "GMRT radio observations of the transiting extrasolar planet HD 189733 b at 244 and 614 MHz". *A&A* 500 (): L51–L54. doi:`10.1051/0004-6361/200912347`. arXiv: `0906.2783 [astro-ph.EP]`.

– . 2011. "GMRT search for 150 MHz radio emission from the transiting extrasolar planets HD 189733 b and HD 209458 b". *A&A* 533, A50 (): A50. doi:`10.1051/0004-6361/201117330`. arXiv: `1108.3730 [astro-ph.EP]`.

Lecavelier des Etangs, A., et al. 2013. "Hint of 150 MHz radio emission from the Neptune-mass extrasolar transiting planet HAT-P-11b". *A&A* 552, A65 (): A65. doi:`10.1051/0004-6361/201219789`. arXiv: `1302.4612 [astro-ph.EP]`.

Leitzinger, M., et al. 2014. "A search for flares and mass ejections on young late-type stars in the open cluster Blanco-1". *MNRAS* 443 (): 898–910. doi:`10.1093/mnras/stu1161`. arXiv: `1406.2734 [astro-ph.SR]`.

Lenc, E., et al. 2018. "An all-sky survey of circular polarization at 200 MHz". *MNRAS* 478 (): 2835–2849. doi:`10.1093/mnras/sty1304`. arXiv: `1805.05482`.

Lenc, E., et al. 2017. "The Challenges of Low-Frequency Radio Polarimetry: Lessons from the Murchison Widefield Array". *PASA* 34, e040 (): e040. doi:`10.1017/pasa.2017.36`. arXiv: `1708.05799 [astro-ph.IM]`.

Liu, Y., et al. 2009. "Relationship Between a Coronal Mass Ejection-Driven Shock and a Coronal Metric Type II Burst". *ApJL* 691 (): L151–L155. doi:`10.1088/0004-637X/691/2/L151`.

Lynch, C. R., et al. 2017. "154 MHz Detection of Faint, Polarized Flares from UV Ceti". *ApJl* 836, L30 (): L30. doi:`10.3847/2041-8213/aa5ffd`. arXiv: `1702.03030 [astro-ph.SR]`.

Lynch, C. R., et al. 2018. "The detectability of radio emission from exoplanets". *MNRAS* 478 (): 1763–1775. doi:`10.1093/mnras/sty1138`. arXiv: `1804.11006 [astro-ph.EP]`.

McMullin, J. P., et al. 2007. "CASA Architecture and Applications". In *Astronomical Data Analysis Software and Systems XVI*, ed. by R. A. Shaw, F. Hill, and D. J. Bell, 376:127. Astronomical Society of the Pacific Conference Series.

Murphy, T., et al. 2015. "Limits on low-frequency radio emission from southern exoplanets with the Murchison Widefield Array". *MNRAS* 446 (): 2560–2565. doi:`10.1093/mnras/stu2253`. arXiv: `1410.6819 [astro-ph.EP]`.

Offringa, A. R., et al. 2014. "WSCLEAN: an implementation of a fast, generic wide-field imager for radio astronomy". *MNRAS* 444 (): 606–619. doi:`10.1093/mnras/stu1368`. arXiv: `1407.1943 [astro-ph.IM]`.

O'Gorman, E., et al. 2018. "A search for radio emission from exoplanets around evolved stars". *A&A* 612, A52 (): A52. doi:`10.1051/0004-6361/201731965`. arXiv: `1801.07753 [astro-ph.EP]`.

Osten, R. A., and S. J. Wolk. 2015. "Connecting Flares and Transient Mass-loss Events in Magnetically Active Stars". *ApJ* 809, 79 (): 79. doi:`10.1088/0004-637X/809/1/79`. arXiv: `1506.04994 [astro-ph.SR]`.

Perley, R. A., and B. J. Butler. 2017. "An Accurate Flux Density Scale from 50 MHz to 50 GHz". *ApJs* 230, 7 (): 7. doi:`10.3847/1538-4365/aa6df9`. arXiv: `1609.05940 [astro-ph.IM]`.

Ribas, I., et al. 2005. "Evolution of the Solar Activity over Time and Effects on Planetary Atmospheres. I. High-Energy Irradiances (1-1700 Å)". *ApJ* 622 (): 680–694. doi:`10.1086/427977`. eprint: `astro-ph/0412253`.

Ribas, I., et al. 2016. "The habitability of Proxima Centauri b. I. Irradiation, rotation and volatile inventory from formation to the present". *A&A* 596, A111 (): A111. doi:`10.1051/0004-6361/201629576`. arXiv: `1608.06813 [astro-ph.EP]`.

Route, M., and A. Wolszczan. 2012. "The Arecibo Detection of the Coolest Radio-flaring Brown Dwarf". *ApJL* 747, L22 (): L22. doi:`10.1088/2041-8205/747/2/L22`. arXiv: `1202.1287 [astro-ph.SR]`.

Sault, R. J., J. P. Hamaker, and J. D. Bregman. 1996. "Understanding radio polarimetry. II. Instrumental calibration of an interferometer array." *A&As* 117 (): 149–159.

Sion, E. M., et al. 2014. "The White Dwarfs within 25 pc of the Sun: Kinematics and Spectroscopic Subtypes". *AJ* 147, 129 (): 129. doi:`10.1088/0004-6256/147/6/129`. arXiv: `1401.4989 [astro-ph.SR]`.

Sirothia, S. K., et al. 2014. "Search for 150 MHz radio emission from extrasolar planets in the TIFR GMRT Sky Survey". *A&A* 562, A108 (): A108. doi:`10.1051/0004-6361/201321571`.

Smith, A. M. S., et al. 2009. "Secondary radio eclipse of the transiting planet HD 189733 b: an upper limit at 307-347 MHz". *MNRAS* 395 (): 335–341. doi:`10.1111/j.1365-2966.2009.14510.x`. arXiv: `0901.2344 [astro-ph.EP]`.

Spangler, S. R., and T. J. Moffett. 1976. "Simultaneous radio and optical observations of UV Ceti-type flare stars". *ApJ* 203 (): 497–508. doi:`10.1086/154105`.

Stroe, A., I. A. G. Snellen, and H. J. A. Röttgering. 2012. "A stringent upper limit to 18 cm radio emission from the extrasolar planet system $\tau$ Boötis". *A&A* 546, A116 (): A116. doi:`10.1051/0004-6361/201220006`. arXiv: `1209.6515 [astro-ph.EP]`.

Sun, X., et al. 2015. "Why Is the Great Solar Active Region 12192 Flare-rich but CME-poor?" *ApJL* 804, L28 (): L28. doi:`10.1088/2041-8205/804/2/L28`. arXiv: `1502.06950 [astro-ph.SR]`.

Tingay, S. J., et al. 2013. "The Murchison Widefield Array: The Square Kilometre Array Precursor at Low Radio Frequencies". *PASA* 30, e007 (): e007. doi:`10.1017/pasa.2012.007`. arXiv: `1206.6945 [astro-ph.IM]`.

Vidotto, A. A., et al. 2013. "Effects of M dwarf magnetic fields on potentially habitable planets". *A&A* 557, A67 (): A67. doi:`10.1051/0004-6361/201321504`. arXiv: `1306.4789 [astro-ph.EP]`.

Villadsen, J., and G. Hallinan. 2019. "Ultra-wideband Detection of 22 Coherent Radio Bursts on M Dwarfs". *ApJ* 871, 214 (): 214. doi:`10.3847/1538-4357/aaf88e`. arXiv: `1810.00855 [astro-ph.SR]`.

West, A. A., et al. 2008. "Constraining the Age-Activity Relation for Cool Stars: The Sloan Digital Sky Survey Data Release 5 Low-Mass Star Spectroscopic Sample". *AJ* 135 (): 785–795. doi:`10.1088/0004-6256/135/3/785`. arXiv: `0712.1590`.

Wild, J. P., J. D. Murray, and W. C. Rowe. 1954. "Harmonics in the Spectra of Solar Radio Disturbances". *Australian Journal of Physics* 7 (): 439. doi:`10.1071/PH540439`.

Winglee, R. M., G. A. Dulk, and T. S. Bastian. 1986. "A search for cyclotron maser radiation from substellar and planet-like companions of nearby stars". *ApJL* 309 (): L59–L62. doi:`10.1086/184760`.

Zarka, P. 1998. "Auroral radio emissions at the outer planets: Observations and theories". *J. Geophys. Res.* 103 (): 20159–20194. doi:`10.1029/98JE01323`.

*Chapter 6*

# A CANDIDATE TIDAL DISRUPTION EVENT DISCOVERED WITH THE CNSS RADIO TRANSIENT SURVEY

Marin M. Anderson[1], Kunal P. Mooley[2,1], Gregg Hallinan[1], Dillon Dong[1]

**Abstract**

We present the discovery of an unusual nuclear radio transient at 3 GHz with the Karl G. Jansky Very Large Array (VLA), as part of the Caltech–NRAO Stripe 82 Survey (CNSS). This source, CNSS J001947.3+003527, exhibited a rapid turn-on, increasing in flux density by almost 2 orders of magnitude at 3 GHz from a $3\sigma$ upper limit of $\sim 0.14$ mJy to a flux density of $4.4 \pm 0.1$ mJy on a timescale of ~1 yr. The location of CNSS J0019+00 in the nuclear region ($< 1$ pc) of a nearby ($z = 0.018$) galaxy and its radio spectral evolution indicates a likely tidal disruption origin for this event. The radio observations are consistent with a $10^4$ km s$^{-1}$ outflow with a peak 3 GHz radio luminosity of $5 \times 10^{28}$ erg s$^{-1}$ Hz$^{-1}$, and indicate this is the first radio-discovered TDE and another of a growing class of radio-detected thermal tidal disruption events (TDEs) that includes ASASSN-14li and XMMSL1 J0740-85. Notably, however, this transient was not accompanied by a detection in X-rays, UV, or optical wavelengths, and we discuss alternate origins for this event, including renewed AGN activity. The implied rates from CNSS indicates there could be as many ~100 such events present in each epoch of the VLA Sky Survey.

*Key words:* accretion, accretion disks, galaxies: nuclei, radiation mechanisms: non-thermal, techniques: interferometric

## 6.1 Introduction

The passage of a star within the tidal radius of a galaxy's central supermassive black hole (SMBH) results in the disruption of the star by the tidal field of the SMBH. The distance from the SMBH at which this tidal disruption event (TDE) occurs is a function of the mass of the SMBH, as well as the mass and radius of the disrupted star (Hills 1975). For a (non-spinning) SMBH with mass $M \lesssim 10^8 M_\odot$

---

[1]California Institute of Technology, 1200 E California Boulevard MC 249-17, Pasadena, CA 91125, USA

[2]National Radio Astronomy Observatory, P.O. Box O, Socorro, NM 87801, USA

disrupting a solar type star, this distance is greater than the Schwarzchild radius of the BH and the stellar material will not be swallowed whole. Instead, approximately half of the stellar mass is accreted onto the SMBH, while the other half is ejected, and a luminous flare is produced that can be observed across the electromagnetic spectrum.

Theoretical predictions for TDEs recognized the potential for at first verifying the existence of, then later probing the central regions around, SMBHs that were usually otherwise dormant at the centers of galaxies (Hills 1975; Rees 1988; Phinney 1989). TDEs were predicted to result in bright flares with super-Eddington luminosities peaking in the soft X-ray and UV bands. These theoretical predictions were found to be consistent with the observational behavior of thermal TDEs, which were first discovered in the soft X-rays, with subsequent discoveries in the soft X-rays and UV (see Komossa 2015 and Lodato et al. 2015 for reviews of TDE observations and theory, respectively). The discovery of *Swift* J1644+57 (Levan et al. 2011), with its extremely luminous hard X-ray (Burrows et al. 2011) and radio (Zauderer et al. 2011) emission indicative of a relativistic outflow from a collimated jet, revealed the existence of non-thermal TDEs (Bloom et al. 2011), and their ability to serve as a laboratory for testing the connection between accretion and launching of jets, as well as measuring SMBH spin (Giannios and Metzger 2011; van Velzen, Körding, and Falcke 2011).

Since the first discovery of TDEs with ROSAT (Bade, Komossa, and Dahlem 1996), there are more than 30 known TDEs, with discoveries being made increasingly in optical surveys, as well as UV and X-rays. Of the known TDEs, 5 have definitive radio detections, including *Swift* J1644+57 (Zauderer et al. 2011; Berger et al. 2012; Zauderer et al. 2013; Eftekhari et al. 2018) and another jetted, non-thermal tidal disruption event, *Swift J2058+05* (Cenko et al. 2012). IGR J12580+0134 is also likely a non-thermal TDE, with a relativistic jet that is viewed off-axis (Nikołajuk and Walter 2013; Irwin et al. 2015; Lei et al. 2016). More recently, ASASSN-14li (Alexander et al. 2016) and XMMSL1 J0750-85 (Alexander et al. 2017) were characterized by radio emission showing sub-relativistic outflows, indicating that these are the first thermal TDEs with detected radio emission, and revealing the possibility that all TDEs are accompanied by radio emission, with earlier non-detections (Bower 2011; Bower et al. 2013; van Velzen et al. 2013; Chornock et al. 2014) a result of their lower radio luminosities – both ASASSN-14li and XMMSL1 J0750-85 were relatively nearby, $z \lesssim 0.02$, whereas the median TDE

redshift is approximately $z \sim 0.1$ (Komossa 2015). While the number of detected TDEs is expected to grow rapidly given the rise of time-domain optical surveys (e.g., ZTF, ASASSN, Pan-STARRS, and eventually LSST), the recent radio detection of thermal TDEs indicates the potential for radio surveys to contribute to the TDE discovery space, as well as follow-up detections, with a detection rate potentially unaffected by obscuration, thereby offering a different window on TDE event rates and host classes.

Here we present the discovery of the radio transient CNSS J001947.3+003527, hereafter CNSS J0019+00, identified in the Caltech–NRAO Stripe 82 Survey (CNSS), and located in the nucleus of a nearby ($z = 0.018$) galaxy. CNSS J0019+00 is likely a TDE, and if so, is the first such radio-discovered event, as well as another entrant in the class of radio-detected thermal TDEs akin to ASASSN-14li and XMMSL1 J0740-85. In Section 6.2 we describe the discovery of CNSS J0019+47 and the subsequent follow-up observations at radio, X-ray, and optical wavelengths. Section 6.3 describes the model fits to the follow-up radio spectra, and how they point to a subrelativistically expanding outflow. Section 6.4 discusses the potential explanations for the origins of CNSS J0019+47, including the likelihood that this is a thermal TDE event as well as alternative explanations to the tidal disruption scenario. In Section 6.5, we describe the implications that the first radio-discovered TDE has on detections of TDEs in future radio surveys.

## 6.2    Observations

**Caltech–NRAO Stripe 82 Survey**

CNSS is a five-epoch survey with the National Radio Astronomy Observatory Karl G. Jansky Very Large Array[1] (VLA; Perley et al. 2011) at S band (2–4 GHz) that was carried out between December 2013 and May 2015. It was designed to probe timescales of days, months, and years, and thus significantly advance the understanding of slow transient phenomena in the radio sky. Each epoch of CNSS covers the full ~270 deg$^2$ Sloan Digital Sky Survey (SDSS) Stripe 82 region with a uniform single-epoch sensitivity of ~80 $\mu$Jy and a spatial resolution of ~3″. Through the use of On The Fly (OTF) mosaicing (Mooley et al. 2019), CNSS combines shallow mapping of the sky with the sensitivity of the VLA, ensuring the delivery of high survey speed without being compromised by large overheads due to slewing between target fields. The results from the 50 deg$^2$ pilot survey were presented

---

[1]The National Radio Astronomy Observatory is a facility of the National Science Foundation operated under cooperative agreement by Associated Universities, Inc.

in Mooley et al. 2016, and included the discovery of radio transients consistent with an RS CVn binary and a dKe star. The full catalog of transients detected in the CNSS five epoch survey will be presented in an upcoming paper (Mooley et al., in prep). CNSS was designed as a pathfinder for wide-field radio surveys, including the VLA Sky Survey (VLASS).

### CNSS J001947.3+003527

CNSS J0019+00 was detected in CNSS epoch 4 on 2015 March 21 at a 3 GHz flux density of $4.4 \pm 0.1$ mJy at the position (R.A., decl.) = ($00^{\mathrm{h}}19^{\mathrm{m}}47^{\mathrm{s}}.3$, $+00°35'27''$). It was not detected in the first three epochs of CNSS between December 2013 and February 2014 at a $3\sigma$ upper limit of ~0.14 mJy in the combined epochs 1–3 coadded image, and was therefore identified as a candidate transient event. There is no coincident source in the Faint Images of the Radio Sky at Twenty-cm (FIRST; Becker, White, and Helfand 1995) survey, with a 0.5 mJy $3\sigma$ upper limit at 1.4 GHz (mean epoch 1999) at the location of CNSS J0019+00. By CNSS epoch 5 on 2015 April 19, the transient had increased to a 3 GHz flux density of $5.1 \pm 0.1$ mJy.

Identification of extragalactic transients was done through the cross-matching of radio transient candidates with galaxy catalogs for the local universe, which are typically developed for gravitational wave (GW) event follow-up. We make use of the Census of the Local Universe (CLU; Cook et al. 2017) to identify objects out to a volume of 200 Mpc, for which we expect a very low false positive rate due to background AGN. CNSS J0019+00 was the only significant extragalactic transient identified on timescales shorter than the duration of the survey, rather than through comparison to existing surveys (e.g., FIRST). Cross-matching with CLU and SDSS established that CNSS J0019+47 is coincident with the nucleus of a Seyfert 2 galaxy at a distance of 77.1 Mpc ($z = 0.018$). Radio, X-ray, and optical follow-up observations of CNSS J0019+00 were immediately scheduled. Figure 6.1 shows the 3 GHz light curve and observation timeline for CNSS J0019+00.

### VLA Observations

Following the discovery of CNSS J0019+00 in 2015 March, we continued to monitor the source with the VLA over the course of the next 14 months (under program codes 15A-421, 15B-364, and 16A-237). It was observed from L through Ku band (1–16 GHz) in order to fully sample the spectrum of the source across four follow-up epochs, spanning 2015 May 10 to 2016 July 08. The follow-up spectra of CNSS J0019+00 are well fit by a slowly evolving synchrotron spectrum, with both the peak
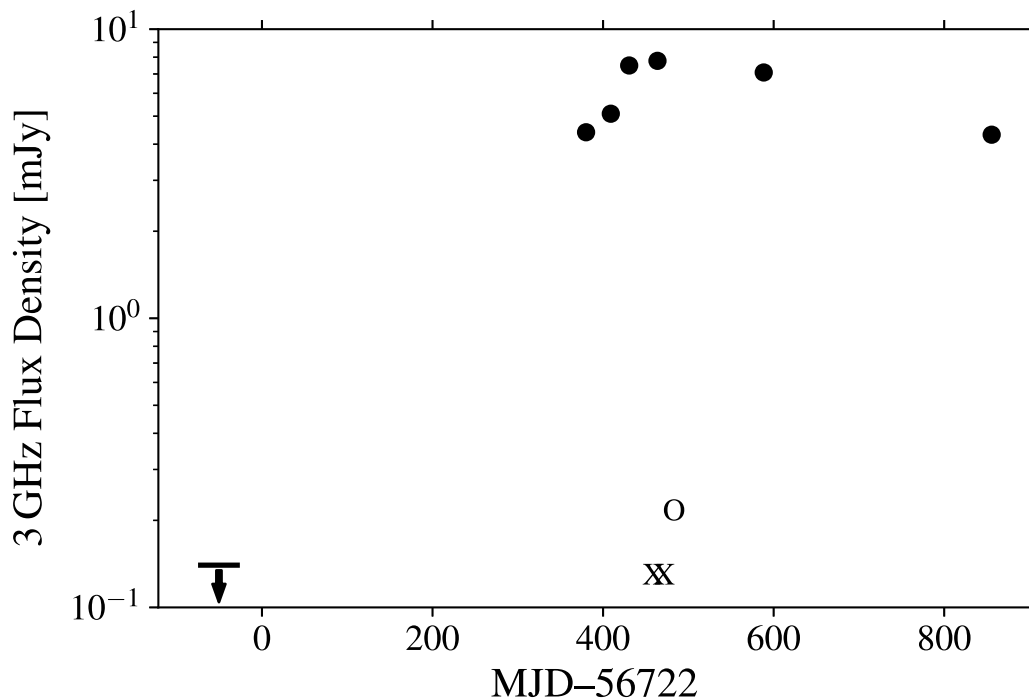
Figure 6.1: CNSS J0019+00 3 GHz light curve. The 0.14 mJy upper limit is from the non-detection in CNSS epochs 1–3. The plotted flux densities are from CNSS epochs 4 and 5, and 4 follow-up observations of CNSS J0019+00 with the VLA spanning approximately 1.5 yr post-discovery. The Xs and O mark the dates of follow-up *Swift* and Keck-II DEIMOS observations, respectively. The dates are referenced to the approximate explosion date on MJD 56722, as determined by fitting the radio SEDs (see Section 4.3).

frequency and peak flux of the spectrum declining over time.

Table 6.1 summarizes the radio follow-up measurements, which are plotted in Figure 6.2. These also include measurements of the flux of CNSS J0019+00 at L band (1–2 GHz) from observations on 2017 Dec 20 (program code 17B-409). For all observations, 3C48 served as the absolute flux and bandpass calibrator. Phase calibration was done using one of J0022+0014, J006-0623, J0022+0608, J0015-0127. All data reduction was done in the Common Astronomy Software Applications (CASA; McMullin et al. 2007).

Table 6.1: VLA follow-up observations of CNSS J0019+00.

| UT Date | Frequency (GHz) | Flux Density (mJy) |
|---|---|---|
| 2015 May 10.53 | 1.4 | 3.31 ± 0.36 |
| | | Continued on next page |

**Table 6.1 – continued from previous page**

| UT Date | Frequency (GHz) | Flux Density (mJy) |
|---|---|---|
| May 10.53 | 1.8 | 4.53 ± 0.41 |
| May 10.53 | 2.6 | 6.80 ± 0.16 |
| May 10.53 | 2.9 | 7.49 ± 0.11 |
| May 10.53 | 3.2 | 7.72 ± 0.07 |
| May 10.55 | 4.4 | 8.21 ± 0.08 |
| May 10.55 | 5.1 | 8.14 ± 0.04 |
| May 10.55 | 7.1 | 6.85 ± 0.04 |
| May 10.55 | 7.8 | 6.50 ± 0.05 |
| May 10.55 | 8.1 | 6.34 ± 0.04 |
| May 10.55 | 8.6 | 6.17 ± 0.04 |
| May 10.55 | 9.1 | 5.93 ± 0.04 |
| May 10.55 | 9.6 | 5.63 ± 0.04 |
| May 10.55 | 10.2 | 5.45 ± 0.04 |
| May 10.55 | 10.7 | 5.23 ± 0.04 |
| May 10.55 | 11.4 | 4.85 ± 0.04 |
| May 10.57 | 13.3 | 4.16 ± 0.05 |
| May 10.57 | 13.8 | 4.06 ± 0.04 |
| May 10.57 | 15.8 | 3.33 ± 0.05 |
| May 10.57 | 16.3 | 3.23 ± 0.04 |
| 2015 Jun 12.71 | 1.3 | 3.80 ± 0.20 |
| Jun 12.71 | 1.5 | 4.38 ± 0.17 |
| Jun 12.71 | 1.8 | 5.14 ± 0.17 |
| Jun 12.72 | 2.4 | 6.64 ± 0.08 |
| Jun 12.72 | 3.0 | 7.77 ± 0.06 |
| Jun 12.72 | 3.4 | 7.88 ± 0.06 |
| Jun 12.72 | 3.8 | 8.08 ± 0.07 |
| Jun 12.72 | 4.5 | 8.19 ± 0.10 |
| Jun 12.72 | 5.1 | 7.74 ± 0.10 |
| Jun 12.72 | 7.1 | 6.24 ± 0.14 |
| Jun 12.72 | 7.7 | 5.96 ± 0.15 |
| Jun 12.73 | 8.5 | 5.68 ± 0.08 |
| Jun 12.73 | 9.8 | 5.03 ± 0.10 |
| Jun 12.73 | 11.0 | 4.32 ± 0.11 |
| | | Continued on next page |

**Table 6.1 – continued from previous page**

| UT Date | Frequency (GHz) | Flux Density (mJy) |
|---|---|---|
| Jun 12.74 | 15.7 | 3.10 ± 0.25 |
| Jun 12.74 | 16.3 | 3.10 ± 0.22 |
| 2015 Oct 15.32 | 1.2 | 2.33 ± 0.55 |
| Oct 15.32 | 1.4 | 4.89 ± 0.39 |
| Oct 15.32 | 1.7 | 4.92 ± 0.29 |
| Oct 15.32 | 1.9 | 5.81 ± 0.25 |
| Oct 15.32 | 2.6 | 7.34 ± 0.13 |
| Oct 15.32 | 3.1 | 7.08 ± 0.09 |
| Oct 15.32 | 3.4 | 7.08 ± 0.09 |
| Oct 15.33 | 4.7 | 6.11 ± 0.05 |
| Oct 15.33 | 5.3 | 5.74 ± 0.05 |
| Oct 15.33 | 5.7 | 5.52 ± 0.04 |
| Oct 15.33 | 6.3 | 5.18 ± 0.06 |
| Oct 15.33 | 8.2 | 3.77 ± 0.04 |
| Oct 15.33 | 8.8 | 3.70 ± 0.04 |
| Oct 15.33 | 9.2 | 3.36 ± 0.04 |
| Oct 15.33 | 9.8 | 3.28 ± 0.04 |
| Oct 15.34 | 13.2 | 1.99 ± 0.04 |
| Oct 15.34 | 13.8 | 2.00 ± 0.03 |
| Oct 15.34 | 14.2 | 2.04 ± 0.03 |
| Oct 15.34 | 14.8 | 1.99 ± 0.03 |
| 2016 Jul 08.60 | 1.3 | 4.04 ± 0.34 |
| Jul 08.60 | 1.5 | 4.71 ± 0.23 |
| Jul 08.60 | 1.8 | 5.74 ± 0.29 |
| Jul 08.60 | 2.4 | 4.86 ± 0.11 |
| Jul 08.60 | 3.0 | 4.32 ± 0.08 |
| Jul 08.60 | 3.4 | 3.90 ± 0.07 |
| Jul 08.61 | 4.5 | 3.26 ± 0.07 |
| Jul 08.61 | 5.1 | 2.76 ± 0.07 |
| Jul 08.61 | 6.1 | 2.34 ± 0.04 |
| Jul 08.61 | 7.1 | 1.75 ± 0.06 |
| Jul 08.61 | 7.7 | 1.55 ± 0.07 |
| Jul 08.61 | 8.2 | 1.40 ± 0.07 |
| | | Continued on next page |

**Table 6.1 – continued from previous page**

| UT Date | Frequency (GHz) | Flux Density (mJy) |
|---|---|---|
| Jul 08.61 | 8.8 | 1.32 ± 0.07 |
| Jul 08.61 | 9.7 | 1.25 ± 0.04 |
| Jul 08.61 | 10.6 | 1.06 ± 0.07 |
| Jul 08.61 | 11.2 | 0.95 ± 0.07 |
| Jul 08.61 | 13.2 | 0.73 ± 0.07 |
| Jul 08.61 | 13.8 | 0.61 ± 0.06 |
| Jul 08.61 | 15.0 | 0.72 ± 0.04 |
| Jul 08.61 | 16.2 | 0.50 ± 0.07 |
| Jul 08.61 | 16.8 | 0.57 ± 0.08 |
| 2017 Dec 20.03 | 1.14 | 2.87 ± 0.29 |
| Dec 20.03 | 1.39 | 1.97 ± 0.17 |
| Dec 20.03 | 1.65 | 1.63 ± 0.18 |
| Dec 20.03 | 1.90 | 1.48 ± 0.12 |
| | | Continued on next page |

NOTE – VLA follow-up observations of CNSS J0019+00, with SEDs spanning approximately 1–16 GHz, following its discovery in CNSS epoch 4 on 2015 March 21. The follow-up observations listed here span approximately 431 to 1385 d post-outburst, with the time since outburst determined from model-fitting of the individual SEDs (see Section 6.3).

**VLBA Observations**

We conducted Very Long Baseline Array (VLBA) observations at the location of CNSS J0019+00 on 2015 Nov 10 and 2016 Aug 31, in order to place a constraint on, or potentially resolve, a relativistically expanding jet (in the event of a non-thermal TDE scenario, e.g. *Swift* J1644+57). Observations were conducted at 4.38 and 7.40 GHz, as part of the Director's Discretionary Time (project code BM444), with J02253+1608 as the fringe finder source and J0016-0015 for phase calibration. Due to the limited LST range accessible for observing equatorial sources with the VLBA, the observations were split across the 2 epochs, with observation blocks of 2.5 hours each.

The source is unresolved in both VLBA epochs, consistent with the source size $\lesssim 1 \times 10^{17}$ cm as determined by modeling of the radio SED (see Section 4.3). From *Gaia*,
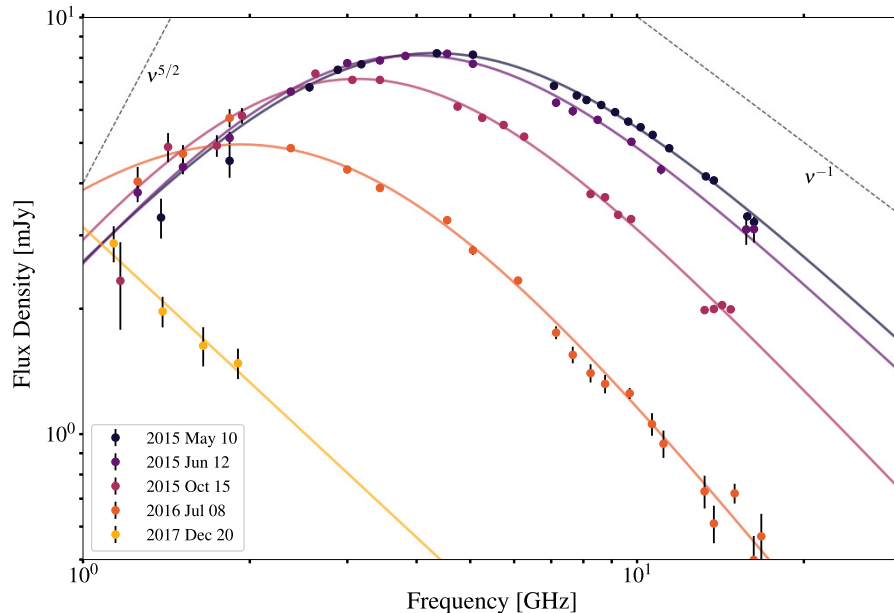
Figure 6.2: The evolution of the broadband spectral energy distribution (SED) of CNSS J0019+00, as observed with the VLA in 5 epochs spaced across 2.5 yr. The synchrotron spectra are modeled according to Granot and Sari 2002 under the assumption that $\nu_m < \nu_{sa} < \nu_c$. The dashed lines on the optically thick and thin sides of the spectral peak correspond to typical spectral slopes of $\nu^{5/2}$ and $\nu^{-1}$, respectively. The latter is expected for a electron energy distribution described by a power law with $p = 3$. Our model fits to the spectra give shallower optically thick spectral slopes (approximately $\nu^{1.5}$), and steeper optically thin spectral slopes that are evolving with time (ranging from $\nu^{-1.3}$ to $\nu^{-1.7}$; see Section 4.3).

the nucleus of the host galaxy is (R.A., decl.) = ($00^h 19^m 47^s.33493$, $+00°35'26''.8126$) ± (0.34, 0.26) milliarcsec (Gaia Collaboration et al. 2016; Gaia Collaboration et al. 2018; Lindegren et al. 2018). The location of CNSS J0019+00 from the VLBA observations is coincident with this optical position to within ~3 mas, implying that CNSS J0019+00 is consistent with the nuclear region of the host galaxy to within ~1 pc.

Table 6.2: *Swift* observations of CNSS J0019+00.

| UT Date | Exposure Time (ks) | Band (keV) | Count Rate (counts s$^{-1}$) | Luminosity ($10^{40}$ erg s$^{-1}$) | |
|---------|--------------------|------------|------------------------------|-------------------------------------|---|
| | | | | power law with photon index 2 | 10,000 K black body |
| 2015 May 26 | 5.8 | 0.3-10 | $\leq 9.3 \times 10^{-4}$ | $\leq 2.4$ | $\leq 4.0$ |
| 2015 Jun 07 | 6.3 | | | | |

NOTE – *Swift* follow-up observations at the location of CNSS J0019+00, starting approximately 464 days after the outflow launch.

*Swift* **Observations**

*Swift* (Gehrels et al. 2004) X-ray observations were triggered within approximately 2 weeks of the first radio follow-up observation (see Table 6.2). No X-ray counterpart was detected in either exposure, and the combined upper limit (90% confidence) to the count rate in the 0.3–10 keV soft X-ray band is $9.3 \times 10^{-4}$ count s$^{-1}$. This corresponds to an upper limit in the X-ray luminosity of less than $2.4 \times 10^{40}$ erg s$^{-1}$ assuming a power law with photon index 2 (typical for non-thermal emission), or an upper limit of less than $4.0 \times 10^{40}$ erg s$^{-1}$ assuming black body emission that peaks at 10,000 K (or 1.2 keV, typical of a disk formed after a TDE). Additionally, the U band magnitudes from *Swift* UVOT, $17.39 \pm 0.02$ and $17.36 \pm 0.02$ (AB magnitude), did not change significantly between the two epochs.

**Keck-II DEIMOS Observations**

Optical observations of the host galaxy were conducted on 2015 June 19, approximately 1.5 months after the first radio follow-up observation, with the DEep Imaging Multi-Object Spectrograph (DEIMOS; Faber et al. 2003) on Keck-II. Figure 6.3 shows our follow-up spectrum of the host galaxy as compared with an SDSS spectrum of the host from 2000 September 29. No significant change in the spectrum is observed before and after the transient event, indicating that either there is no associated optical transient or that any optical signatures had faded by the time of our follow-up observations approximately 476 days after the launch of the outflow.

The host of CNSS J0019+00 is a Seyfert 2 galaxy, with nebular line flux ratios from the SDSS spectrum of log[OIII 5007]/H$\beta$ = 0.73 and log[NII]/H$\alpha$ = -0.57 (Blanton et al. 2017; Cappellari and Emsellem 2004; Dawson et al. 2016; Sarzi et al. 2006). This places the host just above the canonical line separating star-forming galaxies from AGN.

## 6.3 Modeling of the Synchrotron Spectra

The spectra of CNSS J0019+00 (Figure 6.2) are well described by synchrotron emission from an outflow expanding into and shocking the surrounding medium. From the evolution of the synchrotron spectra observed from CNSS J0019+00 in the radio follow-up observations, a number of parameters characterizing the source can be derived as a function of time, including the size of the source, its minimum kinetic energy, the ambient density, and microphysical parameters relevant to the generation of synchrotron emission. Each spectrum provides an independent constraint on these parameters, based only on the frequency and flux at the peak of the spectrum and
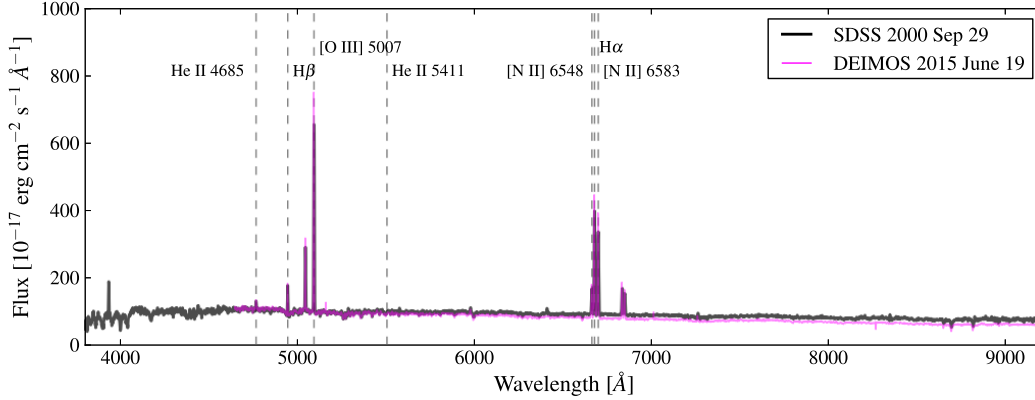
Figure 6.3: Optical spectra of the host galaxy of CNSS J0019+00, with SDSS in 2000 September 29 (black line) and DEIMOS on Keck-II in 2015 June 19 (magenta line) approximately 476 days post-outburst. The host is a Seyfert 2 galaxy, based on the measured nebular line flux ratios and high surface brightness nucleus.

the electron power law index ($p$, where $N_e(\gamma) \propto \gamma^{-p}$ for $\gamma \geq \gamma_m$, and $\gamma_m$ is the Lorentz factor of the lowest energy electrons in the distribution), which determines the slope of the optically thin half of the spectrum. This procedure has been well established and used to study both relativistically and non-relativistically expanding outflows, including for gamma-ray bursts (GRBs; e.g., Wijers and Galama 1999), supernovae (SNe; e.g., Chevalier 1998), and TDEs (.e.g, Zauderer et al. 2011).

In the following analysis, we follow Granot and Sari 2002 to model each synchrotron spectrum around the spectral break and Barniol Duran, Nakar, and Piran 2013 to calculate the source parameters using the observables derived from the synchrotron spectra. We fit the spectra of CNSS J0019+00 for a single spectral break, and assume that the peak frequency corresponds to the synchrotron self-absorption frequency $\nu_{\text{sa}}$. From Equation 1 of Granot and Sari 2002,

$$F_\nu = F_{\nu_b,\text{ext}} \left[ \left( \frac{\nu}{\nu_b} \right)^{-s\beta_1} + \left( \frac{\nu}{\nu_b} \right)^{-s\beta_2} \right]^{-1/s}, \tag{6.1}$$

where $\nu_b$ is the frequency of the spectral break, $F_{\nu_b,\text{ext}}$ is the extrapolated flux density at the location of $\nu_b$ where the power laws on either side of the spectral break, $\beta_1$ and $\beta_2$, respectively, meet. Here, we assume that the parameter $s$ which describes the sharpness of the spectral break, is related to the electron energy distribution power law $p$ by $s = 1.47 - 0.21p$, and that $\beta_2 = (1 - p)/2$ is the power law index in the optically thin region of the spectrum. These assumptions for the form of $s$ and $\beta_2$ correspond to the regime in which $\nu_m < \nu_{\text{sa}} < \nu_c$, where $\nu_c$ is the synchrotron

cooling frequency. We determine the best-fit parameters from the model described by Equation 6.1 for each follow-up spectrum using a Markov Chain Monte Carlo (MCMC) technique. Figure 6.2 shows the fit to each follow-up spectrum. The best-fit values for $p$, and the peak frequency and flux from the model fit, are listed in Table 6.3.

Table 6.3: Table of micro and macrophysical parameters for CNSS J0019+00, based on model fitting of the radio SEDs.

| (1) | (2) | (3) | (4) | (5) | (6) | (7) | (8) | (9) | (10) | (11) |
|---|---|---|---|---|---|---|---|---|---|---|
| $\Delta t$ | $\nu_p$ | $F_{\nu_p}$ | $p$ | $R_{eq}$ | $E_{eq}$ | $v_{ej}$ | $\gamma_e$ | $n_e$ | $B$ | $M_{ej}$ |
| (d) | (GHz) | (mJy) | | ($10^{16}$ cm) | ($10^{47}$ erg) | ($10^4$ km s$^{-1}$) | | (cm$^{-3}$) | (G) | ($10^{-3} M_\odot$) |
| 431 | 4.23 | 8.20 | 3.48 | 4.58 | 75.1 | 1.23 | 392 | 10.6 | 0.20 | 4.95 |
| 464 | 4.04 | 8.09 | 3.51 | 4.79 | 82.0 | 1.20 | 391 | 9.4 | 0.20 | 5.41 |
| 588 | 3.05 | 7.10 | 3.81 | 6.25 | 157.2 | 1.23 | 378 | 4.1 | 0.18 | 10.4 |
| 856 | 1.92 | 4.95 | 4.35 | 9.10 | 395.2 | 1.23 | 354 | 1.2 | 0.16 | 26.1 |

Both the peak flux and the peak frequency are declining with time – on 2015 May 10 the spectrum peaks at 8.2 mJy at 4.2 GHz; by 2016 July 08 the flux has declined to 5 mJy at 1.9 GHz. The optically thin spectral slope also appears to be evolving across epochs, steepening from $\nu^{-1.3}$ to $\nu^{-1.7}$, implying a steepening of the electron power law distribution from 3.48 to 4.35. We note that both the steepening of $p$ across such a short timescale (approximately a year) and such high values of $p$ are unusual, given that in most astrophysical scenarios $2.5 < p < 3$ (Jones and Ellison 1991). We also note that the optically thick spectral slope in each observation is consistent with approximately $\nu^{1.5}$ – this is shallower than the expected $\nu^{5/2}$ for a synchrotron self-absorbed spectrum. However, the optically thick side of our spectra are not well sampled at frequencies far away from the spectral break, and we proceed by assuming that the spectrum can be described by a $F_\nu \propto \nu^{5/2}$ power-law, extrapolating down to lower frequencies.

Knowledge of the synchrotron self-absorption frequency and peak flux at multiple epochs is sufficient for placing a strong constraint on the source size, or radius $R$, as a function of time, and therefore providing an estimate for the average velocity of the outflow. This estimate on the outflow velocity allows the source size to be extrapolated back in time and therefore providing an approximate date for the launch of the outflow $t_0$. As is frequently done for synchrotron-emitting systems for which the synchrotron self-Compton peak frequency and flux is not known, the assumption of equipartition (Pacholczyk 1970; Scott and Readhead 1977) between the energy in electrons and the energy in the magnetic field allows for the calculation of the

equipartition size (or $R_{\rm eq}$ for an assumed source geometry) and the minimum total equipartition energy, $E_{\rm eq}$ (see, e.g., Chevalier 1998).

From Equations 27 and 28 of Barniol Duran, Nakar, and Piran 2013:

$$R_{\rm eq} \approx (1 \times 10^{17}\ {\rm cm}) \left[87.2\,(525)^{p-1}\right]^{\frac{1}{13+2p}} \gamma_m^{\frac{2-p}{13+2p}}$$
$$\times \left[ F_{p,{\rm mJy}}^{\frac{6+p}{13+2p}}\, d_{L,28}^{\frac{2(p+6)}{13+2p}}\, v_{p,10}^{-1}\, (1+z)^{-\frac{19+3p}{13+2p}} \right] f_A^{-\frac{5+p}{13+2p}}\, f_V^{-\frac{1}{13+2p}}, \tag{6.2}$$

$$E_{\rm eq} \approx (1.3 \times 10^{48}\ {\rm erg}) \left[21.8\right]^{-\frac{2(p+1)}{13+2p}} \left[4\,(525)^{p-1}\gamma_m^{2-p}\right]^{\frac{11}{13+2p}}$$
$$\times \left[ F_{p,{\rm mJy}}^{\frac{14+3p}{13+2p}}\, d_{L,28}^{\frac{2(3p+14)}{13+2p}}\, v_{p,10}^{-1}\, (1+z)^{-\frac{27+5p}{13+2p}} \right] f_A^{-\frac{3(p+1)}{13+2p}}\, f_V^{\frac{2(p+1)}{13+2p}}, \tag{6.3}$$

where we are assumed to be in the Newtonian regime ($\Gamma = 1$) of a spherically expanding outflow ($f_A = 1$, $f_V = 4/3$), with $\gamma_m = 2$. We have multiplied both equations by factors of $4^{1/(13+2p)}$ and $4^{11/(13+2p)}$, respectively, to account for the spherical, non-beamed geometry of the outflow in the non-relativistic regime. These formulae are equivalent to the equipartition radius and energy for a non-relativistically expanding outflow described by Chevalier 1998.

Figure 6.4 shows the values of $R_{\rm eq}$ and $E_{\rm eq}$ as a function of time, for each of our radio follow-up observations. The source approximately doubles in size between our first observation on 2015 May to our fourth observation on 2016 July, from an equipartition radius of $R_{\rm eq} \sim 4.6 \times 10^{16}$ cm to $9.1 \times 10^{16}$ cm. This corresponds to an average expansion velocity of $v_{\rm ej} \approx 12{,}000\ {\rm km\,s}^{-1}$, with the equipartition radii well fit by a constant expansion velocity. This allows us to extrapolate the outflow back in time, to determine the age of the event at each of our observation epochs ($\Delta t \approx R_{\rm eq}/v_{\rm ej}$). The outflow was launched on 2014 March 06, 431 d prior to the CNSS epoch 4 observation in which it was discovered on 2015 March 21, and approximately one month after the location of CNSS J0019+00 was observed in CNSS epoch 3.

Using the equipartition radius values determined from Equation 6.2, we can determine the microphysical parameters of the system, including magnetic field strength, $B$, the Lorentz factor of the emitting electrons, $\gamma_e$, and the number of electrons, $N_e$. See Appendix 6.6 for a derivation of these quantities as a function of radius $R$. Combining these with Equation 6.2, we can write:

$$\gamma_e \approx (174.7)\, C_p \left[87.2\,(525)^{p-1}\right]^{-\frac{2}{13+2p}}\gamma_m^{-\frac{4-2p}{13+2p}}$$
$$\times \left[ F_{p,{\rm mJy}}^{\frac{1}{13+2p}}\, d_{L,28}^{\frac{2-2p}{13+2p}}\, (1+z)^{-\frac{1}{13+2p}} \right] f_A^{\frac{2(5+p)}{13+2p}}\, f_V^{\frac{2}{13+2p}}\, \eta^{\frac{5}{3}}, \tag{6.4}$$
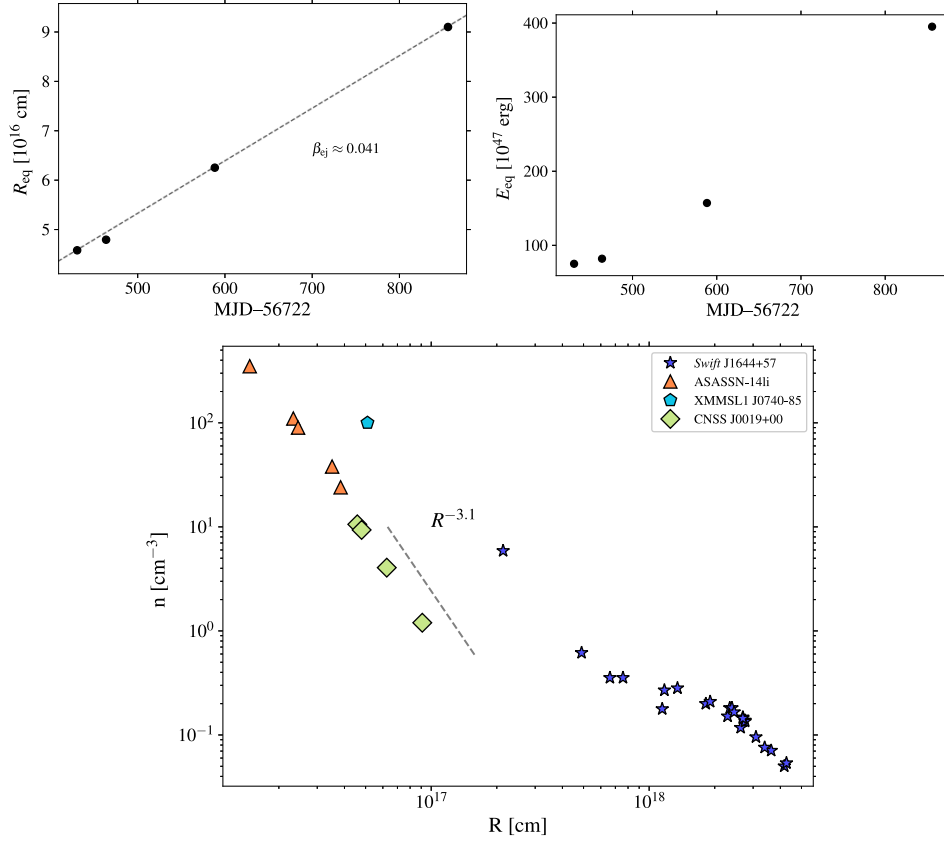
Figure 6.4: Equipartition radius (top) and energy (middle) as a function of time since outflow, as derived from the radio SEDs (see Equations 6.2 and 6.3). Each pair of $(R_{eq}, E_{eq})$ values are independent of the others, using only $F_p$, $\nu_p$, and $p$ as derived from each follow-up observation. Jointly, the equipartition radii from each epoch can therefore provide a strong constraint on the outflow velocity, which for CNSS J0019+00 is constant, at $\sim 12,000\,\mathrm{km\,s^{-1}}$. We also derive the ambient density as a function of the equipartition radius and compare with other radio-detected TDEs (bottom). The dashed line shows the circumnuclear density profile inferred from our observations. Data are from – for *Swift* J1644+57, Eftekhari et al. 2018; for ASASSN-14li, Alexander et al. 2016; for XMMSL1 J0740-85, Alexander et al. 2017.

$$B \approx \frac{(0.078\,\mathrm{G})}{x_p\,C_p^2}\left[87.2\,(525)^{p-1}\right]^{\frac{4}{13+2p}}\gamma_m^{\frac{8-4p}{13+2p}}$$
$$\times\left[F_{p,\mathrm{mJy}}^{-\frac{2}{13+2p}}\,d_{L,28}^{-\frac{4}{13+2p}}\,\nu_{p,10}\,(1+z)^{\frac{15+2p}{13+2p}}\right]f_A^{-\frac{20+4p}{13+2p}}\,f_V^{-\frac{4}{13+2p}}\,\eta^{-\frac{10}{3}}, \tag{6.5}$$

$$N_e \approx (6.9\times10^{53})\,\frac{x_p\,C_p^2}{\phi_p}\left[87.2\,(525)^{p-1}\right]^{-\frac{4}{13+2p}}\gamma_m^{-\frac{8-4p}{13+2p}}$$
$$\times\left[F_{p,\mathrm{mJy}}^{\frac{15-2p}{13+2p}}\,d_{L,28}^{\frac{30+4p}{13+2p}}\,\nu_{p,10}^{-1}\,(1+z)^{-\frac{28+4p}{13+2p}}\right]f_A^{\frac{20+4p}{13+2p}}\,f_V^{\frac{4}{13+2p}}\,\eta^{\frac{10}{3}}, \tag{6.6}$$

for $\eta = 1$ (corresponding to the regime where $\nu_p = \nu_{sa}$). Table 6.3 lists both the microphysical and macrophysical parameters determined from the best-fit model to the radio SEDs. The magnetic field $B$ and number of radiating electrons $N_e$ are all decreasing with time. From the latter, we can place a lower limit on the density of the ambient medium through which the shock is propagating (and assuming that a significant fraction of the electrons are relativistic and participating in the generation of synchrotron radiation). We assume that the radiation is originating from an emission region described by a thin shell (with thickness $dR \sim 0.1R_{eq}$) at the surface of the spherically expanding outflow. We find that the number density $n_e$ decreases by an order of magnitude between our follow-up observations, from $10.6\,\mathrm{cm}^{-3}$ to $1.2\,\mathrm{cm}^{-3}$ on a 14 month timescale (see Figure 6.3), with the density profile well-described as a $n(R) \propto R^{-3.1}$ power law.

We also estimate the minimum ejecta mass, $M_{ej}$, using the equipartition energy and average outflow velocity, $M_{ej} = 2E_{eq}/v^2$, for which we find $M_{ej} \approx 5{\times}10^{-3}-0.03\,M_\odot$. This $M_{ej}$ is more than an order of magnitude higher than what was seen from either ASASSN-14li and XMMSL1 J0740-85 (Alexander et al. 2016; Alexander et al. 2017), and consistent with the fact that the ambient medium we measure for CNSS J0019+00 is under-dense relative to the other two radio-detected thermal TDEs, while also being roughly an order of magnitude more energetic (based on the equipartition energy) than these events. Given that the ambient environment of CNSS J0019+00 is comparatively under-dense, the higher energetics must be explained through the ejection of a larger amount of stellar material.

## 6.4 Discussion

From the radio SEDs of CNSS J0019+00 and their evolution with time, we infer the presence of a sub-relativistically (spherically) expanding outflow moving at constant velocity ($v_{ej} \approx 12,000\,\mathrm{km\,s}^{-1}$), approximately doubling in size from $R_{eq} \sim 4.6 \times 10^{16}$ cm to $9.1 \times 10^{16}$ cm on the timescale of 14 months. Extrapolating this expansion back in time reveals an explosion date of 2014 March 06, approximately 1 yr prior to the discovery of CNSS J0019+00 in epoch 4 of CNSS. From our modeling of the synchrotron spectra, the outflow energy is on the order of $10^{49}$ erg, with an inferred ejecta mass of $\sim 0.03\,M_\odot$. VLBA observations show that the location of CNSS J0019+00 is consistent with the nucleus of the galaxy to within 1 pc. All of this points to a tidal disruption origin for CNSS J0019+00.

X-ray observations of the source around the time of discovery (and at an age of

1 yr) show no evidence for emission, with upper limits on the X-ray luminosity of $L_X \lesssim 4 \times 10^{40}\,\mathrm{erg\,s^{-1}}$. We note that our upper limit on any associated X-ray emission from the TDE are comparable to those placed on XMMSL1 J0740-85 at a similar post-explosion date (see Figure 6.5). We also note the lack of observed variability in the optical continuum or emission lines of the host galaxy (also at an age of 1 yr), including a lack of, e.g., HeII and H$\alpha$ emission lines, which are typically seen in TDEs as the bright continuum emission from the accretion disk is reprocessed by both the circum-nuclear material and tidal debris into emission line radiation (Ulmer 1999; Strubbe and Quataert 2011). However, we note that XMMSL1 J0740-85 showed no optical emission line variability pre- and post-explosion (at an age of ~2 months Saxton et al. 2017), and that for ASASSN-14li the HeII emission lines were largely gone after 178 d. In this context, the lack of emission line variability in the host spectrum of CNSS J0019+00 at ~470 d post-explosion is not unusual.

The presence of CNSS J0019+00 in the nucleus of a Seyfert 2 galaxy raises the possibility that the transient is associated with an accretion disk instability or turn-on of the central active galactic nucleus (AGN) rather than a single accretion event from a stellar tidal disruption. Seyfert 2 galaxies have been known to host TDEs, including NGC 4845, the host of the (off-axis jetted) tidal disruption event IGR J12580+0134 (Nikołajuk and Walter 2013). The Seyfert 2 galaxy IC3599 has shown recurring flaring that is believed to be due to repeated tidal disruption events (Campana et al. 2015), although the nature of this flaring remains controversial, and instabilities in the AGN accretion disk have not been ruled out (Grupe, Komossa, and Saxton 2015). The relatively high occurrence rate of TDEs in Seyfert galaxies may be explained by the influence of the accretion disk (Karas and Šubr 2007). The host of ASASSN-14li harbored a weak but persistent AGN (Alexander et al. 2016).

Any non-tidal disruption scenario for the origins of CNSS J0019+00 must be consistent with a sub-relativistic outflow in the nucleus of the galaxy, with a rapid turn-on (> 2 orders of magnitude increase in the radio luminosity on the timescale of approximately 1 yr). This is not typical of AGN variability, and the timescale is too rapid for an accretion disk instability (see, e.g., Saxton et al. 2015). This timescale is also inconsistent with other, more exotic, classes of TDE impostor (e.g., extreme mass ratio inspirals; Metzger and Stone 2017). The 1 pc offset of the transient from the center of the host galaxy introduces the possibility of this event as a rare circumnuclear supernova (Saxton, Perets, and Baskin 2018) within the dusty torus of the AGN, however CNSS J0019+00 is more than an order of magnitude more
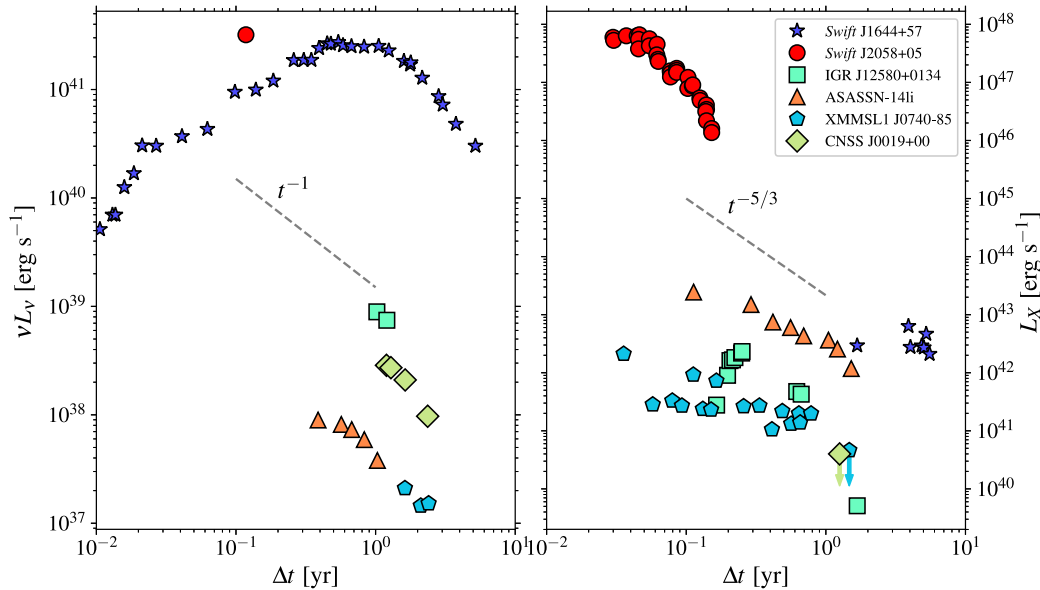
Figure 6.5: Radio luminosity (left) and X-ray luminosity (right) as a function of approximate time since explosion date, for all TDEs with confirmed radio detections. The reported radio luminosities correspond to frequencies between 4.5–6.0 GHz. This frequency range was chosen because it samples the optically thin side of the synchrotron spectrum at late times for the thermal TDE events plotted here. The dashed line shows the expected $\nu L_\nu \propto t^{-1}$ relation for an adiabatically expanding source in the optically thin regime. The radio data are taken from the following – for *Swift* J1644+57, Berger et al. 2012, Zauderer et al. 2013, and Eftekhari et al. 2018; for *Swift* J2058+05, Cenko et al. 2012; for IGR J12580+0134, Irwin et al. 2015; for ASASSN-14li, Alexander et al. 2016; for XMMSL1 J0740-85, Alexander et al. 2017. The X-ray data are taken from the following – for late-time X-ray emission from *Swift* J1644+57, Eftekhari et al. 2018; for *Swift* J2058+05, Cenko et al. 2012; for IGR J12580+0134, Lei et al. 2016 and Nikołajuk and Walter 2013; for ASASSN-14li, Brown et al. 2017; for XMMSL1 J0740-85, Saxton et al. 2017. The values with arrows are upper limits on the X-ray flux. The dashed line shows the theoretical $L_X \propto t^{-5/3}$ relation for fall-back accretion. We note that TDEs frequently deviate from this relation, but we plot it here as a general guide.

energetic than typical supernovae, and is more consistent with a TDE.

## 6.5 Conclusions

We have reported on the discovery of the radio transient CNSS J0019+00, which was found during the VLA Caltech–NRAO Stripe 82 Survey, and is located on the nucleus of a Seyfert 2 galaxy at a redshift of $z = 0.018$. Triggered radio follow-up observations showed a sub-relativistic ($\sim 12,000\,\mathrm{km\,s^{-1}}$), spherically expanding outflow with a kinetic energy of approximately $10^{49}$ erg. Comparison between the
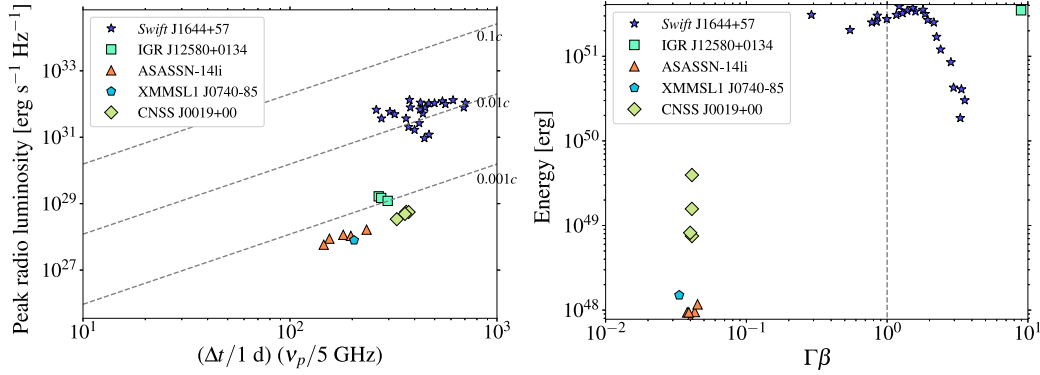
Figure 6.6: Peak radio luminosity as a function of the product of the peak time and peak frequency (left). The outflow velocity is proportional to $F_{p,\mathrm{mJy}}^{(6+p)/(13+2p)}\,\Delta t^{-1}\,v_p^{-1}$, and can therefore be represented on the plot with lines of constant velocity (assuming a constant $p$; see Figure 4 of Chevalier 1998). For the dashed lines here, we assume a canonical value of $p = 3$. The values for the radio luminosity, frequency, and time of peak for each object are determined from model fits to the data, rather than directly from the observations due to the fact that the radio SEDs are frequently poorly sampled. We also plot the total energy as a function of outflow velocity (right). The area to the left (right) of the dashed line represents non-relativistic (relativistic) outflows. CNSS J0019+00 has a constant expansion velocity that is consistent with the other radio-detected thermal TDEs, however it is more than an order of magnitude more energetic. The values from the model fits are taken from – for *Swift* J1644+57, Eftekhari et al. 2018; for IGR J12580+0134, Lei et al. 2016; for ASASSN-14li, Alexander et al. 2016; for XMMSL1 J0740-85, Alexander et al. 2017.

position of the galaxy nucleus in *Gaia* and the location of the radio transient in VLBA observations indicates the source is located 1 pc from the center of the galaxy. All of this indicates CNSS J0019+00 is likely the first radio-discovered TDE, and the third such radio-detection of a non-jetted, thermal TDE.

The theoretically expected TDE rate is approximately $\sim 10^{-5}$–$10^{-4}$ gal$^{-1}$ yr$^{-1}$ (Wang and Merritt 2004; Stone and Metzger 2016), roughly consistent with observational estimates of the TDE rate – e.g., from optical surveys (Holoien et al. 2016; van Velzen and Farrar 2014), or from observations of soft X-ray TDEs (Donley et al. 2002). Metzger, Williams, and Berger 2015 use this rate to calculate the number of TDEs that will be detected by a sample of future and ongoing GHz-frequency sky surveys. We use the numbers from Metzger, Williams, and Berger 2015 for VLASS in order to determine the expected rate in CNSS, given the two surveys' comparable sensitivities, observing frequencies, and survey cadence. The calculation by Metzger, Williams, and Berger 2015 is specific to non-thermal, jetted TDEs (akin to *Swift*

J1644+57), so we scale their values by a factor of $10^4$ to account for the fact that we are no longer restricted to the fraction of TDEs which produce relativistic jets that are also are beamed along our line of sight, in order to get the full, uncorrected rate of TDEs. Because thermal TDE events are less luminous than their jetted counterparts and therefore are detectable out to a smaller volume, we assume an isotropic distribution of TDEs in Euclidean space that scales as $N_{\text{TDEs}}(> F_\nu) \propto F_\nu^{-3/2}$ and multiply the rate by a factor of $\left(L_{\nu,p,\text{jetted}}/L_{\nu,p,\text{thermal}}\right)^{-3/2} \approx 1 \times 10^{-3}$. Taking into account the $270 \deg^2$ survey area of CNSS compared to the $34,000 \deg^2$ survey area of VLASS, we find that the expected rate of TDEs in CNSS is of order $0.1 - 1$, and consistent with our single detection of a TDE event in CNSS J0019+00. From this same calculation, we can expect on the order of 100 such TDE events to be detected in VLASS.

versity, Pennsylvania State University, Shanghai Astronomical Observatory, United Kingdom Participation Group, Universidad Nacional Autónoma de México, University of Arizona, University of Colorado Boulder, University of Oxford, University of Portsmouth, University of Utah, University of Virginia, University of Washington, University of Wisconsin, Vanderbilt University, and Yale University.

## 6.6 Appendix: Microphysical Parameters for a Synchrotron Emitting System

In solving for the microphysical parameters for a synchrotron emitting system, we approximately follow the steps of Kumar and Narayan 2009 and Barniol Duran, Nakar, and Piran 2013. For a synchrotron self-absorbed system, we can write the 3 microphysical parameters that describe the system as a function of the observable parameters $d_L$, the luminosity distance to the source; $z$, the redshift of the source; $\nu_p$, the peak frequency of the synchrotron spectrum; $F_{\nu_p}$, the flux at the peak frequency; and $p$, the power law index of the electron energy distribution, where $N_e(\gamma) \propto \gamma^{-p}$. (There is only a very weak dependence of the microphysical parameters on the value of $p$, however we include it here since it can be determined by fitting the optically thin side of the synchrotron spectrum.) The microphysical parameters are $\gamma_e$, the Lorentz factor of the electrons radiating at the peak frequency; $B$, the magnetic field strength; and $N_e$, the total number of synchrotron emitting electrons in the source. We also assume, in this case, to be in the Newtonian limit of a non-relativistically expanding source ($\Gamma = 1$).

From Rybicki and Lightman 1979, the peak frequency and power radiated per electron are

$$\nu_p = \frac{3x_p e B \gamma_e^2}{4\pi m_e c (1+z)},$$ (6.7)

$$P_{\nu_p} = \frac{\sqrt{3}\phi_p e^3 B(1+z)}{m_e c^2},$$ (6.8)

where $x_p$ and $\phi_p$ are dimensionless factors that are a function of $p$. From Wijers and Galama 1999 $x_p \approx 0.45$ and $\phi_p \approx 0.66$ for an electron power law index of $p = 3$. From 6.8, the source flux at $\nu_p$ is

$$F_{\nu_p} = \frac{\sqrt{3}\phi_p e^3 B N_e (1+z)}{4\pi d_L^2 m_e c^2}.$$ (6.9)

For frequencies below the synchrotron self-absorption frequency ($\nu \leq \nu_{\text{sa}}$), the source flux is equal to the flux of a blackbody in the Rayleigh-Jeans limit:

$$F_{\nu,\text{BB}} = \frac{2\pi m_e \gamma_e \nu^2 (1+z)^3 R^2}{d_L^2}.$$ (6.10)

Then, at the self-absorption frequency, the flux is

$$F_{\nu_{\text{sa}},\text{BB}} = C_p F_{\nu_p} \eta^{-1/3}, \tag{6.11}$$

where $\eta \equiv \nu_p/\nu_{\text{sa}}$, and $C_p$ is another dimensionless factor that is a function of $p$ (see Shen and Zhang 2009). Again assuming a power law index of $p = 3$, and that $\nu_m < \nu_{\text{sa}}$, $C_p \approx 5.2$.

Equations 6.7, 6.9, 6.10, and 6.11 can be combined to solve for $\gamma_e$, $B$, and $N_e$. The result is that

$$\gamma_e = \frac{C_p \eta^{5/3} d_L^2 F_{\nu_p}}{2\pi m_e \nu_p^2 (1+z)^3 R^2}, \tag{6.12}$$

$$B = \frac{16\pi^3 m_e^3 c \nu_p^5 (1+z)^7 R^4}{3 x_p C_p^2 e \eta^{10/3} d_L^4 F_{\nu_p}^2}, \tag{6.13}$$

$$N_e = \frac{3 x_p C_p^2 c \eta^{10/3} d_L^6 F_{\nu_p}^3}{4\sqrt{3}\pi^2 \phi_p m_e^2 e^2 \nu_p^5 (1+z)^8 R^4}. \tag{6.14}$$

The assumption of equipartition between the energy in the electrons and the energy in the magnetic field can be used with the equations above to solve for the equipartition radius, $R_{\text{eq}}$, at which the total energy, $E_{\text{eq}}$, is minimized, as is done in Barniol Duran, Nakar, and Piran 2013 to derive Equations 6.2 and 6.3.

## References

Alexander, K. D., et al. 2016. "Discovery of an Outflow from Radio Observations of the Tidal Disruption Event ASASSN-14li". *ApJL* 819, L25 (): L25. doi:10.3847/2041-8205/819/2/L25. arXiv: 1510.01226 [astro-ph.HE].

Alexander, K. D., et al. 2017. "Radio Observations of the Tidal Disruption Event XMMSL1 J0740-85". *ApJ* 837, 153 (): 153. doi:10.3847/1538-4357/aa6192. arXiv: 1610.03861 [astro-ph.HE].

Bade, N., S. Komossa, and M. Dahlem. 1996. "Detection of an extremely soft X-ray outburst in the HII-like nucleus of NGC 5905." *A&A* 309 (): L35–L38.

Barniol Duran, R., E. Nakar, and T. Piran. 2013. "Radius Constraints and Minimal Equipartition Energy of Relativistically Moving Synchrotron Sources". *ApJ* 772, 78 (): 78. doi:10.1088/0004-637X/772/1/78. arXiv: 1301.6759 [astro-ph.HE].

Becker, R. H., R. L. White, and D. J. Helfand. 1995. "The FIRST Survey: Faint Images of the Radio Sky at Twenty Centimeters". *ApJ* 450 (): 559. doi:10.1086/176166.

Berger, E., et al. 2012. "Radio Monitoring of the Tidal Disruption Event Swift J164449.3+573451. I. Jet Energetics and the Pristine Parsec-scale Environment of a Supermassive Black Hole". *ApJ* 748, 36 (): 36. doi:`10.1088/0004-637X/748/1/36`. arXiv: `1112.1697 [astro-ph.HE]`.

Blanton, M. R., et al. 2017. "Sloan Digital Sky Survey IV: Mapping the Milky Way, Nearby Galaxies, and the Distant Universe". *AJ* 154, 28 (): 28. doi:`10.3847/1538-3881/aa7567`. arXiv: `1703.00052`.

Bloom, J. S., et al. 2011. "A Possible Relativistic Jetted Outburst from a Massive Black Hole Fed by a Tidally Disrupted Star". *Science* 333 (): 203. doi:`10.1126/science.1207150`. arXiv: `1104.3257 [astro-ph.HE]`.

Bower, G. C. 2011. "Constraining the Rate of Relativistic Jets from Tidal Disruptions Using Radio Surveys". *ApJL* 732, L12 (): L12. doi:`10.1088/2041-8205/732/1/L12`. arXiv: `1103.4328 [astro-ph.HE]`.

Bower, G. C., et al. 2013. "Late-time Radio Emission from X-Ray-selected Tidal Disruption Events". *ApJ* 763, 84 (): 84. doi:`10.1088/0004-637X/763/2/84`. arXiv: `1210.0020 [astro-ph.HE]`.

Brown, J. S., et al. 2017. "The Long Term Evolution of ASASSN-14li". *MNRAS* 466 (): 4904–4916. doi:`10.1093/mnras/stx033`. arXiv: `1609.04403 [astro-ph.HE]`.

Burrows, D. N., et al. 2011. "Relativistic jet activity from the tidal disruption of a star by a massive black hole". *Nature* 476 (): 421–424. doi:`10.1038/nature10374`. arXiv: `1104.4787 [astro-ph.HE]`.

Campana, S., et al. 2015. "Multiple tidal disruption flares in the active galaxy IC 3599". *A&A* 581, A17 (): A17. doi:`10.1051/0004-6361/201525965`. arXiv: `1502.07184 [astro-ph.HE]`.

Cappellari, M., and E. Emsellem. 2004. "Parametric Recovery of Line-of-Sight Velocity Distributions from Absorption-Line Spectra of Galaxies via Penalized Likelihood". *PASP* 116 (): 138–147. doi:`10.1086/381875`. eprint: `astro-ph/0312201`.

Cenko, S. B., et al. 2012. "Swift J2058.4+0516: Discovery of a Possible Second Relativistic Tidal Disruption Flare?" *ApJ* 753, 77 (): 77. doi:`10.1088/0004-637X/753/1/77`. arXiv: `1107.5307 [astro-ph.HE]`.

Chevalier, R. A. 1998. "Synchrotron Self-Absorption in Radio Supernovae". *ApJ* 499 (): 810–819. doi:`10.1086/305676`.

Chornock, R., et al. 2014. "The Ultraviolet-bright, Slowly Declining Transient PS1-11af as a Partial Tidal Disruption Event". *ApJ* 780, 44 (): 44. doi:`10.1088/0004-637X/780/1/44`. arXiv: `1309.3009`.

Cook, D. O., et al. 2017. "Census of the Local Universe (CLU) I: Characterization of Galaxy Catalogs from Preliminary Fields". *arXiv e-prints* (). arXiv: `1710.05016`.

Dawson, K. S., et al. 2016. "The SDSS-IV Extended Baryon Oscillation Spectroscopic Survey: Overview and Early Data". *AJ* 151, 44 (): 44. doi:`10.3847/0004-6256/151/2/44`. arXiv: `1508.04473`.

Donley, J. L., et al. 2002. "Large-Amplitude X-Ray Outbursts from Galactic Nuclei: A Systematic Survey using ROSAT Archival Data". *AJ* 124 (): 1308–1321. doi:`10.1086/342280`. eprint: `astro-ph/0206291`.

Eftekhari, T., et al. 2018. "Radio Monitoring of the Tidal Disruption Event Swift J164449.3+573451. III. Late-time Jet Energetics and a Deviation from Equipartition". *ApJ* 854, 86 (): 86. doi:`10.3847/1538-4357/aaa8e0`. arXiv: `1710.07289 [astro-ph.HE]`.

Faber, S. M., et al. 2003. "The DEIMOS spectrograph for the Keck II Telescope: integration and testing". In *Instrument Design and Performance for Optical/Infrared Ground-based Telescopes*, ed. by M. Iye and A. F. M. Moorwood, 4841:1657–1669. in Proc. SPIE. doi:`10.1117/12.460346`.

Gaia Collaboration et al. 2018. "Gaia Data Release 2. Summary of the contents and survey properties". *A&A* 616, A1 (): A1. doi:`10.1051/0004-6361/201833051`. arXiv: `1804.09365`.

Gaia Collaboration et al. 2016. "The Gaia mission". *A&A* 595, A1 (): A1. doi:`10.1051/0004-6361/201629272`. arXiv: `1609.04153 [astro-ph.IM]`.

Gehrels, N., et al. 2004. "The Swift Gamma-Ray Burst Mission". *ApJ* 611 (): 1005–1020. doi:`10.1086/422091`.

Giannios, D., and B. D. Metzger. 2011. "Radio transients from stellar tidal disruption by massive black holes". *MNRAS* 416 (): 2102–2107. doi:`10.1111/j.1365-2966.2011.19188.x`. arXiv: `1102.1429 [astro-ph.HE]`.

Granot, J., and R. Sari. 2002. "The Shape of Spectral Breaks in Gamma-Ray Burst Afterglows". *ApJ* 568 (): 820–829. doi:`10.1086/338966`. eprint: `astro-ph/0108027`.

Grupe, D., S. Komossa, and R. Saxton. 2015. "IC 3599 Did It Again: A Second Outburst of the X-Ray Transient Seyfert 1.9 Galaxy". *ApJL* 803, L28 (): L28. doi:`10.1088/2041-8205/803/2/L28`. arXiv: `1504.01389 [astro-ph.HE]`.

Hills, J. G. 1975. "Possible power source of Seyfert galaxies and QSOs". *Nature* 254 (): 295–298. doi:`10.1038/254295a0`.

Holoien, T. W. -S., et al. 2016. "Six months of multiwavelength follow-up of the tidal disruption candidate ASASSN-14li and implied TDE rates from ASAS-SN". *MNRAS* 455 (): 2918–2935. doi:`10.1093/mnras/stv2486`. arXiv: `1507.01598 [astro-ph.HE]`.

Irwin, J. A., et al. 2015. "CHANG-ES V: Nuclear Outflow in a Virgo Cluster Spiral after a Tidal Disruption Event". *ApJ* 809, 172 (): 172. doi:`10.1088/0004-637X/809/2/172`. arXiv: `1507.00704`.

Jones, F. C., and D. C. Ellison. 1991. "The plasma physics of shock acceleration". *SSRv* 58 (): 259–346. doi:`10.1007/BF01206003`.

Karas, V., and L. Šubr. 2007. "Enhanced activity of massive black holes by stellar capture assisted by a self-gravitating accretion disc". *A&A* 470 (): 11–19. doi:`10.1051/0004-6361:20066068`. arXiv: `0704.2781`.

Komossa, S. 2015. "Tidal disruption of stars by supermassive black holes: Status of observations". *Journal of High Energy Astrophysics* 7 (): 148–157. doi:`10.1016/j.jheap.2015.04.006`. arXiv: `1505.01093 [astro-ph.HE]`.

Kumar, P., and R. Narayan. 2009. "GRB 080319B: evidence for relativistic turbulence, not internal shocks". *MNRAS* 395 (): 472–489. doi:`10.1111/j.1365-2966.2009.14539.x`. arXiv: `0812.0021`.

Lei, W.-H., et al. 2016. "IGR J12580+0134: The First Tidal Disruption Event with an Off-beam Relativistic Jet". *ApJ* 816, 20 (): 20. doi:`10.3847/0004-637X/816/1/20`. arXiv: `1511.01206 [astro-ph.HE]`.

Levan, A. J., et al. 2011. "An Extremely Luminous Panchromatic Outburst from the Nucleus of a Distant Galaxy". *Science* 333 (): 199. doi:`10.1126/science.1207143`. arXiv: `1104.3356 [astro-ph.HE]`.

Lindegren, L., et al. 2018. "Gaia Data Release 2. The astrometric solution". *A&A* 616, A2 (): A2. doi:`10.1051/0004-6361/201832727`. arXiv: `1804.09366 [astro-ph.IM]`.

Lodato, G., et al. 2015. "Recent developments in the theory of tidal disruption events". *Journal of High Energy Astrophysics* 7 (): 158–162. doi:`10.1016/j.jheap.2015.04.003`.

McMullin, J. P., et al. 2007. "CASA Architecture and Applications". In *Astronomical Data Analysis Software and Systems XVI*, ed. by R. A. Shaw, F. Hill, and D. J. Bell, 376:127. Astronomical Society of the Pacific Conference Series.

Metzger, B. D., and N. C. Stone. 2017. "Periodic Accretion-powered Flares from Colliding EMRIs as TDE Imposters". *ApJ* 844, 75 (): 75. doi:`10.3847/1538-4357/aa7a16`. arXiv: `1705.00643 [astro-ph.HE]`.

Metzger, B. D., P. K. G. Williams, and E. Berger. 2015. "Extragalactic Synchrotron Transients in the Era of Wide-field Radio Surveys. I. Detection Rates and Light Curve Characteristics". *ApJ* 806, 224 (): 224. doi:`10.1088/0004-637X/806/2/224`. arXiv: `1502.01350 [astro-ph.HE]`.

Mooley, K. P., et al. 2016. "The Caltech-NRAO Stripe 82 Survey (CNSS). I. The Pilot Radio Transient Survey In 50 deg$^2$". *ApJ* 818, 105 (): 105. doi:`10.3847/0004-637X/818/2/105`. arXiv: `1601.01693 [astro-ph.HE]`.

Mooley, K. P., et al. 2019. "The Caltech-NRAO Stripe 82 Survey (CNSS). II. On-the-fly Mosaicking Methodology". *ApJ* 870, 25 (): 25. doi:`10.3847/1538-4357/aaef7c`. arXiv: `1811.08445 [astro-ph.IM]`.

Nikołajuk, M., and R. Walter. 2013. "Tidal disruption of a super-Jupiter by a massive black hole". *A&A* 552, A75 (): A75. doi:`10.1051/0004-6361/201220664`. arXiv: `1304.0397 [astro-ph.HE]`.

Pacholczyk, A. G. 1970. *Radio Astrophysics. Nonthermal Processes in Galactic and Extragalactic Sources*. Series of Books in Astronomy / Astrophysics, San Francisco: Freeman, 1970.

Perley, R. A., et al. 2011. "The Expanded Very Large Array: A New Telescope for New Science". *ApJL* 739, L1 (): L1. doi:`10.1088/2041-8205/739/1/L1`. arXiv: `1106.0532 [astro-ph.IM]`.

Phinney, E. S. 1989. "Manifestations of a Massive Black Hole in the Galactic Center". In *The Center of the Galaxy*, ed. by M. Morris, 136:543. IAU Symposium.

Rees, M. J. 1988. "Tidal disruption of stars by black holes of 10 to the 6th-10 to the 8th solar masses in nearby galaxies". *Nature* 333 (): 523–528. doi:`10.1038/333523a0`.

Rybicki, G. B., and A. P. Lightman. 1979. *Radiative Processes in Astrophysics*. New York, Wiley-Interscience, 1979. 393 p.

Sarzi, M., et al. 2006. "The SAURON project - V. Integral-field emission-line kinematics of 48 elliptical and lenticular galaxies". *MNRAS* 366 (): 1151–1200. doi:`10.1111/j.1365-2966.2005.09839.x`. eprint: `astro-ph/0511307`.

Saxton, C. J., H. B. Perets, and A. Baskin. 2018. "Spectral features of tidal disruption candidates and alternative origins for such transient flares". *MNRAS* 474 (): 3307–3323. doi:`10.1093/mnras/stx2928`. arXiv: `1612.08093 [astro-ph.HE]`.

Saxton, R. D., et al. 2015. "Was the soft X-ray flare in NGC 3599 due to an AGN disc instability or a delayed tidal disruption event?" *MNRAS* 454 (): 2798–2803. doi:`10.1093/mnras/stv2160`. arXiv: `1509.05193`.

Saxton, R. D., et al. 2017. "XMMSL1 J074008.2-853927: a tidal disruption event with thermal and non-thermal components". *A&A* 598, A29 (): A29. doi:`10.1051/0004-6361/201629015`. arXiv: `1610.01788`.

Scott, M. A., and A. C. S. Readhead. 1977. "The low-frequency structure of powerful radio sources and limits to departures from equipartition". *MNRAS* 180 (): 539–550. doi:`10.1093/mnras/180.4.539`.

Shen, R.-F., and B. Zhang. 2009. "Prompt optical emission and synchrotron self-absorption constraints on emission site of GRBs". *MNRAS* 398 (): 1936–1950. doi:`10.1111/j.1365-2966.2009.15212.x`. arXiv: `0906.2597 [astro-ph.HE]`.

Stone, N. C., and B. D. Metzger. 2016. "Rates of stellar tidal disruption as probes of the supermassive black hole mass function". *MNRAS* 455 (): 859–883. doi:`10.1093/mnras/stv2281`. arXiv: `1410.7772 [astro-ph.HE]`.

Strubbe, L. E., and E. Quataert. 2011. "Spectroscopic signatures of the tidal disruption of stars by massive black holes". *MNRAS* 415 (): 168–180. doi:10.1111/j.1365-2966.2011.18686.x. arXiv: 1008.4131.

Ulmer, A. 1999. "Flares from the Tidal Disruption of Stars by Massive Black Holes". *ApJ* 514 (): 180–187. doi:10.1086/306909.

van Velzen, S., and G. R. Farrar. 2014. "Measurement of the Rate of Stellar Tidal Disruption Flares". *ApJ* 792, 53 (): 53. doi:10.1088/0004-637X/792/1/53. arXiv: 1407.6425.

van Velzen, S., E. Körding, and H. Falcke. 2011. "Radio jets from stellar tidal disruptions". *MNRAS* 417 (): L51–L55. doi:10.1111/j.1745-3933.2011.01118.x. arXiv: 1104.4105 [astro-ph.CO].

van Velzen, S., et al. 2013. "Constraints on off-axis jets from stellar tidal disruption flares". *A&A* 552, A5 (): A5. doi:10.1051/0004-6361/201220426. arXiv: 1210.0022 [astro-ph.HE].

Wang, J., and D. Merritt. 2004. "Revised Rates of Stellar Disruption in Galactic Nuclei". *ApJ* 600 (): 149–161. doi:10.1086/379767. eprint: astro-ph/0305493.

Wijers, R. A. M. J., and T. J. Galama. 1999. "Physical Parameters of GRB 970508 and GRB 971214 from Their Afterglow Synchrotron Emission". *ApJ* 523 (): 177–186. doi:10.1086/307705. eprint: astro-ph/9805341.

Zauderer, B. A., et al. 2011. "Birth of a relativistic outflow in the unusual $\gamma$-ray transient Swift J164449.3+573451". *Nature* 476 (): 425–428. doi:10.1038/nature10366. arXiv: 1106.3568 [astro-ph.HE].

Zauderer, B. A., et al. 2013. "Radio Monitoring of the Tidal Disruption Event Swift J164449.3+573451. II. The Relativistic Jet Shuts Off and a Transition to Forward Shock X-Ray/Radio Emission". *ApJ* 767, 152 (): 152. doi:10.1088/0004-637X/767/2/152. arXiv: 1212.1173 [astro-ph.HE].

*Chapter 7*

# SUMMARY AND LOOKING TO THE FUTURE

As Project Scientist for the OVRO-LWA-352, I will oversee the carrying-out of science goals with the array, as well as continue to lead the 3 key areas of transient science that were covered by this thesis: compact object merger follow-up, exploration of low-frequency transient phase space through non-targeted transient surveys, and targeted searches for extrasolar space weather events.

**Compact Object Mergers and EM-GW Follow-up**

For the duration of the Advanced LIGO–Virgo O3 observing run, which began in 2019 April and will continue for another year, I am leading the OVRO-LWA GW follow-up campaign. The OVRO-LWA is continuously observing, with visibility data stored to a 24 h-long ring buffer. In the event of a gravitational wave trigger, we are the only EM facility with the ability to provide observations coincident with and preceding the time of the GW event detection (provided that all of or a significant portion of the localization error region is above the horizon at OVRO-LWA at the time of the event). This is especially valuable given the latency between event detection and alert notices sent out to the EM community, which is still currently (as of this writing) in the regime of human inspection, verification, and sending of alerts, adding a significant time delay over an automated trigger.

I demonstrated with the work detailed in Chapter 3 and published in Anderson et al. 2018 that placing constraints on models predicting coherent radio emission associated with short GRBs was possible with the OVRO-LWA – indeed, we placed the most sensitive constraints to-date. This successful proof-of-concept has already carried over into the EM-GW domain, with OVRO-LWA observing and responding to GW alerts during the Advanced LIGO–Virgo O2 observing run throughout 2017. The BNS merger GW170817 (Abbott et al. 2017b, 2017a), which yielded such a diversity of EM counterparts (Coulter et al. 2017; Kasliwal et al. 2017; Evans et al. 2017; Troja et al. 2017; Hallinan et al. 2017), was unfortunately below the horizon at the OVRO-LWA, making coincident observations and searches for prompt, low frequency counterparts impossible. However, the ability to carry out de-dispersion searches across large regions of the OVRO-LWA field-of-view was shown through work that was conducted with Caltech LIGO graduate student

Thomas A. Callister, whom I have worked with and mentored for the last year and a half on further developing an OVRO-LWA EM-GW follow-up framework. Utilizing the pipeline and infrastructure I developed to search for prompt emission from short GRB 170112A, we placed similar constraints on emission from the BH-BH merger GW170104 (Callister et al. 2019) – this represents the first search for prompt radio emission from a GW event (see Figure 7.1). In addition, the OVRO-LWA-352 upgrade will include the ability to dump the raw voltage stream from all antennas (for up to a few minutes at a time), specifically to follow-up GW events. Beamforming of the raw data to the location of the GW event significantly more sensitive (and temporally matched) dedispersion searches on millisecond timescales.

While the existence and detectability of prompt radio emission from BNS mergers is speculative at best, such emission from BBH mergers, where there is presumably no associated material from which to generate electromagnetic emission, is speculative in the extreme. However, the risk of pursuing such transient emission is low, while the potential returns are extremely high in providing a prompt, EM counterpart that is localizable to arcminutes and which contains, imprinted on the radio pulse itself, information about the density and magnetic field of the medium through which it propagates, as well as the potential for revealing a pioneering new class of transient sources and associated physics. The Advanced LIGO–VIRGO O3 observing run was predicted to detect as many as 1–50 BNS mergers (Abbott et al. 2018), and already during the final week prior to the submission of this thesis, 2 likely BNS events were found. We have followed up both of these events with the OVRO-LWA (see Figure 7.2), and the search for prompt radio emission is underway.

**Non-Targeted Transient Surveys**

As the results of Chapter 4 demonstrate, the OVRO-LWA is beginning to push into unexplored regions of low-frequency transient phase space. The non-detection of any transients in the 31 hour survey akin to that discovered by Stewart et al. 2016 with LOFAR, despite an expectation of as many as ∼10 such events given their reported event rate, indicates that this potential population of sources is either rarer than expected (with a surface density as low as $2.5 \times 10^{-8}$ deg$^{-2}$ at flux densities of 10.5 Jy and sub-minute timescales) or is associated with exotic emission mechanisms that are intrinsically narrow in bandwidth ($\lesssim$MHz). We also demonstrated the difficulties associated with wide-field, sub-100 MHz surveys, where the sky is anything but quiet due to terrestrial and atmospheric events (RFI, meteor reflections, ionospheric scintillation and refraction).
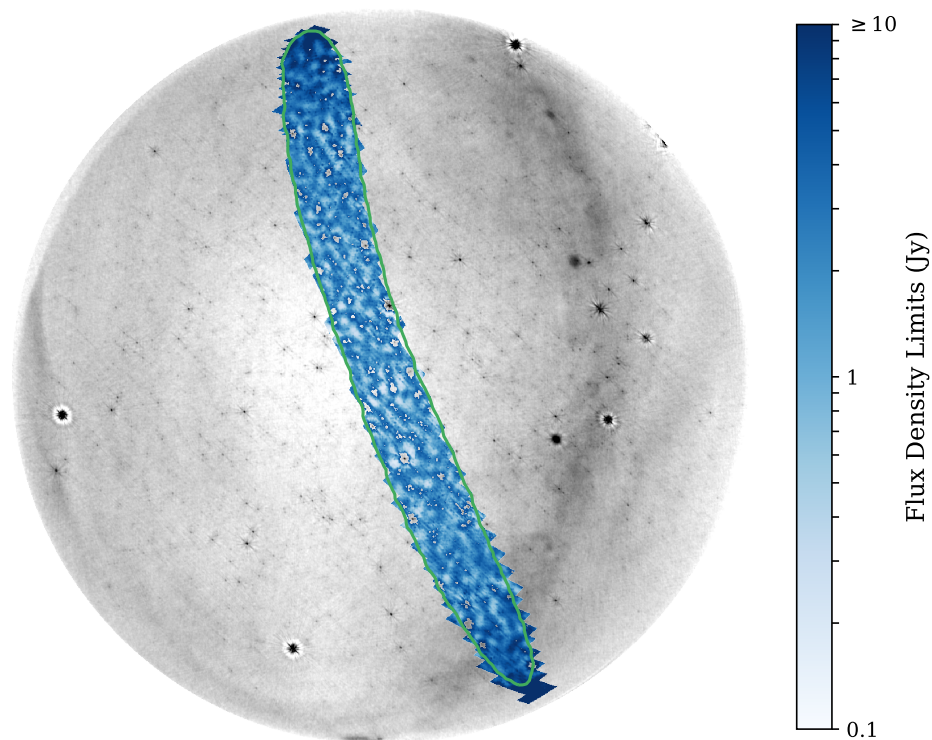
Figure 7.1: 95% confidence upper limits on the flux density of prompt radio emission across the OVRO-LWA frequency band (centered at 56 MHz) over the 95% confidence localization region contained within the OVRO-LWA field-of-view, for GW170104. The error region searched covers approximately 900 deg$^2$, and the median flux density limit is 2.4 Jy. Combining the flux density limits with the distance constraints from the GW signal, the isotropic luminosity of GW170104 across the 27–84 MHz band is $L \leq 2.5 \times 10^{41}$ erg s$^{-1}$. Taken from Figure 7 of Callister et al. 2019.

The next steps with the OVRO-LWA for continuing to push further into this phase space are already underway. I am working with Caltech astronomy graduate Yuping Huang to use the transient pipeline I developed for the 31 hour survey on an expanded, 120 hour dataset that was taken with the OVRO-LWA in 2018 March. We are working to improve multiple components of this larger survey, including incorporating better calibration solutions derived from multiple integrations that average out the errors introduced by the ionosphere; matched filter searches that are more sensitive to different combinations of potential source class emission mechanisms characterized by different bandwidths and timescales; and blind injection
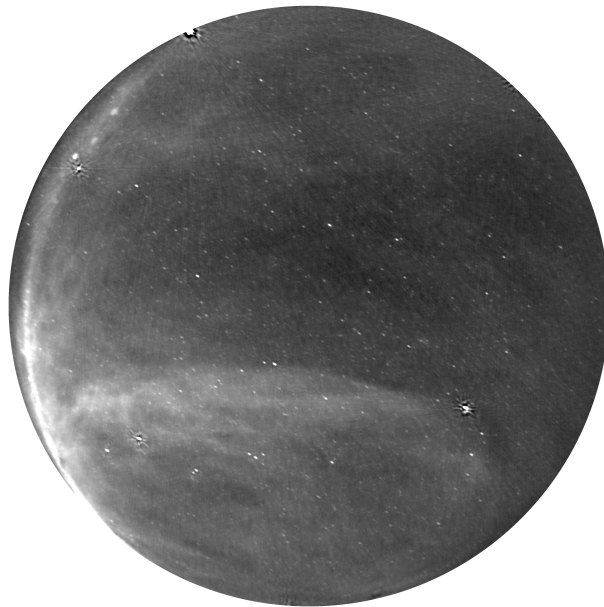
Figure 7.2: OVRO-LWA snapshot image from the time of merger of S190425z, the first BNS merger of the Advanced LIGO–Virgo O3 run. Approximately 57% of the ~10,000 deg$^2$ localization region is covered by the OVRO-LWA field-of-view. The OVRO-LWA is already at a stage where rapid follow-up and data reduction for GW events is possible.

of simulated transient signals in order to better constrain our sensitivity limits and characterize the degree to which any potential transient sources are missed by the existing pipeline.

**Extrasolar Space Weather**

In my capacity as Project Scientist of OVRO-LWA, I am most excited about continuing the search for exoplanetary and stellar radio emission. While no stellar Type II bursts indicative of CMEs have yet been detected, and no ECME from exoplanets providing direct evidence of planetary magnetic fields and insight into the dynamos that power them have been seen, the path forward to detecting these and beginning to piece together a space-weather-centric formulation of planetary habitability is clear. Using the OVRO-LWA to target every system out to distances of 25 pc at sub-100 MHz frequencies is unique and also the necessary route to detecting and characterizing extrasolar space weather environments for a diverse range of planet hosts. What is needed next are more sensitive searches, and at even lower frequencies.

The OVRO-LWA-352 is ideally suited to achieve the former. A planned 1000 hr survey in Stokes I and V, as well as the generation of wide-bandwidth m-mode analysis maps in Stokes I and V, is motivated particularly by the detection of extrasolar space weather events. A significant technical achievement that will be demonstrated with the OVRO-LWA-352, and which will be critical to reaching the necessary sensitivities, is the mapping of the complex gain pattern of each individual dipole in the array. The method I developed and described in Chapter 2 for performing a polarization calibration and correction for the array and generating higher fidelity Stokes V images is limited by the fact that I am using a simulated (and therefore idealized) gain pattern for a single dipole, and generalizing this across the full array. In practice, each dipole's gain pattern will vary, due to effects associated with crosstalk between adjacent antennas, the ionosphere, variations in antenna orientation, etc.

This mapping is being attempted through two independent methods – pulsar beam holography with the 40-m dish located at OVRO, and through beam mapping with drones. The former is akin to what is being done with the Canadian Hydrogen Intensity Mapping Experiment (CHIME; Berger et al. 2016) using the on-site 26-m dish. The latter has been demonstrated at low frequencies by Jacobs et al. 2017, and a similar analysis will be carried out with the OVRO-LWA. However, this work has so far been restricted to amplitude-only information; beam mapping for OVRO-LWA through the use of an antenna mounted on a drone will require the use of a phase reference source, in order to capture both amplitude and phase information and generate accurate full Stokes maps for each LWA antenna.

Fully mapped, per-antenna beams will enable more accurate DD calibration of the OVRO-LWA, and beam corrections (performed during the gridding of visibilities step in the imaging process, akin to A-projection) to reduce artifacts associated with bright source sidelobes in image-space. With this method in place, thermal noise-limited Stokes V maps are achievable, and the delivery of circular polarization images with 150 mJy noise will make the detection of stellar and planetary radio emission much more feasible.

The second requirement, of observations at even lower frequencies, requires moving beyond the Earth's ionosphere and into space, where observations can be conducted well below the ~10 MHz limit normally imposed by the ionosphere's plasma frequency. Such space- or moon-based arrays are already in the planning and development phase; for now, the OVRO-LWA is ideal for demonstrating the methods and

techniques that will be needed for these future arrays.

Our solar system at low radio frequencies is dynamic and bright – there is no reason to think that we are unique among planetary systems in this sense.

I conclude this look to the future with a look to the past. In an article detailing the history and development of the Owens Valley Radio Observatory, Prof. Marshall Cohen wrote in 1994 that OVRO and Caltech "still provides students with hands-on experience at building telescopes and their instrumentation, but there are only a few institutions left in the world where such opportunities now exist. It is much more difficult to provide this experience to graduate students now than it was 30 years ago, because radio observatories everywhere have become more expensive, more formal, and more automated...At Caltech [we] have worked to maintain an environment where students use their hands for more than typing on a keyboard" (Cohen 1994). That particular legacy of OVRO remains true today. As has been the case over the course of my thesis work, I hope to continue to learn from the fundamentals and intricacies of radio astronomy – from the OVRO-LWA-352 in the near future, and from whatever the more distant future brings – through the blood, sweat, and tears wrought during the hands-on work of building an instrument and bringing it into the regime of fully- (or at least semi-) functional machine and ripe for making scientific discoveries.

## References

Abbott, B. P., et al. 2017a. "Gravitational Waves and Gamma-Rays from a Binary Neutron Star Merger: GW170817 and GRB 170817A". *ApJL* 848, L13 (): L13. doi:`10.3847/2041-8213/aa920c`. arXiv: `1710.05834 [astro-ph.HE]`.

– . 2017b. "Multi-messenger Observations of a Binary Neutron Star Merger". *ApJL* 848, L12 (): L12. doi:`10.3847/2041-8213/aa91c9`. arXiv: `1710.05833 [astro-ph.HE]`.

Abbott, B. P., et al. 2018. "Prospects for observing and localizing gravitational-wave transients with Advanced LIGO, Advanced Virgo and KAGRA". *Living Reviews in Relativity* 21, 3 (): 3. doi:`10.1007/s41114-018-0012-9`. arXiv: `1304.0670 [gr-qc]`.

Anderson, M. M., G. Hallinan, M. W. Eastwood, R. M. Monroe, H. K. Vedantham, S. Bourke, L. J. Greenhill, J. Kocz, T. J. W. Lazio, D. C. Price, F. K. Schinzel, Y. Wang, and D. P. Woody. 2018. "A Simultaneous Search for Prompt Radio Emission Associated with the Short GRB 170112A Using the All-sky Imaging Capability of the OVRO-LWA". *ApJ* 864 (22): 1–11. doi:`10.3847/1538-4357/aad2d7`. arXiv: `1711.06665 [astro-ph.HE]`.

Berger, P., et al. 2016. "Holographic beam mapping of the CHIME pathfinder array". In *Ground-based and Airborne Telescopes VI*, 9906:99060D. Proc. SPIE. doi:`10.1117/12.2233782`. arXiv: `1607.01473 [astro-ph.IM]`.

Callister, T. A., et al. 2019. "A First Search for Prompt Radio Emission from a Gravitational-Wave Event". *arXiv e-prints* (). arXiv: `1903.06786 [astro-ph.HE]`.

Cohen, M. H. 1994. "The Owens Valley Radio Observatory: Early Years". *Engineering and Science* 57 (3): 8–23. `http://resolver.caltech.edu/CaltechES:57.3.Cohen`.

Coulter, D. A., et al. 2017. "Swope Supernova Survey 2017a (SSS17a), the optical counterpart to a gravitational wave source". *Science* 358 (): 1556–1558. doi:`10.1126/science.aap9811`. arXiv: `1710.05452 [astro-ph.HE]`.

Evans, P. A., et al. 2017. "Swift and NuSTAR observations of GW170817: Detection of a blue kilonova". *Science* 358 (): 1565–1570. doi:`10.1126/science.aap9580`. arXiv: `1710.05437 [astro-ph.HE]`.

Hallinan, G., et al. 2017. "A radio counterpart to a neutron star merger". *Science* 358 (): 1579–1583. doi:`10.1126/science.aap9855`. arXiv: `1710.05435 [astro-ph.HE]`.

Jacobs, D. C., et al. 2017. "First Demonstration of ECHO: an External Calibrator for Hydrogen Observatories". *PASP* 129, no. 3 (): 035002. doi:`10.1088/1538-3873/aa56b9`.

Kasliwal, M. M., et al. 2017. "Illuminating gravitational waves: A concordant picture of photons from a neutron star merger". *Science* 358 (): 1559–1565. doi:`10.1126/science.aap9455`. arXiv: `1710.05436 [astro-ph.HE]`.

Stewart, A. J., et al. 2016. "LOFAR MSSS: detection of a low-frequency radio transient in 400 h of monitoring of the North Celestial Pole". *MNRAS* 456 (): 2321–2342. doi:`10.1093/mnras/stv2797`. arXiv: `1512.00014 [astro-ph.HE]`.

Troja, E., et al. 2017. "The X-ray counterpart to the gravitational-wave event GW170817". *Nature* 551 (): 71–74. doi:`10.1038/nature24290`. arXiv: `1710.05433 [astro-ph.HE]`.

# INDEX